UNIVERSITÉ DE SHERBROOKE

Faculté de génie
Département de génie électrique et de génie informatique

Optimisation de la Conception du Moteur Synchrone à Excitation Hybride pour Véhicules Électriques à Haut Performance

Design Optimization of Hybrid Excitation Synchronous Motor for Electric Vehicles with Enhanced Performance

Thèse de doctorat
Spécialité : génie électrique et informatique

Ahmad Shah Mohammadi

Jury : João Pedro F. TROVÃO (directeur)
Minh CAO TA
Carlos HENGGELER ANTUNES
Ahmed KHOUMSI
Emmanuel VINOT

Sherbrooke (Québec) Canada Mars 2020

MEMBRES DU JURY

M. João Pedro F. TROVÃO, Directeur

Professeur Agrégé, Université de Sherbrooke (UdeS), QC, Canada

M. Minh C. Ta, Évaluateur

Professeur Associé, Hanoi University of Science and Technology (HUST), Vietnam

M. Carlos Henggeler Antunes, Évaluateur

Professeur Titulaire, University of Coimbra, Portugal

M. Ahmed Khoumsi, Rapporteur

Professeur Titulaire, Université de Sherbrooke (UdeS), QC, Canada

M. Emmanuel Vinot, Évaluateur

Chargé de recherche, HDR, Institut français des sciences et technologies des transports, de l'aménagement et des réseaux (IFSTTAR), France

"The best way to know a city is to get lost in it."

A homeless man

Acknowledgements

I would like to thank my supervisor, prof. João Pedro F. TROVÃO, for his guidance and support through each stage of the process, and also for giving me this great opportunity. This work was supported in part by Canada Research Chairs Program (grant 950-230672),

I would like to acknowledge the respectful jury members for their constructive comments and also their commitment that helped me present my work on the due date.

I would like to thank the staff at university of Sherbrooke, especially, the e-TESC lab members, for helping me to finalize this project. I wish to extend my special thanks to Mr. Mebrahtom Beraki for his wonderful support and friendship during my journey.

My wife, Zahra Akbari, was supportive and harmonious in the path of my research. For this, I am extremely grateful. I also appreciate the overwhelming support of my family back in Iran and here in Québec, especially Madame Lucile Paré Soucy.

Résumé

Depuis 1970, les préoccupations de l'humanité envers les changements climatiques ont poussé les chercheurs à faire des études approfondies pour optimiser les machines électriques pour avoir des véhicules électriques plus performants et moins énergivores. La conception optimale de véhicules électriques (EV) peut contribuer pour un marché automobile plus exigeant et jouer un rôle principal pour le futur du transport durable des biens et des personnes. Les machines électriques se trouvent au cœur de la conversion d'énergie électromécanique, qui ont suscité beaucoup d'intérêts et d'efforts pour augmenter leur rendement et réduire leur coût.

Cette thèse propose une méthodologie et une mise en œuvre pour minimiser le coût et maximiser l'efficacité d'une machine synchrone à excitation hybride (HESM) pour un véhicule donné et un cycle de conduite sélectionné. L'hybridation du système d'excitation peut combiner les qualités favorables comme un couple élevé à basse vitesse avec une capacité de surcharge supérieure, un défluxage exceptionnelle et une plage de vitesse prolongée de puissance constante (CPSR), une efficacité élevée et une contrôlabilité flexible dans les modes de traction et de freinage régénératif. Avec la technologie HESM, nous pouvons également passer des aimants de terres rares aux aimants en ferrite bon marché, et garantir l'approvisionnement pour l'industrie automobile.

Le HESM conçu dans ce travail répond à trois exigences du véhicule : la vitesse de croisière maximale, le temps d'accélération et la capacité de monter une pente, avec un surdimensionnement minimal ou nulle de la chaîne de traction. Une optimisation multiniveau avec une interaction entre la vision composant et la vision système est proposée et validée. L'optimisation au niveau du composant est développée sur la base de l'algorithme génétique de tri non dominé (NSGA-II). Une nouvelle formulation pour les fonctions objectives est proposée pour l'optimisation simultanée de la conception de la machine et de la minimisation de son coût. Après avoir optimisés onze HESM au niveau du composant, pour maximiser l'efficacité, une optimisation au niveau du système est réalisée pour trouver le HESM optimal avec le plus haut rendement global sur le cycle de conduite donné. Une validation de la conception finale de la HESM présente un meilleur rendement global sur le cycle de conduite de 18,65% en relation à une machine synchrone à excitation séparée équivalente et 15,8% en relation à une à aiment permanent.

En raison de la direction 3D du flux magnétique dans la topologie HESM sélectionnée, l'analyse par éléments finis (FEA) prenait beaucoup de temps et de ressources computationnelles. Afin d'évaluer les fonctions objectives lors de l'optimisation, un nouveau modèle a été développé basé sur un réseau de circuits magnétiques équivalents 3D (MEC). Ce modèle prédit bien la non-linéarité des matériaux magnétiques, par rapport aux simulations FEA. Enfin, le HESM optimisé final est évalué grâce à la technique FEA.

Mots clés:

Plage de vitesse de puissance constante, méthodologie de conception véhicule électrique, analyse par éléments finis, efficacité globale, moteur synchrone à l'excitation hybride, rapport d'hybridation, circuit équivalent magnétique, l'algorithme génétique de tri non dominé (NSGA-II), optimisation.

Abstract

Since 1970, the ever-growing concerns of human community for the life-threatening environmental changes have pushed the policy makers to decarbonize those sectors with high energy demands, including the transportation industry. Optimal designs of Electric Vehicles (EVs) can contribute to today's exigent car market, and take the leading role for future sustainable transportation of human and goods. At the heart of electromechanical energy conversion lays the electrical machines, which have attracted lots of interests and efforts for efficiency increase and cost reduction.

In this thesis, a methodology is proposed and implemented to design and optimize the cost and efficiency of a Hybrid Excitation Synchronous Machine (HESM) for a given vehicle and a desired driving cycle. Hybridization in the excitation system can combine the favorable qualities of high-torque at low-speed with superior overloading capability, exceptional flux weakening and extended Constant Power Speed Range (CPSR), high efficiency, and flexible controllability in motoring and generation modes. With HESM technology, we can also shift from the rare-earth magnets towards the cheap ferrite magnets and guaranty the supply for motor industry.

The designed HESM in this work responds to three requirements of the vehicle, namely, the maximum cruising speed, acceleration time, and gradeability, with the least or null overdesign in the drivetrain. At the same time, it will have the maximum global efficiency over the driving cycle, and the minimum cost for the material. The optimization is conducted at either of the component and system levels. The optimization at component-level is developed based on the Non-dominated Sorting Genetic Algorithm-II (NSGA-II). A new formulation for the objective functions is proposed, which deals with the design optimization and cost minimization, simultaneously. To maximize the efficiency, a system-level search is conducted to find the optimum HESM with the highest global efficiency over a given driving cycle.

Due to the 3D direction of magnetic flux in the selected HESM topology, the Finite Element Analysis (FEA) was very time- and process-consuming. To be able to evaluate the objective functions during the optimization, a new model has been developed based on a 3D Magnetic Equivalent Circuit (MEC) network. This model predicts well the non-linearity of magnetic materials, as compared with the FEA simulations. At last, the final optimized HESM is evaluated by the virtue of FEA technique.

Keywords:

Constant Power Speed Range (CPSR), Design Methodology, Electric Vehicle (EV), Finite Element Analysis (FEA), Global Efficiency, Hybrid Excitation Synchronous Motor (HESM), Hybridization Ratio (HR), Magnetic Equivalent Circuit, Non-dominated Sorting Genetic Algorithm II (NSGA-II), Optimization.

Table of contents

List of figures

List of tables

Nomenclature/Symbols

Abbreviations

ANOVA	Analysis of Variance
CPSR	Constant Power Speed Range
CVT	Continuously Variable Transmission
d.f.	degree of freedom
DQEC	D-Q lumped parameter Equivalent Circuit
DSPMM	Doubly Salient Permanent Magnet Machine
DTC	Direct Torque Control
EM	Electric Motor
EMF	ElectroMotive Force
EMR	Energy Macroscopic Representation
Err_HR	Error in HR
ESS	Energy Storage System
e-TESC	Transport, Energy Storage and Conversion
EV	Electric Vehicles
FEA	Finite Element Analysis
F-S	Force–Speed
FSHESM	Flux Switching Hybrid Excitation Synchronous Machine
FW	Flux Weakening
GB	Gear Box
HESM	Hybrid Excitation Synchronous Machine
HESS	Hybridized Energy Storage Systems
HR	Hybridization Ratio
ICE	Internal Combustion Engine
IEA	International Energy Agency
IM	Induction Machine
IPM	Internal Permanent Magnet
MEC	Magnetic Equivalent Circuit
MMF	Magnetomotive Force
MS	mean square
MTPA	Maximum Torque per Ampere
MTPV	Maximum Torque per Voltage
NEDC	New European Driving Cycle
NSGA-II	Non-dominated Sorting Genetic Algorithm - II
OF	Objective Function
PM	Permanent Magnet
PMSM	Permanent Magnet Synchronous Machine
PU	Per-Unit
RM	Reluctance Machine
RPM	Round Per Minute
SPMSM	Surface-mounted Permanent Magnet Synchronous Machine

SRM	Switched Reluctance Machine
SS	sum of squares
T-S	torque-speed
UHDC	US Highway Driving Cycle
US06	Supplemental Federal Test Procedure
WE	Wound Excitation
WESM	Wound Excitation Synchronous Machine

Symbols

A_f	Vehicle front area
B	Magnetic flux density
B_{ag}	Airgap flux density
C_D	Aerodynamic drag coefficient
f	frequency
f_r	Rolling resistance coefficient
F_{t-Vmax}	tractive force at maximum cruising speed
g	Acceleration of gravity, Radial airgap
g_{exc}	Horizontal airgap
g_t	Gearbox transmission ratio
H	Magnetic field intensity
h_{sy}	stator yoke height
h_{st}	Stator tooth height
h_{PM}	PM height (thickness)
h_{ssi}	Outer stator solid iron height
i	Grade Slope at 100 km/h
I	current
I_e	excitation current
I_q , I_d	d- and q-axis currents
I_{qc} , I_{dc}	d- and q-axis core loss currents
I_{qm} , I_{dm}	d- and q-axis magnetizing currents
K_f	excitation coefficient
l_{tot}	Total motor length
l_s	stator active length
l_{ssi}	Outer stator end cap length
l_{s-lam}	Stator stack lamination length
L_d , L_q	d- and q-axis inductances
M	Vehicle mass
M_e	mutual inductance between WE and armature coils
MMF_{WE}	WE Magnetomotive Force
N	Speed, number of coil turns
N_b	Base Speed
N_{max}	Max Speed
N_{exc}	WE coils number of turns
N_s	armature coils number of turns

P	Power, price, permeance
P_{max}	maximum power
P_{FeSi}	silicon steel sheets price
P_{Fe}	Iron–silicon alloy price
P_{PM}	PM material price
P_{sh}	shaft material price
P_{cu}	copper losses, or copper magnetic wire price
P_c	core losses
R_{tot}	Total outside radius
R_a , R_c , R_e	armature, core loss, and excitation resistances
r_d	Wheels radius
R_{ri}	Rotor inside radius
R_{ro}	Rotor outside radius
S_{slot}	total stator slot area
T	torque
T_e	electromechanical torque
t_a	Acceleration Time
V	Voltage, volume, linear velocity
V_{max}	Maximum Speed
V_{acc}	Acceleration Speed
$\boldsymbol{V_q}$, $\boldsymbol{V_d}$	d- and q-axis voltages
V_{rated}	rated speed
W_{exc}	Excitation coil slot width
W_t	stator tooth width
W_{PM}	PM width

Greek symbols

η	efficiency
η_t	Gearbox efficiency
η_{global}	Global efficiency
δ_1	tolerance for norm of error in permeability matrix
δ_2	tolerance for error in elements of permeability matrix
ϕ_{nom}	nominal d-axis flux linkage
ϕ_{exc}	excitation flux
ϕ_{PM}	PM flux
ϕ_{WE}	WE flux
φ_d	d-axis flux linkage
ϕ_{min}	minimum excitation flux
ϕ_{max}	maximum excitation flux
ω_e	electrical angular frequency
ρ_{air}	Air density at 15°C
$\mathcal{R}$	Reluctance
μ_r	relative permeability
μ_0	Vacuum permeability

θ_m	Mechanical angle
θ_e	electrical angle
λ	current angle with respect to EMF vector

indices

$calc$	calculated
max	maximum
min	minimum
n	normalized
in	input
out	output
ave	average
con	continuous
pk	peak
ac or AC	Alternative current
dc or DC	Direct current
ag	airgap
sat	saturation

Chapter 1 Introduction

This chapter is meant to discuss the global context, the outlines, and the original contributions of this thesis. Under the global context, the existing problem of conventional transportation is briefly scanned and the possible solutions are mentioned. As part of the solutions, the motivations and positioning of current study is demonstrated. Later on, the concept of optimal Hybridization Ratio (HR) is explained, which is the cornerstone for understanding the objectives of this thesis. At the end of this chapter, the objectives are set and the thesis outline is described.

1.1 Global context

1.1.1 Electric vehicles: why and not yet in large scale?

a) Why electric vehicles?

Due to unwise exploitation of fossil energy resources, not only the limited reserves are ending, but also we, and certainly other species, are facing several life-threatening environmental problems. The collective behavior of the human being, ruled by the frightening (and legal) pressure of governments and corporations, caused global warming, extreme weather changes, and earth pollutions. The global emissions of CO_2 are reaching 37.1 billion tons of CO_2 per year in 2018, scientists projected in their latest report [1], as shown in Figure 1-1. The expected increase in fossil fuel and industrial emissions is being driven by a nearly 5% growth of emissions in China and more than 6% in India, along with growth in many other nations. Emissions by the United States grew 2.5%, while those of the European Union declined by just under 1 percent.

Energy demand is behind the rise in emissions growth. Total energy consumption around the world increased by one sixth over the past decade, the result of a growing middle-class population and the need to provide energy to hundreds of millions of people. The challenge for all sectors is to decarbonize their economies while responding to the need for energy, particularly in developing countries, where continued growth in energy supply is needed. As one of the main players of this opera, the transportation sector is responsible for about 31% of total CO_2 global emissions, as published by the International Energy Agency (IEA) (see Figure 1-2) [2]. This clearly demonstrates the necessity of ongoing research on transportation, as one of the biggest ever-growing CO_2-producing sectors [3].

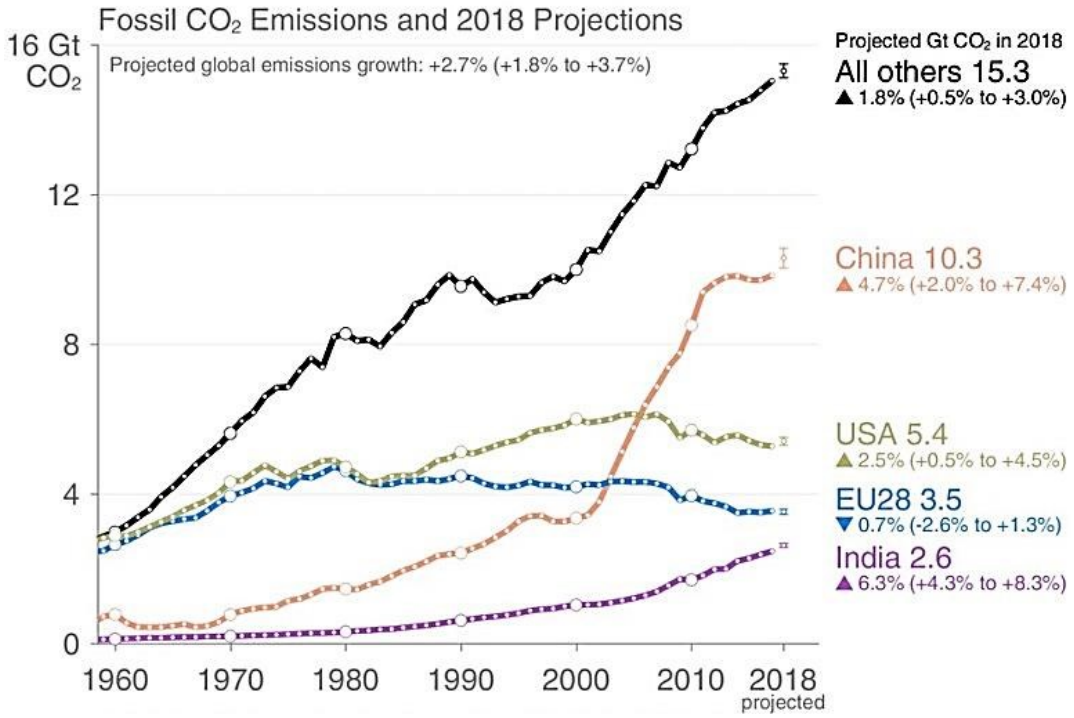

Figure 1-1: Annual global CO_2 emissions to 2017, with the 2018 projection [1]

Electric Vehicles (EVs) can help to confine our transportation activities consequences below the "2 degrees Celsius limit", in order to avoid the catastrophic impacts on the next generations' life. Using electric energy, EVs are quiet with almost zero emissions; they need less maintenance, and their operation costs are less due to electricity being cheaper than gasoline. That is why they can play an important role in the future transportation of humans and goods.

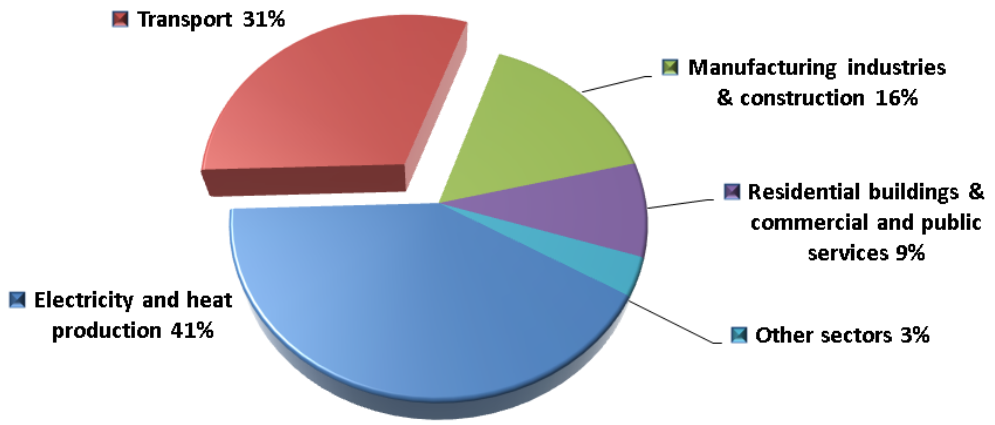

Figure 1-2: global CO_2 emissions by sector (adopted from [2])

b) **Why electric vehicles are not dominant yet?**

The history of EV goes back to the late 19th century. Between 1890 and 1920, the EVs were outperforming the Internal Combustion Engine (ICE) vehicles of that time for urban trips. After 1920, EVs lost their market to ICE vehicles due to technological advancement in the ICEs, accelerated by the flourishment of oil industry [4]. After 1970, the energy crisis and the world-wide pressure due to environmental concerns, combined with the advances in power electronics and digital control, opened a totally new area in front of transportation electrification. The researchers and industries are trying, although progressing slowly, to shift the paradigm of traditional fossil fuel transportation. The global cumulative sales of highway-legal light-duty plug-in vehicles reached 5 million in December 2018 [5], [6]. Sales of plug-in passenger cars achieved a 2.1% market share of new car sales in 2018 [7], up from 1.3% in 2017 [8], and 0.86% in 2016 [9]. As we can see from the numbers, the EVs are taking back, after their loss of market (between 1920 and 1970). However, the market penetration of EVs is not yet as prevalent as ICE Vehicles.

High initial cost of EV, plus its poor performance, such as range anxiety, long charging times, limited cargo and passenger spaces are the reasons for loss of market to ICE Vehicles [10]. In addition, the existing infrastructures and charging stations for EV are not developed sufficiently, and like any new industry, it is facing a number of challenges. Despite the government incentives, the low margin of profit in EV market is not attracting the car industry. Meanwhile, not everyone is interested in buying an EV just because of environmental causes, even though they participate in the Extinction Rebellion movement on a special day of year.

Most of the challenges are tangled with the difficulties in current technologies of Energy Storage System (ESS), which fade away the dominance of EVs to a relatively far future. Current ESS solutions for EV are limited in power mass density (W/kg) and energy mass density (Wh/kg), as compared to the fossil fuels in Figure 1-3.

It can be visualized that none of the sustainable ESS solutions are comparable to fossil fuels in both terms of energy and power mass density. Fuel cell, for instance, has high energy mass density; however, it neither delivers, nor receives, high power levels during the vehicle acceleration or short-time braking. On the other side of this spectrum lies the super-capacitor, which has high power capabilities, but lacks the required energy capacity for long driving distances. Hybridized ESSs aim to develop efficient EVs by combining the advantages of different energy sources, while mitigating their disadvantages.

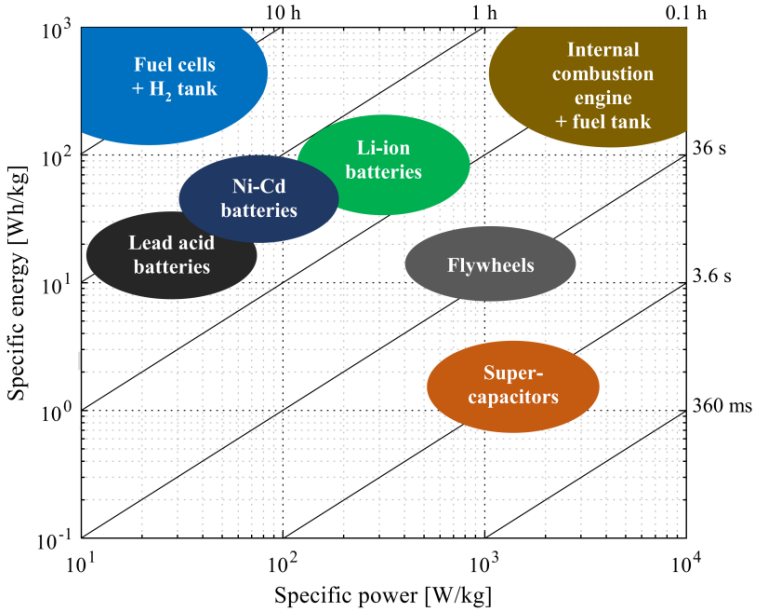

Figure 1-3: comparison of power and energy density for current ESS solutions [11], and [12]

1.1.2 Electric motor contributions to large scale penetration

To make the EV a better competitor of ICE vehicles, optimal drivetrain configurations should be designed, consisting of batteries, converters, and motors [13]. Although the main efforts are focused to address the bottleneck of the problem (ESS), the research on the other components of drivetrain, e.g. electric motors, cannot be abandoned. An optimal traction motor fitted to the drivetrain can give an extra degree of freedom to the designer of EV, and help the mass penetration of EVs in the market.

By increasing the efficiency of motor, the size of ESS can be reduced for the same mileage. In addition, a traction motor-drives with high Constant Power Speed Range (CPSR) can contribute in cheaper and less complex gearbox and transmission systems, while maintaining the same, or better, torque-speed characteristic envelope [14]. More on that, an optimized traction motor with reduced size, weight, and cost will free up more space for other components in EV drivetrain, e.g. batteries, which can help to take over the ICE vehicles. That is how an optimal motor-drive can contribute in the enhancement of performance and cost of EV, and in big picture, to the large penetration of EVs in the market.

1.1.3 Requirements of a perfect Electric Motor for EV

In an ideal traction motor, maximum power is always available over the whole speed range, with 100% efficiency at all operating points. In reality, as shown in Figure 1-4, the torque of a motor-drive in the *constant torque* region is physically limited to maximum allowable temperature rise at windings of the traction motor. For speeds beyond 1 Per-Unit (PU) of the rated speed, the motor is controlled in *constant power* mode (flux weakening), where the deliverable torque depends on the flux control capability and the inverter Volt-Ampere limits. Thereafter, the motor

enters its *natural mode*, where it rapidly stops delivering any torque, due to difficulties in flux weakening and the presence of excessive losses (copper losses, iron losses, frictions and air resistances, and constant losses). A good traction motor is expected to have a characteristic envelope more similar to that of an ideal traction motor. For that it needs to have:

- High CPSR
- High efficiency in a wider range over Torque-Speed (T-S) plane

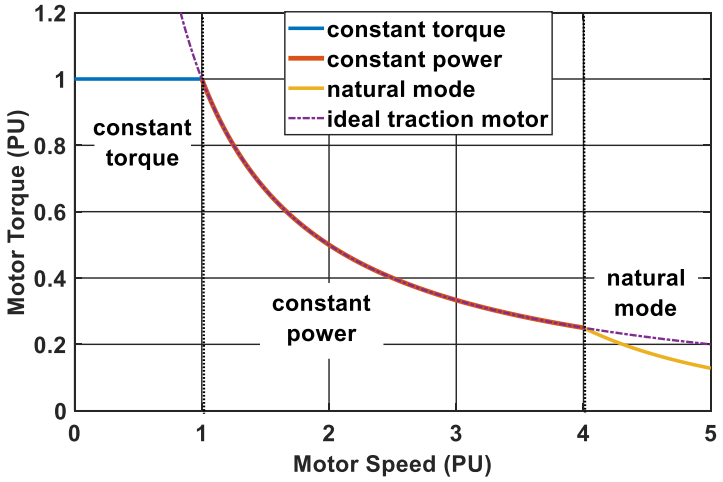

Figure 1-4: Ideal and real traction motor

From the literature, the most demanded specifications of a today traction motor-drive are listed as follows [4], [10], [15]:

- High instant power, and high power (mass and volume) density;
- High torque at low speeds for starting and climbing, as well as high power at high speed for cruising;
- Fast torque response which gives a better controllability and wider frequency band of the control system;
- Expanded high-efficient region at traction and braking, over wide speed and torque ranges [16]. Other than having high efficiency, the motor should also be pushed (or controlled) to work at its high-efficient region [4], [17].
- Highly reliable, robust and fault tolerant for various vehicle operating conditions;
- Mature technology and market availability of the motor and its power converter.

In terms of transient overload capability, most of the time the motor is not a limiting factor, but the inverter [18]; the cost of the motor is to be optimized at system level, because an expensive motor can lead to a lower EV total cost.

1.1.4 Why this thesis inside the Canada Research Chair in Efficient Electric Vehicles with Hybridized Energy Storage Systems

This thesis is fulfilled at the electric – Transport, Energy Storage and Conversion laboratory (e-TESC Lab.), University of Sherbrooke, Quebec, Canada. It is part of the Canada Research Chair in Efficient Electric Vehicles with Hybridized Energy Storage Systems (HESS) aiming at developing efficient EVs and HESS. The Chair has four research axes focused on energy storage systems, energy management, design and control of electrical machines, and development and control of power electronic converters for EV applications. This thesis is under the electrical machine design optimization, focused on the global efficiency enhancement of EV for an arbitrary-selected driving cycle. A schematic summary of the scientific context is provided in Figure 1-5.

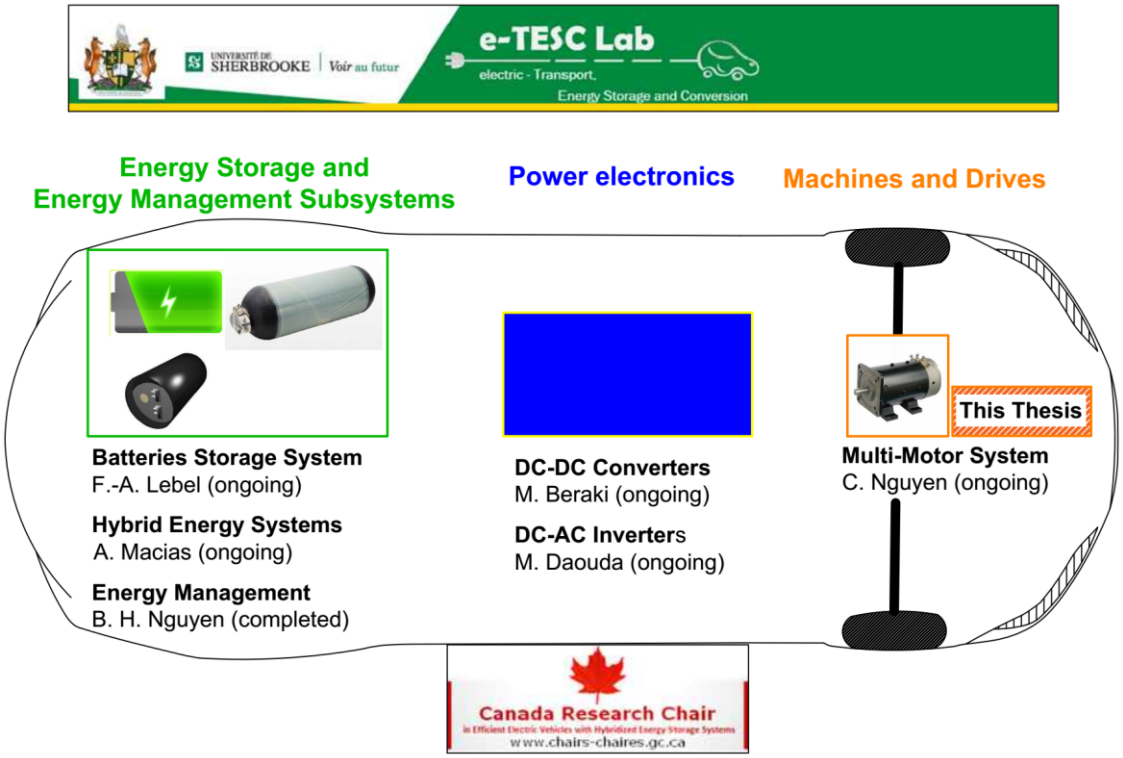

Figure 1-5: Position of the thesis within Canada Research Chair program in e-TESC lab

1.2 The concept of optimal Hybridization Ratio (HR)

HESM has two excitation sources: Permanent Magnet (PM) and Wound Excitation (WE). The reason behind is to combine the advantages of both Permanent Magnet Synchronous Machine

(PMSM) and Wound Excitation Synchronous Machine (WESM). The amount of flux provided by either of the excitation sources (PM and WE) is decided by a design variable, namely, Hybridization Ratio (HR). Simply put, the HR is the ratio of PM flux to the total (sum of PM and WE) flux. WESM and PMSM could be considered as particular cases of HESM. Therefore, HR has values between 0 and 1, which determines how similar the HESM is to either of PMSM or WESM. For HR equal to 1, HESM is a pure PMSM, and for HR equal to 0, it is a pure WESM. HR plays an important role in HESM system-level optimization and will be defined by detailed mathematical equations in the upcoming chapters. Nevertheless, there are two important questions, which are fundamental to understanding of this thesis, and should be responded in the beginning:

1) What is the optimal HR?

2) How to find it?

The answer is to change the HR from 0 to 1 with suitable steps, calculate the global efficiency of HESM over the selected driving cycle for each HR, and then, find the optimal HR which gives maximum global efficiency, as explained in the following.

HR is a design variable; hence, each time HR changes, the design of HESM must be modified accordingly. Finding the optimal HR calls for the design, analysis, and comparison of several HESMs. The comparison could be made through a common framework, i.e. efficiency, which is calculable for any combination of HESM topology, vehicle design, and driving cycles.

Efficiency is a variable which can be measured at any stage, from the component-level, up to the system-level. It serves as a benchmark of today modern transportation and can bring all motor designs inside one unique perspective. In this work, we use the term "*global efficiency*" to perform the comparison and select the optimal HESM. It is defined as the efficiency of each operating point, multiplied by the operating point time ratio; and then the sum of these values for all operating points gives the global efficiency, as obtained by (1-1).

$$\eta_{global} = \sum_{i} \eta_i . \frac{t_i}{t_{tot}} \tag{1-1}$$

where t_{tot} is the total time of driving cycle, t_i is the duration of operating point i, and η_i is efficiency at that point. It is understood from (1-1), that the most-frequent operating points should be placed as close as possible to the high-efficient area of the motor, thereby, maximizing the global efficiency. But, how should we do this?

Fortunately, changing the HR can change the place of high-efficient area of HESM over the T-S plane. For three HRs, Figure 1-6 shows an efficiency maps for each corresponding HR. As we can follow from the efficiency maps, the place of high-efficient area changes as a function of HR, and consequently, the global efficiency also changes as a function of HR. The optimal HR is related to the HESM with highest global efficiency, the one that takes more of the operating

point inside its high-efficient region (see Figure 1-6(b)). So, the problem of optimal HR is well-addressed through the common framework of efficiency at system-level.

Traditionally, the global efficiency maximization is also doable by changing the gear box ratio [19]. However, it results in identical efficiency maps with exactly the same CPSRs (see Figure 1-7). Gearbox only changes the operating points, rather than the shape of efficiency map. In addition, the ratio of single-speed gearbox is often constrained by the maximum torque or speed requirements. In case of multiple-speed gearbox or Continuously Variable Transmission (CVT), the system will be deteriorated in terms of cost, complexity, and reliability. This clarifies another superior advantage of HESM over the other competitors, where, the HR can change the CPSR of HESM. High CPSR is the key point in powertrain optimal design for EVs with enhanced performance [20], and it also extends the speed limit of single-speed gearbox. This flexibility of HESM (due to HR) gives an extra degree of freedom to the EV designer. A HESM having maximum global efficiency and high CPSR becomes more similar to an ideal traction motor, as stated in section 1.1.3.

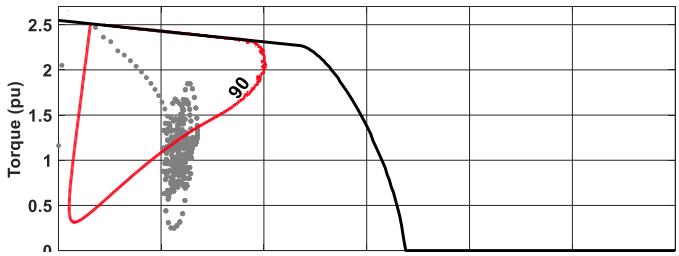

(a) HR = 1 (pure PMSM)

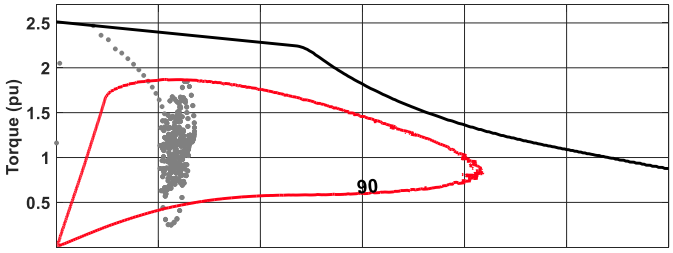

(b) HR = 0.6 (optimal HESM)

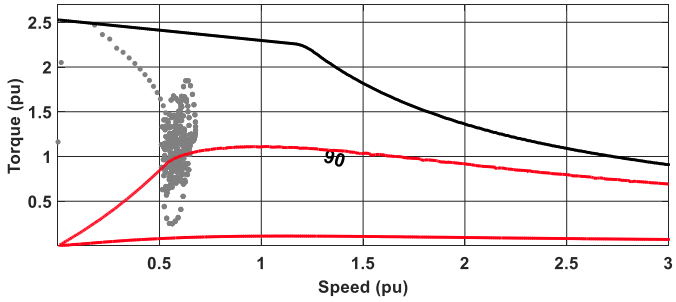

(c) HR = 0 (pure WESM)

Figure 1-6 Moving the high-efficient area of HESM as a function of HR over EMPA-C2 driving cycle

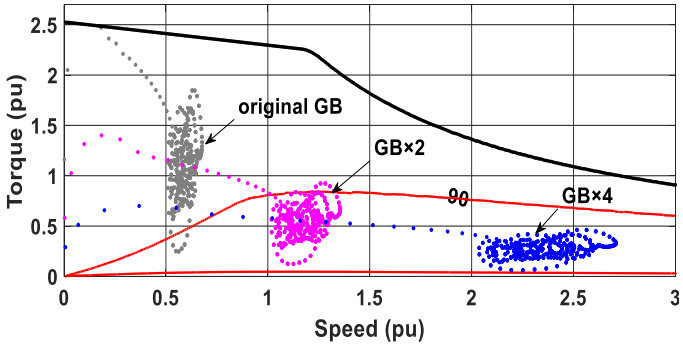

Figure 1-7 Moving the operating points as a function of gearbox (GB) ratio for HR=0

1.3 Original contribution

The major original contribution in this work is the development of a 2-level HESM design optimization for a given EV and driving cycle, as explained in the followings:

1) Optimization methodology: using a D-Q lumped-parameter model of HESM, the equations and algorithms for system-level optimization of HESM are proposed to maximize the global efficiency. In addition, overdesign due to low CPSR in the existing PMSM is reduced by HESM, thanks to the effect of HR on CPSR. The relation between CPSR, HR, and motor d-axis inductance is analytically deduced.

2) Detailed component-level optimization of a HESM for a target HR: being a design variable, any change in HR will bring considerable changes in the HESM nominal values. This calls for design modification of HESM as a function of HR. Using the Non-dominated Sorting Genetic Algorithm (NSGA-II), a new formulation is proposed, which deals simultaneously with the design of HESM and its cost minimization. In addition, a more comprehensive definition is provided for HR, which deals with any flux condition in the HESM. A 3D non-linear Magnetic Equivalent Circuit (MEC) model of HESM is used to evaluate the objective functions during the optimization.

3) Detailed system-level optimization: at this stage, the procedure in 2nd contribution is followed and repeated for eleven HRs between 0 and 1 with the steps of 0.1. For each HR (there are eleven HRs), a HESM is designed and its cost is minimized. The global efficiency of each HESM over US06 driving cycle is calculated and compared, and the final optimum HESM is found. The HESM 3D MEC model is developed in details and is evaluated by virtue of Finite Element Analysis (FEA). This model is used in the optimization process.

There are also two minor contributions as follows:

1) Inverse distance weighted interpolation: To calculate the efficiency of any operating point on the T-S plane using limited available test data, an approach based on "inverse distance weighted interpolation" has been developed. In this approach, efficiency of any arbitrary operating point is calculated based on the efficiency of 4 surrounding points, for which, the test data is available [14]. This method is originally applied in the surveying and construction of topographic maps based on the picked-up data from the location. As the construction of motor efficiency contours imitates the same principles, this approach has been applied to enrich the resolution of motor efficiency contours.

2) A comparison of different modeling techniques for electric machines, namely, the FEA, D-Q lumped-parameter model, and MEC is performed and published in [21]. This contribution is mainly integrating all existing models for PMSM, in order to correctly select the analysis tool for optimization of HESM.

1.4 Thesis outline

After this introduction, Chapter 2 provides the state of the art of HESM in transportation, its different topologies for hybridization, models and analyses, optimization methods, and control methods. The methodology for HESM system-level optimization is covered in Chapter 3 (first major contribution). In Chapter 4, a reduced scale 2 kW HESM is designed and optimized for HR equal to 0.5 (second major contribution). The system-level optimization for a battery powered three-wheel vehicle prototype over the US06 driving cycles is addressed in Chapter 5 (third major contribution). In addition, the 3D MEC model of HESM is fully explained in this chapter. The conclusions, challenges, and the future works are summarized in Chapter 6.

To complete this thesis at the end, Appendix I is dedicated to the first minor contribution, explaining the inverse distance weighted interpolation. In addition, the procedure to calculate an EV characteristic envelope, based on its design data, requirements, and expectations is described. In Appendix II, a comparison of different models for PMSM, i.e. dq-circuit model, MEC model, and FEA model is provided and compared to show the suitability of each modelling technique for motor optimization (second minor contribution). To elaborate and finalize the prototyping stage, the optimal HESM in reduced scale (2 kW), its dimensions, and its materials are reported in Appendix III, and the reasons behind the selection of the nominal power, voltage, and speed are elaborated.

1.5 Conclusion

In this chapter, the necessity of this thesis and its objectives as part of a bigger endeavor in e-TESC lab is clarified. It has been stated that the HESM can help to change the balance of car

market in favor of EVs to address the related concerns. The contributions and outlines of the present work were demonstrated in this chapter to provide a clear perspective to the next chapters.

Chapter 2 Literature Review on Design, Modelling, Optimization, and Control of Hybrid Excitation Synchronous Machines (HESMs) for Electric Vehicles

Due to the increasing desire for transportation electrification, the EVs powertrain and the motor topologies has been recently flourished vigorously in any transportation industry or research center. Selecting the most suitable electric motor for EVs is still a much-debated issue. The electric motors mostly used in EVs have, up to now, been Induction Machine (IM), Permanent Magnet Synchronous Machines (PMSM), Wound Excitation Synchronous Machine (WESM), Switched Reluctance Machine (SRM), and Hybrid Excitation Synchronous Machine (HESM). It is difficult to suggest one particular motor type, topology, or design as a general solution for all vehicles types and configurations. Some suggest IM [22], [23], some PMSM [24], and some SRM [25], [26].

PMSMs are used in the most today electric vehicles and have benefits such as high torque and power density, and high efficiency at low speeds. Their main problem is the cost and availability of rare earth Permanent Magnets (PMs), with some difficulties in flux weakening and safe control. Due to strong fixed PM excitation, it is difficult to operate efficiently over a wide speed range, and PMSM has a limited CPSR. IM does not use magnet and is robust, but its efficiency and torque density is less than PMSM, and its power factor is low, especially at partial loads. SRMs have the same benefits as IMs with higher efficiencies, but they suffer from low torque density, vibration plus acoustic noise, and low power factor [27].

2.1 Hybridization of electrical machines

Considering advantages of different kinds of electric machines, it is favorable to integrate some desired qualities of one machine into another, which already lacks them. This is called *hybridization*. Internal Permanent Magnet (IPM) synchronous machine, for instance, demonstrates a brilliant hybridization of Surface-mounted PMSM (SPMSM) and Reluctance Machine (RM). RM suffers from low torque density due to limited practical saliency ratio, but they have theoretically infinite maximum speed. On the other hand, the most prominent feature of PM machines is its high torque/power density, but their CPSR is very limited. The

hybridization results in the IPM machine which interstates good qualities from both SPMSM and RM.

Although hybridization aims at combining favorite features, there is no such thing as a free lunch. In IPM, several good features of RM will be damaged, such as its low cost, mechanical robustness, and temperature resistant character. Their inherently zero back-EMF results in a safe operation at high speeds (in case of a faulty control shutdown), which is also lost in IPM. Optimization, and application-oriented trade-offs are needed to mitigate certain undesirable effects and keep the favorable ones. There are several novel hybridizations of electric machines with different electromagnetic working principles [28]. They can be hybridized in, but not limited to, the following ways:

- IM and PMSM and IM and RM: line-start synchronous motors [29], [30], [31];
- RM and PMSM:
  - PM on rotor: single or multi-layer, internal, inset, spoke, and v-shaped IPM machines;
  - PM on stator: doubly salient machines [32];
- WESM and PMSM and RM: Flux Switching Machines [33], Flux Reversal PM machine [34], [35], [36], PM memory machine [37], [38], and Double Excitation Synchronous Machine (DESM) [15], [18], [24], [26], [39], [40], [41], [42].

Each hybridized motor has its own benefits and drawbacks and each application has specific needs. For instance, price is not a penalty for race cars or space vehicles, whereas for city passenger cars it is indeed. Adding the number of different topologies (inner-outer rotor, radial-axial-transversal flux, rotating or linear [43], [44]), different cooling methods, different advanced materials and production technologies, etc., we will end up in a very large pool of viable motor candidates for the transportation application.

Hybrid Excitation Synchronous Machine (HESM) is a hybrid result of PMSM and WESM, which is among the most promising propulsion candidates for electric transportation, regarding its outstanding capabilities inheriting from both PMSM and WESM [20], [35], [45], [46], [47]. It can combine the favorable qualities of high torque at low speed with superior overloading performance, exceptional flux weakening and extended CPSR, high efficiency, and flexible controllability in motoring and generation modes. In generating mode, connecting HESM to a diode rectifier gives an adjustable DC source, controlled by WE current. It constitutes an interesting alternative to PM alternators associated to an active power converter. In motoring mode, the HESM allows an optimal high-speed operation. In addition, it allows reducing PM volumes, or using abundantly available ferrite PMs.

2.2 HESM configurations and topologies

In scientific and technical literature, different names are selected for this type of machine, namely:

- Hybrid excitation synchronous machines
- Double excitation synchronous machine
- Dual excitation synchronous machines
- Combined excitation synchronous machines
- Permanent magnet synchronous machines with auxiliary excitation windings

There is a wide variety of motor configurations, over which, numerous HESM topologies has been invented. The designers throughout the world have benefited from their imagination to push further the revolutionary and efficient design of electric machines. The enormous created topologies can be classified upon several base criteria. This type of classification has nothing to do with the hybridization topology, but rather a traditional way of classification of all electric machines.

- Radial-flux [48], [49], [50], axial-flux [51], [43], [52] and transverse-flux machines [53]: Either of radial, axial, and transverse-flux machines have their own cons and pros, which could be exploited according to the application, available space, and needed speed-torque characteristics.

- Outer-rotor [33], [54] and inner-rotor machines [48], [49], [50]: depending on the vehicle design, this kind of machines can offer the key solution, e.g. for in-wheel electric machines, outer-rotor machines offer ‘no axle, no gears solution, plus more room in the vehicle.

- 2D and 3D flux structure machines [43], [44]: 2D machines are preferable and more appreciated, as measured from the FEA simulation time and resources, and eddy currents suppression with the existing core material. 3D machines, however, contribute to most of the creative and modern electric machines, which can compensate the difficulties in the FEA analysis. In addition, there are other equivalent alternatives to FEA, such as MEC, which demand much less processing resources. The advances in the modern magnetic materials and 3D printing technology have opened new doors to the prototyping of electric machines with complex 3D configurations.

HESMs can be also classified in another way, i.e. the position of PM and WE. They can be both on the rotor (see Figure 2-1) [48], [49], [50], both on the stator (Figure 2-2) [55], [56], PM on the rotor and WE on the stator, or vice versa, as in ,[57], [58].

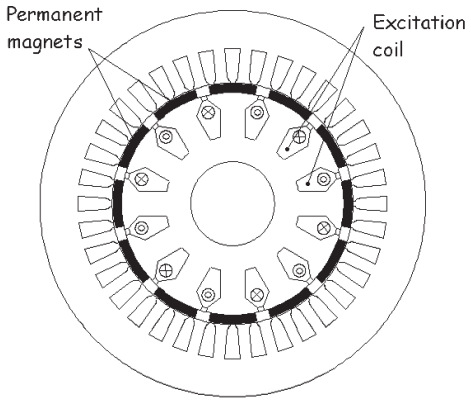

(a) [48]

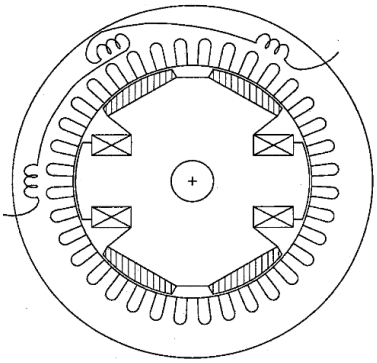

(b) [49]

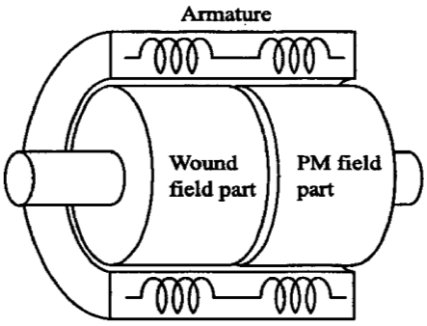

(c) [50]

Figure 2-1 HESMs with both PM and WE on the rotor

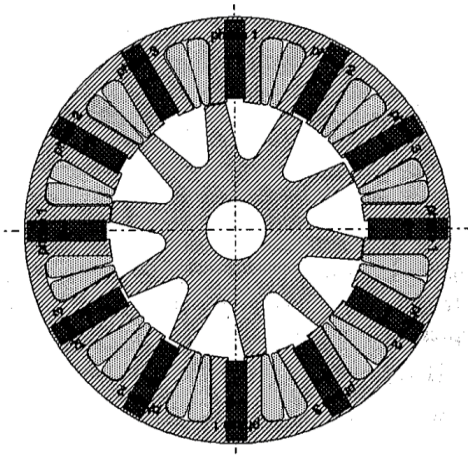

(a) [55]

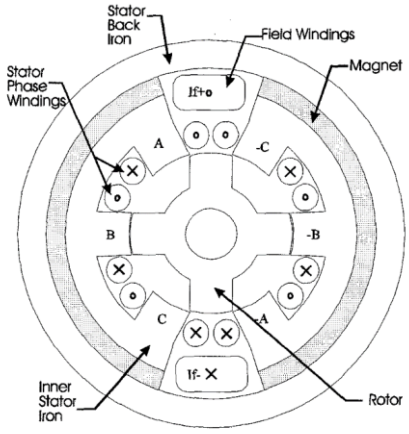

(b) [56]

Figure 2-2 HESMs with both PM and WE on the stator

Another approach could be the flux interactions of PM and WE, in analogy with electrical circuits, which focuses on how WE flux is combined with PM excitation flux. This is more important, as the flux paths and cross-effects of the two excitation systems mainly affects the

output variables, such as, torque, flux regulation, losses, and efficiency. In this regard, HESM configuration can be divided into the following two groups, [35]:

1) **Series hybridization:** In these machines, the flux created by excitation coils passes through the PMs. Since the permeability of PM is close to that of the air, the reluctance of WE magnetic circuit is relatively high. Subsequently, high Magnetomotive Force (MMF) is needed to remove the strong PM flux from the stator, hence increasing copper losses. Furthermore, the risk of demagnetization of magnets should be considered. They have 2D structure, as seen in one of its examples in Figure 2-3 [59].

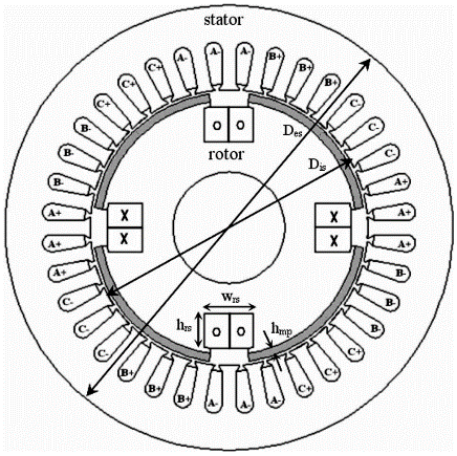

Figure 2-3 Series HESM [59]

2) **Parallel hybridization:** In these machines, the flux created by PMs and WE have different trajectories and the WE flux does not pass through PMs. So, the danger of demagnetization have been removed, and also the reluctance of the WE have been reduced, as displayed in Figure 2-4, [60], and [49].

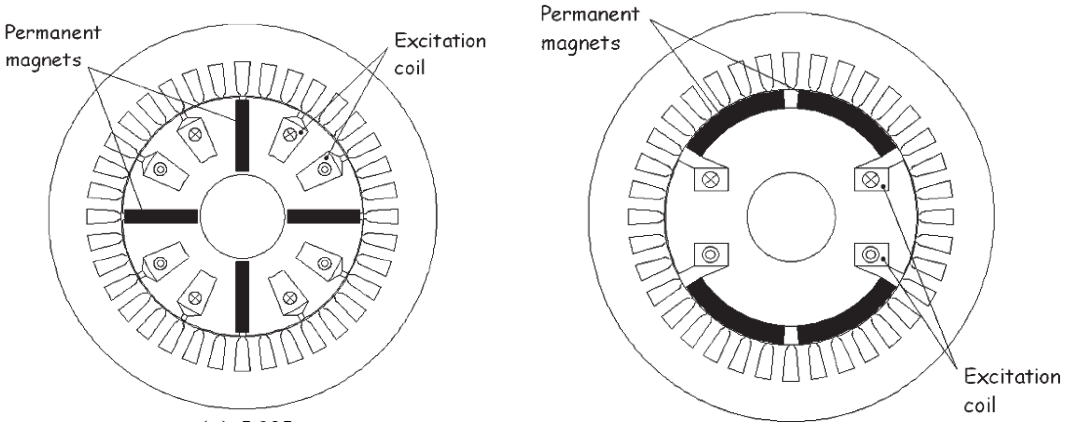

(a) [60] (b) [49]

Figure 2-4 Parallel HESM, both excitations on the rotor

When the excitation coils are on rotor, it is difficult to connect them to electric source. It is connected by some means such as slip rings and brushes, rotary transformers, etc., which will

cause some limitations and extra losses. It is also possible to leave the PMs on the rotor, and place the auxiliary winding on the stator for better thermal operation and ease of connections [58]. However, due to the existence of 3D flux paths, part of the PM flux is leaked without linking the stator windings. In addition, the 3D flux path makes it a challenging task to reduce eddy current losses, especially at higher speeds. It also brings some manufacturing difficulties. Figure 2-5 depicts two structures for this type of HESM [58], [61].

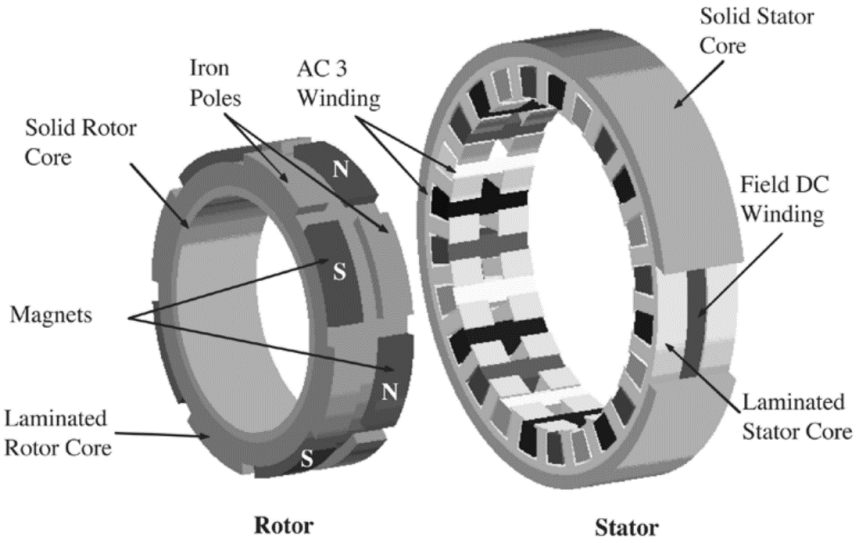

(a) Consequent pole HESM [58]

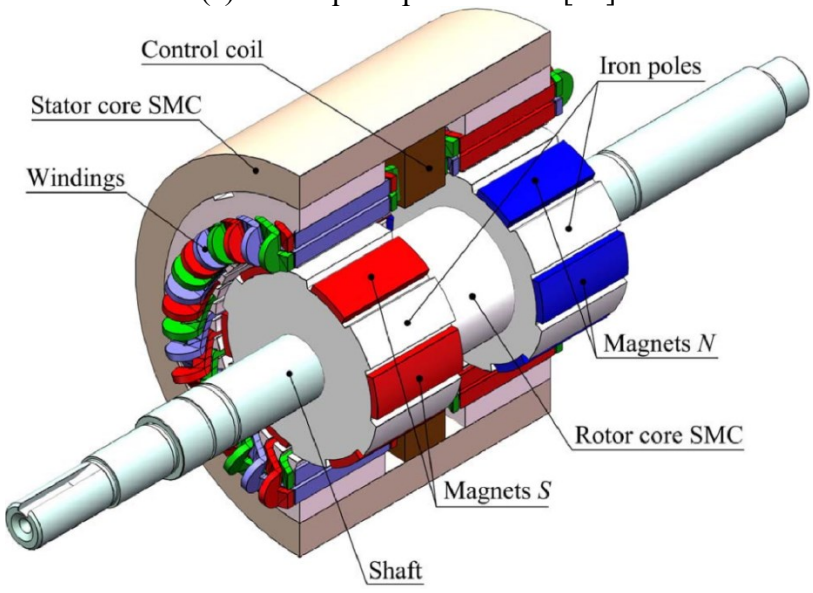

(b) electric controlled, PM excited synchronous machine [61]

Figure 2-5 Parallel HESM, PM excitations on the rotor and WE on the stator

Both PMs and auxiliary coils may be put on the stator. To produce torque in this case, the rotor should be salient, as the topology seen before in Figure 2-2 (b). This is called by the authors as Doubly Salient PM Machines (DSPMM) machines [56]. Putting magnets on stator has two advantages for them, namely, better cooling and no centrifugal forces. The major drawback of this topology is its low torque density due to unipolar (or monopolar) flux linkage. However, its torque and efficiency is superior to IM with the same dimensions. Another problem is its non-negligible torque ripple resulting from the mutual inductance variation [62]; yet, in theory, no cogging torque is expected [56].

Today, Flux Switching HESM (FSHESM) is better than DSPMM in terms of bipolar excitation flux regulation, and efficient WE system [63]. By precisely optimizing stator and rotor teeth shapes, perfect sinusoidal flux waveform at no-load could be obtained which will decrease the cogging torque [55]. In [55], the authors have invented an optimal topology and have given the basic sizing and performance analysis for it. Their performance is closely comparable to IPM machines, still they suffer from the cogging torque, acoustic noise, and vibration due to their salient rotor structure [64]. The new designs use an iron bridge in the outer side of the stator to increase the WE system efficiency, as in Figure 2-6 (b). As a result, part of the torque is sacrificed due to PM flux shortcut through the iron bridge. The optimal control is also a challenge, due to the complicated magnetic analytical model. Another disadvantage of this topology is the use of rare-earth magnets to increase the torque density. Their advantages are the 2D structure, and the location of both PM and WE on the stator. The former advantage makes it simpler to study and design and more attractive for the industry. The later advantage brings a better thermal performance and a robust simple rotor, which is really attractive for traction applications. Two examples of this topology are presented in Figure 2-6. The concentrated winding brings shorter end winding connections for this topology.

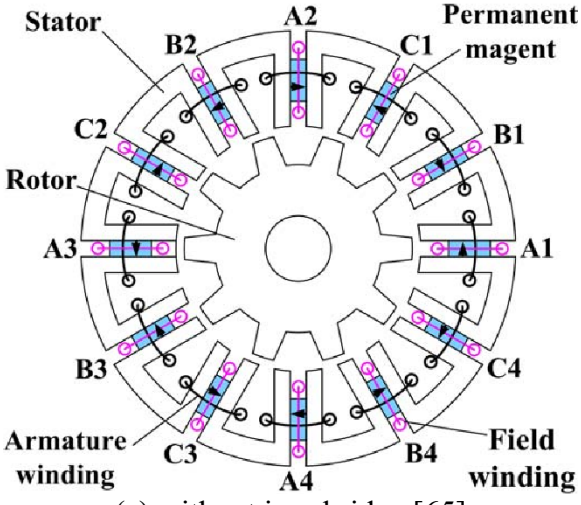

(a) without iron bridge [65]

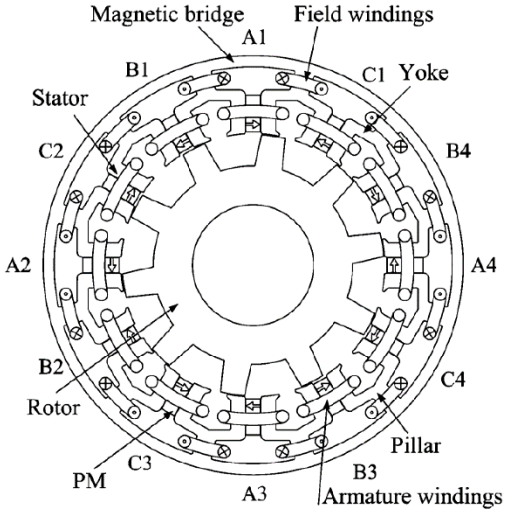

(b) with iron (magnetic) bridge [66]

Figure 2-6 FSHESM, PM and WE on the stator

Recently, a new FSHESM topology with 3D flux path and a static global WE is proposed by [53] (Figure 2-7). The 3D flux structure is limited to the iron bridge in the outer part of the stator.

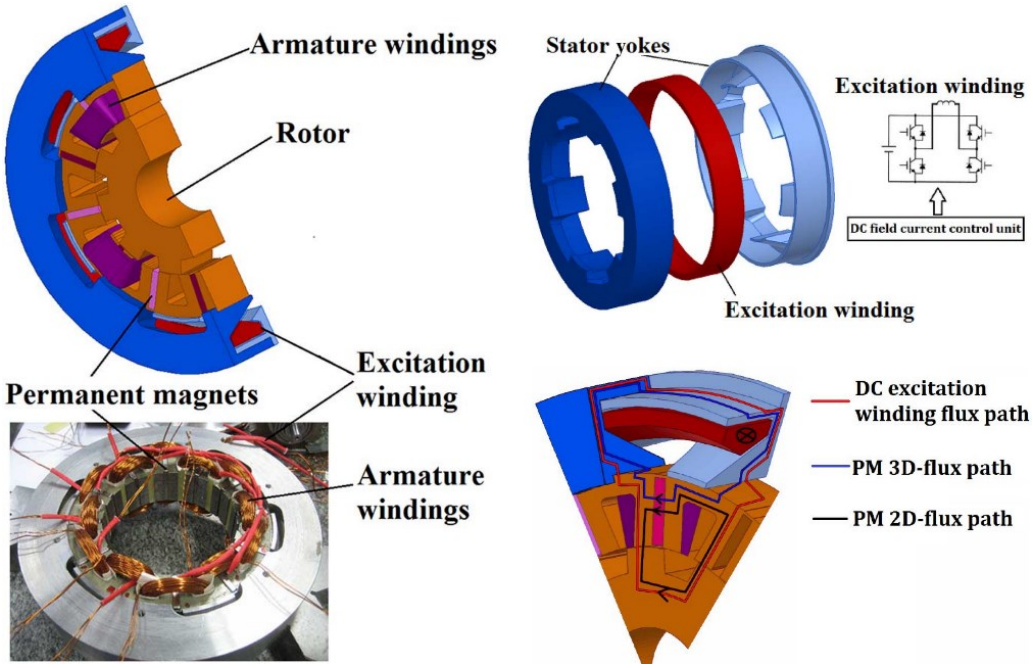

Figure 2-7 New FSHESM with a global excitation winding [53]

2.2.1 Selected topology of HESM

The topology selected to prove the proposed concept is a radial flux motor. The PM is located on the rotor and WE on the stator. It have been proposed by Amara et al. in 2009 [35], and studied theoretically and experimentally in [67], [68], [69]. Figure 2-8 provides a 3D view of the selected topology for HESM (modelled in MagNet Infolytica). The main flux paths for PMs and WE, as well as, the PM leakage flux are displayed in the motor. For this research work, some modifications in the magnetic and mechanical design of the rotor and outer stator are made. The left-side excitation coil regulates the S-pole flux, whereas the right-side coil is responsible for the flux regulation of the N-pole. The outer stator provides a magnetic path for WE flux. In this parallel hybridization topology, the rotor claw-pole structure prevents the flux from the N-pole to interfere into the S-pole. This design has easy flux control, high efficiency, wide CPSR, and good reliability [70]. However, it has 3D flux paths, for which the FEA analysis is very time- and process-consuming. The homopolar and leakage fluxes contribute in the hard saturation of outer stator magnetic material (see Figure 2-8). This motor will be studied and optimally designed in the following chapters.

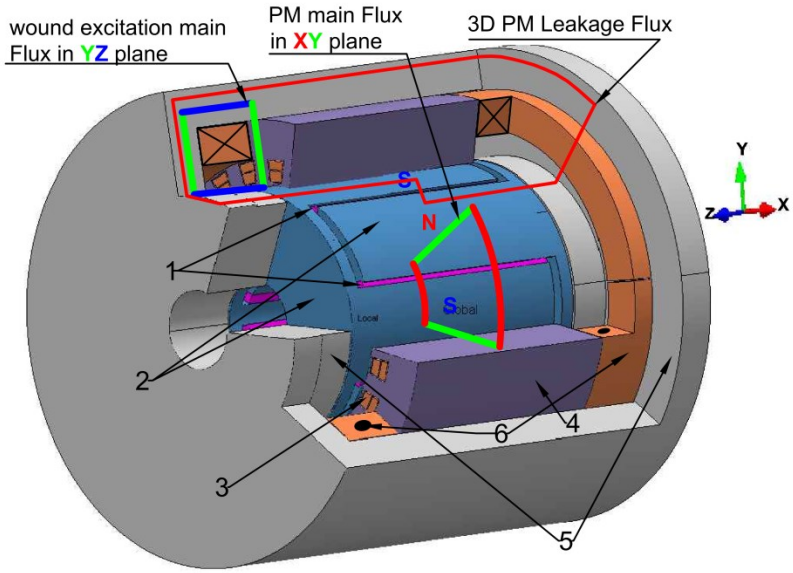

Figure 2-8 Selected HESM topology with minor modifications: 1- PMs (ferrite), 2-rotor claws (iron–silicon alloy), 3- stator coils (copper), 4- stator (silicon steel lamination), 5-outer stator (iron–silicon alloy), 6-WE coils (copper)

2.3 HESM modelling and analysis

The commonly used tools for electromagnetic analysis include Finite Element Analysis (FEA), analytical model and winding function theory, and Magnetic Equivalent Circuit (MEC) [71], [72]. In the design optimization of HESM, the number of simulation to build the efficiency maps for different HRs is enormous. FEA approach is very accurate, but takes lots of time and resources, especially for machines with 3D flux directions. FEA can be practical for one or limited number of operating points; however, it is not applicable here. Analytical approximate formula and winding function theory lack desirable accuracy. Being semi-analytical semi-numerical, the non-linear MEC can make a trade-off between the time and accuracy, and can be very helpful in the design optimization of HESM with 3D flux paths [73], [74], [75]. This approach provides acceptable accuracy, with fast simulation to reduce the processing burden of optimization.

MEC has long been an alternative, yet effective, method to FEA for electrical machines, with shorter computation time and accuracy of results. It has been used for the design and analysis of different types of electric machines, such as switched reluctance motors, asynchronous motors, and permanent magnet motors [76], [77], [78], [79], [80]. It has gained more attention and applicability recently in the literature [81], [82]. Several universities are working on MEC modelling and have their own developed software, which is flexible for different motor designs, materials, and analyses. In University of Grenoble Alpes, for instance, researchers in G2ELab have developed a software tool for MEC analysis, namely Reluctool [83].

There are two circuit laws governing the formulation of MEC, namely, Kirchhoff Current and Voltage laws [84]. The nodal-based analysis is applying the Kirchhoff Current lows and is widely appreciated due to its simplicity of implementation. The principles are the same as that of the electric circuits; only here we use the magnetic variables. There are two methods for nodal-based analysis, namely, tooth contour and flux tube. The flux tube method has been selected to be applied to the HESM. The approach in [85], [86], and [87] are the guidelines with more detailed explanation,. The final non-linear 3D MEC model of the HESM under study is developed, explained, and evaluated by FEA in [88].

2.4 HESM optimization

Having developed the HESM model using MEC technique, optimization algorithms can find the optimal design. The design optimization of HESM is simply composed of two stages: design, and optimization. The objective of design stage is to provide feasible solutions for the problem under study, and then, the optimization takes it towards the optimal point regarding the desired objective functions. The optimization algorithms used for the optimization of electric machine are divided into two main groups, i.e. gradient-based algorithms and intelligent optimization algorithms, as displayed in Figure 2-9.

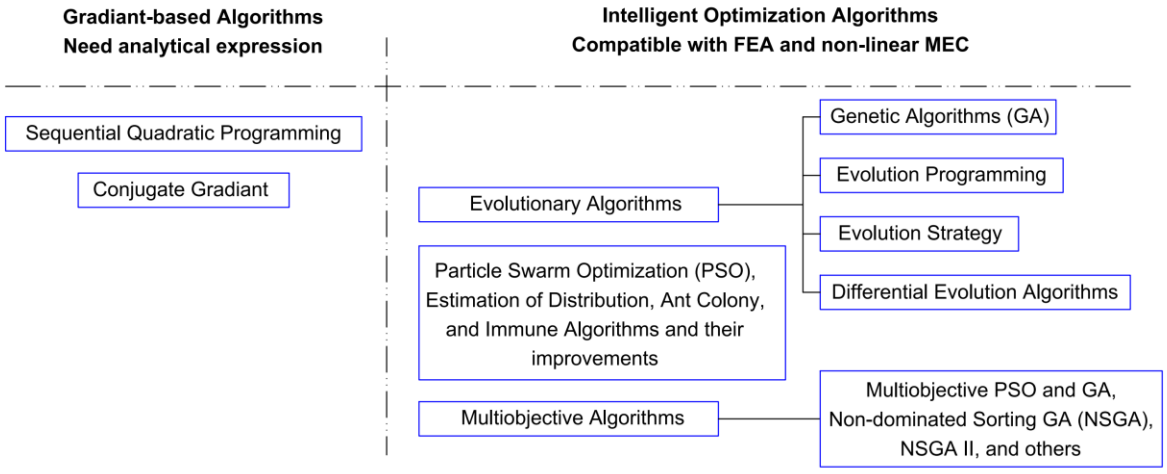

Figure 2-9 Optimization algorithms used for design of electrical machines (based on [89])

Gradient-based algorithms need analytical expressions and linear MEC models for the evolution of objective functions towards the optimal point. However, today electrical machine optimization is using non-linear models, such as FEA or non-linear MEC for the motor modelling and analysis. Therefore, intelligent optimization algorithms have been employed for the optimization of electrical machines in the past several years [90]. As the nature of electrical machine optimization consists of several objective functions, multi-objective optimization has become popular in this field [19], [91], [92]. These objective functions are sometimes paradoxical, e.g. efficiency and cost, and multidisciplinary, e.g. electric, magnetic, thermal, and mechanical

objective functions. Typical structure of an optimization process is displayed in Figure 2-10, which comprises of main stages (left-hand boxes) and exemplary tasks (right-hand boxes); bold solid lines give loops for possibly required iteration(s).

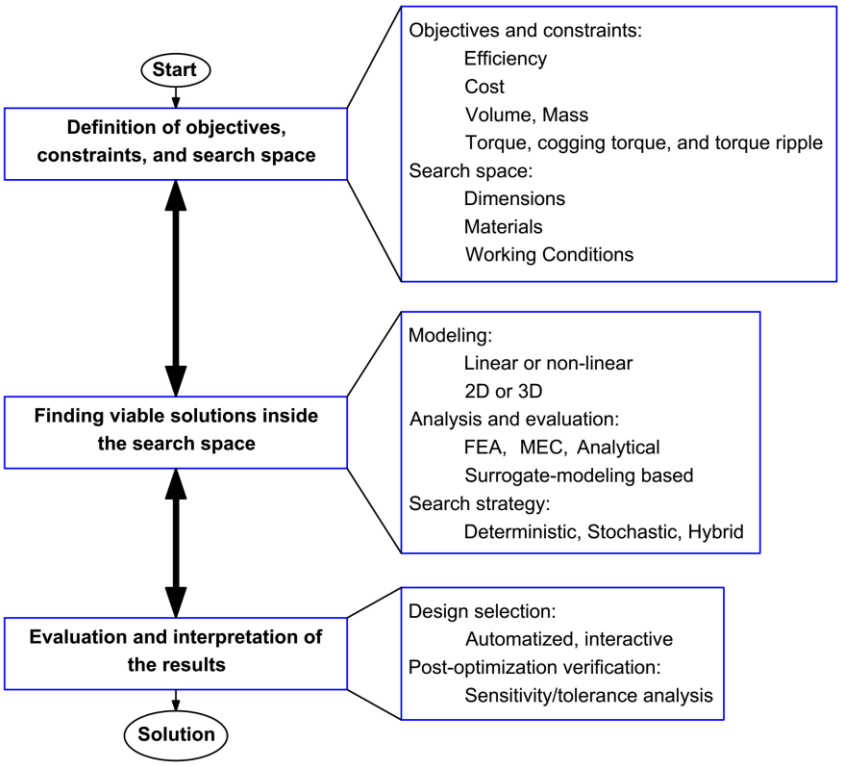

Figure 2-10 Typical structure of an optimization process (based on [93]).

NSGA-II [94] is generally considered the state of the art algorithm in evolutionary multi-objective optimization, which has provided good results in the optimization of electric machines [95], [96] and [97]. Our contribution regarding the optimization of electric machines using NSGA-II is described in [98].

2.5 HESM control

The well-known principles of dq-reference control of PM machines can be fully absorbed in HESM control. PM machine control through d- and q-axis currents applies different control strategies for different regions of motor T-S plane. For instance, prior to base (rated) speed, Maximum Torque per Ampere (MTPA) strategy is applied. From base speed to maximum speed, the voltage constrain is reached, and Maximum Torque per Voltage (MTPV) control should be applied. The nonlinearities can be taken into consideration by a nonlinear inductance computation through curve fitting techniques for different current levels [99]. Combining these techniques with the PMSM and WESM loss minimization control [100], [101] provides the possibility to achieve multi-objective control strategies for HESM [102].

In HESM, the control of WE current gives another degree of freedom to enhanced flux weakening and operation at higher speeds. It includes minimum-loss (maximum efficiency) control, unity power factor control, MTPA, MTPV, and so on. This will result in a wide range of operation speeds and higher CPSRs with higher efficiencies. High CPSR, as will be explained in the following chapter, removes, or reduces the overdesign in the drivetrain of high-performance EVs.

Each HESM topology imposes certain requirements on the inverter and field converter hardware and software design. To completely benefit from the advantages of HESMs, the most prosperous topology should be accompanied by a proper control scheme. Despite numerous articles about the topology of HESM, the publications on their control are not comparable. Loss minimization through accurate computation of excitation and armature current is one essential part of all control strategies.

In [103], Amara et al. have proposed three flux weakening techniques to have maximum output power, constant armature current, or maximum efficiency. The relationships and discussions are given for the maximum attainable CPSR. In [104] they have proposed a control strategy to compute the armature and excitation currents. Its aim is to keep constant the output voltage of a Hybrid Excitation Synchronous Generator (HESG), connected to an uncontrolled diode rectifier. In [105], Kefsi et al. have proposed a new flux weakening control strategy for traction applications, which improves the efficiency in the most frequent operating points of the driving cycle. However, it is not examined by experimental validation.

The first proposition of HESM control for unity power factor is demonstrated in [106] through simulation and experiment for a series HESM as an integrated starter/alternator. They propose a control structure for both motoring and generation operating modes. In addition, the online q-axis and WE current references are computed to minimize the copper losses for lower torques. A high CPSR (10:1) at unity power factor is proved by experimental verification.

Researchers in [107] have analyzed and compared different parallel HESMs and HESGs flux weakening capability. They have applied both WE and armature current control for HESG, however, its dynamic response was not satisfactory. Further, they have applied Direct Torque Control (DTC) to develop a system having enhanced dynamic and steady-state response. Compared to the generators connected to a simple diode rectifier, they also offer the use of controlled DC converters to improve the performance, however, this adds to the system complexity and cost.

In [47] authors have demonstrated the power capability of HESM when operating in motoring mode. Maximum power limits and partial load operation are both examined by idealized inverters with limited volt–ampere ratings. Based on a per-unit d-q model, different control strategies are explored for different motors parameters. Since WESM and PMSM could be considered as particular cases of HESM, their findings would be applicable to all synchronous motors.

In [63], a control strategy for a HESM with iron flux-bridges have been proposed. They have taken further the concept of field and armature current control. The field current is used to increase the flux linkage in constant torque operation mode. It is put to zero in flux weakening mode, and the d-axis current is used, as its inductance is higher than that of the WE circuit. The references for current are produced based on voltage error, and the controller presents satisfying robustness against machine parameters change.

The researchers in [47] and [108] have provided a complete strategies for flux weakening of HESM which fills the gaps of previous researches, and is found to be a reliable starting points for the contributions in HESM control. In [108] authors present five different flux weakening strategies for HESM, and simulations and experimental validation have been provided. Comparison between different control strategies have been made, which makes it possible to select the best strategy. The selected strategy, referred as SR1-FW, provides unity power factor operation, with theoretically infinite CPSR.

In fact, there are three practical limits in reaching the theoretical CPSR. The first is that the regulator of WE and d-axis current is designed to follow the current reference at fundamental frequency. The harmonics of higher orders, especially at higher speeds, remain untreated. This effect can be addressed by feed forward compensation. Nevertheless, at higher speeds, the higher orders of harmonics get beyond the bandwidth of the current regulator and the relevant switching frequency. The second limitation is due to d- and q-axis inductances change, as a result of saturation. This can also be accounted for in the control, by using least-squares regression and 2^{nd} order polynomial relations for the inductances [99]. The third limitation is due to the PM flux penetration into armature windings, despite the flux weakening. At high speed, this causes iron losses, causing heat which reduces the armature current capacity. As will be explained in 3.5, the optimal design of HESM will use ferrite magnets. Their flux is weaker than that of the rare earth magnets, which hopefully will make it easier to remove it from the armature windings and avoid excessive iron losses at high speed.

2.6 Conclusion

In this chapter, the hybridization of electric machines is reviewed and it is stated that the objective of hybridization is to amplify the favorable characteristics of different motors, while keeping mitigated the unwanted features. Several hybrid traction motors, already published in the literature, was reviewed and a topology was selected to study the effect of HR on the maximization of global efficiency over selected driving cycles.

To optimize the design of this HESM, a modelling and analysis technique, together with an optimization algorithm was called for. The literature of modelling, analysis, and optimization of electric machines was then briefly reviewed to find the proper approach. The selected HESM will be modelled using 3D non-linear MEC, and will be optimized using NSGA-II. Meanwhile, the construction of efficiency maps and the calculation of global efficiency need the control currents. The control currents will be calculated by an offline minimum-loss control method. The following chapters are dedicated to the design, analysis, and optimization of the selected HESM.

Chapter 3 Proposal and Methodology

Original Title:
Hybridization ratio for hybrid excitation synchronous motors in electric vehicles with enhanced performance

Authors and Affiliations:
- **Ahmad Shah Mohammadi,** Ph.D. student, e-TESC Laboratory, Department of Electrical & Computer Engineering, University of Sherbrooke
- **João Pedro F. Trovão,** Professor, e-TESC Laboratory, Department of Electrical & Computer Engineering, University of Sherbrooke
- **Maxime R. Dubois,** Professor, e-TESC Laboratory, Department of Electrical & Computer Engineering, University of Sherbrooke

State: Published - doi: 10.1049/iet-est.2017.0029

Journal: IET Electrical Systems in Transportation (Volume: 8, Issue: 1, 2018), https://ieeexplore.ieee.org/document/8281565

Context of the chapter

This chapter is dedicated to present the first major contribution. The Ph.D. proposal and its methodology were published to seek a feedback from the scientific community. To have a rough estimation and to examine the feasibility of the proposed work, a general-purpose model is selected to study the HESM behavior. The model is the well-known dq circuit model, which can represent the torque, copper losses, and iron losses in several lumped parameters on the d- and q-axis. Although the model lacks several capabilities in predicting the correct behavior of the machine, it gives a fast and useful evaluation of the studied concept. This provided us with a rapid glimpse over the idea whole, rather than getting lost in the details of a precise analysis at the very beginning of this journey.

3.1 Abstract

For electric vehicles (EVs) with severe acceleration requirement, the selected motor would be inevitably overdesigned to meet the acceleration requirement. To address this, the motor constant power speed ratio (CPSR) should be increased to remove part of the overdesign. There are different flux weakening techniques that are used to increase motor maximum speed (and increase the CPSR). Among them, hybrid excitation synchronous motor (HESM) advantages have been benefited in this study. CPSR depends on hybridization ratio (HR) of the excitation system, and the motor inductance. The relation is analytically derived in this study. In addition to increasing CPSR, HR can control the place of motor high-efficient area over the efficiency map, which can increase EV global efficiency. A search algorithm has been developed, here, to find the optimal HR of a non-optimal HESM. The final design gives an efficient motor performance with less overdesign in drivetrain. Compared with the original permanent magnet synchronous motor, 4.1% improvement in global efficiency for an average city-highway driving cycle has been achieved, and 16% decrease in rated values of drivetrain elements is obtained.

3.2 Introduction

Although lots of research efforts are dedicated to developing sustainable transportation systems, still, the market penetration of electric vehicles (EVs) is slow. This leaves one of the biggest ever-growing CO2-producing sectors untreated [3]. Initial cost of EV, plus its poor performance, such as range anxiety, long charging times, limited cargo and passenger spaces, and slow acceleration are reasons for loss of the market to internal combustion engine (ICE) vehicles [10]. To have an EV with more enhanced performance, optimal drivetrain (batteries, converters, motor, gearbox, and transmission) configurations should be used [109]. Among them, an efficient electric traction motor can reduce the size of batteries, which is the bottleneck for the mass penetration of EVs in the market. In addition, the motor should also be pushed to work at its high-efficient region [4].

In ICE vehicles, the operating points of the vehicles should be mapped over the engine high-efficient region. This is typically achieved by using a multi-speed gearbox, for EVs, however, single-speed gearbox is mostly used [110]. To have the motor drive working at its efficient region, its constant power speed ratio (CPSR) should be around 4:1 to 5:1 for passenger EVs [111], and around 25:1 for heavy EVs such as electric tractor [108]. CPSR is the ratio of maximum speed to rated speed during constant power operation of the electric motor [112]. Low CPSR can be a limiting factor, and in certain situations, it can force the designer to select a motor drive with a power more than the EV needs. This results in an overdesigned drivetrain [15], [25], [113], [114].

One of such situations is when the EV acceleration is the dominant criterion, which determines its maximum needed power, in which case, a motor drive with infinite CPSR is needed to avoid the overdesign [115]. Infinite CPSR is not feasible due to several reasons, such as thermal and mechanical limits, hence, the overdesign is inevitable. Finding the optimal CPSR to remove part

of the overdesign and enhance the EV cost and performance is the outcome of this research. In this regard, the efficiency, as one of the most essential aspects of the EV, cannot be neglected.

Hybrid excitation synchronous motors (HESMs) are invented to hybridize permanent magnet synchronous motors (PMSMs) into the wound excitation synchronous motors (WESMs), in order to exploit the advantages of both of them. The level of hybridization between the two is called hybridization ratio (HR). The result is two favorable features in the scope of this work:

- First, decreasing HR increases the CPSR, which can reduce the drivetrain overdesign.
- Second, HR can change the place of high-efficient region of the motor over the efficiency map [116].

The second benefit can improve motor global efficiency over the selected driving cycle, which here after is briefly referred as the global efficiency. This paper develops a methodology to improve a primary HESM design, by finding the optimal value for HR. The result will be an enhanced global efficiency, with less-overdesigned drivetrain.

The remainder of the paper is organized as follows. In section 3.3 the problem statement and its solution is presented. In subsection 3.3.1, the overdesign problem is highlighted. In subsection 3.3.2, HESM is suggested to address the problem, and the HR definition is given. HESM equivalent loss circuit model is provided for efficiency calculation, and the HR relation to CPSR have been analytically derived. Before starting the next section, an insight to the optimal HR is provided. In section 3.4, the paper proposes the methodology to find the optimal HR and formulates the problem. The results are presented and discussed in section 3.5, and the optimal HR for the HESM is proposed. Finally, the conclusions are made in section 3.6.

3.3 Problem statement and HESM as a solution

Figure 3-1 presents the specifications of a battery powered three-wheel vehicle prototype, developed at CTA-BRP-UdeS, and the original motor efficiency map [117]. The original motor was a PMSM, with a CPSR 1.55:1, meaning that its maximum speed in constant power operation is 1.55 times its rated speed. The motor could provide 28 kW power, which was not sufficient for our purpose, and needed to be changed. Our efforts were to enhance the EV performance, while reducing the motor power. There are two operating modes for the motor. In continues mode, the motor can operate for long times. Beyond the continuous mode and up to the peak power, the motor can deliver temporary loads. This is limited to the thermal performance of the motor and the cooling system, as well as, the motor material endurance against the temperature; typically, the temporary loads can be delivered up to 20 seconds.

Variable	Value	Units
EV design specifications		
Vehicle mass with passengers	500	kg
Rolling resistance coefficient	0.02	--
Aerodynamic drag coefficient	0.75	--
Vehicle front area	1.25	m^2
Wheels radius	0.305	m
EV performance requirements		
Maximum Speed	120	km/h
Acceleration Speed	100	km/h
Acceleration Time	7	s
Grade Slope at 100 km/h	0.03	%

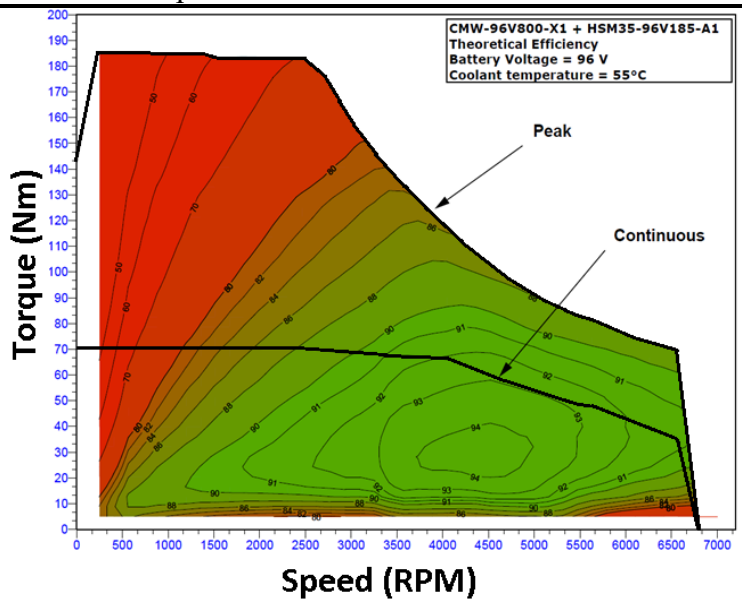

Figure 3-1: global Specifications and requirements of the three-wheel vehicle [117]

3.3.1 Overdesign problem statement

There are three requirements for every EV to be met, namely, cruising at maximum speed, accelerating in less than a time, and gradeability. Each requirement may change the shape of the EV torque envelope which is well documented in other works [4], [118]. EV torque envelope is the famous Force–Speed (F–S) curves, like those in Figure 3-2, which is obtained for the vehicle under study. The torque envelope that characterizes EV power needs is called characteristic envelope (Figure 3-2 (a)).

Afterwards, a proper traction motor with a torque envelop equal or greater than that of the characteristic envelope should be selected. This is called rated envelope (Figure 3-2 (b)). The power difference between characteristic and rated envelopes is considered as overdesign. Sometimes the designer himself intentionally puts an overdesign factor in order to increase the

EV dynamics and performance. However, at conditions which the CPSR of motor drive envelope is lower than that of the characteristic envelope, an overdesign will happen (Figure 3-2 (b)). It has an unfavorable effect on EV mass, cost, and performance.

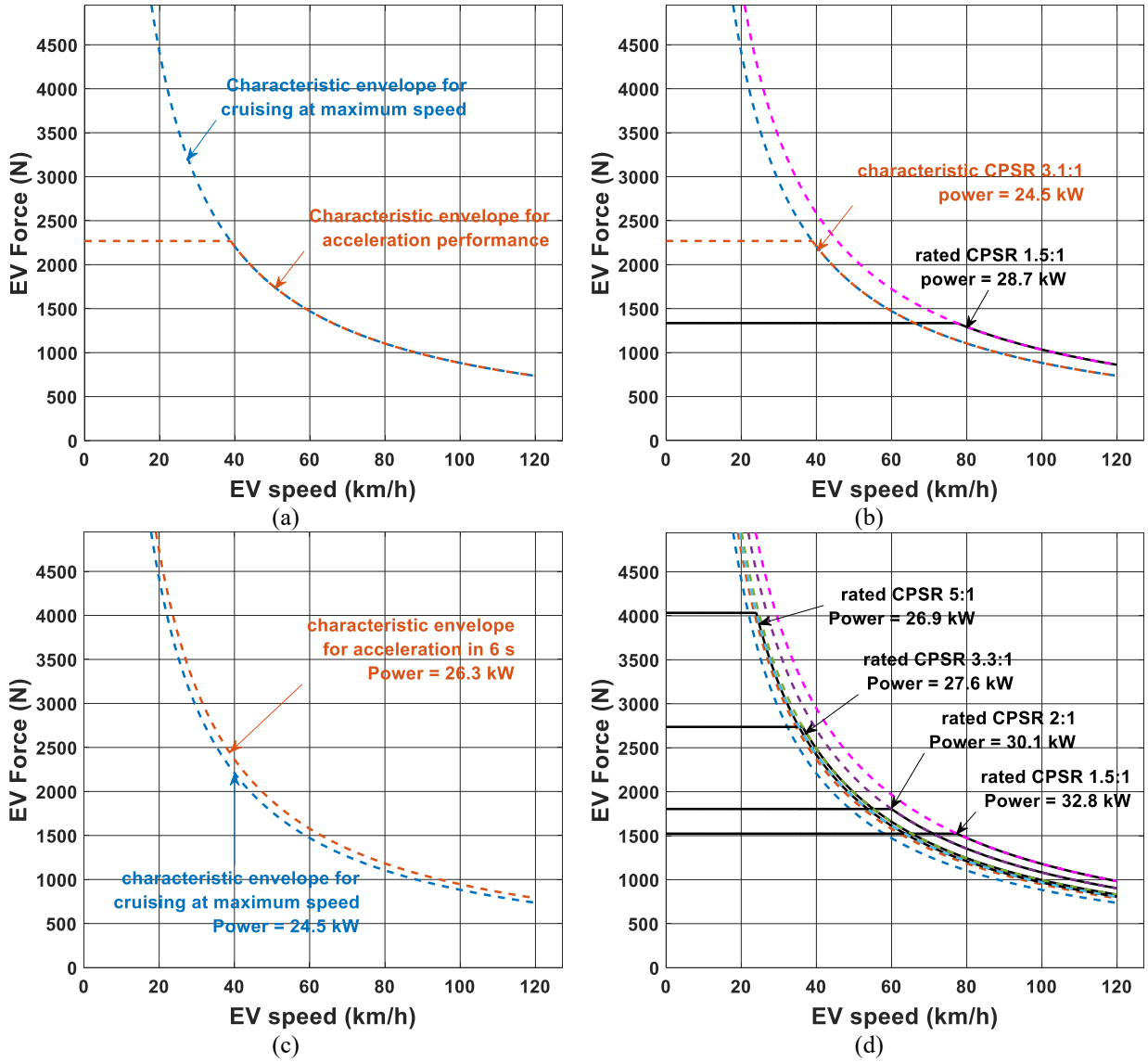

Figure 3-2: Drivetrain overdesign problem due to limited CPSR (a), (b) cruising at maximum speed is dominant, (c), (d) acceleration criterion is dominant

In Figure 3-2 (a), characteristic power for EV under study is determined by the maximum speed requirement, and acceleration requirement only determines the maximum force (or, CPSR) of the characteristic envelope. The EV needs a motor drive with a CPSR more than 3.1:1 to avoid the drivetrain overdesign. If a PMSM with the same CPSR as the original motor was to be used, it would cause 4.2 kW overdesign (Figure 3-2 (b)). Detailed characteristic and rated envelope definition for EVs is explained in [115].

To ameliorate the EV performance to be more comparable to ICE vehicles, efforts were made to reduce the acceleration time of the EV from 7 to 6 s. Similar ICE vehicles in the market have more wild acceleration, mostly <5 s. In this situation, the acceleration criterion gets dominant, for which, the EV characteristic envelope has an infinite CPSR (Figure 3-2 (c)). Considering real motor physical limits, the overdesign in this situation is inevitable, implying, the lower CPSR we have, the greater overdesign we face (Figure 3-2 (d)).

Looking back at Figure 3-2 (d), to remove part of the overdesign, the question is: 'How the CPSR should be increased, and what is the optimal value for it?' The objective is to primarily enjoy the high efficiency of original PMSM, and then remove part of the overdesign.

Increasing the motor maximum speed will increase the CPSR without causing any change to motor torque. Different Flux Weakening (FW) techniques can be applied to Permanent Magnet (PM) machines [119]. HESM, among them, is a very suitable candidate that has recently attracted many attentions [108], [57], [120], [121]. In this paper, we start with a primary non-optimal HESM design, and by finding the optimal HR, the overdesign problem will be addressed with higher efficiency.

3.3.2 HESM as the solution to overdesign problem

3.3.2.1 HR definition

Different kinds of electric motors have certain benefits and drawbacks. Hybrid machines aim at applying desired qualities of one machine into another that already lacks them, and at the same time, keeping all other benefits untouched or even improved. For instance, PM machines have problems in FW due to low efficiency, active material saturation, or permanent loss of magnet remnant induction [67]. The most prominent feature of Wound Excitation (WE) machine, on the other hand, is perfect FW, lower core losses, and smooth control on air gap flux, as it is achieved by independent DC-current regulation [116]. While hybridizing wound machine features into PM machine, some benefits could be damaged, such as, simple mechanical structure and robust rotor, high power and torque density, and its low-loss excitation system [57]. The most promising benefit of excitation system hybridization, therefore, is a wide CPSR in motoring mode, and proper control on the output voltage in generation mode [107], [122], plus unity power factor capability, loss minimization, and fault tolerance [108], [45].

HR in excitation system is a design variable of HESM between one and zero. It is defined as the ratio of PM excitation flux (ϕ_{PM}) over maximum excitation flux (ϕ_{max}), as presented in the following equation: (*3-1*).

$$HR = \frac{\phi_{PM}}{\phi_{max}} \tag{3-1}$$

HR equal to one indicates that only PM excitation is used, and HR equal to zero means that only WE is applied. Excitation flux (ϕ_{exc}), composed of PM (ϕ_{PM}) and WE flux (ϕ_{WE}), is formulated as follows (3-2).

$$\phi_{exc} = \phi_{PM} + \phi_{DC} = K_f \phi_{max} \;\; where\, K_f \in [0.1] \tag{3-2}$$

$$\phi_{DC} = M_e I_e \tag{3-3}$$

where K_f is excitation coefficient, ideally between one and zero. Its lower boundary is determined by saturation, thermal, or demagnetisation limits. M_e is mutual inductance between WE and armature coils, and I_e is the excitation current. Depending on the converter used for WE, it can be unidirectional for only FW, or bidirectional, where it is applied for both flux strengthening and weakening.

3.3.2.2 HESM equivalent circuit model:

Although hybrid excitation gives opportunity to a variety of design structures to rise, still, the first harmonic steady-state d–q circuit model can be adopted for torque and efficiency calculation (Figure 3-3).

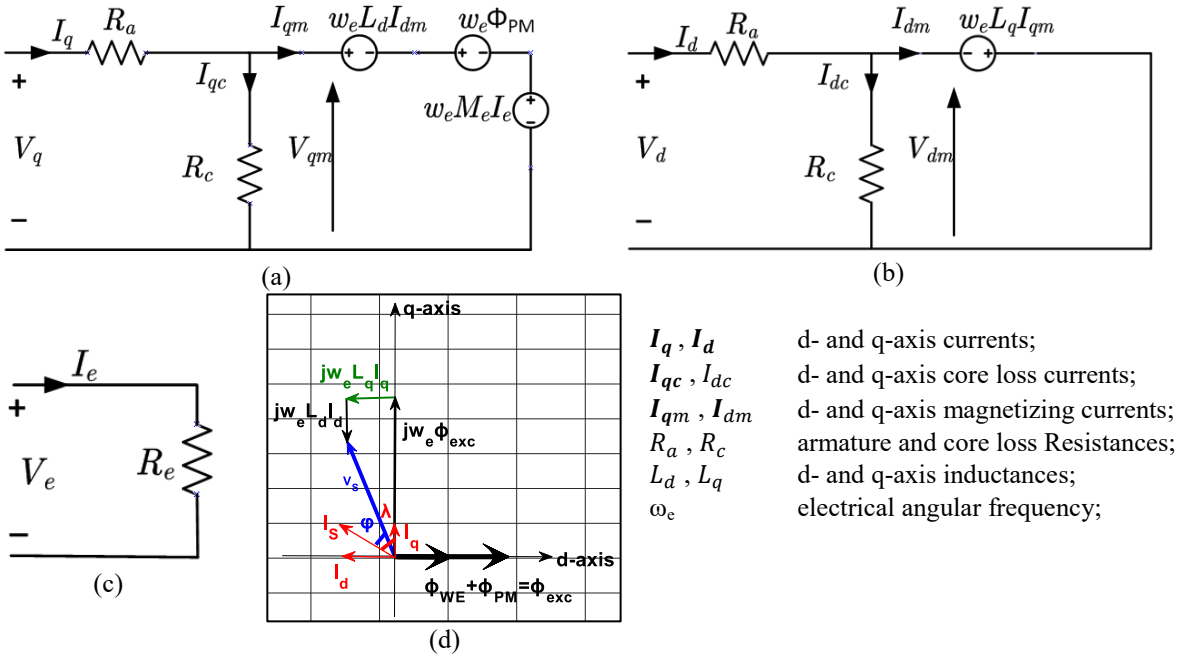

I_q , I_d	d- and q-axis currents;
I_{qc} , I_{dc}	d- and q-axis core loss currents;
I_{qm} , I_{dm}	d- and q-axis magnetizing currents;
R_a , R_c	armature and core loss Resistances;
L_d , L_q	d- and q-axis inductances;
ω_e	electrical angular frequency;

Figure 3-3: HESM first harmonic steady-state circuit model: (a), (b) q- and d-axis model, respectively, (c) WE system model, (d) dq reference frame

All losses can be accounted for by lumped resistances, and the hybrid excitation has been also included [123]. Figure 3-3 shows d-axis, q-axis, WE steady-state equivalent circuits, and the dq frame representation of the HESM. As the main purpose, here, is to find the optimal value of some electromagnetic variables, the efficiency of motor is calculated up to electromechanical torque output (T_e). Mechanical and stray losses have minor effect on electromagnetic design, and are neglected

While studying motor performance as a result of changes in design parameters, like in [24], normalized, or per-unit (pu) model, serves better in decision making. Looking through the common frame, it equalizes the effects from all design variables and provides a better judgment (Appendix I). Figure 3-4 provides normalized parameters of a non-optimal HESM and its three-dimensional cut view [14], for which, an optimal HR will be found in Sections 3 and 4 to address the overdesign problem.

Name	Symbol	Value
d-axis inductance	L_{dn}	0.5
q-axis inductance	L_{qn}	0.5
excitation-armature mutual inductance	M_{en}	1
armature resistance	R_{an}	0.1
core loss resistance	R_{cn}	20
excitation coil resistance	R_{en}	1

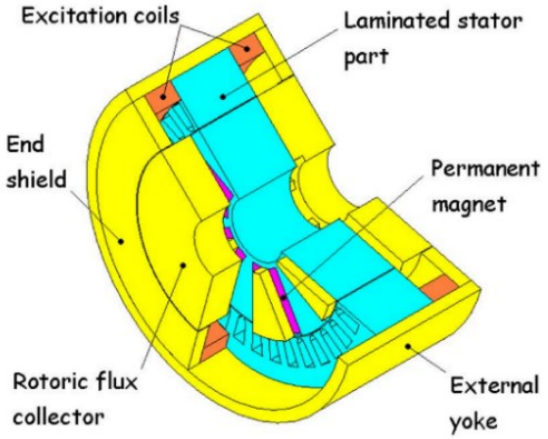

Figure 3-4:HESM normalized parameters and three dimensional cut view [116]

As the torque and loss calculation is critical in optimal HR searching algorithm, the circuit model is solved for normalized variables (with index n) in the loss model.

$$I_{qn} = I_n \cos(\lambda);\ I_{dn} = -I_n \sin(\lambda) \tag{3-4}$$

$$I_{qmn} = -R_{cn}\frac{K_f\omega_n - I_{qn}R_{cn} + I_{dn}L_{dn}\omega_n}{{R_{cn}}^2 + L_{qn}L_{dn}{\omega_n}^2} \tag{3-5}$$

$$I_{dmn} = \frac{I_{dn}{R_{cn}}^2 + I_{qn}L_{qn}R_{cn}\omega_n - K_f L_{qn}{\omega_n}^2}{{R_{cn}}^2 + L_{qn}L_{dn}{\omega_n}^2} \tag{3-6}$$

$$I_{qcn} = \frac{\omega_n\left(K_f + I_{dmn}L_{dn}\right)}{R_{cn}};\ I_{dcn} = \frac{\omega_n I_{qmn}L_{qn}}{R_{cn}} \tag{3-7}$$

$$emf = K_f\omega_n \tag{3-8}$$

$$T_n = I_{qmn}\left(K_f + \left(L_{dn} - L_{qn}\right)I_{dmn}\right) \tag{3-9}$$

where, λ is current angle with respect to EMF vector. For efficiency computing, the copper losses (P_{cun}) and core losses (P_{cn}) are calculated from (3-10) and (3-11), respectively.

$$P_{cun} = R_{an}\left(I^2{}_{dn} + I^2{}_{qn}\right) + R_{en}I^2{}_{en} \tag{3-10}$$

$$P_{cn} = R_{cn}\left(I^2{}_{dcn} + I^2{}_{qcn}\right) \tag{3-11}$$

3.3.2.3 HR and CPSR relation

HR and CPSR relation is developed based on the lossless model. There are different strategies to control HESM [108]; prior to motor base (rated) speed, the control is similar to maximum torque per ampere control in non-salient PM machines, and the d-axis current is null. While ω_n increases from zero to unity, the output normalized power also increases from zero to unity. This region is generally called constant torque region (see Figure 3-5).

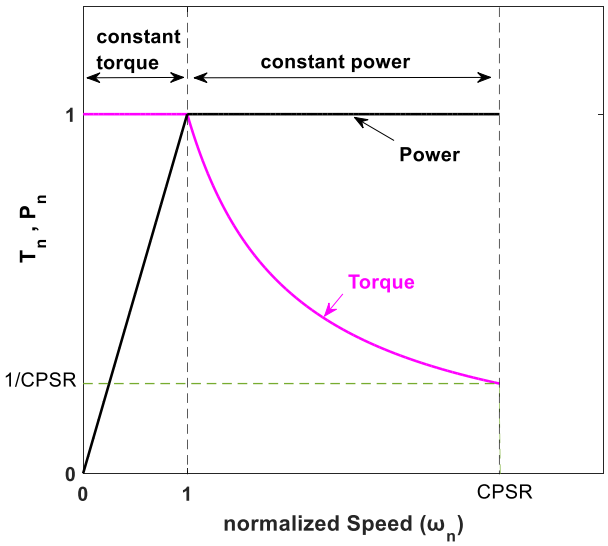

Figure 3-5 HESM operating modes, constant torque and constant power

L_{qn} and L_{dn} are equal for non-salient motors, such as our motor in Figure 3-4, and will be mentioned here after as L_n. At rated condition (see Figure 3-6), where ω_n, P_n, I_{qn}, and T_n are equal to unity, the motor reaches its voltage limits,

$$V_{maxn} = \sqrt{V^2{}_{dn} + V^2{}_{qn}} \leq \sqrt{1 + L^2{}_n} \tag{3-12}$$

$$\varphi_{rated} = arctan(L_n) \tag{3-13}$$

The current limit should be respected, which is,

$$I_{maxn} = \sqrt{I^2{}_{dn} + I^2{}_{qn}} \leq 1 \tag{3-14}$$

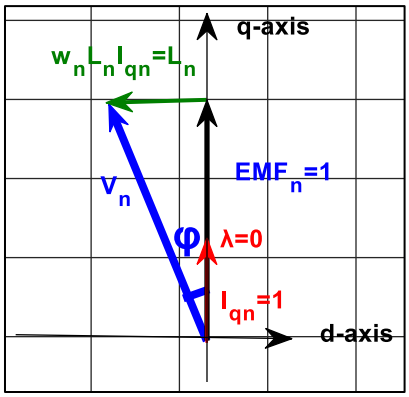

Figure 3-6 HESM dq representation at rated condition

Before and up to rated speed, the excitation flux is maximum (ϕ_{max}) [108], which is comprised of PM excitation (ϕ_{PM}) and WE (ϕ_{WEmax}),

$$\phi_{max} = \phi_{PM} + \phi_{WEmax} \tag{3-15}$$

Considering HR definition in (*3-1*), maximum WE is calculated as follows,

$$\phi_{WEmax} = (1 - HR)\phi_{max} \tag{3-16}$$

Above the rated speed and in constant power operating mode, excitation current together with d- and q-axis currents are controlled to have constant power operation ($P_n = 1$). Control in this mode is complicated and out of the scope of this paper. Details can be found in [108], [46]. It strongly depends on FW techniques, to keep voltage and current values under their limits. Thanks to HESM capabilities in FW, other objectives, such as unity power factor control is also achievable. As explained in [108], in constant power operation with unity power factor, the voltage is already at its limit (3-12), and the current can be calculated as,

$$I_n = \frac{1}{V_n cos\varphi} = \frac{1}{\sqrt{1 + L^2{}_n}} \tag{3-17}$$

Where, $cos\varphi$ is the power factor which is unity. As the speed is increasing linearly, the torque will be decreased to satisfy constant power operation. At the end of the constant power region we have,

$$T_n = \frac{1}{\omega_n} \tag{3-18}$$

The torque is also calculated from (3-19),

$$T_n = I_{qn} K_{fmin} \tag{3-19}$$

Which gives q-axis current at the end of constant power region ($\omega_n = \text{CPSR}$),

$$I_{qn} = \frac{1}{\omega_n \times K_{fmin}} \tag{3-20}$$

d-axis normalized current (I_{dn}) will be calculated from (3-17) and (3-20),

$$I_{dn} = -\sqrt{{I^2}_n - {I^2}_{qn}} = -\frac{1}{\omega_n \times K_{fmin}} \sqrt{\frac{\left(\omega_n \times K_{fmin}\right)^2}{1 + {L^2}_n} - 1} \tag{3-21}$$

Using (*3-1*), (3-2), and (3-16), K_{fmin} is calculated as,

$$K_{fmin} = \frac{\phi_{min}}{\phi_{max}} = \frac{\phi_{PM} - \phi_{WEmax}}{\phi_{max}} = 2HR - 1 \tag{3-22}$$

Which is limited to zero and cannot be negative, so for values of HR <0.5, K_{fmin} will be zero.

At all operating points, including $\omega_n = CPSR$, voltage and current limits should be respected. Current limit has been already seen in (5-21). To find the CPSR, we apply voltage limit, as the most CPSR is achieved through voltage and current limits of the motor drive.

$$v_{dn} = L_n I_{qn} \omega_n = \frac{L_n}{K_{fmin}} \tag{3-23}$$

$$v_{qn} = \omega_n K_{fmin} + L_n I_{dn} \omega_n = \omega_n K_{fmin} - \frac{L_n}{K_{fmin}} \sqrt{\frac{\left(\omega_n \times K_{fmin}\right)^2}{1 + {L^2}_n} - 1} \tag{3-24}$$

Applying voltage limit,

$$\left(\frac{L_n}{K_{fmin}}\right)^2 + \left(\omega_n K_{fmin} - \frac{L_n}{K_{fmin}} \sqrt{\frac{\left(\omega_n \times K_{fmin}\right)^2}{1 + {L^2}_n} - 1}\right)^2 = 1 + {L^2}_n \tag{3-25}$$

Solving for ω_n, and replacing K_{fmin} from (3-22), the ω_n at the end of constant power region will be,

$$CPSR = \omega_n = \frac{1 + {L^2}_n}{\sqrt{4HR{L^2}_n(HR - 1) + (2HR - 1)^2}} \tag{3-26}$$

We can infer that for PM excitation (HR = 1), the constant power range will depend on d-axis inductance,

$$CPSR_{PMSM} = 1 + L^2{}_n \tag{3-27}$$

Another result from (3-26) is that for HR values less than HR_{inf}, the CPSR will be infinite,

$$HR_{inf} = \frac{L_n}{2\sqrt{1 + L^2{}_n}} + \frac{1}{2} \tag{3-28}$$

It shows that for L_n equal to zero, HR should be 0.5. This means equal share is given to PM and WE, in order to have the PM flux completely removed [124].

The above equations are derived based on theoretical assumptions, such as:

- Maximum speed is not limited to mechanical effects of the rotor
- Only the maximum speed at the end of constant power operation is considered, yet, the motor speed increases in natural operating mode. In this mode of operation, the torque depends inversely to the second order of the speed until it drops to zero at the maximum speed [25].
- The converter ratings, i.e. its current and voltage limits, is the same for all cases.
- The losses are not accounted for.

3.3.2.4 HESM capability to address overdesign problem

When bidirectional excitation current is applied, which is used in this work, it is possible to change the location of high efficient region of the motor. Following this, it is possible to increase the global efficiency over the driving cycle [116].

High-efficient region is around the area, where the excitation current is zero, and the excitation system copper losses are minimum. In Figure 3-7 (a), high value of HR (equal to one) gives more shares to PM excitation and the high efficient area is inclined to the rated speed to make it similar to a PMSM machine. As it can be seen, some operating points are out of the highly efficient region, and this, results in non-optimal situation.

Decreasing HR from one drags the high efficient region towards higher speeds, as is shown in Figure 3-7(b), and more operating points are confined into this region which increases the global efficiency. Reducing the HR even more, gives more share to WE and the motor efficiency map tends to look like that of a WE motor, as in Figure 3-7(c); this results in some operating points to get out of the efficient region, and again the global efficiency is reduced. The optimal HR should give the highest global efficiency over the studied driving cycle, which means more frequent operating points being confined inside the high-efficient area. It can be inferred that HR gives another degree of freedom that lets the designer to optimize the HESM for the target driving cycles.

For more evident presentation, the efficiency maps are only plotted for positive torques, as the efficiencies for symmetrical operating points in first quadrant (forward-traction) and second quadrant (forward-regenerative breaking) is supposed to be identical.

(a)

(b)

(c)

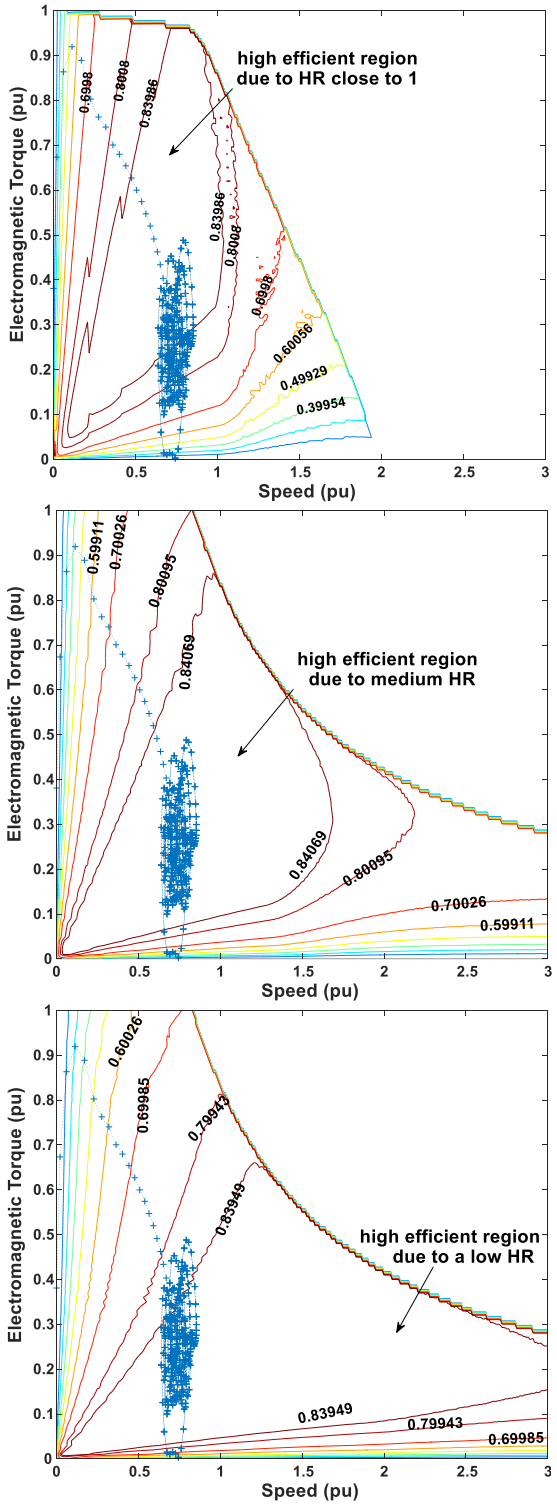

Figure 3-7 High efficient area move due to HR change, operating points for EMPA.C-2: (a) HESM with HR=1, η=83.3%, (b) HESM with HR=0.72, η=87.1%, (c) HESM with high HR=0.51, η=85.1%.

3.4 Search algorithm to find the optimal HR

HESM gives opportunities to minimize the losses in both design and control stages. In design, HR can map the high-efficient area of the motor over EV frequent operating points. It also can increase the CPSR and reduce the overdesign. In control, the stator and the excitation currents are controlled for many objective [125], such as minimizing total losses and operation at unity power factor.

The objective function, given in (3-29), is to maximize the global efficiency over studied driving cycles, considering design and control variables.

$$f = max\left[\eta_{tot}\left(HR.I_n\,.\lambda.K_f\right)\right] \tag{3-29}$$

Subjected to:
Design variable: $0 < HR < 1$
Control variables: $0 < I_n < 1.\quad 0 < \lambda < 1.\quad 0 < K_f < 1$
The studied driving cycles are presented in Table 3-1, and HR optimization flowchart is presented in Figure 3-8, with five search loops: one for HR, three for normalized control variables, and one for the normalized speed map. The big loop is for HR, and the small loops are for control variables and normalized speed.

Table 3-1 Studied driving cycles

Driving Cycles	Max. Speed (km/h)	Time (s)	Distance (km)
UHDC*	96.4	764	59.4
NEDC**	120	1219	39.6
UHDC + NEDC	120	3202	99

* US Highway Driving Cycle
** New European Driving Cycle

For any change in HR, there will be a change in CPSR, as mentioned in (3-26). As presented in Figure 3-2, higher CPSR may reduce the overdesign and change the required motor power. Then, for every speed (from 0 to 3 pu), the algorithm proceeds into the calculation of electromagnetic torque, terminal voltage, and efficiency for all combinations of three control variables. When all these loops are searched, the points violating maximum terminal voltage will be discarded. Among the remaining data, the combinations of design and control variables which respond to the efficiency map torque–speed mesh grid will be selected.

Then, those combinations that give the highest efficiency are found, and the efficiency map of the motor is built for each HR. After that all values of HR have been searched, global efficiency over the studied driving cycles is calculated, according to the method explained in [115].

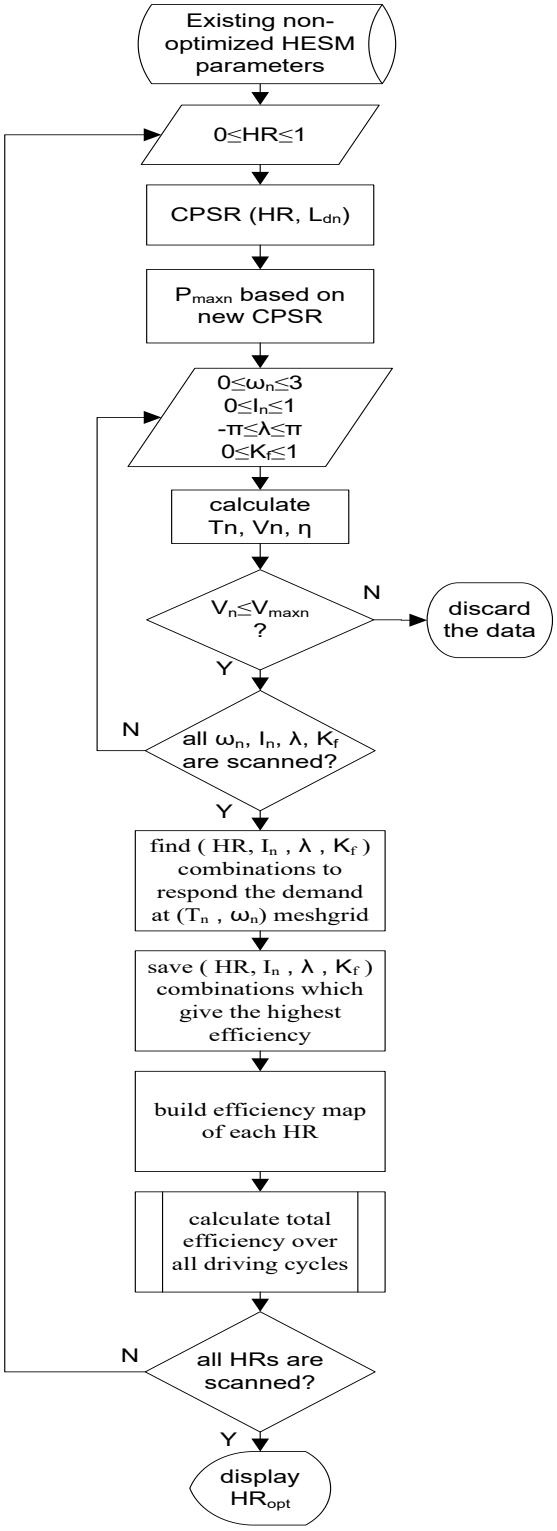

Figure 3-8 HR exhaustive search algorithm

Global efficiency over a specific driving cycle (η_{global}) is calculated from (3-30),

$$\eta_{global} = \sum_{i} \eta_i . \frac{t_i}{t_{tot}} \tag{3-30}$$

Where, t_{tot} is total time of the driving cycle, t_i is duration time of an operating point (i), and η_i is efficiency at that operating point. From (3-30), to maximize the global efficiency, more frequent operating points should be confined inside the most efficient region of the motor. In contrast, efficiency of other points with less frequency of occurrence has less impact.

Different motors evaluation could be made considering their global efficiency over selected driving cycle (η_{global}). The optimal HR is the one which gives the highest global efficiency over the studied driving cycles.

3.5 Results and discussions

To answer the question in the beginning of the paper and to find the proper CPSR for the overdesign problem, HESM approach was selected to increase the CPSR. An exhaustive search program was developed to propose an HR which results in higher global efficiency over the combined driving cycle. For the EV presented in Figure 3-1 and the driving cycles in Table 3-1, efficiency maps for the optimal HR are depicted in Figure 3-9.

More details about Figure 3-9 is summarized in Table 3-2. In Figure 3-9(a), UHDC is a highway driving cycle and the high-speed, low-torque operating points dominate, so, the algorithm tries to give more shares to WE due to its good efficiency at high speeds. Comparing it to Figure 3-9(b), NEDC is recognized more as a city driving cycle and the algorithm is inclined to give a high HR value as the solution. This specifies more share to PM excitation (higher HR value), as the PM motors are more efficient at low speeds. When combining the driving cycles together, the result would be Figure 3-9(c), where the optimal HR stays somewhere between the two values.

(a)

(b)

(c)

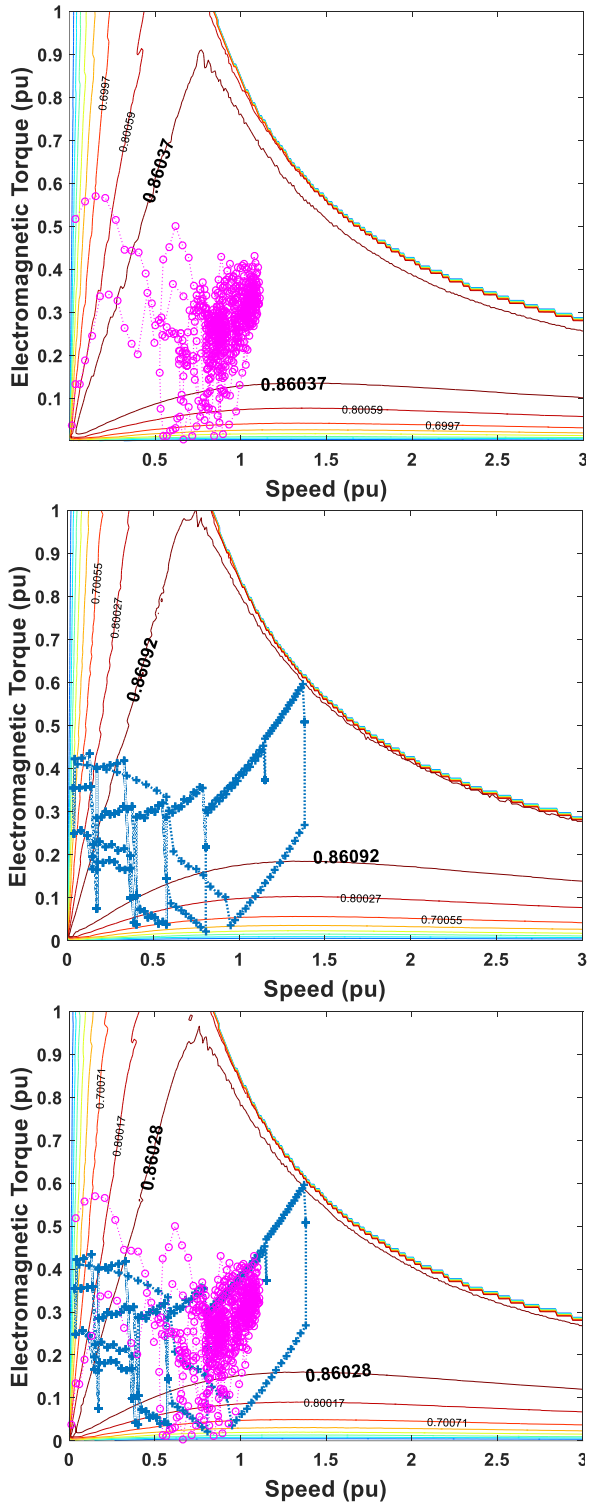

Figure 3-9 Efficiency maps and driving cycles operating points at optimal HRs: a) UHDC, (b) NEDC, (c) UHDC+ NEDC.

Table 3-2 Global efficiency at optimal HR

Name	HR_{opt}	HESM η_{tot}	Original motor η_{tot}	$\Delta\eta_{tot}$
UHDC	0.72	88.4%	84.2%	4.2%
NEDC	0.83	84.9%	80.9%	4%
UHDC + NEDC	0.78	86.5%	82.4%	4.1%

High-efficient region of the motor moves over T–S plane, as a function of HR value. This will change the global efficiency over the driving cycle, depending on how many of the operating points are inside or outside the high-efficient region. For NEDC, UHDC, and a combination of them, Figure 3-10 is presenting the efficiency trend to HR variation from 0 (pure WE) to 1 (pure PM excitation). Comparing to pure PM excitation, optimized HR in UHDC gives 1.7% improvement of global efficiency, and for NEDC, it is possible to have 0.8% higher global efficiency. For a combination of the two, the improvement would be 1.1%. It states that the HESM approach is more appropriate for highway transportation.

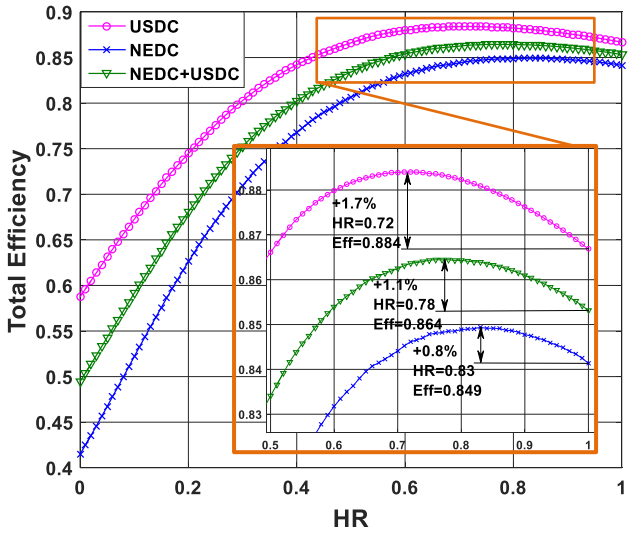

Figure 3-10 Global efficiency of HESM as a function of HR for different driving cycles

Table 3-3 presents the results in accordance with what was stated in the beginning of the paper, and then analyzed to this point.

Table 3-3 comparing motors for combined driving cycle

Motor Type	CPSR	Power (kW)	Speed (RPM)	η_{tot}
Original PMSM	1.55:1	32.8	4200	82.4%
Optimal HESM	3.3:1	27.6	3550	86.5%

As a result of finding optimal HR for EVs with fast acceleration, HESM power has been decreased 16%, in comparison with the original PMSM, and the global efficiency over combined driving cycle has been enhanced 4.1%.

For the HESM design with L_n equal to 0.5, HR values <0.7236 give infinite CPSR.

3.6 Conclusion

Motor design for EVs with enhanced acceleration performance is a challenge. In this paper, HESM was proposed to address this challenge and an algorithm was proposed to search and find the optimal HR. The algorithm is independently valid, no matter what the vehicle design is or which driving cycles have been selected. It can be applied to any vehicle design, and depending on different driving cycles as input, the output is optimal HR of a supposed HESM design. The objective was to maximize the global efficiency of the motor, which maximizes the EV efficiency over studied driving cycles, and remove part of the overdesign in drivetrain due to acceleration requirement.

Removing the overdesign, motor power is reduced. After finding optimal HR, it is possible now to fully optimize all drivetrain elements, as well as the motor dimensions and materials. This will be dealt in our future works. Also, an analytical relation between motor HR and CPSR was developed, which should be validated through experimental results.

Due to optimal HR selection for the HESM, compared with the original PMSM, global efficiency over NEDC, UHDC, and a combination of the two, was increased 4, 4.2, and 4.1%, respectively. In addition, due to increase in motor CPSR, required motor power was reduced 16%, which is less than the original motor power. So, benefiting from HESM prominent features, with a lower motor power, better performance and higher efficiency is obtained. Having an enhanced global efficiency together with power reduction, less battery resources would be needed to give the same performance as before with original PMSM.

Chapter 4 HESM Optimization: Component Level

Original Title:
Component-Level Optimization of Hybrid Excitation Synchronous Machines for a Specified Hybridization Ratio Using NSGA-II

Authors and Affiliations:
- **Ahmad Shah Mohammadi,** Ph.D. student, e-TESC Laboratory, Department of Electrical & Computer Engineering, University of Sherbrooke
- **João Pedro F. Trovão,** Professor, e-TESC Laboratory, Department of Electrical & Computer Engineering, University of Sherbrooke
- **Carlos Henggeler Antunes,** Professor, R&D Unit, INESC Coimbra, Rua Sílvio Lima, Pólo II, 3030-290 Coimbra, Portugal

State: Submitted (2019/10/29)

Journal: IEEE Transactions on Energy Conversion

Context of the chapter

After evaluating the Ph.D. proposal and its methodology using the dq lumped parameter model in Chapter 3, it is time to delve into the complexity of the HESM under study, which is our second major contribution. The model used here, is a non-linear 3D Magnetic Equivalent Circuit (MEC) model, which itself, is evaluated by FEA technique. The concept of Hybridization Ratio (HR) and the phenomenon of hard and soft saturation are precisely defined using the developed MEC model. At the end of this chapter, we will be able to optimally design a HESM for a given HR using NSGA-II and MEC modelling. This procedure can be repeated to scan all HRs between 0 and 1 and find the optimal HR, which will be dealt with in Chapter 5.

4.1 Abstract

In this paper, a Hybrid Excitation Synchronous Machine (HESM) is optimally designed for a given Hybridization Ratio (HR). A new formulation of the design problem is proposed to be tackled by the Non-Dominated Sorting Genetic Algorithm II (NSGA-II). While minimizing the material cost, this formulation includes a more comprehensive explanation of the key concept, HR, which considers the soft and hard saturation effects in the HESM design. The HESM model is based on a 3D nonlinear Magnetic Equivalent Circuit (MEC). For faster convergence, the number of design variables is reduced using two statistical analyses, namely Analysis of Level and Analysis of Variance (ANOVA). The optimal HESM for HR=0.5 is validated by a commercial Finite Element Analysis (FEA) software.

4.2 Introduction

Hybrid Excitation Synchronous Machines (HESMs) have opened new opportunities to enhance efficiency and performance of Electric Vehicles (EVs) [35]. In this type of electric machine, the hybrid excitation has two sources: Permanent Magnet (PM) excitation and Wound Excitation (WE). HESMs benefit simultaneously from the advantages of PM, i.e. high torque/power density, and WE, i.e. controllability of the airgap flux. A suitable topology combined with an optimal Hybridization Ratio (HR) between the two excitation sources can add the following favorable features to the traction motor [35], [20].

Although hybridization in the excitation subsystem adds to the complexity and the cost of motor, it gives a very special property to the HESM: the shape of its efficiency map can change as a function of HR. By changing the HR (between 0 and 1), one can match the high efficient area over the most frequent operating points, as explained in [35], [20] and shown in Figure 4-1. Moreover, setting the HR enables to control the Constant Power Speed Range (CPSR) (as can be seen in Figure 4-1), which in turn has an effect on the gearbox ratio, the acceleration performance, as well as the sizing of the motor and other drivetrain elements [20]. Thanks to the HR, the HESM offers an extra degree of freedom to the designer for system-level optimization. However, the task is very complicated. The complete design of the HESM for the maximization of global efficiency over the selected driving cycle has two levels (see Figure 4-2).

1. Component-level: a minimum cost HESM is designed to optimally satisfy the flux regulation requirements for a specified HR. Here, we are incorporating the HR as a design variable in the component-level optimization. The algorithm used for this purpose is NSGA-II [3]. The optimization for each specific HR at the component-level is necessary, if the consistency of comparison at the system-level is sought for.

2. System-level: by executing the component-level for all HRs between 0 and 1 (with adequate intervals), each HESM corresponding to each HR is optimally designed. Then, an efficiency map is constructed for each HESM and the global efficiency over the selected driving cycle is calculated. In analogy with Fig. 1, all efficiency maps and their global efficiencies are compared to find the optimal HR.

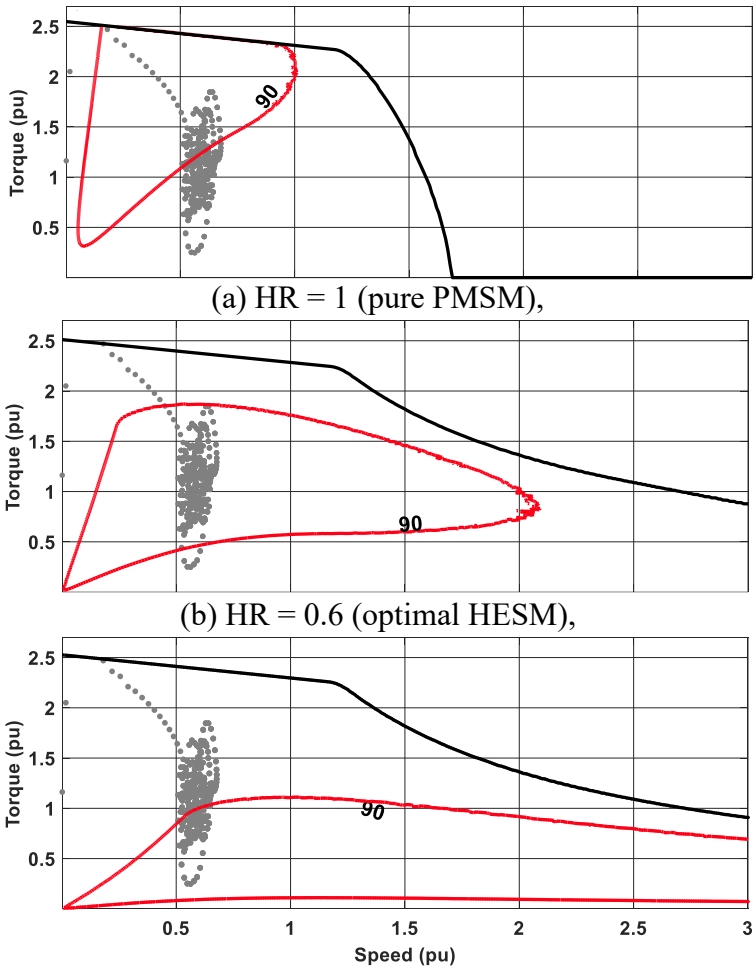

(a) HR = 1 (pure PMSM),

(b) HR = 0.6 (optimal HESM),

(c) HR = 0 (pure WESM)

Figure 4-1: Global efficiency over EMPA-C2 driving cycle as a function of HR.

Due to its impact on the success of HESM optimization, the component-level optimization is in the focus of this paper. To benefit from several advantages of HR for system-level optimization, it is necessary to incorporate the HR as a design variable at the component-level optimization of HESM. That is to investigate whether the HESM really acquires the requirements regarding the specified HR, and to see if it is capable to attain certain flux levels (explained in section 4.3). In the literature, the optimization of HESM at component-level has been almost always performed without considering the HR as a design variable [4], [5]. At system-level, on the other hand, researchers have used one single HESM design for all HRs, and applied the DQ equivalent circuit model to analyze the HESM [1], [2]. In this model, all the lumped parameters are considered constant regarding the HR change. They have defined the HR as the ratio of PM excitation (ϕ_{PM}) to the maximum excitation flux linkage (ϕ_{max}) [1], [2], [6], [7], [8]. This is not realistic for all HRs at all working conditions, due to saturation and asymmetrical flux regulation in HESMs, which is observable in [9] and [10]. This concept is explored in section 4.3.

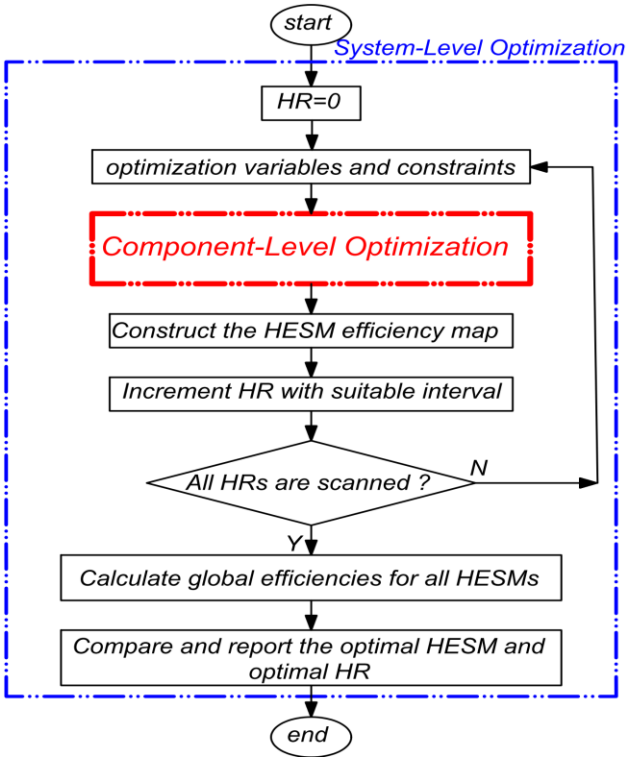

Figure 4-2: Component-level optimization as part of HESM system-level optimization (for details about the component-level optimization, see Figure 4-9).

This paper has two main contributions. 1) A novel comprehensive definition of the key concept HR. This is achieved through a detailed study on HESM flux regulation using FEA simulation. 2) Proposing a new design optimization method for any specified HR, using NSGA-II. A new formulation for simultaneous design and optimization of HESM is proposed to be tackled by NSGA-II. Using this formulation, the error of design is constrained for a HESM with HR=0.5, and its cost is minimized. The final design of the HESM is validated using Finite Element Analysis (FEA).

4.3 Definitions and problem statement

The aim of this section is to describe the design complexities of HESM, and the necessity of design modification for each HR. This is mostly due to soft and hard saturation in HESM, which is also provided here.

4.3.1 HESM under study and the target variables

Figure 4-3 provides a 3D view for the HESM, which is designed and modeled in FEA software (MagNet, Infolytica). The hybridization topology and the main flux paths for PMs and WE are displayed in this figure. This topology was proposed and theoretically and experimentally studied in [35], [67], [68], and [69]. We did some minor modifications in the magnetic and

mechanical design. The left-side excitation coil regulates the S-pole flux, whereas the right-side coil is responsible for the flux regulation of the N-pole. The outer stator provides a magnetic path for WE flux. In this parallel hybridization topology, the rotor claw-pole structure prevents the flux from the N-pole to interfere into the S-pole. This design has easy flux control, high efficiency, wide CPSR, and good reliability [70]. However, it has 3D flux paths, for which the FEA analysis is very time- and process-consuming.

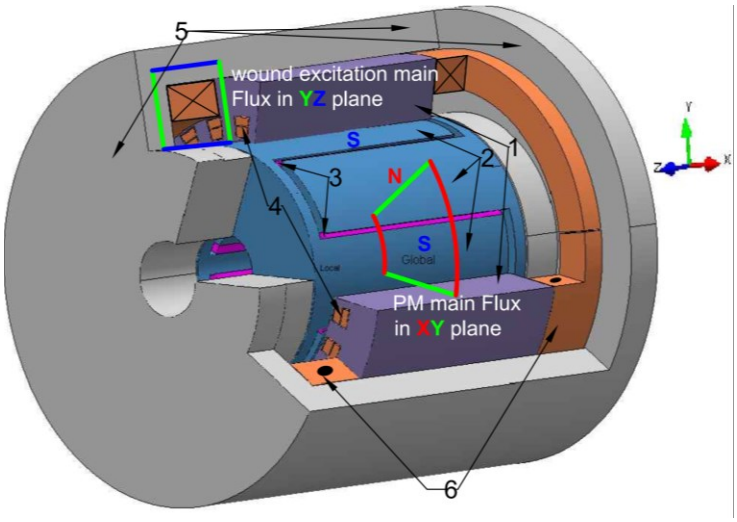

a) 1-stator (silicon steel lamination), 2-rotor claws (iron–silicon alloy), 3-PMs (ferrite), 4-stator coils (copper), 5-outer stator (iron–silicon alloy), 6-WE coils (copper)

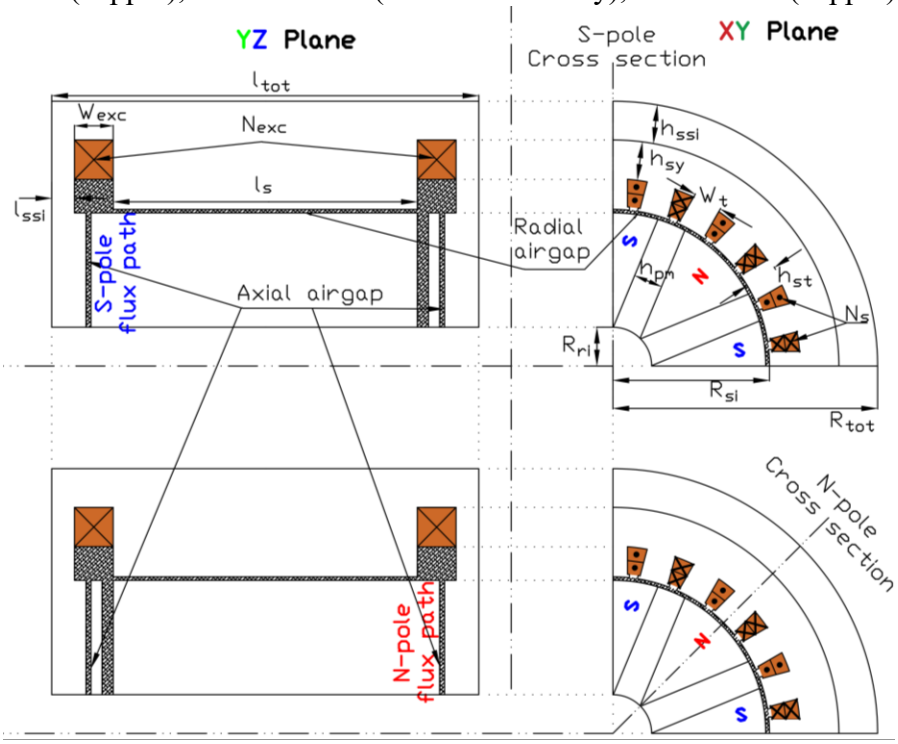

b) The cross sections of S-pole (top) and N-pole (bottom)

Figure 4-3: HESM under study with 3D flux directions

Table 4-1 displays the design input specifications for all design candidates in the optimization.

Table 4-1 design specifications and constraints

Name	*Value*	*Name*	*Value*
Max. DC bus voltage (V)	109	Airgaps length (mm)	0.5
Min. DC bus voltage (V)	83	Stator inside radius (mm)	115
Nom. Power (W)	2000	Max height (mm)	200
Nom. speed (rpm)	2000	Max total length (mm)	300
Num. of phases	3	Stator winding turns	2
Num. of pole pairs	4	Slot opening (mm)	5
Slot/pole/phase	1	HR	0.5
φ_{nom} (Wb.)	0.0852		

The motor nominal d-axis flux linkage (ϕ_{nom}) must reach 0.0852 Wb to produce the nominal voltage at nominal speed. The variables for HESM design optimization are listed in Table 4-2 (see Figure 4-3 for further clarification).

Table 4-2 Optimization Variables (see Figure 4-3)

Parameter	*Description*
R_{ri}	Rotor inside radius
W_t	Stator tooth width
h_{sy}	Stator yoke height
h_{PM}	PM height (thickness)
h_{ssi}	Outer stator solid iron height
l_s	Stator active length
l_{ssi}	Outer stator end cap length
N_{exc}	WE coils number of turns

4.3.2 Design complexity: Soft and hard saturation in HESM

HESMs are well-known for their flux regulation capability. One challenge is the homopolar and leakage fluxes created by PM, closing all or part of their loop from one pole to the other, through the outer stator magnetic core (see Figure 4-4). This results in the so-called effects of soft and hard saturation. These effects are discussed in [128] for two power inductors with ferrite and powder iron materials. The same phenomenon is present in our HESM, but for one material in two different regimes, i.e. flux-weakening and flux-strengthening.

Figure 4-5 displays the flux density of a HESM for three excitation currents, over the cross sections of S-pole and N-pole (for cross sections, see Figure 4-3(b)). For zero excitation current, the flux from PMs has already leaked into the WE magnetic path, and has occupied part of the capacity of magnetic materials (Figure 4-5(a)). Injecting positive current into the excitation coils

(flux strengthening) will prevent the leakage from PMs, and releases back the flux-carrying capacity of the material in outer stator (Figure 4-5(b)). Unfavorably, with negative excitation current (flux weakening), the magnetic material saturates very fast (Figure 4-5(c)). As we see, flux strengthening is easier than flux weakening, meaning that it needs less excitation current or number of turns for the same amount of flux regulation. This asymmetry depends on the HR and the motor dimensions, as will be explained later in this section.

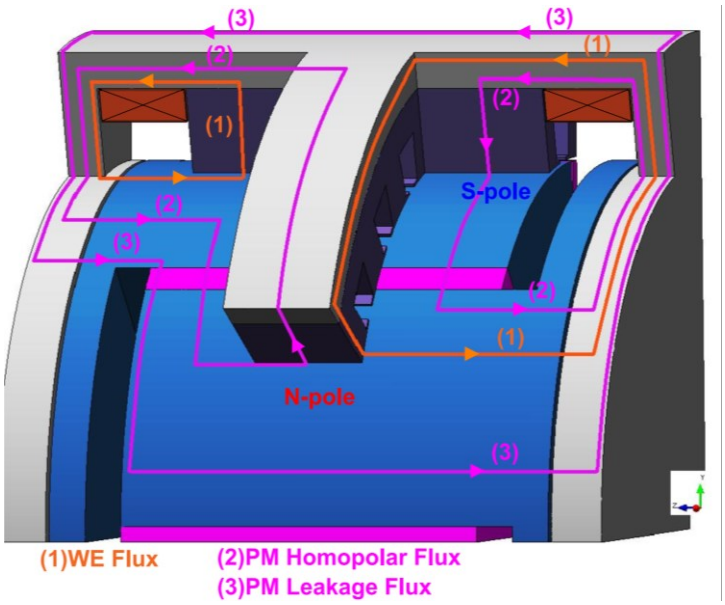

Figure 4-4: Interactions of PM and WE flux paths in flux weakening

Figure 4-6 plots d-axis flux linkage (φ_d) and average relative permeability (μ_r) of the outer stator (see Figure 4-3(b)) as a function of WE Magnetomotive Force (MMF_{WE}). During the flux weakening, while the MMF_{WE} increases negatively, the μ_r rolls off abruptly at the point of saturation, which results in hard saturation. On the other hand, in flux strengthening (MMF_{WE} increasing positively) we have the soft saturation phenomenon, where theμ_r is constant over a wide range of MMF_{WE}, and then it exhibits a gradual reduction. There is a counter-effect (reduction) in φ_d at higher MMF_{WE} due to excessive saturation, which is not of our interest.

In terms of HR, the hard and soft saturation is more evident as we move from either HR=0 or HR=1 towards HR=0.5. For HR=0 there is no PM, hence the flux regulation is perfectly symmetrical. For HR=1, neither excitation coils nor the regulation of flux exists. Between the two, the asymmetry is proportional to the level of interactions between PM and WE fluxes. However, the motor dimensions play an important role, as in overdesigned motors these effects are not relevant.

For instance, for HR=0.5, the excitation subsystem should regulate the flux between minimum flux (ϕ_{min}=0 Wb) and maximum flux (ϕ_{max}=0.0852 Wb). If the motor is targeted to give ϕ_{max} at nominal MMF_{WE}, then it would be thermally, magnetically and electrically impossible to attain ϕ_{min}=0 Wb within the same design. The design should be certainly modified in favor of the dominant mode, which is the flux weakening in this case.

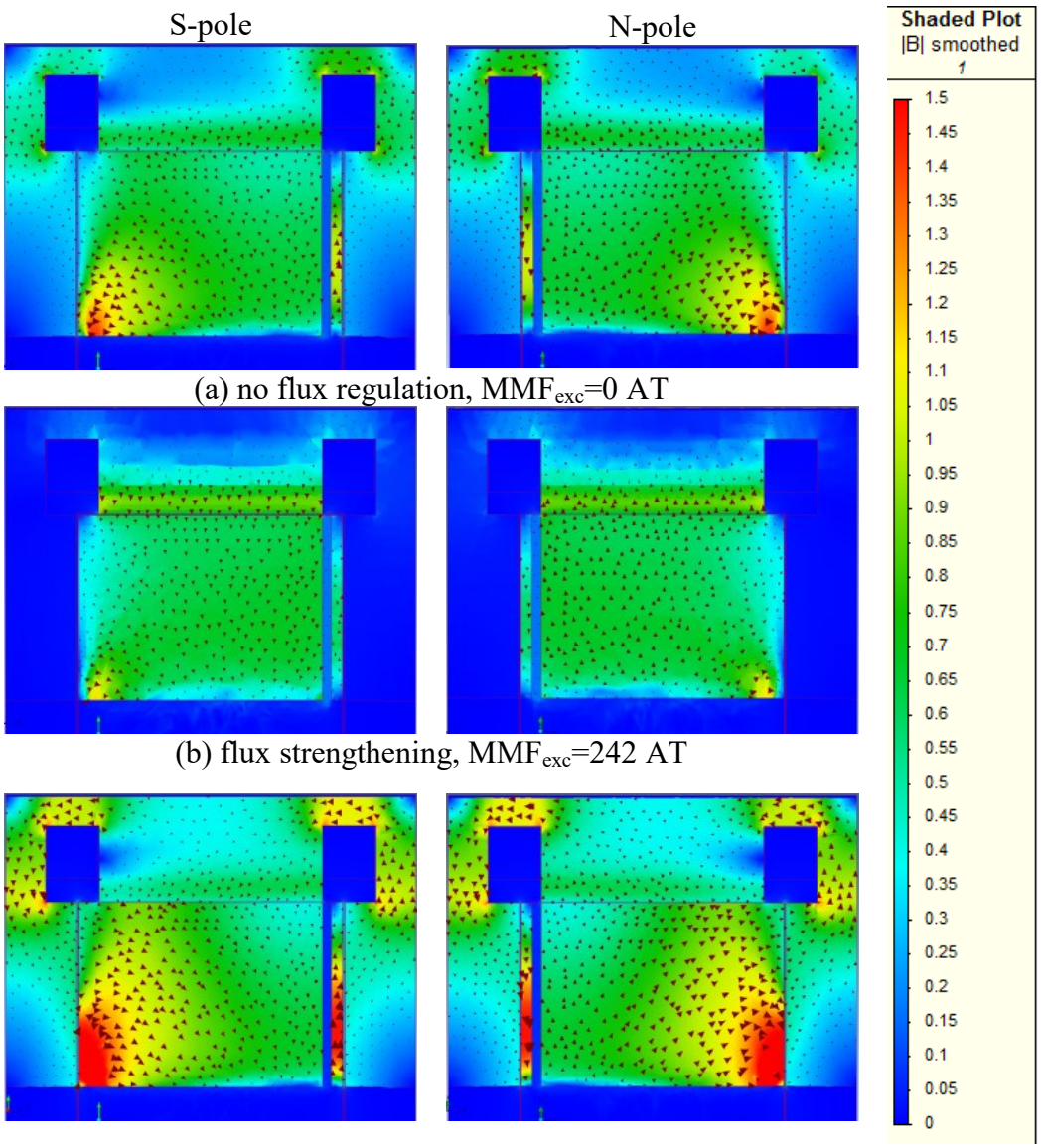

(a) no flux regulation, MMF_{exc}=0 AT

(b) flux strengthening, MMF_{exc}=242 AT

(c) flux weakening, MMF_{exc}=-242 AT

Figure 4-5: FEA simulation of soft and hard saturation phenomenon

4.3.3 Comprehensive definition of Hybridization Ratio (HR)

In the literature, HR is defined as the ratio of the flux linkage from PM (ϕ_{PM}) to the maximum flux linkage (ϕ_{max}) [35], [20], [45], [47] and [67], as in (4-1)

$$HR = \frac{\phi_{PM}}{\phi_{max}} \tag{4-1}$$

To give a more practical aspect to this definition, we have derived the specified PM flux (ϕ_{PM}), maximum flux (ϕ_{max}) and minimum flux (ϕ_{min}) from ϕ_{nom} and HR:

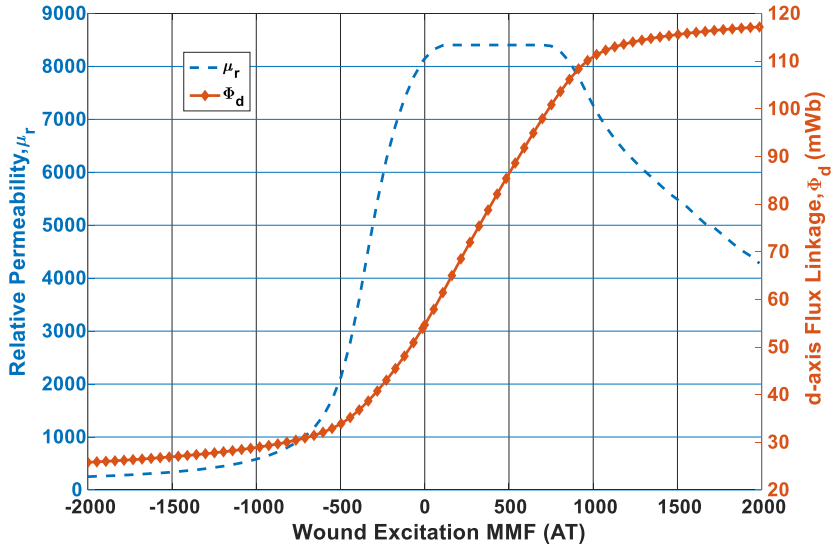

Figure 4-6: Airgap flux density (B_{ag}) and average relative permeability of the outer stator (μ_r) as a function of WE current at no-load (zero armature current)

$$\phi_{PM} = HR\phi_{nom} \tag{4-2}$$

$$\phi_{WE} = (1 - HR)\phi_{nom} \tag{4-3}$$

$$\phi_{min} = max\ (0,\ \ \phi_{PM} - \phi_{WE}) = max\ (0, (2HR - 1)\phi_{nom}) \tag{4-4}$$

$$\phi_{max} = \phi_{nom} \tag{4-5}$$

As was shown in Figure 4-4 to Figure 4-6, the assumption of symmetrical flux regulation cannot be trusted at all HRs. To achieve the true meaning of HR, the HESM should be able to regulate the flux at any desired level between ϕ_{min} and ϕ_{max}. For any design modification, the following fluxes can be calculated and compared to the specified fluxes:

$$\phi_{PM-calc} = \phi_{PM} + e_1 \tag{4-6}$$

$$\phi_{min-calc} = \phi_{min} + e_2 \tag{4-7}$$

$$\phi_{max-calc} = \phi_{max} + e_3 \tag{4-8}$$

where e_1 to e_3 are error values between the calculated flux linkages and the specified ones. It should be noted that these fluxes can be calculated from any reliable model of HESM, given that it can take into consideration the non-linearity of magnetic materials.

The reduction of error e_1 is straightforward and this should be reduced nearly to zero and make $\phi_{PM-calc}$ as close as possible to ϕ_{PM}. It has a visual effect on the motor efficiency map, as the

high-efficient area is roughly around the point where the WE current is zero and its copper losses are absent.

Concerning e_2 and e_3, it is impossible to address them both, as will be explained, and only the dominant error will be fully addressed. Generally, e_2 is dominant at high HRs, where a higher share of the airgap flux is assigned to the PMs. Removing the strong flux coming from PMs is not an easy task, provided that we are facing the hard saturation effect. On the other side, at low HRs e_3 is more dominant. For instance, if HR=0.1, we should provide $\frac{9}{10}\phi_{max}$ by WE. With negative excitation current, this flux can easily attenuate the flux from PMs ($\frac{1}{10}\phi_{max}$) and attain ϕ_{min}=0.

Figure 4-7 provides a visual representation of e_2 and e_3 with respect to the specified ϕ_{min} and ϕ_{max} (see equations (4-4) and (4-5)). Depending on the $\phi_{min-calc}$ and $\phi_{max-calc}$, there are six different possibilities, each of which shows the dominant mode in red hatches over a yellow background.

In case 1 and 2 ($e_2 < 0$ and $e_3 > 0$), the motor is overdesigned, and the flux is tunable between ϕ_{min} and ϕ_{max}. With $|e_2| > |e_3|$ (in case 1), the dominant error is in flux strengthening. In case 2 ($|e_2| < |e_3|$), the dominant error is in flux weakening.

Oppositely, in cases 3 and 4 the specified fluxes cannot be reached. With $|e_2| > |e_3|$ (case 3), the dominant error is in flux weakening; with $|e_2| < |e_3|$ (case 4), the dominant error is in flux strengthening.

In cases 5 and 6, the dominant errors are in flux strengthening and flux weakening, respectively.

In all cases, we must first reduce the dominant error, while the other error could not be removed completely. As an example, in cases 3 and 6, we need to modify the design for stronger WE flux, in order to reduce the difference between $\phi_{min-calc}$ and ϕ_{min}. Having reduced e_2 to zero, there would be still a surplus of flux in flux strengthening due to the asymmetry in flux regulation. The error e_3 would be always a non-zero positive value, meaning that $\phi_{max-calc}$ would be always greater than ϕ_{max}. Fortunately, this overdesign is favorable, e.g., in EV acceleration. The peak torque capability of the machine is improved approximately in proportion to ($\phi_{max-calc} - \phi_{max}$).

The design of HESM for a given HR is a much more complex problem than it seems at a first glance. All the three errors should be addressed simultaneously; otherwise the error reduction would be catastrophic, because the three errors have counter effects on each other. We may tune all design variables to obtain a very small e_1 (say <0.1%), but thereafter, when we try to reduce e_2 or e_3, the value of e_1 will increase. In case 6, for instance, selecting higher h_{PM} in order to increase $\phi_{PM-calc}$ will increase $\phi_{min-calc}$ and $\phi_{max-calc}$ (e_2 and e_3) too. Another contradictory situation is when we want to reduce homopolar and leakage PM flux by lowering h_{ssi} and l_{ssi}. This will increase $\phi_{PM-calc}$, but it would have a negative effect on the flux regulation of $\phi_{max-calc}$ and $\phi_{min-calc}$ due to the WE flux path saturation. To address all these complexities

in the HESM design and achieve the true meaning of HR, we have developed a new design formulation to be tackled by an evolutionary algorithm.

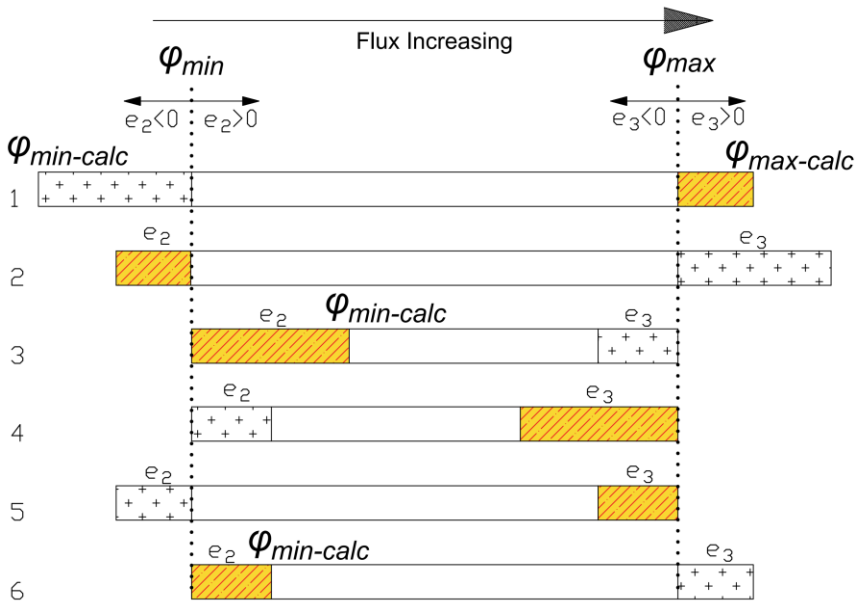

Figure 4-7: Different possible error values and the dominant mode

4.4 Design optimization formulation

As it is repetitively executed inside the system-level optimization loop for each HR, the component-level optimization cannot be very time- and resource consuming in order to allow for a fast convergence (see Figure 4-2). NSGA-II [94] is generally considered the state of the art algorithm in evolutionary multi-objective optimization, which has provided good results in the optimization of electric machines [95], [96] and [97]. This section is devoted to proposing a new formulation to deal with the optimal design of HESM. Firstly, the decision variables and the two objective functions (OFs), i.e. error in HR and Cost, are defined. Taguchi method, together with Analysis of Variance (ANOVA), is applied to reduce the number of decision variables. Then, the NSGA-II deals with the design complexity and cost minimization of the motor.

4.4.1 Decision Variables

The variables for design optimization of HESM are displayed in Table 4-2, which should be optimized to achieve the specified HR=0.5 and the minimum cost for our HESM, while respecting the design constraints in Table 4-1.

4.4.2 HESM model to calculate the objective functions

In every design optimization problem, a model is mandatory to predict the output as a function of input parameters. As the selected topology had 3D flux directions, the use of FEA technique was limited to the available time budget and computational resources. To overcome this difficulty,

we used the MEC technique, which considers the non-linearity in magnetic materials and the effect of hard and soft saturation. Being semi-analytical semi-numerical, the MEC can make a tradeoff between the time and accuracy of calculations, while preserving the most relevant details.

The model used in this paper is a nodal-based analysis of Kirchhoff's current law, with the branches of magnetic flux tubes. The approach in [129] and [85] is the guideline used for model development. The 2D model developed can be found in [21] for a PMSM with the same rotor and stator configuration, whereas the full implementation and evaluation of the 3D model is carried out in [21]. We have considered more sections and divisions in all directions at areas with hard and soft saturation effects. This enables to provide more details of the flux behavior and losses. The motor dimensions, the material properties and the coils currents are given as inputs to the model. The user also controls the time and accuracy of the results by controlling the resolution of the meshes and the error tolerances in the model. The meshing, solving and post-processing phases are automatically done by a program dedicated to this purpose.

4.4.3 The definition of Objective Functions (OFs)

Two *OFs* are defined to minimize the error in the fluxes specified by HR (Err_{HR}), and the Cost. The efficiency is handled at system level, as discussed in the introduction and illustrated in Figure 4-1. The design of HESM for a specified HR is a complicated task and is addressed by the first objective function. The error minimization OF serves to bring the calculated fluxes ($\phi_{PM-calc}$, $\phi_{min-calc}$, $\phi_{msx-calc}$) as close as possible to the specified fluxes (ϕ_{PM}, ϕ_{min}, ϕ_{max}) for the given HR (see (4-6), (4-7), and (4-8)). As this task was difficult to deal with, it was handled by considering it as an objective function, using the outstanding capabilities of NSGA-II. This new formulation regarding the design problem helped us to address the complexity of the design, and at the same time, keep the focus on the minimization of cost.

4.4.3.1 Err_{HR} (OF_1)

To guarantee the specified HR for the HESM under study (HR=0.5), we have to reduce the errors, in (4-6) to (4-8), as much as needed. OF_1 is defined to calculate the error ratio and has two terms. The first term (OF_{11}) concerns the e_1, as calculated in (4-9).

$$OF_{11} = \frac{e_1}{\phi_{PM}} \tag{4-9}$$

The second term of error ratio (OF_{12}) deals with e_2, and e_3 as defined by the pseudo-code in In the pseudo-code, whenever ϕ_{min}=0, as it in the denominator of calculations, we replace it with $\frac{\phi_{max}}{1000}$. The OF_1 is defined in (4-10).

$$min\ \ OF_1 = OF_{11} + OF_{12} \tag{4-10}$$

Cost minimization (OF_2)

The cost of materials is calculated from (4-11).

$$min\ OF_2 = P_{cu}V_{cu} + P_{FeSi}V_{FeSi} + P_{Fe}V_{Fe} + P_{PM}V_{PM} + P_{sh}V_{sh} \quad (4\text{-}11)$$

where V_j is the volume of material j and P_j is its price per unit volume, as displayed in Table 4-4.

Table 4-3 (see Figure 4-7 to better understand the code). In the pseudo-code, whenever ϕ_{min}=0, as it in the denominator of calculations, we replace it with $\frac{\phi_{max}}{1000}$. The OF_1 is defined in (4-10).

$$min\ \ OF_1 = OF_{11} + OF_{12} \quad (4\text{-}10)$$

4.4.3.2 Cost minimization (OF_2)

The cost of materials is calculated from (4-11).

$$min\ OF_2 = P_{cu}V_{cu} + P_{FeSi}V_{FeSi} + P_{Fe}V_{Fe} + P_{PM}V_{PM} + P_{sh}V_{sh} \quad (4\text{-}11)$$

where V_j is the volume of material j and P_j is its price per unit volume, as displayed in Table 4-4.

Table 4-3 Pseudo-code for the calculation of second term in Err_{HR} (OF_{12})

1:	**if** (e_2<0 **and** e_3>0) **then**
2:	**if** $\|e_2\| > \|e_3\|$ **then**
3:	$OF_{12} \leftarrow \frac{\|e_3\|}{\phi_{max}}$
4:	**else**
5:	$OF_{12} \leftarrow \frac{\|e_2\|}{\phi_{min}}$
6:	**end if**
7:	**else if** (e_2>0 **and** e_3<0)
8:	**if** $\|e_2\| > \|e_3\|$ **then**
9:	$OF_{12} \leftarrow \frac{\|e_2\|}{\phi_{min}}$
10:	**else**
11:	$OF_{12} \leftarrow \frac{\|e_3\|}{\phi_{max}}$
12:	**end if**
13:	**else if** (e_3<0 **and** e_2<0)
14:	$OF_{12} \leftarrow \frac{\|e_3\|}{\phi_{max}}$
15:	**else if** (e_3>0 **and** e_2>0)
16:	$OF_{12} \leftarrow \frac{\|e_2\|}{\phi_{min}}$
17:	**end if**

4.4.4 Sensitivity Analysis (Taguchi Method)

In this section, the number optimization variables is reduced from eight to five, using an extended version of Taguchi method [130]. Performing a sensitivity analysis on the Taguchi table, this method together with Analysis of Variance (ANOVA) will help us to select the most significant variables for further optimization. In this method, a fractional orthogonal array of 125 experiments is organized, in order to simulate the effect of all eight variables at five different levels (see Table 4-5). Each level of each variable is simulated 25 times. The number of fractional-factorial experiments (125) is usually controlled by the number of variables and the number of levels [22]. The number of variables is equal to 8, so a proper number of levels for each variable should be found and then the number of experiments will be determined. The number of levels is found by means of trial and error. The number of levels is increased, until the results do not differ from each other. The two OFs are calculated for these 125 experiments; then, two different analyses are conducted, namely the analysis of level and ANOVA. The selection of variables for further optimization is dealt with at last.

Table 4-4 Price/m^3 of different materials in the HESM*

Variable	VALUE ($US)
Copper magnetic wire (P_{cu})	89,400
M-19 29Ga silicon steel sheets (P_{FeSi})	22,950
Iron–silicon alloy (P_{Fe})	15,748
Ceramic10 PM material (P_{PM})	11,951
304 stainless steel (P_{sh})	16,060

* www.alibaba.com

Table 4-5 Variables and levels

Levels	R_{ri}	W_t	h_{sy}	h_{PM}	h_{ssi}	l_s	l_{ssi}	N_{exc}
1	20	18	18	0	0	90	0	0
2	21	19	19	3.75	10	97.5	10	200
3	22	20	20	7.5	20	105	20	400
4	23	21	21	11.25	30	112.5	30	600
5	24	22	22	15	40	120	40	800

4.4.4.1 Analysis of level

With this analysis, we obtain a visual sensation of each variable's effect on the OFs. First, the experiments that have a certain variable at a certain level, e.g. R_{ri} at level-1 ($R_{ri} = 20$), are found. Then, for each OF, e.g. OF_1, the average value among those experiments having $R_{ri} = 18$ is calculated. This should be repeated for each level of R_{ri} (up to level 5). If we follow this procedure for all variables, we get the line charts in Figure 4-8.

From this analysis, we can see that h_{PM}, h_{ssi}, l_{ssi} and N_{exc} have visible effect on OF_1. The components of OF_1, i.e. ϕ_{PM}, ϕ_{min}, and ϕ_{max}, take effect from h_{PM}, h_{ssi}, l_s, l_{ssi}, and N_{exc}. The

effect of h_{ssi}, l_s, l_{ssi}, and N_{exc} on OF_2 is also observable. The variables' optimal level for each OF is displayed in Table 4-6.

Table 4-6 Optimal level of each variable

OF	R_{ri}	W_t	h_{sy}	h_{PM}	h_{ssi}	l_s	l_{ssi}	N_{exc}
OF_1	5	4	3	2	5	1	2	3
OF_2	3	2	3	2	1	1	1	1

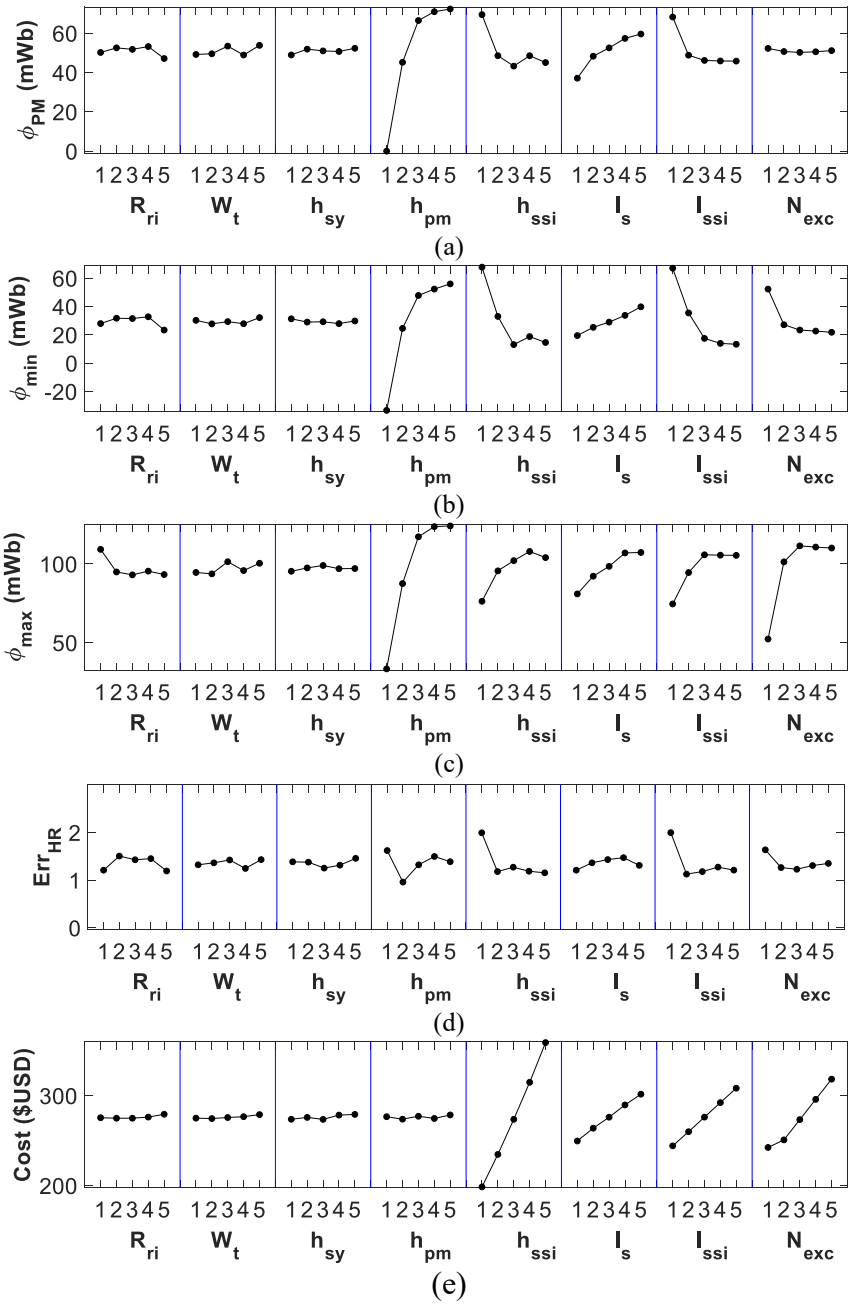

Figure 4-8: The effect of variables on the OFs by analysis of levels

Although the analysis of level can visually illustrate each variable effect, it is not enough to predict exactly how much effect a variable has on each OF. In this regard, ANOVA offers a quantitative measure to find the significant variables.

4.4.4.2 ANOVA

It is a well-known statistical analysis [22], aimed to compare the amount of variation between groups with the amount of variation within groups. In this analysis, we try to reject the insignificance, i.e. the null hypothesis, of the variables under study. In other words, it would be improbable for those variables to be insignificant, given our data. For the results of 125 experiments at hand, we obtain Table 4-7 and Table 4-8 from ANOVA for OF_1 and OF_2, respectively. The Statistics and Machine Learning Toolbox™ functions (anovan) in MATLAB have been used to perform N-way ANOVA.

In the ANOVA tables, SS is the sums of squares, DF is the degree of freedom of each variable (DF is equal to the number of levels minus 1), MS is the mean of sum of squares ($MS = \frac{SS}{DF}$), and F-value is the Fischer-value. The column before the last is the p-value, which is the probability of falsely rejecting the insignificance of a variable, whereas it was actually insignificant. When the p-value for a variable is less than a certain value, say α=0.05, we can reject the insignificance of that variable with 0.95 of certainty.

From Table 4-7, we can see that h_{PM}, h_{ssi}, and N_{exc} have significant effects on OF_1. From the ANOVA for OF_2, we get the results as shown in Table 4-8. As it is highlighted, there are four significant variables for the cost of materials OF_2, namely h_{ssi}, l_s, l_{ssi}, and N_{exc}. One may verify that the results from ANOVA approximately follow those from the analysis of level with more certainty. Now, we can conclude the five optimization variables as h_{PM}, h_{ssi}, l_s, l_{ssi} and N_{exc}.

Table 4-7 ANOVA for OF_1

Source	SS	d.f.	MS	F-value	p-value	Significance
R_{ri}	0.59	4	0.15	1.06	0.38	
W_t	0.42	4	0.11	0.76	0.56	
h_{sy}	0.69	4	0.17	1.23	0.30	
h_{PM}	9.02	4	2.26	16.16	0.00	“Yes”
h_{ssi}	4.61	4	1.15	8.26	0.00	“Yes”
l_i	0.70	4	0.18	1.25	0.29	
l_{ssi}	5.26	4	1.32	9.43	0.00	“Yes”
N_{exc}	1.37	4	0.34	2.46	0.051	
Error	12.84	92	0.14			
Total	35.51	124				

Table 4-8 ANOVA for OF_2

Source	SS	d.f.	MS	F-value	p-value	Significance
R_{ri}	337	4	84	0.27	0.89	
W_t	300	4	75	0.24	0.91	
h_{sy}	651	4	163	0.53	0.71	
h_{PM}	359	4	90	0.29	0.88	
h_{ssi}	402792	4	100698	327.64	0.00	"Yes"
l_s	42240	4	10560	34.36	0.00	"Yes"
l_{ssi}	64451	4	16113	52.43	0.00	"Yes"
N_{exc}	98983	4	24746	80.51	0.00	"Yes"
Error	28276	92	307			
Total	638389	124				

4.4.4.3 The selection of variables

Until now, we have found the significant variables based on the analysis of levels and ANOVA. However, the non-significant variables, i.e. R_{ri}, W_{st}, and h_{sy} should be set to their optimal levels in order to continue the optimization. The procedure of selection of these levels is as follows: if a variable's optimal level corresponding to both OFs is identical (see h_{sy} in Table 4-6), this parameter can be immediately set to its optimal level (level 3). If not, it can be set according to the level corresponding to the OF, whose F-value (Fisher-value) is bigger in its ANOVA table (see W_t in Table 4-6, and compare its F-value for each OF in Table 4-7 and Table 4-8). Finally, the design optimization of HESM is formulated as a non-linear two-objective problem (4-12).

$$\begin{aligned} &min\ OF_1 = Err\_HR(x) \\ &min\ OF_2 = Cost(x) \\ &s.t.: LB_x \le x \le UB_x \end{aligned} \tag{4-12}$$

where the decision variables x and their lower/upper bounds (LB_x/UB_x) are displayed in Table 4-9. The value of OF_1 must be further constrained by the designer.

Table 4-9 Decision Variables

Name	Value or range	Further optimization?
R_{ri}	24	
W_t	21	
h_{sy}	20	
h_{PM}	[0-15]	"Yes"
h_{ssi}	[0-40]	"Yes"
l_s	[90-120]	"Yes"
l_{ssi}	[0-40]	"Yes"
N_{exc}	[0-800]	"Yes"

4.4.5 The optimization algorithm

Initialization: The NSGA-II [94] starts with building the initial population, usually by generating a number of uniformly distributed random individuals. A larger population, in general, reduces the probability of the evolutionary process getting stuck in local optima points.

Non-dominant sorting: The population is sorted to form the non-dominated fronts using a sorting procedure. The individuals in the first front are not dominated by any other individual in the population; individuals in the second front can only be dominated by individuals in the first front, and so on. A rank is assigned to every individual, which is associated with the rank of the front the individual belongs to. The crowding distance for each individual is computed. Selecting individuals with larger crowding distance helps the algorithm to better spread in order to efficiently search the whole feasible space, thus potentially enhancing the diversity of the population which is key to avoid being trapped in local optima.

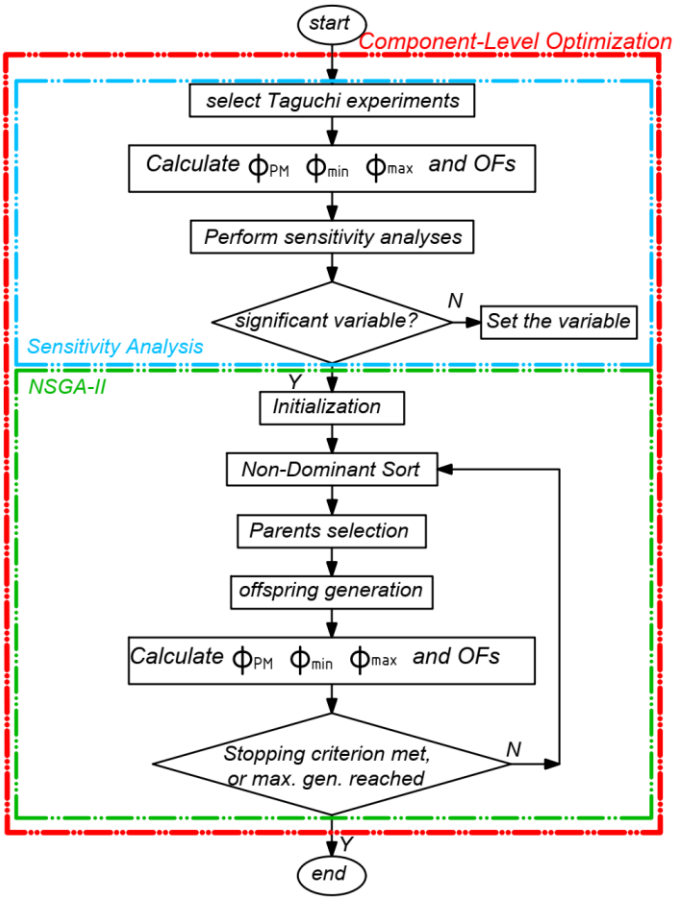

Figure 4-9: Flow chart of proposed optimization method

Parent selection: From a population of individuals, parents are selected using binary tournament. Offspring are generated using adequate crossover and mutation operators, to which a probability is assigned. Simulated Binary Crossover [131] and polynomial mutation [132], [133] were used.

Next generation population: The population for the next generation is selected from a combination of the current population and the generated offspring using the non-dominant sorting procedure.

Stop criterion: The algorithm runs until either a maximum number of generations or a stability criterion is met (e.g., the OFs do not change for a predefined consecutive number of generations). The flowchart in Figure 4-9 provides a more holistic view to the optimization process.

4.5 Optimization results

The optimization process described in the previous section was applied to the design of HESM for HR=0.5. Figure 4-10 displays the nondominated (Pareto optimal) front. This information enables to exploit the tradeoffs between the competing OFs for different solutions on this front. If we select to have smaller design errors, then the material price would be higher and vice-versa. The analysis is made for three different design errors, i.e. 1.39%, 12%, and 20.8%, for which the cost is 218, 214.8 and 199.2 $US, respectively. These solutions are shown on Figure 4-10, which displays the material cost vs. design error trade-off.

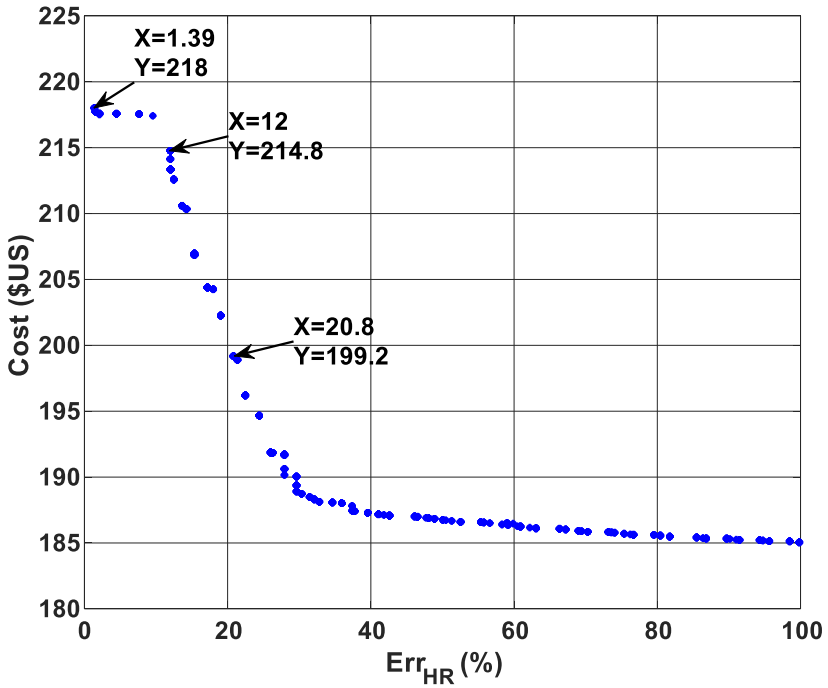

Figure 4-10: The Pareto optimal front

The first objective function mainly aims at finding viable designs for the specific HR, and the second objective function minimizes the cost. The solutions with higher values for the first objective function on the Pareto front do not acquire the specified flux levels for the given HR. The HR is a key variable, which will be traced from the component-level, up to the system-level

design. The HESM global efficiency comparison at the system-level is totally based on the HR. Therefore, a higher priority is given to OF_1 (Err_{HR}), to privilege the reliability of optimization at system-level. In the introduction section, we discussed about the HR and its effect on the shape of the efficiency map, the high-efficient area, and the Constant Power Speed Range (CPSR) of the machine (as shown in Figure 4-1). These specifications depend on the HR as a design variable; if the HR is not guaranteed, the system-level analysis could not be trusted. To acquire a specific HR at the component-level, Err_{HR} concerning the different errors in HESM fluxes should be reduced sufficiently. That is why the other solutions with $Err_{HR} > 0.02$ on the Pareto front are not studied. The final HESM selection and validation is performed for the solution with Err_{HR}=1.39% and Cost=218 $US. The value of decision variables for this selected solution is reported in Table 4-10. The value of OFs and flux linkages for the optimal design, the number of executed generations before convergence, and other information about the selected optimal solution are displayed in Table 4-11.

The design optimization results are verified by an FEA simulation, as displayed in Figure 4-11(a) and Figure 4-11(b). The flux and back EMF of the final HESM is plotted against the angular position (in electrical degrees) at 2000 RPM. For HR=0.5, the dominant mode is in flux weakening, meaning that the design is optimized to reduce e_1 and e_2 and give $\phi_{PM-calc}$ very close to ϕ_{PM}, and $\phi_{min-calc}$ very close to ϕ_{min}. In this case, e_3 is unremovable; that is why the maximum flux for phase-A (in Figure 4-11(a)) is bigger than the nominal d-axis flux, ϕ_{nom} = 0.0852 Wb. The average torque at nominal current and speed is shown in Figure 4-11(c), which is obtained from the Flux-MMF diagrams [134].

Table 4-10 Optimized HESM design

Variable	Unit	VALUE
Rotor inside radius (R_{ri})	mm	24
Stator tooth width (W_t)	mm	21
Stator yoke height (h_{sy})	mm	20
PM height (thickness) (h_{PM})	mm	7
Stator solid iron height (h_{ssi})	mm	19.6
Stator active length (l_s)	mm	90
Stator solid iron length (l_{ssi})	mm	22.9
WE number of turns (N_{exc})	mm	193
Total length (l_{tot})	mm	187.4
Total outside radius (R_{tot})	mm	159.2
Stator tooth height (h_{st})	mm	5.9
Excitation coil slot width (W_{exc})	mm	25.8

(a)

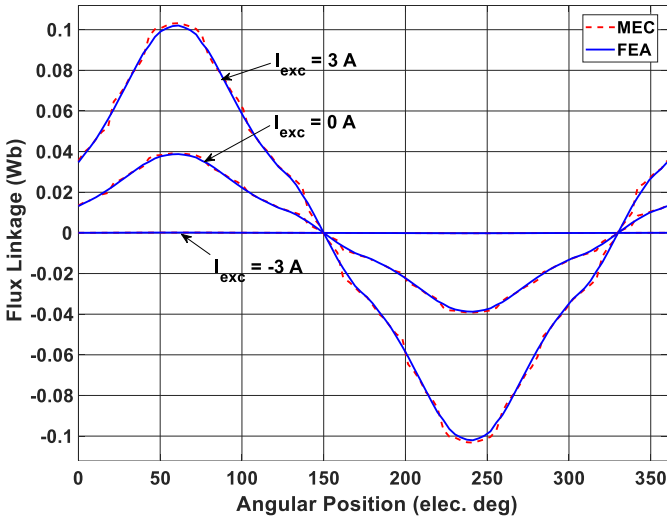

(b)

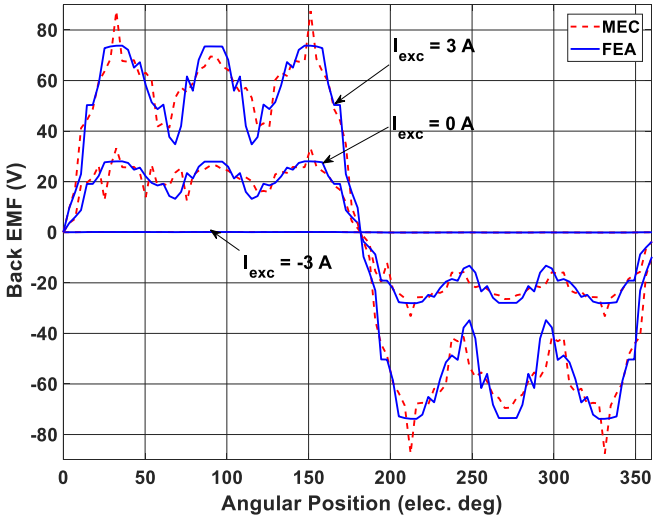

(c)

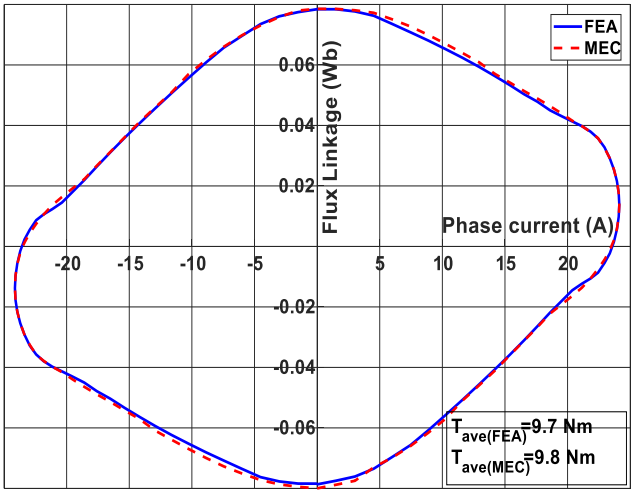

Figure 4-11: FEA evaluation of the final HESM: (a) Flux regulation capability of the final HESM (phase-A), (b) Voltage regulation capability of the final HESM (phase-A), (c) Average nominal torque for the final HESM.

Table 4-11 Optimization configurations and results

Variable	VALUE
Number of generations before convergence	51
Cross-over probability	0.85
Population size	150
Parents selection pool size	75
OF_1 (Err_{HR})	0.0139
OF_2 (Cost in $US)	218
$\phi_{PM-calc}$ (Wb)	0.0421
$\phi_{max-calc}$ (Wb)	0.1127
$\phi_{min-calc}$ (Wb)	2.3e-7

4.6 Conclusion

In this work, we provided a novel perspective to the concept of HR and the HESM design. For this purpose, a new approach was proposed based on the NSGA-II, which could constrain the design error of HESM and minimize its cost, despite of the complex behavior of HESM. By means of two statistical analyses, better knowledge was acquired about the system, and the number of design variables was cut down before the optimization process was carried out. The tradeoff analysis between the two OFs was made with the information derived from the Pareto optimal front, the design error was constrained, and a final nondominated solution was selected (by the designer). This solution was then evaluated by means of FEA simulations for validation.

Chapter 5 HESM Optimization: System Level

Original Title:
System-level Optimization of Hybrid Excitation Synchronous Machines for a Three-Wheel Electric Vehicle

Authors and Affiliations:
- **Ahmad Shah Mohammadi,** Ph.D. student, e-TESC Laboratory, Department of Electrical & Computer Engineering, University of Sherbrooke
- **João Pedro F. Trovão,** Professor, e-TESC Laboratory, Department of Electrical & Computer Engineering, University of Sherbrooke

State: Submitted (2019/12/03)

Journal: IEEE Transactions on Transportation Electrification

Context of the chapter

In Chapter 4, a HESM was optimally designed for HR=0.5, using NSGA-II and MEC modelling technique. This process will be repeated in this chapter for all HRs from 0 to 1 with steps of 0.1, which is our third major contribution. For each HR, the HESM is optimally designed and its efficiency map is constructed, and then, the global efficiency of the HESM over a selected driving cycle is calculated. After having calculated the global efficiencies for all HRs, they are compared to each other and the optimal HR, which results in the highest global efficiency, is selected. The 3D non-linear MEC model is selected for the sake of accuracy and speed of optimization process, which takes into consideration the saturation of magnetic materials.

5.1 Abstract

In this paper, a two-level methodology is proposed to optimize the design of Hybrid Excitation Synchronous Machine (HESM) for a given Electric Vehicle (EV) over an arbitrary-selected driving cycle. We are looking at a huge analysis problem of finding an optimal Hybridization Ratio (HR) between the two excitation sources, namely, Permanent Magnet (PM) and Wound Excitation (WE). To find the optimal HR, the HR is scanned from 0 to 1, or from pure WE to pure PM excitation. For each HR, the motor is optimally designed at the component-level, its cost is minimized, and its global efficiency over the selected driving cycle is calculated. Then at the system-level, the global efficiencies associated to each HR are compared to find the optimal HR. The complexity of the design optimization at the component-level is addressed by Non-dominated Sorting Genetic Algorithm II (NSGA-II). To make a compromise between accuracy and speed of calculations, a non-linear 3D dynamic Magnetic Equivalent Circuit (MEC) model is developed and evaluated by commercial Finite Element Analysis (FEA) software. Following the proposed methodology and thanks to 300 hours of computations with 48 CPU cores in parallel, the final HESM design can achieve up to 18.65 % higher global efficiency than pure Wound Excitation (WE), and 15.8 % higher than pure a Permanent Magnet (PM) excitation.

5.2 Introduction

Transportation electrification progressively stresses out new design methods to reduce the electric vehicle (EV) initial cost and excel its performance. In this regard, EV range optimization seeks enhanced global variables, such as cost and efficiency, over selected driving cycles [1], [2]. Due to insecurity in the supply of rare earth Permanent Magnets (PMs), the trend of machine design is shifting towards PM-free alternatives, or Ferrite-based PMs [3]. In this regard, Hybrid Excitation Synchronous Machine (HESM) uses both Permanent Magnet (PM) excitation and Wound Excitation (WE), which can compensate the low remanent flux density of ferrite PMs. HESM combines high-efficiency and high-torque with better flux-weakening; characteristics, highly demanded for a traction motor [4], [5]. In addition, the design optimization of EV drivetrain components could be a challenging task, where, HESM can offer several advantages [6].

Design optimization of HESM can be realized both at system-level, as well as, component-level. The HESM models and analyses at the system-level are much simplified, while the component-level studies lose the holistic track over the design problem. That is why multilevel optimization of HESM have been evolved and been trended recently [2], [7], [8]. Likewise, we are proposing a new multilevel HESM optimization methodology, using Hybridization Ratio (HR) as the key interconnecting parameter between component-level and system-level optimization.

The HR between the two excitation sources in HESM has interesting capabilities, which can open new opportunities to EV global optimization. One can change the place of highly-efficient area as a function of HR (from 0 to 1), as shown in Figure 5-1. Depending on the application of EV and its target market, there is an optimal HR which enhances the global efficiency [9], [10]. In a city driving, HR close to one is mostly selected, as there are lots of starts and stops and the

motor is working in high-torque low-speed region, where, the PMSM has advantage. On the other hand, for an inter-city or highway driving, more share is assigned to the WE [10]. HR has another major effect on the traction system optimal sizing: by removing part of PM fixed flux, and replacing it with WE, one can increase the Constant Power Speed Range (CPSR) of the motor. This capability gives more flexibility in the selection of gearbox ratio and can reduce the overdesign in the powertrain, if there is any, or reach the challenging 10:1 CPSR for the demanding applications, such as starter-alternators [10], [11]. However, researchers in [9] and [10] apply one single design for all HRs, and use the dq circuit model for analysis. In this regard, they neglect the details of component-level optimization of HESM, due to the limitations arising from one single design and the lumped parameter analysis.

At the component-level, on the other hand, several Objective Functions (OFs), such as torque, torque ripple, core losses, efficiency, and so on are considered, but the HR and its system-level effect on HESM (see Figure 5-1) is not recognized [12], [13].

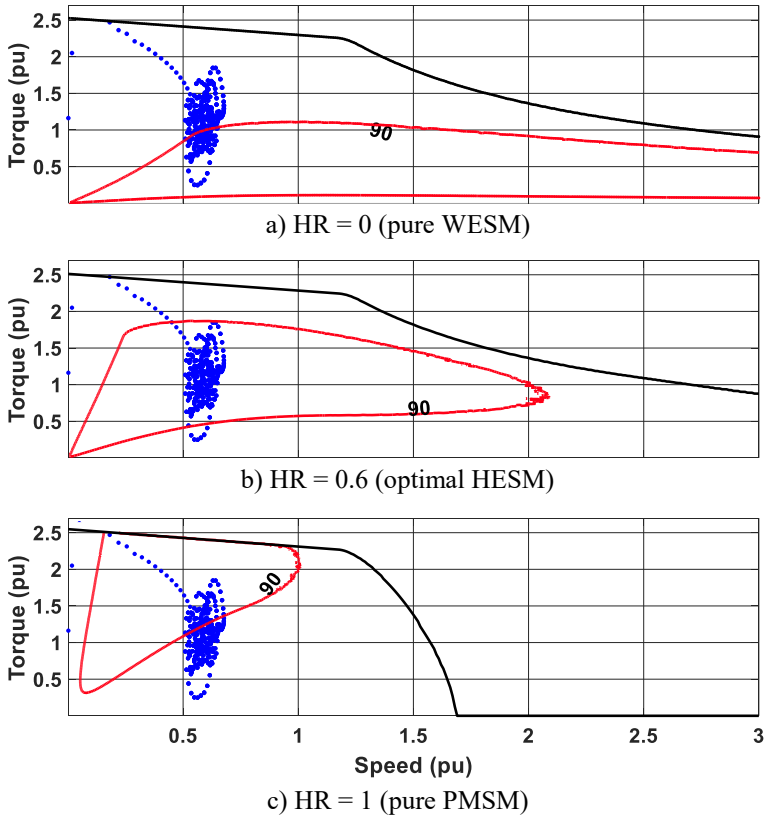

a) HR = 0 (pure WESM)

b) HR = 0.6 (optimal HESM)

c) HR = 1 (pure PMSM)

Figure 5-1: Changing the place of highly-efficient area as a function of HR

In this paper, we are proposing a multi-level optimization methodology, incorporating the HR in component-level and system-level design. At the component-level, we have dedicated an objective function to guarantee achieving the specified HR. The HESM design should be modified at this level, in order to be able to regulate the flux between certain minimum and maximum levels specified by each HR (as demonstrated in the section 5.3.2). This task was so

complicated to perform, so, a new formulation is proposed to deal with the design at component-level, using the outstanding features of NSGA-II. After having stablished the HR at the component-level, at system-level, we have used the HR as a design variable. An exhaustive search with suitable intervals is carried out between 0 and 1 to find the optimum HR. The HR is connecting the two levels, by playing an important role at both levels.

1. Component-level: Here, the HESM design is optimized for a specified HR (not the optimum one). The HESM geometry is modified for two reasons: first, to satisfy the requirements of flux regulation capabilities for the specified HR, while respecting all design constraints (i.e. torque, voltage, etc.), and second, to minimize the motor cost. The motor cost minimization is mandatory to guaranty the reliability of comparison at the system-level. The component-level optimization is realized using the NSGA-II algorithm.

2. System-level: At this level, the HR is incremented from 0 to 1 with suitable intervals, and for each HR, the HESM is optimization program at the component-level is called for. After having scanned all HRs, the global efficiency of the vehicle with each HR is calculated and compared to find the optimal Hybridization Ratio. As all HESMs were optimally designed at component-level, it provided us with homogenous HESM alternatives to choose from.

In section 5.3, after the problem statement, the HESM design optimization for a specified HR is briefly explained and our methodology is proposed. Later on in section 5.45.4, we have developed and validated a 3D Magnetic Equivalent Circuit (MEC) model for HESM, which takes into account the non-linearity of magnetic materials. Using the MEC and the proposed methodology, in section 5.55.5, the optimal HR is found which achieves the highest global efficiency for the selected driving cycle.

5.3 Definitions and problem statement

5.3.1 System under study

The specifications of a battery powered three-wheel vehicle prototype, developed at University of Sherbrooke, is presented in Table 5-1 [10]. An optimal HESM should be designed and simulated into the drivetrain of this EV. Figure 5-2: HESM under study with 3D flux directions provides a 3D view of the selected topology and the used materials for HESM (modeled in MagNet Infolytica). The PMs are on the rotor and the field windings on the stator. This gives a robust rotor structure, with better cooling on the stator. The PM main and leakage flux paths, together with the Wound Excitation (WE) main flux path are displayed. It was proposed in [9] and theoretically and experimentally studied in [14], [15], and [16]. This design has easy flux control, high efficiency, wide CPSR, and good reliability [17]. However, it has 3D flux paths, which is time- and process-consuming in FEA analysis.

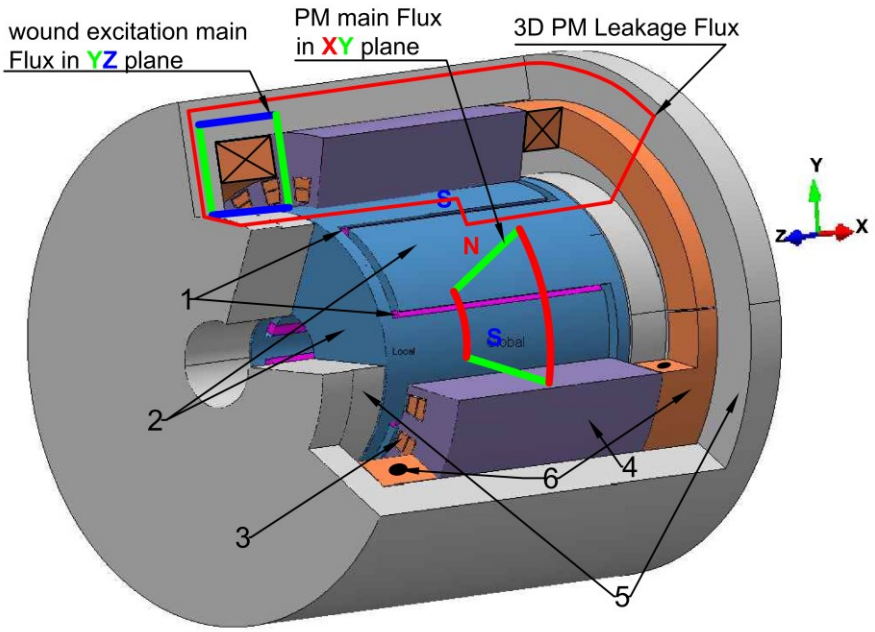

a) 1- PMs (ferrite), 2-rotor claws (iron–silicon alloy), 3- stator coils (copper), 4- stator (silicon steel lamination), 5-outer stator (iron–silicon alloy), 6-WE coils (copper)

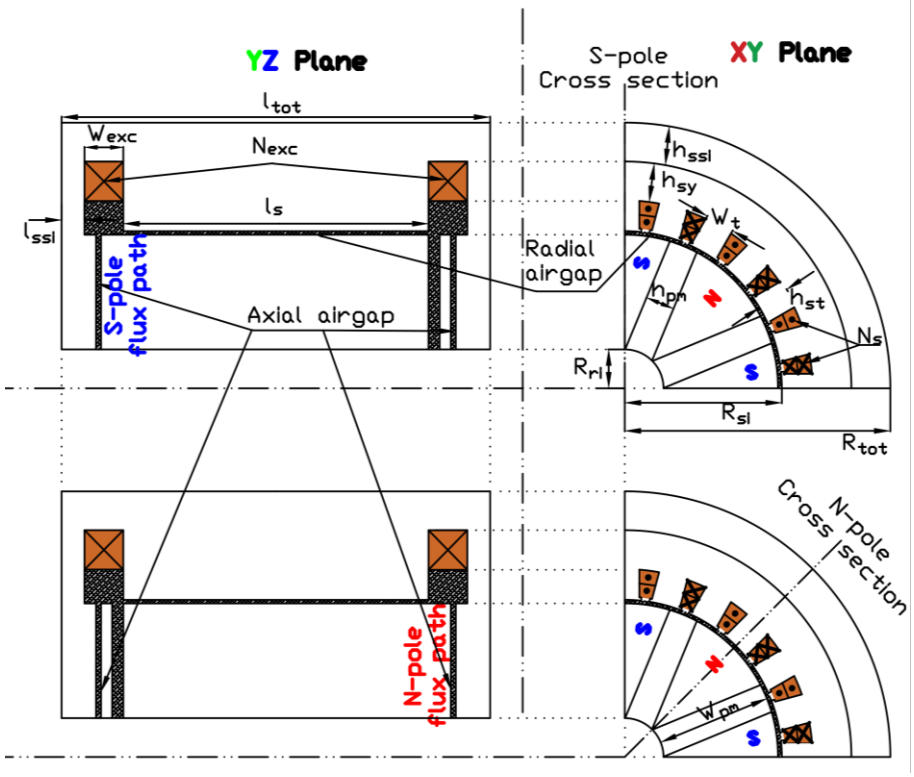

b) The cross sections of S-pole (top) and N-pole (bottom)

Figure 5-2: HESM under study with 3D flux directions

Table 5-1 The specifications of EV under study

Item	Value
Vehicle mass with passengers (kg)	500
Rolling resistance coefficient	0.02
Aerodynamic drag coefficient	0.75
Vehicle front area (m^2)	1.25
Wheels radius (m)	0.305
Gear box ratio	5.033

5.3.2 HESM design optimization for a target HR

Component-level optimization is dedicated to a specified HR, although the optimal HR is not found yet. The reasons for component-level optimization are as follows:

- to realize the flux regulation capabilities demanded for that specified HR;
- to minimize the HESM cost.

HR can be adapted by PM dimension modification, or only by increasing the current capacity of excitation conductors with better cooling. However, as the component-level is executed for all HRs between 0 and 1 with increments of 0.1, there would be a HESM for each corresponding HR. These designs will be later compared to each other at system-level to find the optimal HR. If the reliability of comparison (at system-level) is demanded, a geometrical optimization at component-level is called for, in order to provide a homogenized pool of design candidates. Modifying the machine geometrical variables can increase the performance of the machine. For a case study, the flux controlling capability of HESM can reach up to 100 % of difference (+4 mWb in Max. flux per turn) due to geometry modification, as investigated in [18].

The component-level optimization is quite challenging due to the complex flux behavior in HESM. The interaction between PM excitation and WE introduces a so-called phenomenon of hard and soft saturation, which causes an asymmetrical flux regulation. The design constraints are tabulated in Table 5-2, which should be respected for all design candidates. These constrains are coming from the vehicles requirements, as well as, our available resources.

Table 5-2 design specifications and constraints

Name	Value	Name	Value
Max. DC bus voltage (V)	109	Airgaps length (mm)	0.5
Min. DC bus voltage (V)	83	Stator inside radius (mm)	115
Nom. Power (W)	2000	Stator tooth width (mm)	21
Nom. speed (rpm)	2000	Stator yoke height (mm)	20
Num. of phases	3	Rotor inside radius (mm)	24
Num. of pole pairs	4	Max height (mm)	200
Slot/pole/phase	1	Max total length (mm)	300
Slot opening (mm)	5	Stator winding turns	2
Nom. d-axis Flux (Wb)	0.0852	HR	0.5

The optimization variables and their corresponding ranges are displayed in Table 5-3 (see Figure 5-2: HESM under study with 3D flux directions-b for more clarification on symbols). The principles of selection of these variables are as follows. The number of variables will be firstly reduced from 8 to 5, using sensitivity analyses. From these analyses, three variables (W_t, h_{sy}, and R_{ri}) are recognized to be non-significant on the optimization results, and their values will be fixed before the start of NSGA-II algorithm. This is accomplished using 125 Taguchi experiments and two statistical analyses, namely, analysis of levels and the analysis of variance (ANOVA), as explained in [19]. The remaining variables (h_{PM}, h_{ssi}, l_s, l_{ssi}, N_{exc}) have significant effect on the value of Objective Functions (OFs). The OFs are explained further in this section.

Table 5-3 Design Variables

Name	Symbol	range
Stator tooth width (mm)	W_t	[18-22]
Stator yoke height (mm)	h_{sy}	[10-22]
Rotor inside radius (mm)	R_{ri}	[20-24]
PM height (thickness)	h_{PM}	[0-15]
Outer stator solid iron height	h_{ssi}	[0-40]
Stator active length	l_s	[90-120]
Outer stator end cap length	l_{ssi}	[0-40]
WE coils number of turns	N_{exc}	[0-600]

The parameters' ranges are determined using heuristic approach and parameter variation on the HESM model. The parameters' upper and lower bounds are then increased, in order to give broader search space to the optimization program. Here, we give an intuitive sense for each parameter and it selected range.

h_{PM} and N_{exc} are controlling the Magnetomotive Force (MMF) originated from PMs and WE coils, respectively. The lower bound of h_{PM} is 0 for pure wound excitation, and the upper range is tested to satisfy the nominal criteria (flux linkage, voltage, and torque). The range of N_{exc} follows the same logic as h_{PM}. At lower bound it is 0 to let the optimization program to come to this solution when the HR=1 (pure PM excitation). The upper bound was selected to address the nominal design criteria at all HRs. For instance, at HR=0 the WE should alone provide the nominal flux, whereas at HR=0.5, it should attenuate the flux down to 0 Wb.

h_{ssi} and l_{ssi} work like a gate, but in two contradictory ways. If we reduce h_{ssi} and l_{ssi}, the PM flux leakage will be reduced, and more of the PM flux will be linked with armature windings in XY-plane (see Figure 5-2: HESM under study with 3D flux directions-a for PM main and leakage flux paths). The lower bounds of h_{ssi} and l_{ssi} is 0 for pure PM excitation. On the other hand, we cannot only reduce h_{ssi} and l_{ssi}, because we simply need to provide a path for the WE flux to be linked with the armature windings through YZ-plane. The upper bounds are examined to meet the nominal criteria at different critical HRs, such as HR=0 to 0.5.

The stator stack length (l_s) lets us attaining critical flux levels, otherwise was not achievable with any possible combinations of all other four variables. This way we guaranty always a valid response for the optimization problem.

Here, we need to provide a comprehensive definition for HR. The term flux, wherever is used in this work, means the flux linking the armature windings at d-axis. To have the true meaning of HR, the machine fluxes, i.e. ϕ_{PM} (PM flux), ϕ_{WE} (WE flux), ϕ_{min} (minimum flux), and ϕ_{max} (maximum flux) should be equal to the following equations:

$$\phi_{PM} = HR\phi_{nom} \tag{5-1}$$

$$\phi_{WE} = \phi_{nom} - \phi_{PM} = (1 - HR)\phi_{nom} \tag{5-2}$$

$$\phi_{min} = min(0, \ \ \phi_{PM} - \phi_{WE}) = min\ (0, (2HR - 1)\phi_{nom}) \tag{5-3}$$

$$\phi_{max} = \phi_{nom} \tag{5-4}$$

where ϕ_{nom} is the nominal d-axis flux in the machine. In the HESM with the specified HR, the flux should be controllable at any desired level between ϕ_{min} and ϕ_{max}, with ϕ_{PM} as specified above. During the optimization, each time the decision variables are modified and the different fluxes are calculated through the model, the following conditions exist:

$$\phi_{PM-calc} = \phi_{PM} + e_1 \tag{5-5}$$

$$\phi_{min-calc} = \phi_{min} + e_2 \tag{5-6}$$

$$\phi_{max-calc} = \phi_{max} + e_3 \tag{5-7}$$

where e_1 to e_3 are the error values between the calculated fluxes and the specified fluxes for the specified HR. The fluxes can be calculated from any reliable model of HESM (such as MEC), provided that it can take into consideration the non-linearity of magnetic materials.

From the designer's point of view, these errors must be reduced under a certain value, and the motor cost should be minimized. For this purpose, two *OF*s are defined; OF_1 for the errors e_1 to e_3, and OF_2 for the motor cost. The two *OF*s are defined as the followings:

1. *Err_{HR} Minimization (OF_1):* To guarantee the specified HR for the HESM, we have to reduce the errors in (5-5) to (5-7), as much as needed. OF_1 is defined to calculate the error ratio and has two terms. The first term (OF_{11}) concerns the e_1, as calculated in (*5-8*).

$$OF_{11} = \frac{e_1}{\phi_{PM}} \tag{5-8}$$

The second term of error ratio (OF_{12}) deals with e_2, or e_3, whichever is dominant, as will be explained in Figure 5-13 and defined by the pseudo-code in 5.7.

In the pseudo-code, whenever ϕ_{min}=0, as it in the denominator of calculations, we replace it with $\frac{\phi_{max}}{1000}$. The OF_1 is calculated as in (5-9).

$$min\ OF_1 = OF_{11} + OF_{12} \tag{5-9}$$

2. *Cost Minimization (OF_2):* The cost of materials is calculated from (5-10).

$$min\ OF_2 = P_{cu}V_{cu} + P_{FeSi}V_{FeSi} + P_{Fe}V_{Fe} + P_{PM}V_{PM} + P_{sh}V_{sh} \tag{5-10}$$

where V_j is the volume of material j and P_j is its price per unit volume, as displayed in Table 5-4.

Table 5-4 Price/m3 of different materials in the HESM*

Variable	VALUE ($US)
Copper magnetic wire (P_{cu})	89,400
M-19 29Ga silicon steel sheets (P_{FeSi})	22,950
Iron–silicon alloy (P_{Fe})	15,748
Ceramic10 PM material (P_{PM})	11,951
304 stainless steel (P_{sh})	16,060

* www.alibaba.com

Finally, the design optimization of HESM at the component-level is formulated as a non-linear two-objective problem (5-11).

$$\begin{gathered} min\ OF_1 = Err_{HR}(x) \\ min\ OF_2 = Cost(x) \\ s.t.: LB_x \le x \le UB_x \end{gathered} \tag{5-11}$$

where the decision variables x and their lower/upper bounds (LB_x/UB_x) are displayed in Table 5-3. The minimization of the two OFs is tackled by NSGA-II. We have targeted an error limit of 2 % for the first objective function ($OF_1 \le 2\,\%$), for which, the corresponding value of OF_2 should be found on the Pareto front. An example of optimization convergence and Pareto front for an arbitrarily selected HR (HR=0.3) is displayed in Figure 5-3. To have $OF_1 \le 2\,\%$ and a minimum cost, the selected solution will be as demonstrated on the Pareto front in Figure 5-3. The component-level optimization with a similar procedure as presented in Figure 5-3 should be repeated for all HRs between 0 and 1, with increments of 0.1.

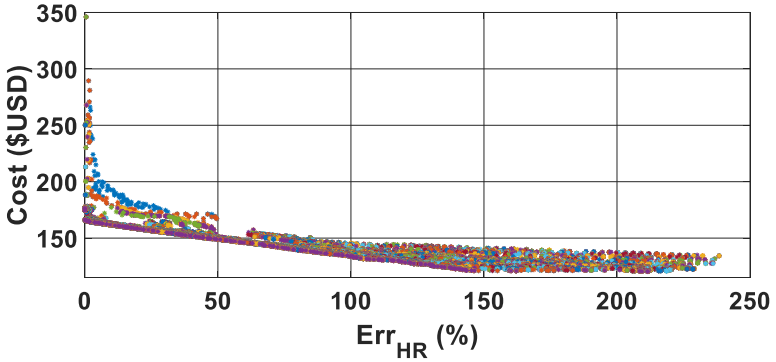

a) The succession of generations towards the Pareto Front

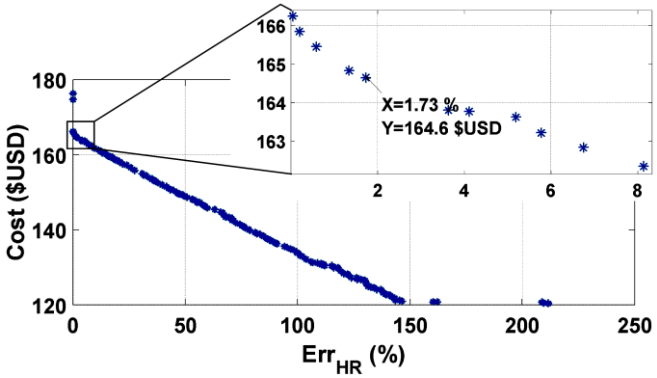

b) The Pareto front and the selected design

Figure 5-3: NSGA-II results for an arbitrarily-selected HR (HR=0.3)

5.3.3 The proposed methodology

The proposed methodology is demonstrated in Figure 5-4 and established as follows:

1) For each HR from 0 to 1 with intervals of 0.1, the component-level design optimization is executed. At the beginning of this stage, a sensitivity analysis is performed to find the optimal value of three non-significant design variables (W_t, h_{sy}, and R_{ri}). Then, using the NSGA-II, the optimal values of five other variables are found.

2) For each HR, an efficiency map is built up. To calculate efficiency for a given torque-speed operating point, the armature and excitation currents are calculated offline to give minimum copper and iron losses [20]. Other control approaches are applicable as well.

3) Using the efficiency maps constructed at previous step, the global efficiencies are computed for each HR over the selected driving cycle [14]. The global efficiency (η_{global}) is obtained from (5-12)

$$\eta_{global} = \sum_i \eta_i . \frac{t_i}{t_{tot}} \tag{5-12}$$

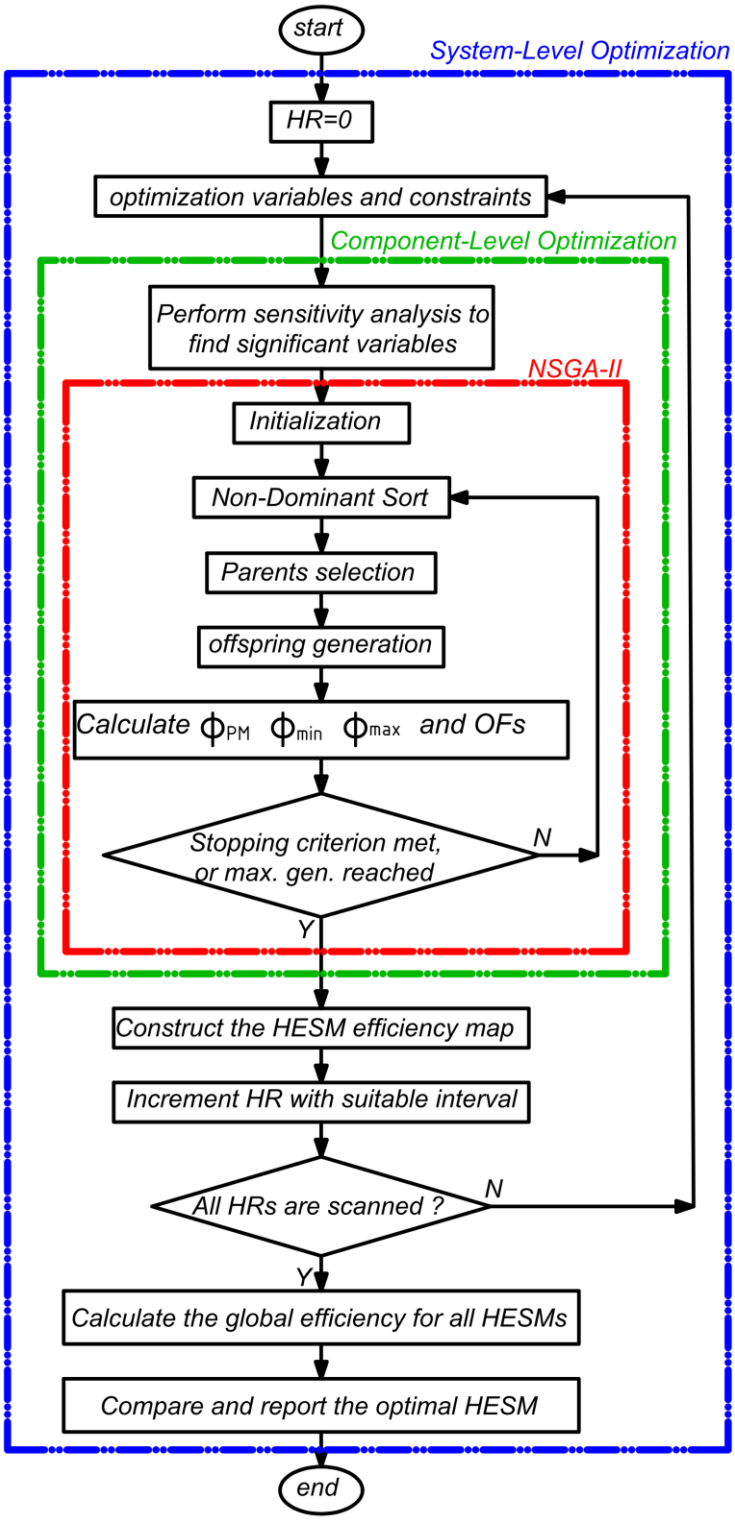

Figure 5-4: Proposed methodology for multilevel optimization of HR in HESM

where t_{tot} is total time of the driving cycle, t_i is the duration of operating point (i). and η_i is efficiency at that operating point. Several driving cycles can be applied according to the designer will.

4) The global efficiencies are compared. The HESM with maximum global efficiency is the optimal design we are looking for.

This methodology finds out an optimal HR, which places more of the driving cycle operating points inside its high-efficient area. The proposed methodology is generic, and can be applied to any combination of driving cycles, EV, and HESM design. The amount of analysis needed for design optimization and efficiency maps construction (step 1 and 2) is considerably heavy, which makes it inevitable the use of MEC model.

5.4 HESM MEC modelling and evaluation

Due to the enormous repetition of HESM analysis in the design optimization, and then the construction of efficiency maps, the selected analysis tool has a trivial impact on the calculation time, as well as, its accuracy of results. The commonly used tools for electromagnetic analysis include Finite Element Analysis (FEA), analytical model and winding function theory, and Magnetic Equivalent Circuit (MEC) [71], [72].

FEA analysis is very accurate, but it takes lots of time and resources, especially for motors with 3D flux directions. FEA can be practical for one or limited number of operating points; however, it is not applicable here. Analytical approximate formula and winding function theory lack desirable accuracy. Being semi-analytical semi-numerical, the MEC can make a trade-off between the time and accuracy. Depending on the network mesh size and the error limits, the conversion time and the accuracy of the results can be controlled by the user (designer). It can be very helpful in the design optimization of HESM, especially for those with 3D flux paths [73], [74], [75] and system-level optimization [137]. It has gained more attention and applicability recently in the literature [81], [82]. In this section, we have fully developed a dynamic 3D non-linear MEC model of HESM. It is a nodal-based analysis of Kirchhoff's current law, with the branches of magnetic flux tubes. The approach in [85] and [86] are the guidelines used for our purpose.

5.4.1 MEC system of equations

In MEC modelling, it is assumed that the permeability is constant inside the mesh volume; however, it can change from one mesh to another. The reluctance of each flux tube is calculated from (5-13).

$$\mathcal{R} = \int_0^L \frac{dl}{\mu_0 \mu_r S(l)} \tag{5-13}$$

where L is the length of flux tube, and $S(l)$ is the surface perpendicular to flux direction. An analytical formula is deduced for every mesh type in the model, after simplifying the

complicated mesh structures. There are two kinds of MMF sources, PM and coil. The MMF for meshes having PM magnetized in x-direction is given by (5-14).

$$F_{pm} = \frac{B_r lx(i)}{\mu_0} \tag{5-14}$$

where B_r is the PM remanent flux density, and $lx(i)$ is the length of mesh i in x direction. F_{pm} can be either positive or negative, according to the direction of magnetization.

The MMF distribution for armature coils is in Y-direction, as displayed for one phase in Figure 5-5, for the area between the horizontal dashed lines. Starting from the middle of the left coil, the MMF increases linearly from zero to its maximum value obtained by (5-15).

$$F_{max} = \frac{S_1}{S_{slot}} 2N_s i_{ph} \tag{5-15}$$

where, S_1 is the hypothetical mesh area in XY plane highlighted in Figure 5-5, S_{slot} is the total stator slot area, N_s is the number of turns of armature coils (2-layers winding), and i_{ph} is the phase current. The global MMF of armature is obtained from algebraic sum of MMFs of all phases.

After applying the flux tube method, a network of *n* nodes and *n* sources will be formed, and the magnetic potential of all nodes, u_i $(i = 1{:}n)$ can be found from (5-16).

$$\begin{bmatrix} P_{11} & \cdots & P_{1n} \\ P_{21} & & P_{2n} \\ \vdots & \ddots & \vdots \\ P_{n1} & \cdots & P_{nn} \end{bmatrix} \begin{bmatrix} u_1 \\ u_2 \\ \vdots \\ u_n \end{bmatrix} = \begin{bmatrix} \varphi_1 \\ \varphi_2 \\ \vdots \\ \varphi_n \end{bmatrix} \tag{5-16}$$

with,

$$P_{ij} = \begin{cases} -\dfrac{1}{\mathcal{R}_{ij}} & if\ i \neq j \\ \displaystyle\sum_{\substack{k=1 \\ k \neq i}}^{n} \frac{1}{\mathcal{R}_{ki}} & if\ i = j \end{cases} \tag{5-17}$$

$$\varphi_k = \sum_{\substack{i=1 \\ i \neq k}}^{n} F_{ik} P_{ik} \tag{5-18}$$

where, F_{ik} is the MMF between node i and k and P is the permeance matrix. Having u_i $(i = 1{:}n)$ from (5-16), the flux density, flux linkage, back EMF, and other variables can be calculated. Equation (5-19) shows the formula for flux density calculation; where i and j are two adjacent mesh elements and S_{ij} is the common surface area between them.

$$B_{ij} = \frac{(U_i - U_j - F_{ij})P_{ij}}{S_{ij}} \tag{5-19}$$

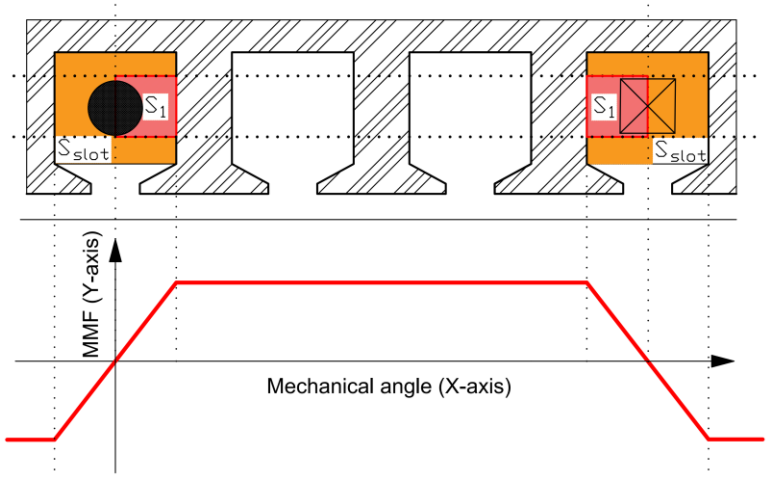

Figure 5-5 Armature coils MMF distribution

5.4.2 MEC meshing

For HESM meshing, firstly, the machine is divided into several sections based on the geometry and types of materials, of which it is made. The main flux paths and the areas of more interest influence the sectioning of model. A sections itself can be then divided into more meshes depending on the needed resolution. Figure 5-6 demonstrates the HESM sections in XY and Z directions, as well as, the airgap mesh. The model has eleven sections in z-direction to provide more details on the flux behavior and losses in highly-saturated areas. The airgap meshing is quite special and is called remeshing region, for which the meshing is reconstructed with every move of rotor. When a mesh wall is crossed, either in stator or rotor, a new mesh wall is considered in the airgap (see Figure 5-6(a)). Sections in stator are meshed only once, whereas, rotor meshing in the first and last column need a little bit of modification with every move of rotor.

The motor dimensions, the material properties, and the coils current are given as inputs to the model, and the user can try different materials. The mesh resolution in each section and the error limits are determined by the user to make a trade-off between the accuracy and time of simulation. The meshing, solving, and post-processing phases are automatically done by a program devoted to this task.

(a)

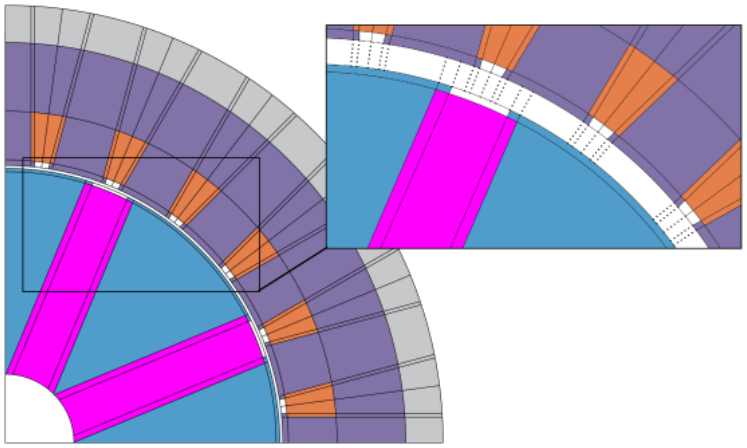

(b)

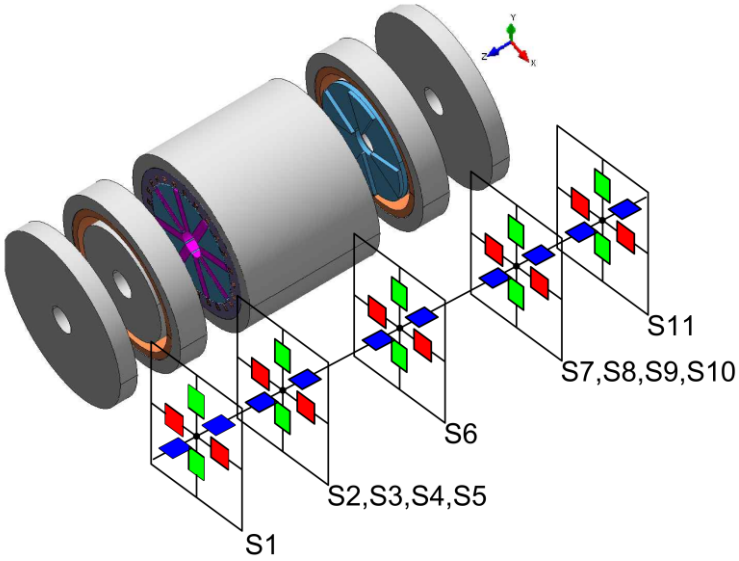

(b)

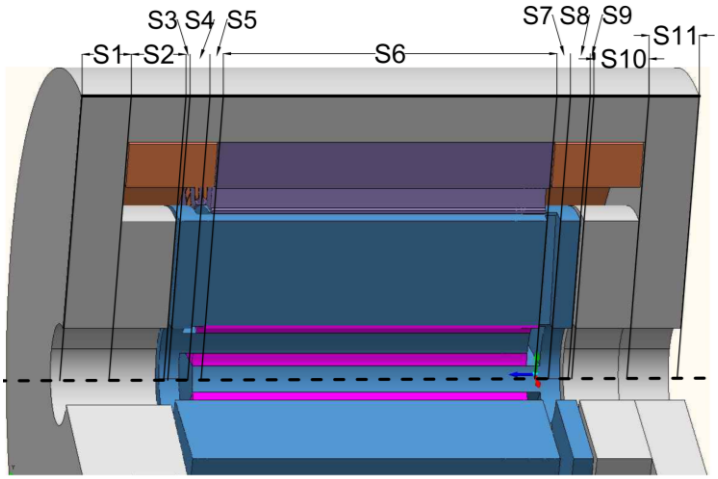

Figure 5-6: HESM sections in: a) XY plane b) Z direction

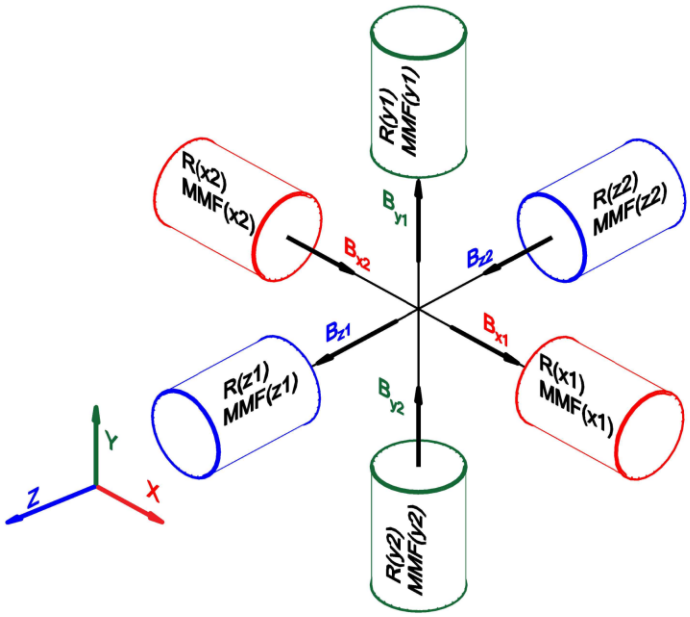

Figure 5-7: A generic mesh element

A generic mesh element is modeled by six bi-directional reluctances, each of which has a MMF source in parallel, as displayed in Figure 5-7. There are also six vectors for flux density which are coming from, or going to, the adjacent mesh element. For these vectors, one equivalent flux density for the mesh should be found. This equivalent flux density will be used to estimate the saturation level and permeability of magnetic material in the mesh. The equivalent flux density (B_{eq}) is deducted from the energy conservation low in (5-20).

$$\frac{{B_{eq}}^2 V_{tot}}{2\mu_0\mu_r} = \sum_{d=x,y,z} \sum_{i=1,2} \frac{{B_{di}}^2 V_{di}}{2\mu_0\mu_r} \tag{5-20}$$

The mesh volume in each direction (x, y, z) consists of two equal half-volumes; for instance, the volume in z-direction is divided into one half-volume to the left of XY plane (for B_{z1}), and another half-volume to the right of the XY plane (for B_{z2}), and we can write:

$$V_{z1} = V_{z2} = \frac{V_{tot}}{2} \tag{5-21}$$

From (5-20) and (5-), B_{eq} can be obtained by (5-22).

$$B_{eq} = \sqrt{\frac{({B_{x1}}^2 + {B_{x2}}^2 + {B_{y1}}^2 + {B_{y2}}^2 + {B_{z1}}^2 + {B_{z2}}^2)}{2}} \tag{5-22}$$

5.4.3 Magnetic material non-linearity

The most crucial role of MEC is to take into consideration the magnetic material non-linearity. Here, a bolded symbol is used for a matrix, whereas a normal symbol is used for the element of that matrix. As described in Figure 5-8, the non-linear MEC solving starts with the construction of permeance matrix ($\boldsymbol{P}$), which takes the permeability matrix as input ($\boldsymbol{\mu_{in}}$). Then, solving the system of equations will lead to the flux density matrix ($\boldsymbol{B}$) from (5-22). The problem is that the initial $\boldsymbol{\mu_{in}}$, with which we found the $\boldsymbol{B}$, depends itself on the value of $\boldsymbol{B}$. In other words, one needs to update the $\boldsymbol{\mu_{in}}$ based on this new $\boldsymbol{B}$, and then the whole system of equations needs to be resolved again, as demonstrated in Figure 5-8. This loop will be continued, until the error between the two consequent permeability matrices (as presented by (5-23)) gets less than an error limit predefined by user (δ_1). The division is an element-wise (scaler) division.

In Figure 5-10, for *mesh*(*i*), if $\mu_{in} = 1$, the material in the mesh is either air, PM, or copper. For these meshes, the next permeability (μ_{next}) will be always equal to one. For magnetic materials with $\mu_{in} > 1$, if *fix*(*i*)=1, it means that the error between μ_{in} and the calculated permeability (μ_{calc}) for the mesh was previously fallen inside a predefined error limit δ_2 (see the bottom of algorithm):

$$\left\| \frac{\boldsymbol{\mu_{in}} - \boldsymbol{\mu_{calc}}}{\boldsymbol{\mu_{in}}} \right\|_{\infty} \leq \delta_1 \tag{5-23}$$

The $\boldsymbol{\mu_{calc}}$ is the relative permeability matrix, calculated from $\boldsymbol{B}$ ($\boldsymbol{\mu_{calc}} = f(\boldsymbol{B})$). The simplest way is to interpolate $\boldsymbol{\mu_{calc}}$ from the BH curve of the magnetic material in the datasheet (see Figure 5-9 as an example). This is the approach taken here; however, when the data points are not available with enough resolution, an analytical formula can be related to the available data, using curve fitting techniques. In the literature, one can find several efforts on this subject, from [138], [139] to more recently in [140]. The next permeability matrix ($\boldsymbol{\mu_{next}}$) is constructed element by element (μ_{next}) through an algorithm devised to minimize the error δ_1. In the absence of minimization algorithm, the convergence of the whole problem disappears and δ_1 gets bigger. The approach taken here is a creative kind of fixed-point error minimization algorithm, as demonstrated in Figure 5-10. For each loop of the non-linear solve in Figure 5-8, the algorithm in Figure 5-10 starts from the first mesh, and continues until the last mesh in the model.

$$1 - \frac{\mu_{calc}}{\mu_{in}} \leq \delta_2 \tag{5-24}$$

For each loop of the non-linear solve in Figure 5-8, the algorithm in Figure 5-12 starts from the first mesh and continues until the last mesh in the model is scanned. For *mesh*(*i*), if $\mu_{in} = 1$, the material in the mesh is either air, PM, or copper. For these meshes, the next permeability (μ_{next}) will be always equal to one. For magnetic materials with $\mu_{in} > 1$, if *fix*(*i*)=1, it means that the error between μ_{in} and the calculated permeability (μ_{calc}) for the mesh was previously fallen inside a predefined error limit δ_2 (see the bottom of algorithm). For this mesh, the permeability is meant to stay fixed, and we put $\mu_{next} = \mu_{in}$. Thereafter at the bottom of algorithm, the error

δ_2 is rechecked, and based on the error value, the flag of fixed permeability is set to 0 or 1 for the next round of non-linear solving.

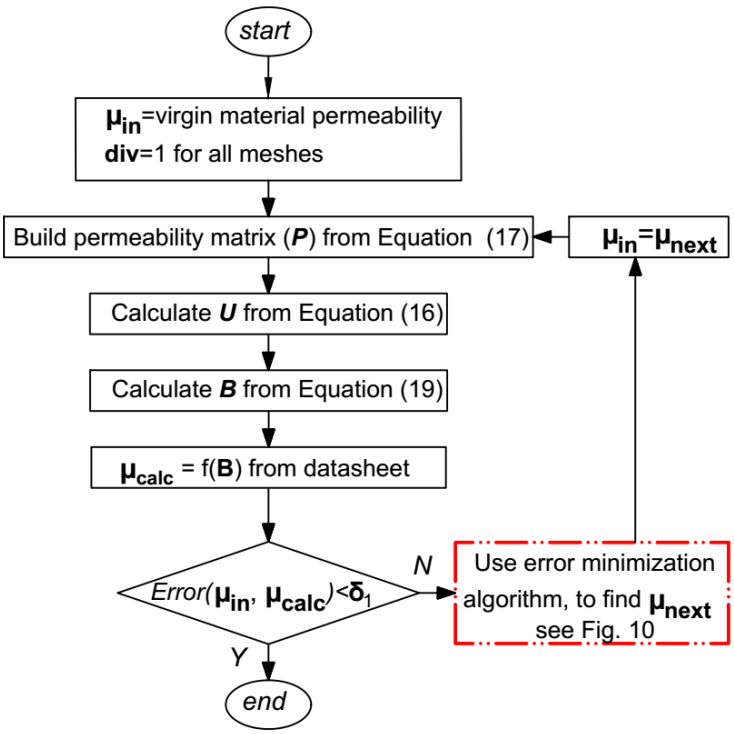

Figure 5-8: Non-linear MEC solving

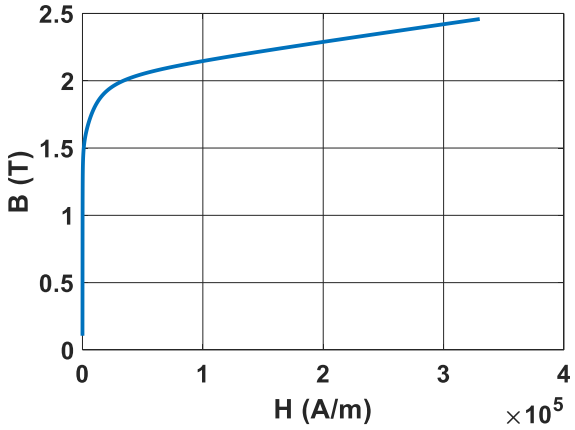

Figure 5-9: BH curve for M-19 29Ga (source: MagNet Infolytica)

If $\mu_{in} > 1$ and $fix(i) \neq 1$, the algorithm will try to find the best guess for μ_{next}. It proceeds with the calculation of the difference between input and calculated permeability (μ_{diff}). The μ_{next} is then obtained from (5-25).

$$\mu_{next}(i) = \mu_{in}(i) - \frac{\mu_{diff}}{div(i)} \tag{5-25}$$

where, $div(i)$ is a division factor which determines the step size to be taken towards the correct answer. At the beginning of non-linear solve in Figure 5-8, all meshes start with $div(i)$=1 and the maximum permeability of virgin material, so μ_{diff} is positive at start; thereafter, when μ_{diff} gets negative, it means our previous guess for μ_{next} (or μ_{in} in this round) was too much reduced. As $\mu_{diff} < 0$, now (5-25) gives an increase to μ_{next}, but with an smaller step due to $div(i)$=2. Each time μ_{diff} changes its sign, the $div(i)$ for that mesh is increased one unit in order to reduce our step size towards the final solution. By repeating this procedure, the μ_{next} will make a damped oscillation around the final permeability. At the end, the next permeability matrix ($\boldsymbol{\mu_{next}}$) is reported. This procedure is repeated inside the upper-level algorithm (see Figure 5-8), until the error limit δ_1 is satisfied.

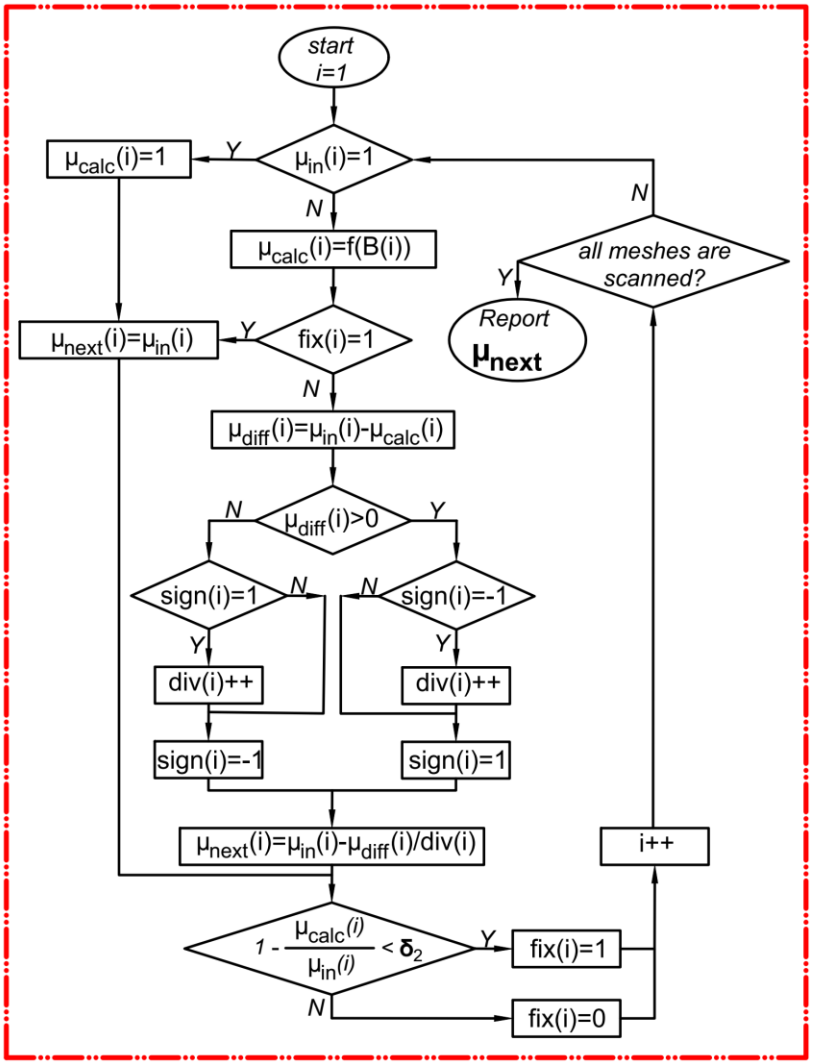

Figure 5-10: Error minimization algorithm (i: index of mesh element)

5.4.4 FEA validation of MEC model

Following the approach explained in section 5.4, the MEC model of HESM is developed, solved, and now will be compared to the FEA simulation results from MagNet Infolytica. The HESM evaluated here, is the final optimal design, which is reported in Table 5-6 (Appendix). The MEC and FEA configurations are also presented in Table 5-7. The comparison is made between the primary, as well as, the post-processed variables. For primary variables, airgap and teeth flux densities at no-load and full-load are compared. At each loading condition, positive, zero, and negative excitation current is tested with the model. For the post-processed variables, the flux linkage, voltage, and cogging torque are selected for comparison. This will consolidate the foundations for the whole optimization process. Figure 5-11 represents the flux density at airgap and teeth for normal, flux-weakening, and flux-strengthening conditions. The average error between the MEC and FEA, at its maximum, is always less than 5 %. Figure 5-12 represents the post-processed variables, e.g. flux linkage of phase-a, and back EMF of phase-b, again for normal, flux-weakening, and flux-strengthening conditions.

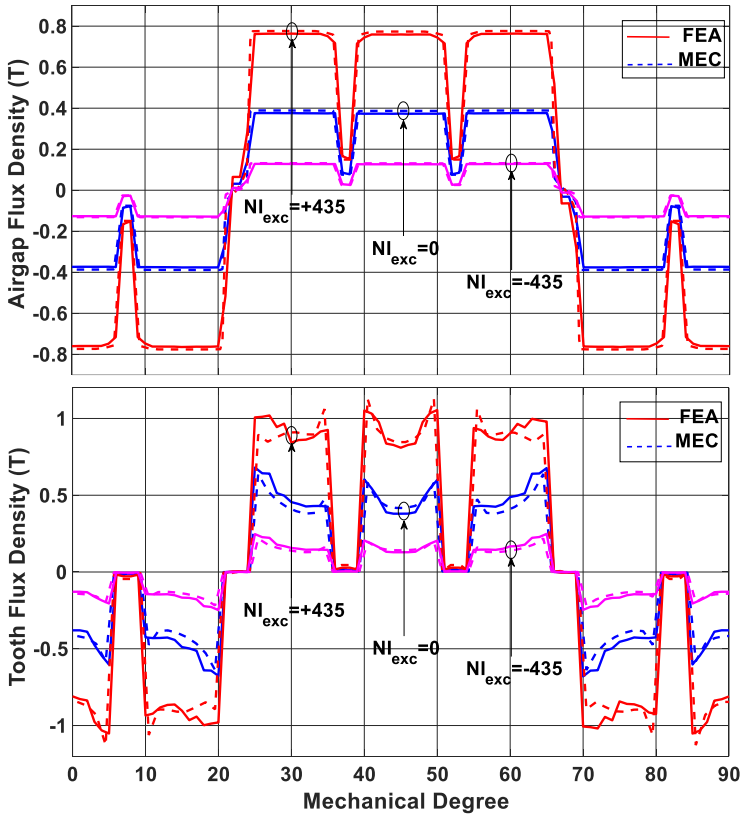

Figure 5-11: MEC Evaluation: flux density at different excitation currents

The torque and cogging torque is calculated based on the virtual displacement method, as presented in [141] and [142]. Considering that the flux distribution is homogeneous all over the mesh volume, the magnetic energy stored in each mesh element is obtained from (5-26).

$$W_i = \frac{1}{2\mu_0\mu_r}\int_v {B_i}^2 dv \tag{5-26}$$

where, B_i is equivalent flux density in the mesh (see (5-18)), and v is the volume of mesh element. The total magnetic energy is obtained by summing up the energies of all mesh elements in the model. The torque is then calculated from (5-27),

$$T = -\frac{\partial W}{\partial \theta_m} \tag{5-27}$$

where, θ_m is the rotor angular position in radians. Due to the spoke-type structure of the rotor, the cogging torque with this topology is a bit high, which can be addressed by either skewing the stator slots, mechanically shaping the rotor poles to produce sinusoidal waveforms, or adding another objective function for cogging torque to the multiobjective design optimization of HESM.

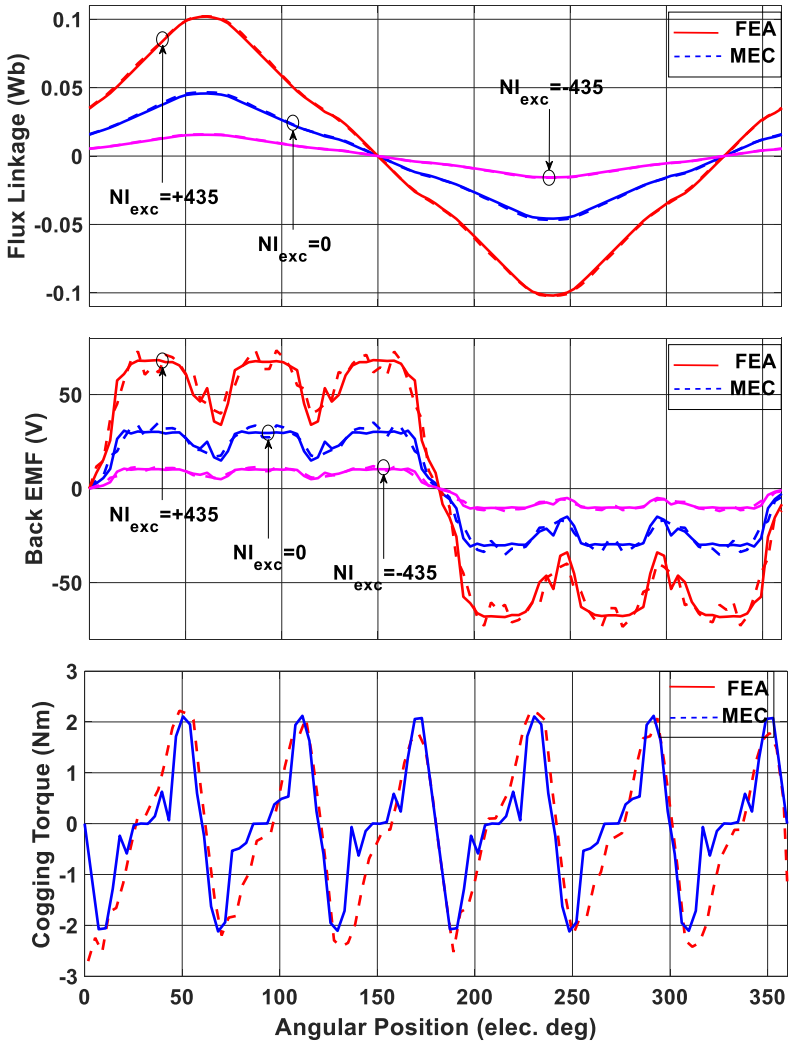

Figure 5-12: Evaluation: rated flux linkage, voltage, and cogging torque

The core loss calculation is mainly based on a dynamic core loss model for arbitrary (non-sinusoidal) flux waveforms, as presented in [143] and obtained from (5-28).

$$P_{Fe} = k_h f {B_{pk-pk}}^{\alpha} + \frac{k_e}{2\pi^2 T}\int_0^T \left(\frac{dB}{dt}\right)^2 \tag{5-28}$$

where, k_h, k_e, α are core loss coefficients extracted from material datasheet. f and T are the electrical frequency and period, respectively. The evaluation of core loss is also verified at less than 8% of error.

5.5 Optimization results and discussions

Following the proposed methodology in section 5.3.3 and using the MEC modelling technique and NSGA-II optimization method, a reduced scale HESM is optimally design for the vehicle in Table 5-1. The optimization at system-level is formulated in (5-29).

$$\begin{gathered} max\ OF = \eta_{global}(HR) \\ s.t.: 0 \le HR \le 1 \end{gathered} \tag{5-29}$$

Where, we are trying to maximize the global efficiency, by doing an exhaustive search for different HRs from 0 to 1.A per-unit (pu) system is employed to adopt the different quantities in vehicle and motor sides. In addition, the per-unit representation helps the designer to take a better decision, as all variables are seen from a uniform perspective.

It takes around 4 hours with FEA to perform one 3D static analysis for HESM, and can take even more time depending on the saturation level in the model. With the same computer specifications, MEC needs about a minute or two to have a valid solution (with less than 5 % of error). However, for more accurate solution around the highly saturated areas, e.g. stator tooth tip or in the outer stator, the mesh size and error limits should be confined to smaller values.

The HESM model and the optimization algorithm are implemented in MATLAB™, benefiting from the outstanding features of parallel computing toolbox. To find the optimal HR, an exhaustive search is conducted for HRs from 0 (pure WE) to 1 (pure PM excitation), with the steps of 0.1 (11 HRs). At each step, the motor is optimized at the component-level by NSGA-II for the corresponding HR, as mentioned in section 5.3.2. For each HR, 48 CPUs for 24 hours are hired to work in parallel. Then an efficiency map is constructed for each HESM, and the global efficiencies are compared to find the optimum HR.

Figure 5-13 displays for the optimally designed HESMs, the specified fluxes in solid lines ($\phi_{PM}, \phi_{min}, \phi_{max}$), while calculated fluxes in dashed lines ($\phi_{PM-calc}$, $\phi_{min-calc}$, $\phi_{max-calc}$). ϕ_{PM} linearly increases from 0 to 0.0852 Wb (see (5-1)), ϕ_{max} is equal to the nominal flux for all HRs (see (5-4)), and ϕ_{min} is obtained from (5-3). For HRs less than 0.5, a flux weakening down to 0 Wb is enough, whereas, for HRs greater than 0.5, the minimum flux gradually increases up to the nominal flux at HR=1. Bringing the calculated fluxes into account, the three errors (e_1 to

e_3 in (5-5) to (5-7)) must be addressed properly, in order to control the flux between the specified ϕ_{min} and ϕ_{max}.

The error between $\phi_{PM-calc}$ and ϕ_{PM} (e_1) will be traced nearly to zero for all HRs. Between e_2 and e_3, it is only possible to address one of them, depending on the dominant error. The dominant error corresponds to the dominant operating mode, which can be flux weakening (e_2) or flux strengthening (e_3):

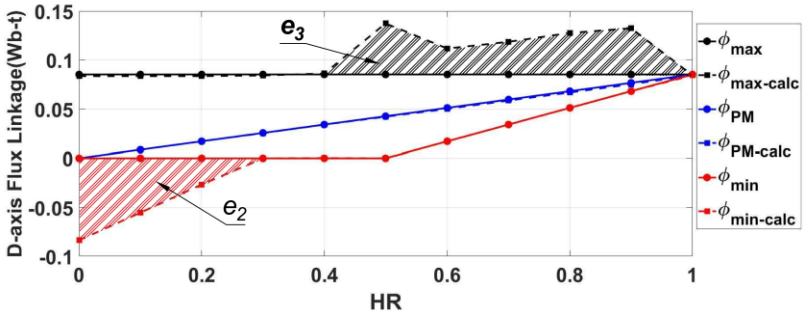

Figure 5-13: Specified and calculated d-axis flux linkages as a function of HR

1) At lower HRs, flux strengthening is more dominant, meaning that e_3 will be addressed properly, while the other error (e_2) cannot be perfectly reduced. For instance, at HR=0.1, ϕ_{WE} should provide 90 % of the nominal flux, which is quiet demanding and makes the flux strengthening to be dominant. In flux weakening with negative excitation current, the strong WE can easily attenuate the little flux coming from the PMs ($\frac{1}{10}\phi_{nom}$), and attain even negative fluxes for $\phi_{min-calc}$. Off course, this negative flux has no use.

2) At higher HRs, where a higher share of airgap flux is assigned to PMs, the flux weakening is more difficult and dominant (only e_2 can be reduced to nearly zero). Removing the strong flux coming from PMs is not an easy task and needs high MagnetoMotive Force (MMF) in WE coils, provided that we are facing the hard saturation phenomena. In flux strengthening and with positive excitation current, this high MMF together with PM flux can produce $\phi_{max-calc}$ bigger than what is needed (ϕ_{nom}). This extra flux can help in the acceleration or hill climbing of EV.

In Figure 5-14, the design variables for 11 optimally designed HESMs are normalized based on their corresponding maximum values in Table 5-3, and are plotted against HR. The cost of material for each HR is also displayed in $US.

As HR increases from 0 to 1, we are expecting a gradual increase in h_{PM}, and a continuous decrease in h_{ssi}, l_{ssi}, and N_{exc}. Our expectations are met for h_{PM}, however, for in h_{ssi}, l_{ssi}, and N_{exc} it is not the case. For HRs around 0.5 and 0.9, we see an increase in N_{exc}. At HR=0.5, due to high interactions between PM and WE fluxes, we are facing a severe hard saturation. This calls for a higher number of turns to attain 0Wb with negative excitation current. h_{ssi} and l_{ssi}, are accordingly adopted to provide enough path for WE flux.

Around HR=0.9, the problem comes from the low remanent flux density of ferrite magnets. At this HR, to reach $\phi_{PM} = \frac{9}{10}\phi_{nom}$ with ferrite magnets, the optimization algorithm have selected higher l_s, plus lower h_{ssi} and l_{ssi}, in order to confine the PM flux into its main path and prevent leakage (see Figure 5-2-a). As a result, higher N_{exc} is demanded to force the WE flux through the narrow path of h_{ssi} and l_{ssi}. Although the reduction of errors (e_1 to e_3) at HR=0.9 could be achieved in other ways, this solution is selected by NSGA-II for the sake of cost minimization.

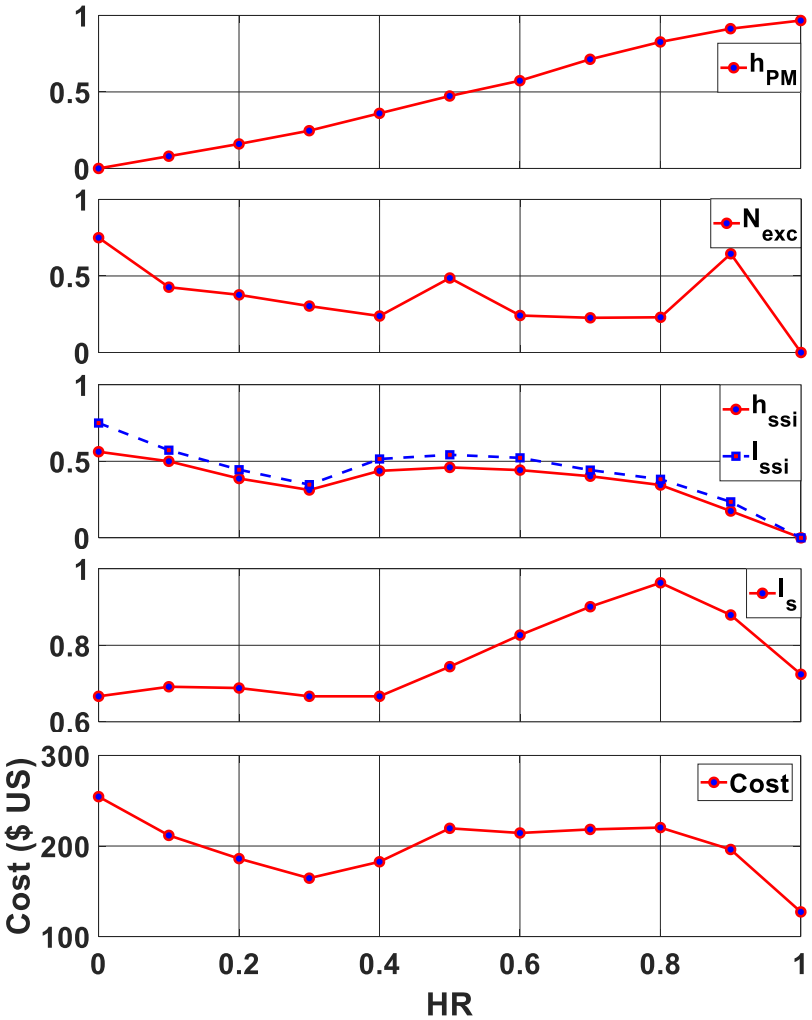

Figure 5-14: Normalized design variables and Cost ($ US) as a function of HR

In Figure 5-15, the normalized dq equivalent lumped parameters of the optimal solutions are displayed against the HR, (see [10] for normalization of dq parameters). As can be noticed from this figure, by following the proposed methodology using the MEC model, more reliable and detailed dq parameters are obtained for each HR.

In the search for the optimal HR, 11 efficiency maps are built up using the MEC model of HESM. The control currents (armature current and WE current) for a given Torque-Speed operating point are calculated offline from the minimum-loss control method. Then, it remains only to calculate the global efficiency of each HESM over the driving cycle, and to compare them. Figure 5-16 compares the global efficiencies of all eleven HESMs as a function of HR and proposes the optimal HR=0.8. Figure 5-17 shows the efficiency map of this optimal HESM, for which the highly efficient area is optimally mapped over the operating points of US60 driving cycle. This design is superior to all other HESMs and gives more 18.65 % global efficiency than the HESM with pure WE, and more 15.8 % than the HESM with pure PM excitation. By following the same principle as explained to this point, the design optimization can now be pursued and repeated for HRs between 0.7 and 0.9 with higher resolution.

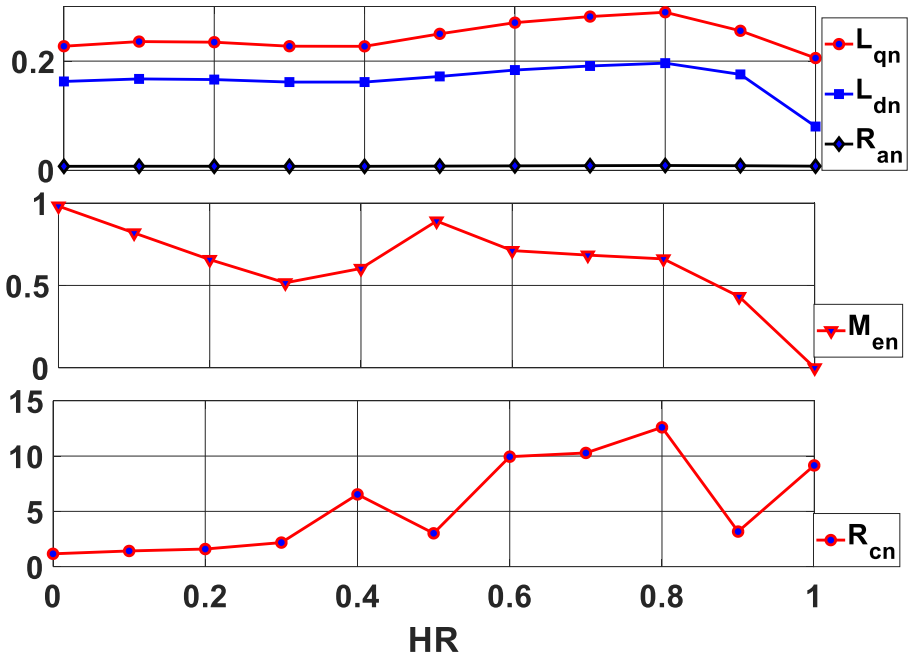

Figure 5-15: Normalized dq parameters as a function of HR

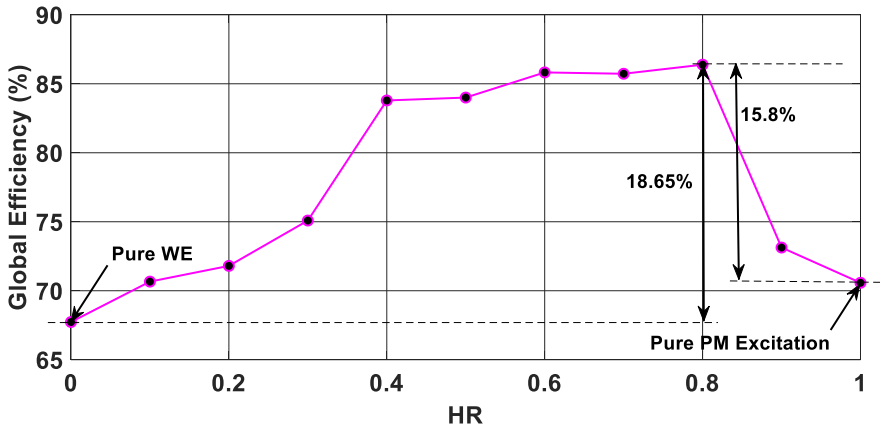

Figure 5-16: Global efficiency over US06 driving cycle as a function of HR

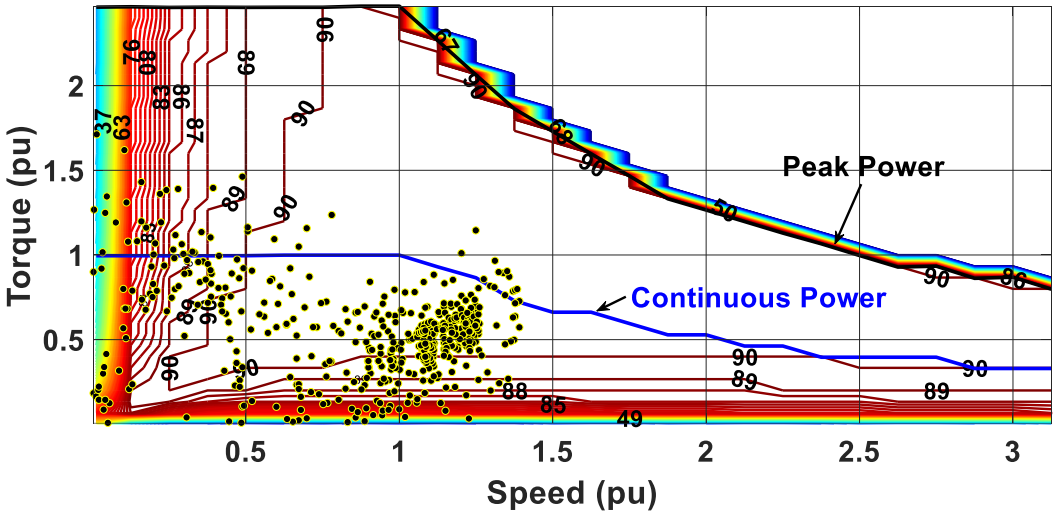

Figure 5-17: Optimal HESM (HR=0.8) over US06 driving cycle (η_{global}=86.38 %)

5.6 Conclusion

Through a case study, a two-level methodology was proposed for HESM design optimization. It effectively integrates more details of component-level optimization into the system-level optimization of EV drivetrain, using the HR as the interconnecting variable. This helps the EV designer to enhance the cost and performance of EV. We had difficulties and complexities analyzing the HESM, due to its flux leakage and 3D magnetic structure. These difficulties are addressed with the developed MEC model and the NSGA-II algorithm. Having a step-by-step meticulously evaluated methodology, this work proposes a generic and reliable framework to enhance the global efficiency of any EV powertrain, over any arbitrary-selected driving cycles, using a suitable HESM. Using a three-wheel Roadster EV over US06 driving cycle as a case study, 11 HESMs were designed and compared. The final optimal HESM can make 18.65 % of difference in global efficiency to the HESM with HR=0, and 15.8 % of difference to the HESM with HR=1.Appendix (Chapter 5).

5.7 **Appendix** (Chapter 5)

Table 5-5 Pseudo-code for the calculation of second term in Err_{HR} (OF_{12})

1:	**if** (e_2<0 **and** e_3>0) **then**
2:	**if** $\|e_2\| > \|e_3\|$ **then**
3:	$OF_{12} \leftarrow \frac{\|e_3\|}{\phi_{max}}$
4:	**else**
5:	$OF_{12} \leftarrow \frac{\|e_2\|}{\phi_{min}}$
6:	**end if**
7:	**else if** (e_2>0 **and** e_3<0)
8:	**if** $\|e_2\| > \|e_3\|$ **then**
9:	$OF_{12} \leftarrow \frac{\|e_2\|}{\phi_{min}}$
10:	**else**
11:	$OF_{12} \leftarrow \frac{\|e_3\|}{\phi_{max}}$
12:	**end if**
13:	**else if** (e_3<0 **and** e_2<0)
14:	$OF_{12} \leftarrow \frac{\|e_3\|}{\phi_{max}}$
15:	**else if** (e_3>0 **and** e_2>0)
16:	$OF_{12} \leftarrow \frac{\|e_2\|}{\phi_{min}}$
17:	**end if**

Table 5-6 Optimized HESM design

Variable	Unit	VALUE
Max. DC bus voltage	V	109
Min. DC bus voltage	V	83
Number of phases	---	3
Number of pole pairs	---	4
Number of slot/pole/phase	---	1
Excitation coil no. of turns (N_{exc})	---	138
Armature coil no. of turns (N_s)	---	2
Motor total length (l_s)	mm	238.5
Total outside radius (R_{tot})	mm	139.5
Excitation yoke (h_{exc})	mm	21.8
Stator yoke (h_{sy})	mm	10
Stator tooth height (h_{st})	mm	7.2
Radial airgap (g)	mm	0.5
Horizontal airgap (g_{exc})	mm	0.5
PM width (W_{PM})	mm	84
PM height (h_{PM})	mm	3.3
Rotor inside radius (R_{ri})	mm	15
Excitation coil slot width (W_{exc})	mm	41
Excitation endcap length (l_{ssi})	mm	28
PM material	---	Ceramic10
Ferromagnetic material	---	M-19 29Ga, Iron–silicon alloy

Table 5-7 Mesh and solver configurations

Variable	Unit	VALUE
FEA Configurations		
Maximum element size at airgap	mm	1
Curvature refinement angle at airgap	degree	2
Maximum element size (other)	mm	5
Curvature refinement angle (other)	degree	10
Material type	---	Non-linear
Solving method	---	Newton-Raphson
Solver polynomial order (3D)	---	2
Newton tolerance	%	1
CG tolerance	%	0.01
MEC Configurations		
Total number of elements	---	1548-1556
Fixed point error limit	---	1e-8
Permeability matrix error limit	---	1

Chapter 6 Conclusions and Future Directions

The demand for EVs that can compete with ICE cars in the market has been intensified due the environmental causes in recent years. This has motivated the research world to look for optimal EVs with less cost and enhanced performance. In this regard, the optimization of each component in the EV drivetrain is a must. As a very important component in the drivetrain, the electric machine has the principal role of electrical to mechanical energy conversion. Although the research on conventional electric machines has reached to a semi-saturated state, the hybridization of different types of electric machines has opened new opportunities in this realm. That is why a HESM was selected to be optimized for a given three-wheel EV at e-TESC lab.

6.1 Conclusions

In this work, a methodology was proposed to optimize the HESM for the given EV over an arbitrarily-selected driving cycle. The optimization was conducted at both the component and system level. At the heart of our methodology, there is a very important decision variable, namely, Hybridization Ratio (HR). The HR is defined as the ratio of PM excitation to the total excitation in the motor. It determines how similar to PMSM or WESM the HESM would be. It can have any values between 0 and 1. By selecting HR equal to 0 or 1, the WESM and PMSM would be just a special case of HESM. The optimal HR will attribute the HESM with favorable characteristics of PMSM or WESM, in order to maximize the global efficiency of EV over selected driving cycle.

For the optimization of HESM, we needed a model to predict the behavior of the motor. The optimization methodology was first proposed and consolidated by a lumped-parameter dq equivalent circuit model. This model was simple, and provided us with a very fast feasibility study of the proposed methodology. However, in order to benefit from the full capacity of the materials and reduce the motor cost, most of the motors are designed to work in the non-linear operating conditions. In these conditions, the lumped parameters could not correctly represent the motor and output variables, such as voltage, torque, and losses. This conducted us towards more sophisticated models for HESM.

At first, we tried FEA; but it was soon abandoned due to excessive time and process required in the 3D analysis. Then, it took us a long time to develop and validate a new model based on reluctance networks which could correctly predict the non-linear behavior of 3D flux in HESM.

The non-linear 3D Magnetic Equivalent Circuit (MEC) model gave the possibility to make a trade-off between the speed and accuracy of computations. Within a minute, the MEC model could result a solution with less than 5% of error compared to the FEA simulation. Otherwise, FEA could take about 4 to 14 hours with the same computer. The MEC model lets us to develop a methodology with more reliable results for system optimization design.

At the component level, the HESM cost was minimized for a target HR. But as simple as it may seem in this short sentence, the task was quiet complicated. One of the challenges was the complexities existing in the asymmetrical (hard and soft) saturation of material in flux weakening and flux strengthening. The previous definitions of HR were not precise and accurate anymore. Due to several dimensional variables acting in contradicting ways, only finding a single HESM design for the target HR was a big challenge, not even talking about the cost minimization. To overcome this challenge, a new formulation of the design problem was proposed, which was tackled by the capabilities and merits of Non-Dominated Sorting Genetic Algorithm II (NSGA-II). This new formulation addressed, simultaneously, the design and cost minimization of HESM for a target HR.

At the system level, the optimal HR was found to result in maximum global efficiency of HESM over the selected driving cycle. At the component level, for each HR between 0 and 1 with steps of 0.1, the corresponding HESM was optimally designed to have the desired HR and minimum material cost. This provided us with a homogenous design space, which guarantied the reliably of the comparisons. Then, for each HESM, an efficiency map was constructed using the minimum-loss control currents. Afterwards, the global efficiency of each HESM over the US06 driving cycle was calculated, using the inverse distance weighted interpolation algorithm. The final step was to compare these results and select the optimal HESM which had the highest global efficiency. The optimal HESM was evaluated by the virtue of FEA simulation, and the required steps were taken to construct a prototype for experimental validations. All needed materials were selected and the corresponding CAD drawings were added to the project log.

6.2 Future Works Suggestion

For the future works, the prototype construction should be completed and the HESM should be tested under partial and full loads. This consists of the procurement and construction of different motor parts, assembly, and test. The ideas to be tested are listed below:

- **Optimal HESM behavior in reality**: The HESM efficiency map should be constructed and the operating points of US06 driving cycle should be more concentrated in the highly-efficiency region.

- **Comparison of different models with the experimental results**: This can be comprehensively accomplished by comparison at the echelle of an efficiency map, with four approaches: dq lumped parameter, MEC, FEA, experimental.

- **Implementation of control**: Considering the extra degree of freedom added to HESM by WE current control, a controller with the objective of achieving the minimum-loss (copper and iron losses) or unity power factor can be designed and implemented. This controller can then be compared to the results from control currents found by an off-line exhaustive search.

- **Analytical equations validation**: Several analytical equations are deduced in Chapter 3, which can be explored in experimental set up, especially those related to the CPSR calculation of HESM in (3-26).

- **Driving cycle approximation**: Investigation of an algorithm to approximate a driving cycle and reduce the operating point for optimization purposes. The original and approximated versions of the driving cycle should result in, more or less, the same global efficiencies. Firstly, the T-S plane should be divided into several equal areas. Then, based on the position of operating points in each specific area, one point, together with a number representing the frequency of occurrence, should be proposed. The proper number of division in each direction of T-S plane can be part of the algorithm. At the most extreme case, the original driving cycle is approximated with one point which is the most frequent operating point.

- **Investigation of cogging torque reduction**: Due to the configuration of V-shaped PMs, the airgap reluctance varies according to the positions of rotor. Because of this, the rotor prefers certain positions to the others, which will result in a pulsation in the torque. In this work, the skewing of stator slots will be applied to address this issue, which reduces the torque a little bit. There are certain ways, both at design and control stages, to reduce the cogging torque without losing on the torque, which should be investigated.

- **Study of Gallium Nitride (GaN)-based power converters on the HESM**: The HESM can be tested by some modern switching devices, in order to study the effects of high frequency switching effects on HESM.

6.3 Conclusion (in French)

Dans ce travail, une méthodologie a été proposée pour optimiser le HESM pour un véhicule électrique donné sur un cycle de conduite choisi arbitrairement. L'optimisation a été réalisée au niveau des composants et du système. Au cœur de notre méthodologie, il y a une variable de décision fondamentale à déterminer, le ratio d'hybridation (HR). Le HR est défini comme le rapport de l'excitation des aimants permanents et l'excitation totale du moteur. Il détermine la semblance du PMSM ou du WESM d'un HESM. Il peut avoir n'importe quelle valeur entre 0 et 1. En sélectionnant HR égal à 0 ou 1, le WESM et le PMSM ne seraient qu'un cas spécial de HESM. Le HR optimale attribuera au HESM des caractéristiques favorables de PMSM et de WESM, afin de maximiser l'efficacité globale du véhicule électrique sur un cycle de conduite sélectionné.

Pour l'optimisation du HESM, nous avons besoin d'un modèle pour prédire le comportement du moteur. La méthodologie d'optimisation a d'abord été proposée et consolidée par un modèle de circuit équivalent dq. Ce modèle était simple et nous a fourni une étude très rapide de la méthodologie proposée. Cependant, afin de bénéficier de la pleine capacité des matériaux et de réduire le coût du moteur, la plupart des moteurs sont conçus pour fonctionner dans des conditions de fonctionnement non linéaires. Dans ces conditions, le modèle équivalent dq ne pouvait pas représenter correctement le comportement du moteur, tel que la tension, le couple et les pertes. Cela nous a conduits vers des modèles plus complexes pour HESM.

Au début, nous avons utilisé FEA; mais il a été rapidement abandonné en raison du temps et du processus excessifs requis dans l'analyse 3D. Ensuite, il nous a fallu beaucoup de temps pour développer et valider un nouveau modèle basé sur des réseaux de réluctance qui pourrait correctement prédire le comportement non linéaire du flux 3D dans un HESM. Le modèle non linéaire de circuit équivalent magnétique 3D (MEC) a permis de faire un compromis entre la vitesse et la précision des calculs. Dans une minute, le modèle MEC pourrait obtenir une solution avec moins de 5% d'erreur par rapport à la simulation FEA. FEA pourrait prendre environ 4 à 14 heures avec le même ordinateur. Le modèle MEC nous a permis de développer la méthodologie avec des résultats plus fiables pour l'optimisation de la conception de système.

Au niveau des composants, le coût du HESM a été minimisé pour un HR donné. Mais aussi simple que cela puisse paraître dans cette courte phrase, cela représente une difficulté majeure. L'un des défis était la complexité de la saturation asymétrique (dure et douce) du matériau dans le défluxage et l'augmentation du flux dans la machine. Les définitions existantes dans la littérature du HR n'étaient pas assez précises et exactes pour une conception optimisée. En raison de plusieurs variables dimensionnelles agissant de manière contradictoire, juste trouver un seul design de HESM pour le HR donné était un grand défi, sans même parler de la minimisation du coût. Pour faire face à ce défi, une nouvelle formulation du problème de conception a été proposée, qui a été abordée par les capacités et les mérites de l'algorithme génétique de tri non dominé (NSGA-II). Cette nouvelle formulation abordait simultanément la conception et la minimisation des coûts du HESM pour un HR donné.

Au niveau système, le HR optimale a été déterminé pour avoir une efficacité globale maximale du HESM sur le cycle de conduite sélectionné. Au niveau composant, pour chaque HR entre 0 et 1 avec des incréments de 0,1, le HESM correspondant a été conçu de manière optimale pour avoir un HR souhaité et un coût minimum des matériaux. Cette approche a permis de déterminer

un espace de conception homogène, qui garantit la fiabilité des résultats et des comparaisons entre différents HESM. Ensuite, pour chaque HESM, une carte d'efficacité a été construite en utilisant les courants de contrôle de perte minimale. Ensuite, l'efficacité globale de chaque HESM sur le cycle de conduite US06 a été calculée. La dernière étape consistait à comparer ces résultats et à sélectionner le HESM optimal qui a la plus grande efficacité globale sur le cycle de conduite. Le HESM optimal a été évalué grâce à des simulations en FEA, et les étapes requises ont été prises pour construire un prototype pour future validation expérimentale. Tous les matériaux nécessaires ont été sélectionnés et les dessins CAD correspondants ont été ajoutés au projet.

Appendix I. Electric Motors Evaluation

Original Title:
Electric Motors Evaluation Algorithm based on their Effect on Electric Vehicle Mass Reduction

Authors and Affiliations:
- **Ahmad Shah Mohammadi,** Ph.D. student, e-TESC Laboratory, Department of Electrical & Computer Engineering, University of Sherbrooke
- **João Pedro F. Trovão,** Professor, e-TESC Laboratory, Department of Electrical & Computer Engineering, University of Sherbrooke

State: Published - doi: 10.1109/VPPC.2016.7791673

Conference: 2016 IEEE Vehicle Power and Propulsion Conference (VPPC), Hangzhou, China, (17-20 Oct. 2016), https://ieeexplore.ieee.org/document/7791673

Context of the appendix

This contribution was primarily meant to provide a tool for the comparison of different electric motors with different characteristics through an efficiency perspective. In this contribution, an algorithm is proposed to interpolate the efficiency of electric motor at an arbitrary operating point, based on the efficiency of four surrounding points on the Torque-Speed (T-S) plane. This algorithm is the prerequisite for calculating one of the most fundamental variables in this thesis, namely, the global efficiency. With global efficiency, the comparison of electric machines is made possible. In addition, the concept of overdesign in the drivetrain of EV due to limited Constant Power Speed Range (CPSR) is also explained. By reading this paper, together with the first major contribution in Chapter 3, one could construct the EV characteristic envelope, select several motors to respond to EV requirements, and then, compare their global efficiency over the desired driving cycles.

Abstract

If properly selected, an electric motor (EM) with a fitted power envelope could respond the Electric Vehicle (EV) needs and avoid overdesign. This paper proposes an iterative algorithm upon which, EV designers could define a proper motor and evaluate it by its impact on EV total mass reduction. To simplify the EV design, two characteristics of EM have been recognized to be more essential to enhance, namely, constant power speed range (CPSR) and global efficiency over the selected driving cycles. A full-battery powered three-wheel roadster prototype and its motor is analyzed, then, another sample motor with higher CPSR is proposed to remove part of the powertrain overdesign. Having limited test data, inverse distance weighted interpolation has been applied to extract the efficiency of electric motor at any operating point. Finally, based on the EV overdesign and its global efficiency, a comparison between the two motors has been made.

Introduction

In academia and industry reports, all types of AC Electric Motors (EMs) have been suggested for Electric Vehicles (EVs) under certain conditions; being very unclear, it is a very demanding task to select and evaluate an EM for an EV. Initial cost of EV plus its poor performance, such as range anxiety, long charging times and limited cargo and passenger space are the weaknesses which make it to loss market race to internal combustion engines (ICEs) [4], [144]. If properly selected, an EM with fitted power envelope could perfectly meet EV needs and achieve considerable enhancement in cost and performance of the EV.

For this to happen, its constant power speed range (CPSR) should be increased to be equal to or greater than that of the EV. Traction motor CPSR should be increased by increasing its maximum speed, because increasing its maximum torque has negative effects on size, efficiency and cost of the motor; but, to achieve CPSRs up to 5, it has been proven that increasing motor maximum torque have a positive effect on EV overall performance and cost [145]. Solutions to extend the maximum speed and CPSR of EMs, in both design and control phases, is well presented in literatures and it is still an ongoing research domain in EMs for traction, integrated starters/alternators, machine spindle drives, air conditioning compressors and similar applications [146]–[149].

There were no clear and concise paper devoted to selection and evaluation of an EM for EV in literature review. Proposing an algorithm, this paper will help other researchers to be aware of EM limits while selecting them for traction applications, e.g. during the algorithm, when acceleration criteria is dominated, the designer has to select the EM before finalizing EV torque-speed (T-S) envelope. Here, CPSR of the motor will be a limiting factor which will cause an overdesign in EV powertrain; lower the CPSR, higher the overdesign in motor, converter, batteries and gearbox.

The objective of this paper is to develop an algorithm for evaluation of selected motor for an EV; once established, it could be iteratively applied to move towards a better motor selection. A full-battery powered three-wheel roadster prototype adapted at e-TESC laboratory, presented in

Figure A.I. 1, has been chosen, just to clarify the algorithm. It should be noted that here, the purpose is not to find the perfect motor for the prototype.

The paper is structured as follows. Firstly, the EV overdesign, if there was any, will be reduced by selecting another motor with higher CPSR. Then, the global efficiencies of tow motors over New European Driving Cycle (NEDC) and US Driving Cycle (USDC) will be calculated. Inverse distance weighted interpolation approach has been applied to find the efficiency of electric motor at any operating point. Finally, the two motors will be evaluated based on the total reduction in EV mass that they have brought.

Figure A.I. 1 Three-wheel roadster example

After a brief review on traction motor specifications in Section II, Section III describes EV power envelope definition with special stress on motor CPSR effect on EV overdesign. Section IV addresses efficiency of motor for the selected driving cycles. Section V clarifies and discusses aforementioned algorithm, using the prototype as an example, while Section VI outlines the conclusion and ongoing works.

Traction motor characteristics

In an ideal EM for a vehicle, maximum power is always available for traction, over the whole speed range, with 100% efficiency at all operating points. However, in real world, the infinite torque at zero speed is limited to maximum allowable temperature rise at windings of the traction motor. As shown in Figure A.I. 2, after the constant torque operating mode (#1), as speed increases, the motor enters into constant power mode (#2). Again, infinite speed at zero torque is not possible, due to lots of reasons such as nonlinearity in control, low inductance of stator, motor and inverter voltage and current limits, demagnetization effects, constant losses, frictions and air resistances which increases with higher orders of motor speed; at a certain speed, finally, the motor enters its natural operating mode (#3) in which it will rapidly stops delivering any torque.

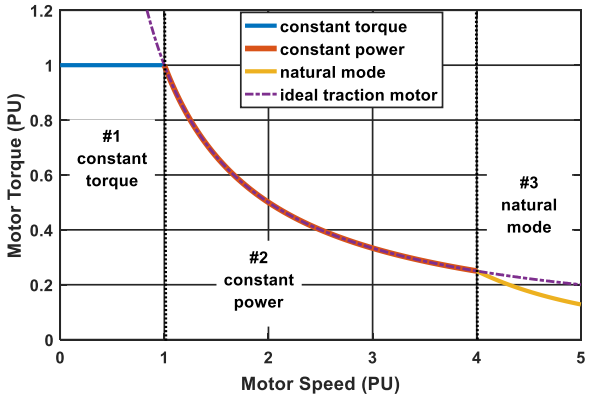

Figure A.I. 2 Ideal and real traction motor

The choice of electric propulsion system for EV mainly depends on three factors: driver expectation, vehicle constraint and energy source. The most important specifications that a real world traction motor should have are as follows [4], [10], [15], [144]:

- High instant power and high power density;
- High torque at low speeds for starting and climbing, as well as high power at high speed for cruising. It emphasizes staying in the constant power mode as long as possible;
- Very wide speed range which means higher gear ratio, lower maximum torque and lower motor size, with different CPSRs in hand. The higher speed a motor could possesses, the lower size and higher power density it will gain [18];
- Fast torque response which gives a better controllability and wider frequency band for the control system;
- High efficiency at traction and regenerative braking, over wide speed and torque ranges;
- Highly reliable, robust and fault tolerant for various vehicle operating conditions;
- Mature technology and market availability for the motor and its power converter.

In terms of transient overload capability, most of the time the motor is not a limiting factor, but the inverter [18]; the cost of the motor is to be dealt with and optimized at system level. To have a curve similar to an ideal traction motor, a real world EM should possess:

a) higher maximum speed with higher possible CPSR;

b) higher efficiency for the selected driving cycles.

Once got close to ideal curve, other above mentioned characteristics could be realized through today's technology.

Algorithm for Power Envelope Definition

Every vehicle aimed at a target market, which means designed for relevant driving cycles [144], needs to pass three requirements which are maximum continuous cruising speed, acceleration time and gradeability. Each requirement may change the shape of ideal EV T-S curve which is well documented in others works [4], [118]. This will result in changes in either the maximum power or CPSR of EV T-S curve. After finalizing, EV power envelope will need a proper traction motor, with minimum possible power, maximum efficiency and reasonable cost. Sometimes, the motor itself should be selected during this algorithm. Table A.I. 1 shows the specifications and requirements of the three-wheel roadster prototype [150].

Table A.I. 1 Specification and requirement of the three-wheel roadster prototype 8

variable	symbol	value	units
EV Specification			
Vehicle mass*	M	450	kg
Rolling resistance coefficient	f_r	0.02	--
Aerodynamic drag coefficient	C_D	0.075	--
Vehicle front area	A_f	1.25	m2
Wheels radius	r_d	0.305	m
Gearbox transmission ratio	g_t	5.033	--
Gearbox efficiency (ideally)	η_t	100%	--
* this is to be changed iteratively			
EV Requirement			
Maximum Speed**	V_{max}	140	km/h
Acceleration Speed	V_{acc}	100	km/h
Acceleration Time	t_a	20	s
Grade Slope at 100 km/h	i	0.03	--
** Variable should be transferred to SI units to be used in the formulas			
other Constants			
Acceleration of gravity	g	9.807	m/s2
Air density at 15°C	ρ_{air}	1.225	kg/m3

Figure A.I. 3 proposes an algorithm to determine EV power envelope and the procedure is as follows.

A. P_{max} based on maximum cruising speed

Determine maximum power of the vehicle based on maximum cruising speed and needed tractive force at that speed. Maximum cruising speed is defined as "the constant cruising speed that the vehicle can develop with full power plant load on a flat road" [4].

$$P_{max} = F_{t-Vmax} V_{max} \quad \text{(AI-1)}$$

$$F_{t-Vmax} = Mgf_r + \frac{1}{2}\rho_{air}C_D A_f V^2{}_{max} \quad \text{(AI-2)}$$

where P_{max} is EV maximum power and F_{t-Vmax} is required tractive force at maximum cruising speed. Other parameters are explained in Table A.I. 1; all values must be entered in all formulas by SI units. The result is a constant power curve on T-S plane (Figure A.I. 4).

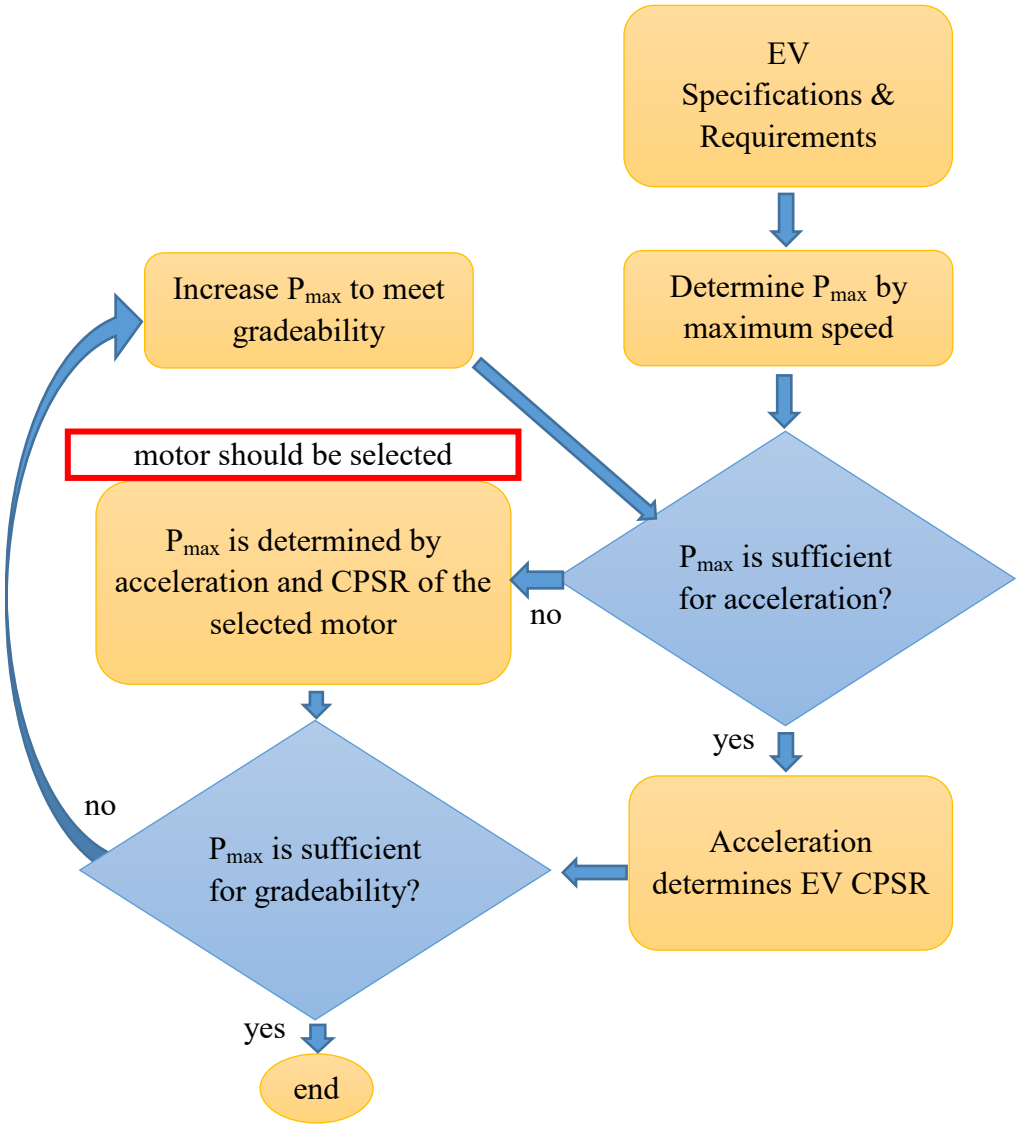

Figure A.I. 3 Proposed flowchart for EV T-S envelope definition

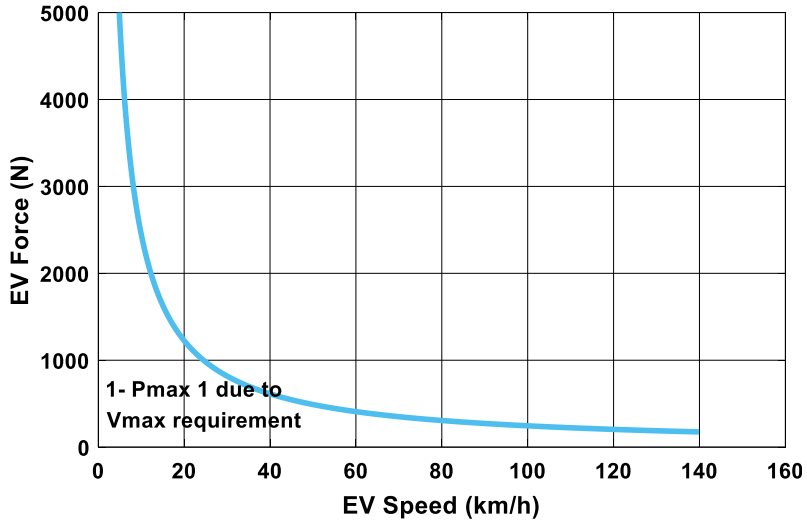

Figure A.I. 4 P_{max} resulted from needed V_{max}

B. P_{max} based on acceleration requirement

Acceleration time is defined as "the time needed to reach to a specific level of speed (V_{acc}=100 km/h, for example) [4].

$$t_a = \int_0^{V_{acc}} \frac{M\delta}{F_t - (Mgf_r + \frac{1}{2}\rho_{air}C_D A_f V^2)} \qquad \text{(AI-3)}$$

where F_t is tractive force at speed V and δ is called rotational inertia factor (δ = 1.1292, for our EV). There are two cases:

i) ***The maximum power is sufficient for acceleration***: In this case, the required acceleration time will determine CPSR of the EV, faster accelerations need higher CPSRs.

ii) ***The maximum power should be increased***: If the acceleration time is less than what an ideal traction motor could provide, the maximum power should be increased which is the most happening case with passenger EVs. The result is shown in Figure A.I. 5 which is an ideal EV T-S curve and should be realized by a motor.

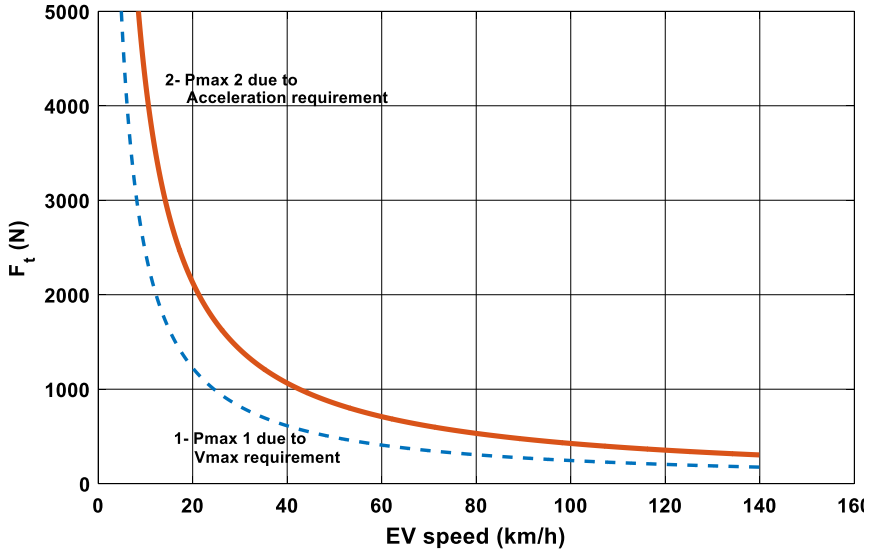

Figure A.I. 5 Increase in EV P_{max} due to acceleration requirement

At this stage, the motor drive should be selected and this is where the overdesign happens; the motor CPSR and the acceleration criteria will determine EV maximum power. As shown in Figure A.I. 6, lower CPSRs cause higher EV maximum power and also more overdesigned powertrain. Put the CPSR of EV equal to the CPSR of the selected motor and determine the EV maximum power.

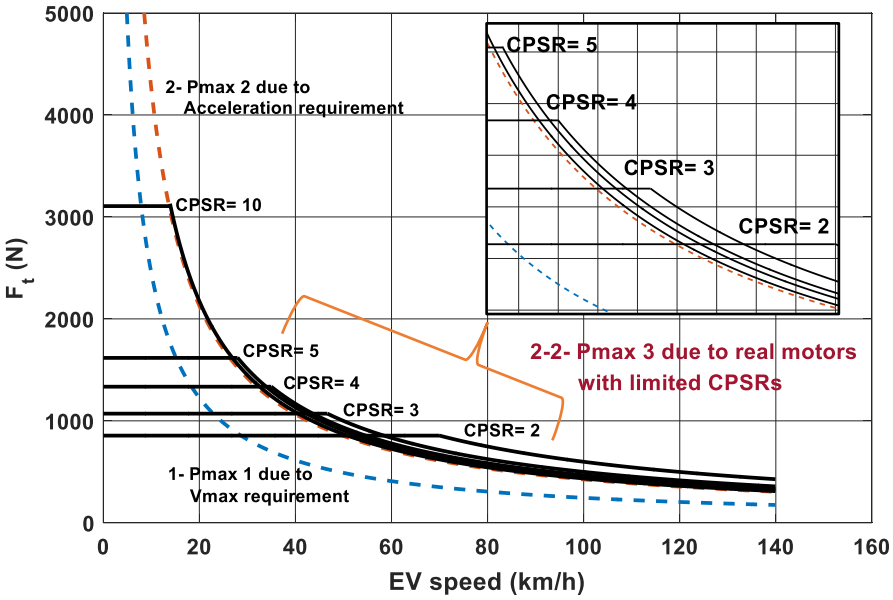

Figure A.I. 6 P_{max} of EV due to a motor with limited CPSR

C. P_{max} based on gradeability

Check the EV power envelope adequacy for the gradeability criteria. Gradeability is defined as "the maximum slope that the vehicle can overcome at its rated constant speed" (3% slope at the speed of 100 km/h) [4]. For small angles the tractive force is:

$$F_{t-Grade} = Mgf_r + \frac{1}{2}\rho_{air}C_D A_f {V_{rated}}^2 + Mgi \qquad \text{(AI-4)}$$

where V_{rated} is EV rated speed and i is the slope. From EV power envelope at rated speed, if F_t was not equal or greater than $F_{t-Grade}$ from (AI-4), change the maximum power to

$$P_{max} = F_{t-Grade}.V_{rated} \qquad \text{(AI-5)}$$

If maximum power increased, start again from stage B, as it will reduce the CPSR of EV power envelope. The result of this algorithm is a finalized EV power envelope with a specific CPSR, which should be responded by a motor possessing the same or higher CPSR; otherwise, one has to select a motor with higher power to satisfy the EV power envelope. To be able to evaluate and compare different motor candidates, an efficiency check will be needed, as most of the motors with higher CPSRs, have poor global efficiency over driving cycles.

Efficiency over Driving Cycles, EM Evaluation

While couple of EM candidates exist, global efficiency check would be beneficial which is depicted in Figure A.I. 7.

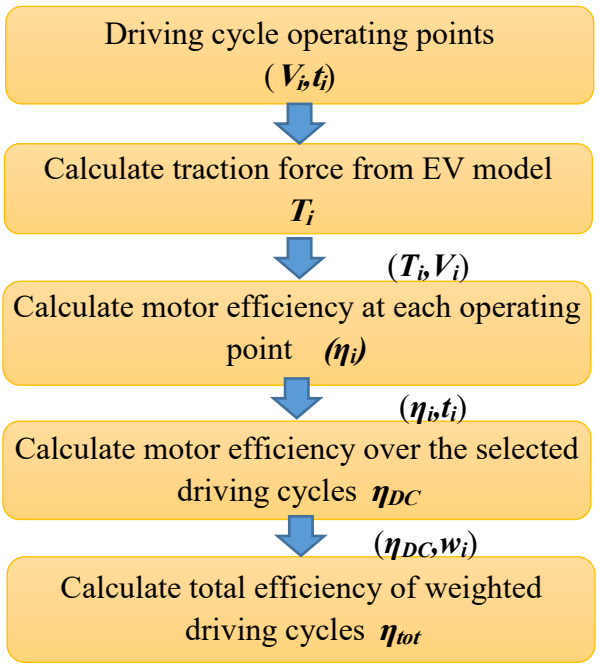

Figure A.I. 7 Efficiency routine flowchart

For every operating point of driving cycle (V_i,t_i), motor torque (T_i) will be calculated from (AI-6).

$$T_i = \frac{r_d}{g_t \eta_t}\left(Mgf_r + \frac{1}{2}\rho_{air} C_D A_f {V_{rated}}^2 + \delta M \frac{dV_i}{dt_i} + Mgi\right) \quad \text{(AI-6)}$$

To calculate the efficiency of every operating point (T_i,V_i) on motor T-S envelope, using limited test data available, an interpolation based on "inverse distance weighted interpolation" has been applied. In this approach, efficiency of each operating point is suggested based the efficiencies of 4 surrounding points on the T-S mesh-grid for which the test data is available (Figure A.I. 8).

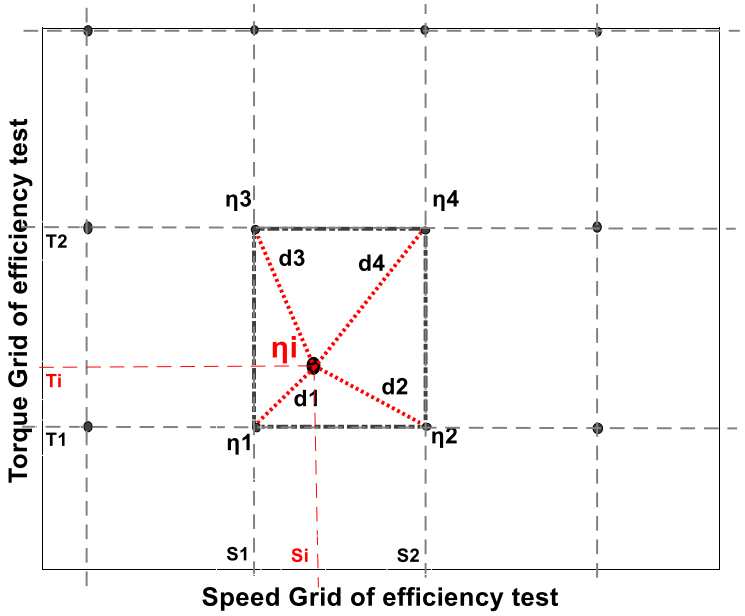

Figure A.I. 8 Inverse distance weighted interpolation from test data mesh-grid

This method is generally used in computer science approach to several applications [151], [152], but its application to EM efficiency map is totally new. Typically, this method is used to form the elevation contours on a map, based on the picked up data from the location. Assuming that the motor efficiency change is continuous, this approach has been applied to find motor efficiency contours on T-S mesh-grid and its validation is our ongoing research.

The efficiency of each operating point is calculated from (AI-7),

$$\eta_i = \frac{\sum_{n=1}^{4} \frac{\eta_n}{d_n}}{\sum_{n=1}^{4} \frac{1}{d_n}} \quad \text{(AI-7)}$$

here η is efficiency and d is distance. Having (T_i,V_i) pairs of mesh-grid and the operating point, the distances is calculated from Pythagoras equation; e.g. $d_1 = \sqrt{(T_1 - T_i)^2 + (S_1 - S_i)^2}$. Global efficiency for a specific diving cycle (η_{DC}) will be calculated from (AI-8).

$$\eta_{DC} = \sum_i \eta_i . \frac{t_i}{t_{tot}} \tag{AI-8}$$

where t_{tot} is total time of the driving cycle, t_i is the duration of the operating point (i). and η_i is its efficiency. From (AI-8) one can deduce that the more frequent operating points in the selected driving cycle should fall into the most efficient area of EM to maximize the global efficiency. In contrast, efficiency of other points with less frequency is less important. For several weighted driving cycles, their efficiency should be summed:

$$\eta_{global} = \sum_i W_i . \eta_{DCi} \qquad while \qquad \sum_i W_i = 1 \tag{AI-9}$$

where W_i is the weighting factor that the designer of EV assigns to each driving cycle, depending on their resemblance to the driving styles and routs of the target market. Different motors evaluation could be made considering the total EV mass reduction due to both the overdesign and global efficiency; this will be more explained in Section V.

For the sake of simplicity and without loss of generality, an ideal single-speed gear has been assumed. The ratio of the gear will be determined from (AI-10) after finalizing the traction motor.

$$g_t = \frac{(\omega_{max} \times r_d)}{V_{max}} \tag{AI-10}$$

where ω_{max} is motor maximum angular speed.

Discussions

While characterizing the EV power envelope, if acceleration criteria is dominated, as is most frequent with passenger EVs, the CPSR of the motor will be a limiting factor and an overdesign would occur, which would need high rated power electronics, gearbox and batteries [145]. This is not favorable in terms of the cost and performance, which are exactly the drawbacks of EVs compered to ICEs.

Here, for a full-battery powered three-wheel roadster (Figure A.I. 1 and Table A.I. 1), selected motor CPSR effect on EV overdesign is analyzed, and then, with the new insight from the proposed algorithm, just to clarify that a little increase in motor CPSR will considerably reduce P_{max} of EV, an alternative motor with higher CPSR will be proposed. Consequently, the mass of EV decreases mostly due to decrease in batteries nominal power. Then, driving cycle global efficiency will be calculated for them. Finally, total EV mass reduction due to both the overdesign and global efficiency comparison between the two motors will be discussed.

As is shown in Figure A.I. 9, with an ideal traction motor, 6.8 kW power is needed to continuously ride at 140 km/h. This power is not sufficient for acceleration and again with an ideal traction motor, 11.8 kW power is required to accelerate up to 100 km/h in 20 seconds. As

mentioned earlier, while determining P_{max} of most passenger cars, acceleration requirement is dominated and CPSR of the selected motor will be a limiting factor. Lower the CPSR, higher the P_{max}. The selected motor CPSR is 1.55, hence, 20.1 kW power is needed which means 70% overdesign in EV powertrain.

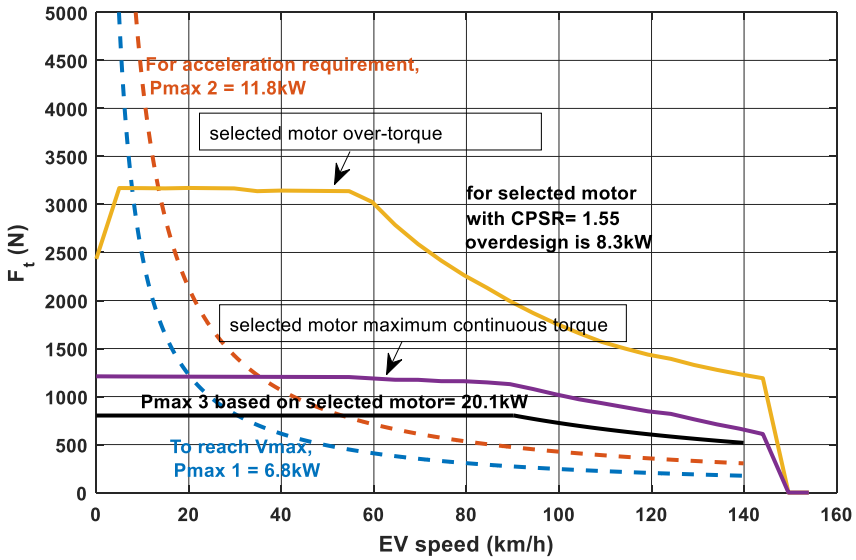

Figure A.I. 9 EV P_{max} at different steps of the proposed algorithm

If, for example, replaced by another motor with higher CPSR equal to 3.64 [153], as shown in Figure A.I. 10, maximum power of EV would be 13.2 kW which is sufficient to accelerate the vehicle and the overdesign will be 13.6% which means 56.4% reduction in batteries weight and inverter rated power. Here, 42.3 kg reduction in mass and 15-liter reduction in volume of the battery pack is expected.

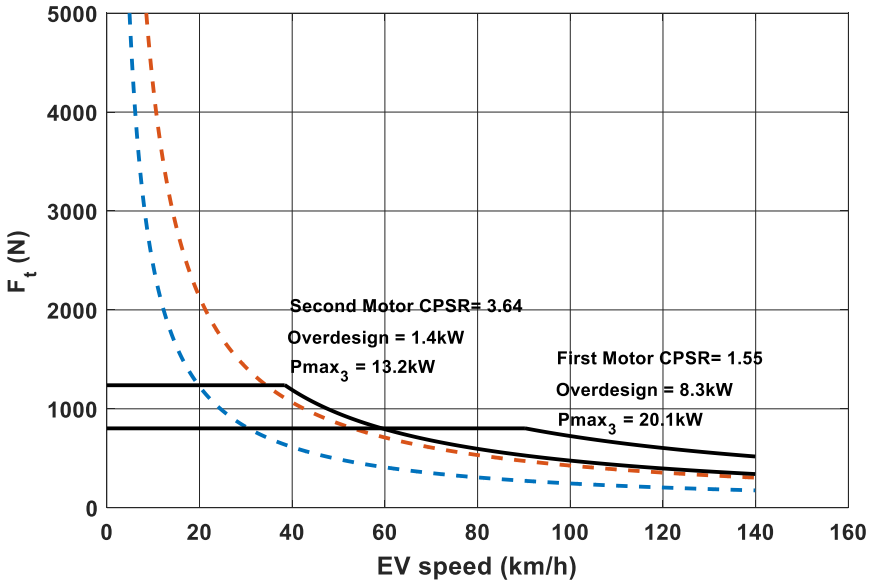

Figure A.I. 10 EV P_{max} reduction due to increase in motor CPSR

Both motors have similar maximum speed which means the increase in CPSR of the new motor has been obtained by extending the constant power area into the constant torque area which increases its maximum torque and will have a negative effect on motor size, efficiency and cost.

To compare the efficiency of two motors over NEDC, an efficiency routine check is required. The first selected motor shows global efficiency of 85% and the proposed one shows 66%. Figure A.I. 11 and Figure A.I. 12 show NEDC operating points over the efficiency map of first and second motor, as well as their over-torque and maximum continuous torque envelopes.

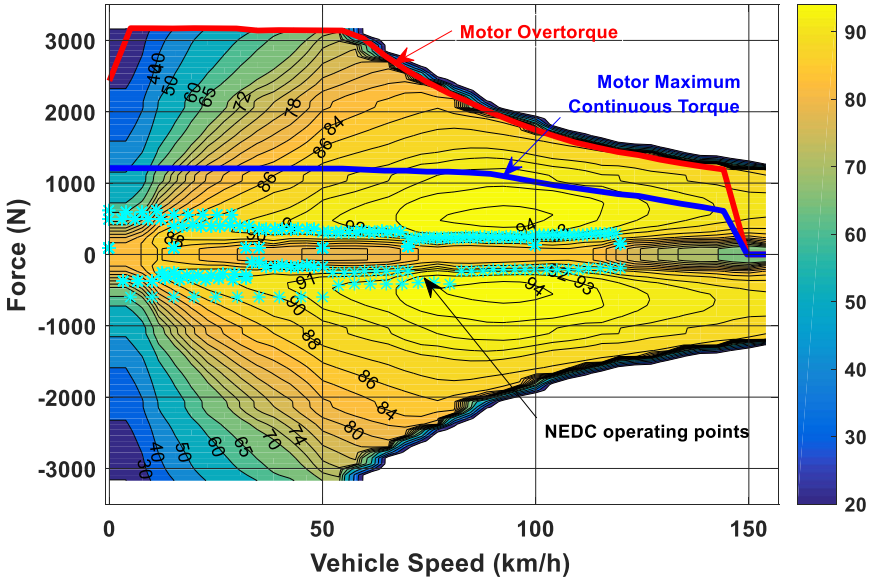

Figure A.I. 11 First motor NEDC operating points on efficiency map

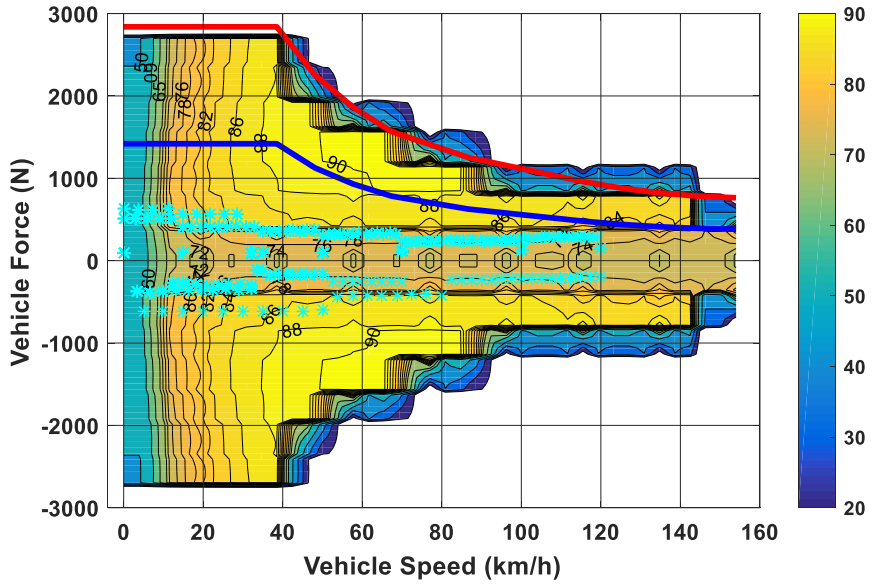

Figure A.I. 12 Second motor NEDC operating points on efficiency map

If USDC is applied, the first motor shows global efficiency of 88% and the proposed motor global efficiency is 75%. It is clear that the new motor has less efficiency compared to the old one. Here, there is a trade-off between efficiency and CPSR. The efficiency of Permanent Magnet Synchronous Motors (PMSMs) is higher where the operating points are under constant torque area, as depicted in Figure A.I. 13, rather than the field weakening area (Figure A.I. 14).

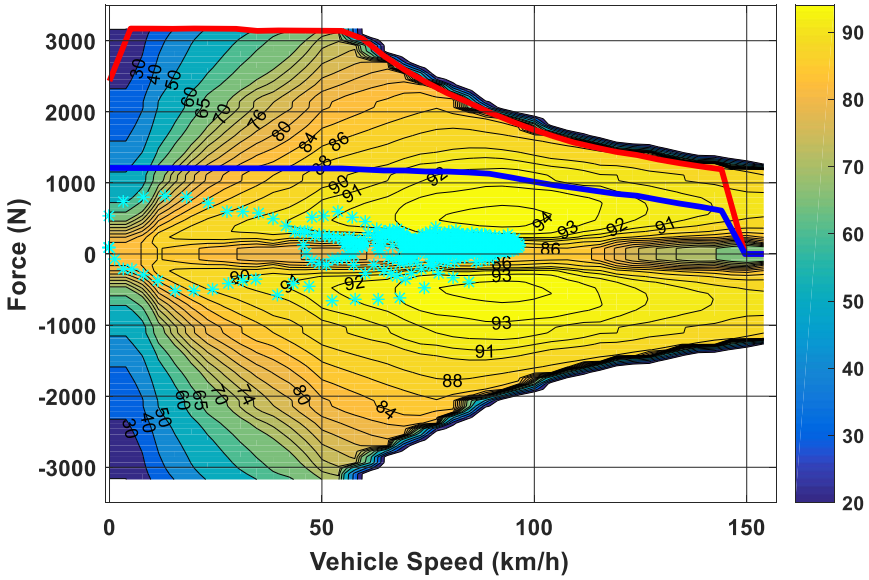

Figure A.I. 13 First motor USDC operating points on efficiency map

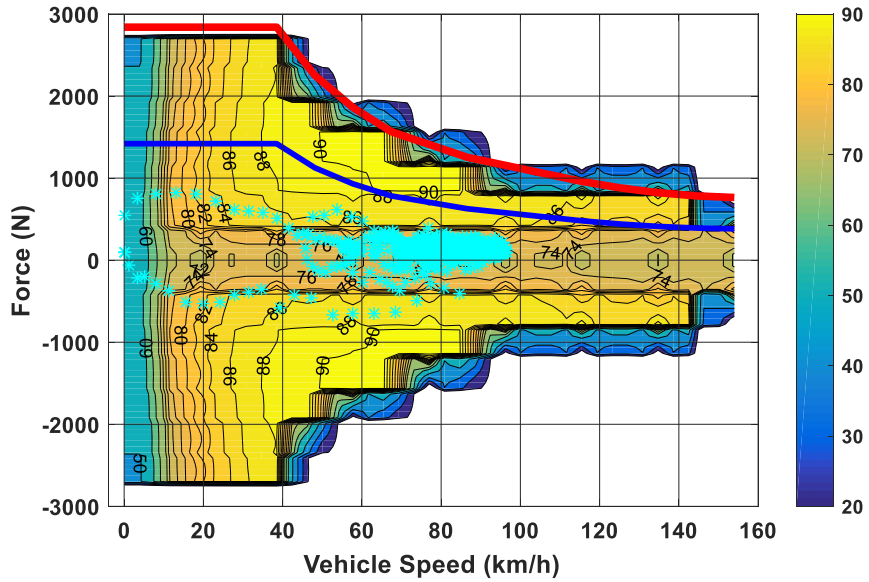

Figure A.I. 14 Second motor USDC operating points on efficiency map

Table A.I. 2 summarizes the results and gives η_{global} for both motors based on the hypothetical weighting factors of the two sample driving cycles (W_{NEDC} and W_{USDC}).

Table A.I. 2 Efficiency results

	η_{NEDC}	η_{USDC}	W_{NEDC}	W_{USDC}	η_{global}
EM1	85%	88%	0.40	0.60	87%
EM2	65%	75%			71%

As it is clear from above table, 16% reduction in global efficiency of the new motor has been occurred. In hybrid energy storage EVs, which is the case with our prototype, supercapacitors will take care of high specific power demands from the system while batteries are responsible for high specific energy demands [154]. To cover the reduction in efficiency in hybrid energy systems, the capacity, size and mass of the batteries should be increased, if the driving range without refueling is to be maintained. Despite the negative effect of motor global efficiency reduction on mass and available space in EV, still, 40% reduction in size and mass of batteries will happen due to overdesign removal.

Owing to considerable reduction in EV's mass, the new mass value is to be iteratively used in the algorithm to have more accurate results.

Conclusion

The purpose here was providing a tool to evaluate selected motor impact on reduction of EV mass. Most of the mass reduction lies under the reduction in batteries due to removing part of the EV overdesign. While determining EV power envelope, if acceleration criteria is dominated, EMs with higher CPSRs will cause lower overdesigned EVs. Another way to decrease the batteries volume and mass is to increase the global efficiency over selected driving cycles. The reduced mass, itself, would have a positive effect on EV cost and performance, or it could be used to increase the driving range or have more cargo space. Having a motor with high maximum speed, high CPSR, and at the same time high efficiency, will give the designer of EV another angle of freedom to have an optimized design.

With recent progresses in design and control of field weakening performance, and considering its outstanding torque and efficiency at low speeds, PMSMs would be more promising for future developments. High and ultra-high speed motors with enhanced performance over field weakening operation area, will be our future research field for traction motors.

Appendix II. Comparison of Modeling Techniques for Electric Machines

Original Title:
A Comparison of Different Models for Permanent Magnet Synchronous Machines: Finite Element Analysis, D-Q Lumped Parameter Modelling, and Magnetic Equivalent Circuit

Authors and Affiliations:
- **Ahmad Shah Mohammadi,** Ph.D. student, e-TESC Laboratory, Department of Electrical & Computer Engineering, University of Sherbrooke
- **João Pedro F. Trovão,** Professor, e-TESC Laboratory, Department of Electrical & Computer Engineering, University of Sherbrooke

State: Published - doi: 10.1109/ISIE.2019.8781540

Conference: 28th IEEE International Symposium on Industrial Electronics (ISIE), Vancouver, BC, Canada, (12-14 June 2019), https://ieeexplore.ieee.org/document/8781540

Context of the appendix

During the optimization of HESM, the MEC model was used. However, the selection of this model was conducted through the comparison of different models. Part of our search for the proper model is already made public, which is represented here as our second minor contribution. The motor selected for this analysis, was a PMSM with the stator and rotor configuration similar to those of the selected HESM. The comparison is made between 2D FEA, 2D MEC, and dq equivalent circuit model. Due to overdesigned machine in this paper, the difference between the three approaches was not sufficiently magnified, whereas, for a more volume-constrained design with saturated areas, it was revealed that the dq model fails to predict the correct behavior of the machine. That is why we have selected the MEC as our modelling approach in the HESM optimization.

Abstract

In the optimization of Electric Vehicle (EV), the motor-drive can be modeled and analyzed in several ways. Depending on the selected analysis technique, the optimization time and its accuracy of results could vary a lot. This paper examines three different techniques, namely, Finite Element Analysis (FEA), D-Q lumped parameter Equivalent Circuit (DQEC), and 2D Magnetic Equivalent Circuit (MEC), for Permanent Magnet Synchronous Machine (PMSM). For this purpose, an efficiency map is constructed for the motor using each technique. The FEA is set as baseline, and the two other techniques are compared to it. The output power, losses, and efficiency are calculated at the whole torque-speed range of the motor. A comparison is driven to highlight the advantages and disadvantages, limitations, and applicability of each method.

Introduction

Electric Vehicle (EV) is one of the solutions to the energy crisis and CO_2 emission problem in the transportation sector. However, they suffer from high initial cost, range anxiety, long charging times, limited cargo and passenger spaces, and slow acceleration [10]. In this regard, much attention should be given to the design and simulation of EV drivetrain. Among others, the traction motor is one of the most crucial components that plays a decisive role on the performance and cost of EV [155]. That is the motivation to a noticeable amount of research dedicated to the design and optimization of both EV and traction motors [156]. Integration of the traction motor design optimization, with the EV system-level design optimization program, is a vital task [156].

For design and simulation of an EV, simplified and general model for each of components, such as, batteries, inverter, motor, etc. is demanded. However, the amount of simplification has certain effects on the reliability of EV optimization results. A new research interest has been emerged to find the optimal design of each component based on their effect on some global variables, such as efficiency, cost, performance, and so on [157]. In these techniques, the component model cannot be a simple global model; instead, a more detailed model is called for. These models are used to find the optimum design for each component over several selected driving cycles [20]. In this regard, the efficiency of each component should be calculated for many times at various operating points. That is why the selected modeling technique will have a trivial effect on the time of optimization, as well as, its accuracy of results.

The model used for the traction motor analysis should correctly predict the behavior of motor over a vast range of torque-speed combinations. As for the construction of efficiency map for a motor all possible operating points of the motor are scanned, it is a suitable measure concerning the validity of analysis. So, if the efficiency maps are constructed and compared to each other using different modeling techniques, one can say that the reliability of comparison is guaranteed. Efficiency map of motor-drive is already used in the EV performance studies, such as in Advanced Vehicle Simulator in MATLAB/Simulink™ and the Energy Macroscopic Representation (EMR) approach [11]. As it incorporated the control signals, inverter, and motor in one block, it leads to easy and fast computation of efficiency of vehicle. Putting the operating points of the motor-drive over the efficiency map helps to graphically discern the lossy operating

regions in the driving cycle [158]. If the objective is to study the EV efficiency, researchers have shown that a static model (efficiency map) with a precise loss-table is enough [159]. The changes in the motor efficiency map as a function of changes in the motor design variables could be subsequently under interest.

There are three different techniques to model an electric motor, and thereafter study its efficiency before the prototyping. These methods are: Finite Element Analysis (FEA), DQ Equivalent Circuit (DQEC), and Magnetic Equivalent Circuit (MEC). FEA analysis is very accurate, but it takes lots of time and resources. FEA can be applied for optimization over one or couple of operating points; however, it is not applicable for global efficiency optimization over a driving cycle. DQEC is very fast, however, its accuracy is not guaranteed at all operating points. In addition, it does not take into account several effects such as saturation in the magnetic material, magnetic cross-coupling between the d- and q-axis, and inductance variations with load condition [160]. Other researchers have adjusted the DQEC to incorporate the nonlinearities in the model and to increase its accuracy [161], [162]. A saturated flux-linkage and loss model for efficiency map calculation is presented in [163], [164]. Being semi-analytical semi-numerical, the MEC can make a trade-off between the time and accuracy. Depending on the network mesh size and the error limits, the conversion time and the accuracy of the results can be controlled by the user (designer). It can be applied to all kinds of electric machine analysis, and has gained lots of attention and applicability recently in the modeling of electromagnetic devices [165], [82].

In this paper, the three techniques are explained, developed, and compared to each other in a common frame. For this purpose, a Permanent Magnet Synchronous Machine (PMSM) is designed and presented0. Then, we will explain the methodology for efficiency map construction by FEA, DQEC, and 2D MEC. Applying these techniques, the efficiency maps are obtained and compared for all operating points of the motor-drive, and the applicability and respective errors for each method is explored. Finally, the conclusion is drawn.

PMSM under study

A non-optimal spoke-type PMSM, which is designed using conventional techniques, is represented in Figure A.II. 1. There are four major parts, namely, stator, rotor, Permanent Magnets (PMs), and armature coils. End-windings effect is neglected in all three methods, in order to reduce the complexity of model and enhance the speed of simulation. The design specifications are given in Table A.II. 1.

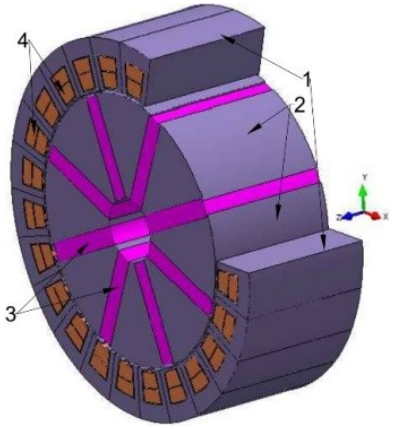

Figure A.II. 1 Designed PMSM (1-stator, 2-rotor, 3-PMs, 4-armature coils)

Table A.II. 1 The PMSM dimensions and materials

Item	Unit	Value
Reduced scale motor power	W	500
Motor base speed	rpm	500
DC bus voltage	V	96
RMS phase current	A	3.96
Armature coil no. of turns	---	26
Motor active length	mm	63
Stator outside radius	mm	87
Airgap thickness	mm	1
PM width (W_{PM})	mm	8.6
Magnet material	---	Ceramic10
Active material	---	M-19 29Ga

Efficiency Map Calculation

To obtain the efficiency at a given torque-speed operating point, one will have to calculate the armature coils currents. In this work, these currents are calculated by an offline Maximum Torque Per Ampere (MTPA) control approach, to produce the desired torque and speed, while keeping the terminal voltage constrained. The MTPA calculates the control currents based on motor D-Q parameters.

A. Efficiency map Calculation by FEA

The PMSM in is modeled and simulated in a FEA software (MagNet Infolytica) to calculate the torque, losses, and efficiency. The torque is between 0.1 to 10 Nm with the steps of 1 Nm. The rotation speed changes from 4.6 to 716 rpm with the steps of 46 rpm. Finally, we have to run the FEA simulation for 137 points, considering only the viable control currents that respect the motor-drive current and voltage limits. Each of these simulations takes about 12 minutes, including the post-processing time to extract the losses and average torque. Concordia and Park

formulas are applied to transform the values from stator 3-phase coordinates to rotor dq (2-phase) coordinates and vice versa, as shown in (AII-1), (AII-2), and (AII-3).

$$K_{32} = \sqrt{\frac{2}{3}} \begin{pmatrix} cos(\theta) & cos(\theta - \frac{2\pi}{3}) & cos(\theta + \frac{2\pi}{3}) \\ -sin(\theta) & -sin(\theta - \frac{2\pi}{3}) & -sin(\theta + \frac{2\pi}{3}) \\ \frac{1}{\sqrt{2}} & \frac{1}{\sqrt{2}} & \frac{1}{\sqrt{2}} \end{pmatrix} \quad \text{(AII-1)}$$

$$X_{dq} = K_{32} \times X_{abc} \quad \text{(AII-2)}$$

$$X_{abc} = {K_{32}}^{T} \times X_{dq} \quad \text{(AII-3)}$$

where, θ is the electrical angle in radians. The FEA configuration is tabulated in Table A.II. 2, and the obtained efficiency map using this technique is represented in Figure A.II. 2. The D-Q model parameters are calculated at nominal speed and torque by the FEA method, as tabulated in Table A.II. 3, in order to be used in the following section.

Table A.II. 2 FEA model configuration

Item	Unit	Value
Maximum element size at airgap	mm	1
Curvature refinement angle at airgap	degree	1
Maximum element size (other)	mm	5
Curvature refinement angle (other)	degree	5
Material type	---	Non-linear
Solving method	---	Newton-Raphson
Solver polynomial order (2D)	---	1
Newton tolerance	%	1
CG tolerance	%	0.01

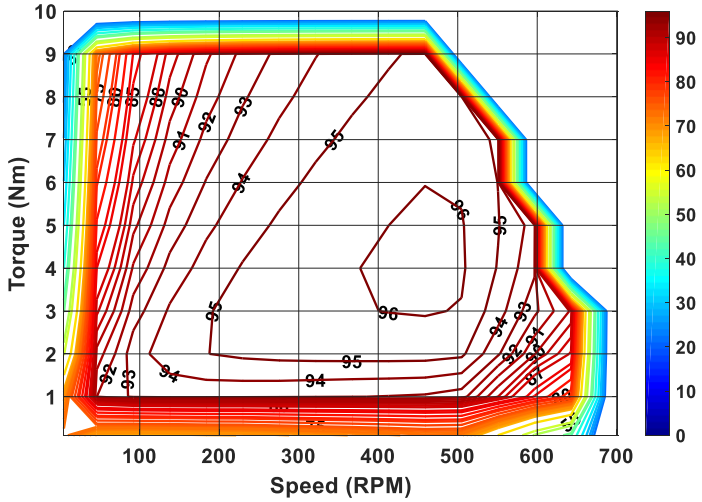

Figure A.II. 2 The PMSM Efficiency map, constructed by FEA

Table A.II. 3 PMSM d-q parameters

Parameter	Unit	Value
L_d, L_q	mH	12.6, 24.3
R_a, R_c	Ω	0.34, 733.48
φ_{PM}	Wb	0.333

B. Efficiency map Calculation by DQEC

Although in experimental motor operation with variable speed drives, several harmonics are produced and observed, yet, the first-harmonic D-Q circuit model is an essential tool for motor analysis and control. It can be used to calculate the voltage and torque. Figure A.II. 3 provides the steady-state loss-model of the motor in D-Q frame, where the losses and magnetic elements are modeled in lumped resistances and inductances. The efficiency of motor is calculated up to the electromechanical average torque (T_{ave}), and mechanical and stray losses are neglected. The D- and Q-axis core loss branch currents and the input currents are calculated from (AII-4) and (AII-5), respectively.

$$I_{qc} = \frac{\omega_e(\varphi_{PM} + I_{dm}L_d)}{R_c} \qquad I_{dc} = -\frac{\omega_e I_{dm} L_d}{R_c} \tag{AII-4}$$

$$I_d = I_{dc} + I_{dm_{23}} \qquad I_q = I_{qc} + I_{qm} \tag{AII-5}$$

As the torque and loss formulas are important for efficiency map construction, the DQEC is solved for these variables. The D-Q magnetizing currents ($I_{dm}$and I_{qm}) are obtained from MTPA control strategy, with which the electromagnetic torque and the output power is calculated in (AII-6) and (AII-7).

$$T = I_{qm}(\varphi_{PM} + (L_{dn} - L_{qn})I_{dm}) \tag{AII-6}$$

$$P_{out} = T \times \omega_m \tag{AII-7}$$

The copper and core losses (P_{cu} and P_c) are obtained from (AII-8) and (AII-9). Having all the losses and output power in hand, the efficiency calculation would be straight forward, as in (AII-10).

$$P_{cu} = R_a\left(I^2{}_d + I^2{}_q\right) \tag{AII-8}$$

$$P_c = R_c\left(I^2{}_{dc} + I^2{}_{qc}\right) \tag{AII-9}$$

$$\eta = \frac{P_{out}}{P_{out} + P_{cu} + P_c} \tag{AII-10}$$

where, ω_m is the mechanical angular speed and η is the efficiency at that speed-torque operating point.

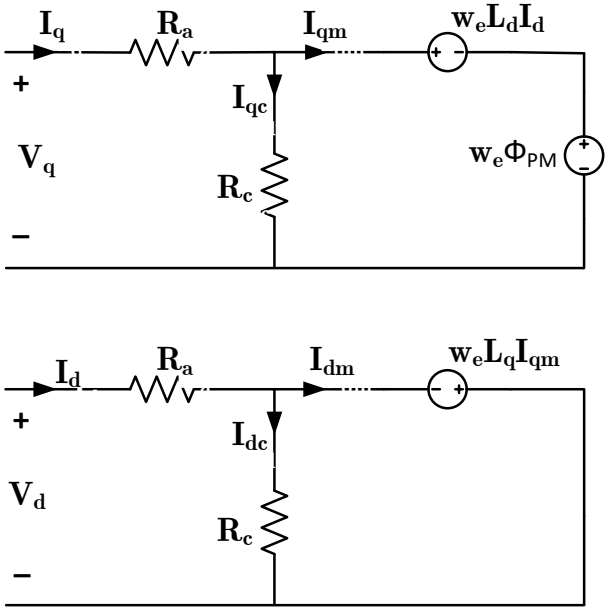

I_d, I_q	D- and Q-axis currents;
I_{dc}, I_{qc}	D- and Q-axis core loss currents;
I_{dm}, I_{qm}	D- and Q-axis magnetizing currents;
R_a R_c	armature and core loss Resistances;
L_d, L_q	D- and Q-axis inductances;
ω_e	electrical angular frequency;

Figure A.II. 3 PMSM first-harmonic steady-state D-Q circuit model

C. Efficiency map Calculation by 2D MEC

To develop and validate the 2D MEC model of PMSM, the approach in [135] is used for our purpose, and the efficiency is calculated based on this model. The development is implemented using a nodal-based analysis of magnetic flux tubes. The PMSM is divided into several meshes, and over the mesh volume, it is assumed that the permeability is constant. However, from one mesh element to another, the permeability changes depending on the value of magnetic field obtained for that mesh element. The motor dimensions and materials, the coils currents, and the rotation speed, are given as inputs to the model. The speed and accuracy of calculations is controlled by adjusting the mesh resolution and error-limits. The airgap mesh is different from that of the stator and rotor and is called remesh region, for which, the meshing is reconstructed at every rotor position. Meshes in stator are constructed only once, whereas, the rotor meshing will require small modifications for each rotor position. The total number of mesh elements in the model at start is 704, however, when the motor rotates, it can go up to 706 mesh elements. Figure A.II. 4 represents the 2D mesh and a generic mesh element for the mesh (i).

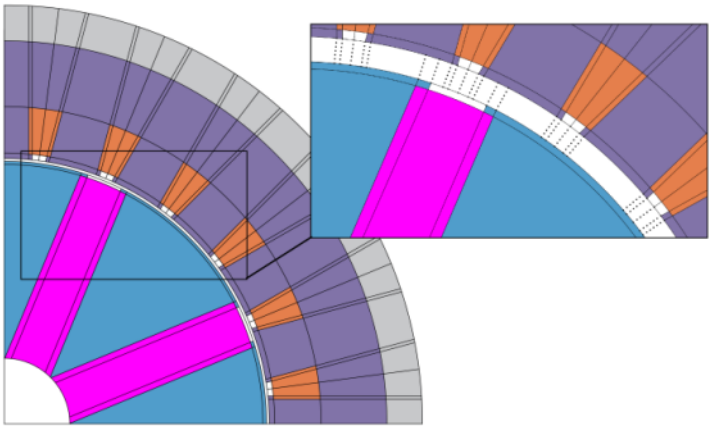

(a)

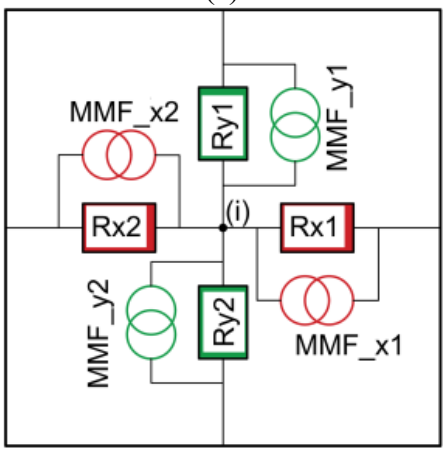

(b)

Figure A.II. 4 (a) Stator, airgap, and rotor mesh (b) a generic mesh element

The developed MEC model takes into account the saturation in the magnetic material. This is made possible by resolving the model with new calculated permeabilities. It starts with a virgin magnetic material and finds the flux density matrix ($\boldsymbol{B}$). With this $\boldsymbol{B}$, the permeability matrix is calculated using the material datasheet. Based on the error between the input permeability and the calculated one, the next permeability matrix is predicted in a way to minimize the error between them. This loop is repeated all over again to constrain the error inside a predefined limit, which is determined by user. Table A.II. 4 represents the configurations for MEC model.

Table A.II. 4 2D MEC model configuration

Item	Value
Total number of elements	704
tolerance for Norm of error in permeability matrix (δ_1)	0.1
tolerance for error in elements of permeability matrix (δ_2)	1E-8

The MEC model is developed, solved, and evaluated by FEA simulation. Flux density at airgap is selected as the primary variable for evaluation. Flux Linkage and no-load back ElectroMotive

Force (EMF) are selected as the post-processed variables to be evaluated. Figure A.II. 5 represents the primary and post-processed variables evaluation.

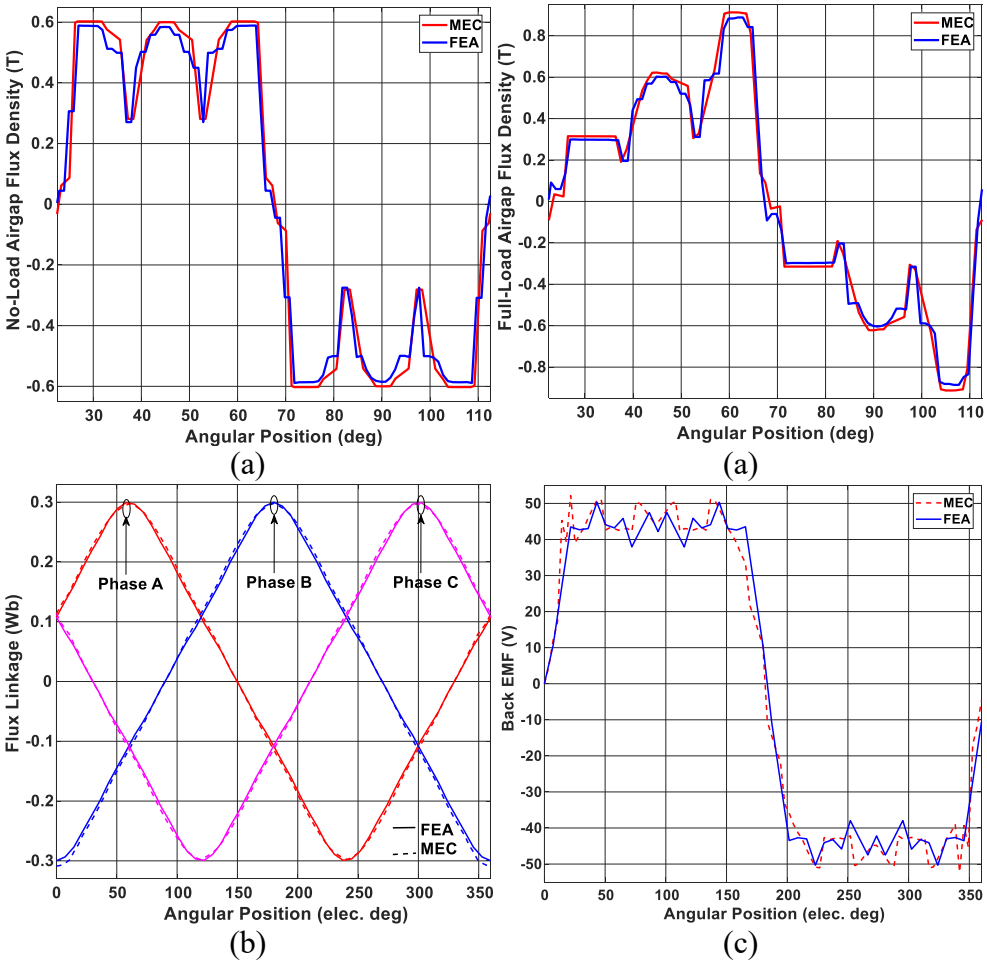

Figure A.II. 5 2D MEC model evaluation: a) flux density, b) flux linkage, and c) no-load back EMF

The average torque (T_{ave}) is calculated based on the famous Flux-MMF diagrams, as is presented in [134] and is formulated in (AII-11).

$$T_{ave} = mp\frac{\Delta W_{co}}{2\pi} \tag{AII-11}$$

where m is the number of phases, p is the number of pole pairs. ΔW_{co} is the amount of co-energy converted per phase over an electrical cycle, and is equal to the surface area constrained by Flux-MMF diagram. Figure A.II. 6 shows the comparison of average torque calculation by MEC and FEA at the nominal current and speed of rotation.

To find the efficiency, it remains only to calculate the losses. The copper loss is calculated from the Ohm's low, for a given current and wire resistance. The core loss calculation is mainly based

on a dynamic core loss model for arbitrary (non-sinusoidal) flux waveforms, presented in [143], and calculated from (AII-12).

$$P_{Fe} = k_h f {B_{pk-pk}}^{\alpha} + \frac{k_e}{2\pi^2 T}\int_0^T \left(\frac{dB}{dt}\right)^2 \quad \text{(AII-12)}$$

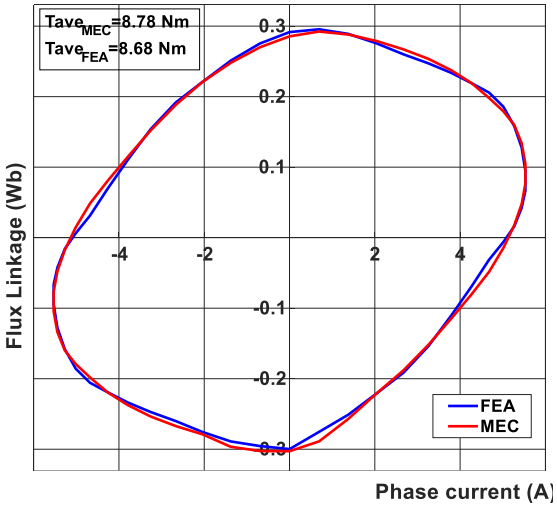

Figure A.II. 6 2D MEC model average torque evaluation

where, k_h and k_e are the coefficients for hysteresis and eddy current losses, respectively. f is the electrical frequency, and B_{pk-pk} is the peak-to-peak value of the flux density over one electrical cycle. Equation (AII-12) is calculated for all mesh elements, and then added to each other to give the total core losses.

Results and Discussions

After applying the above explained methods, the efficiency map for DQEC and MEC is calculated and compared with that of the FEA in Figure A.II. 2. The constructed efficiency maps by the DQEC and MEC techniques are represented in Figure A.II. 7. The error percentage of efficiency map for each method in respect to the baseline method (FEA) is explored in Figure A.II. 8. The norm of the error matrix, e.g. for the MEC efficiency map, is defined as in (AII-13), where, the division is an element-wise division (not a matrix division).

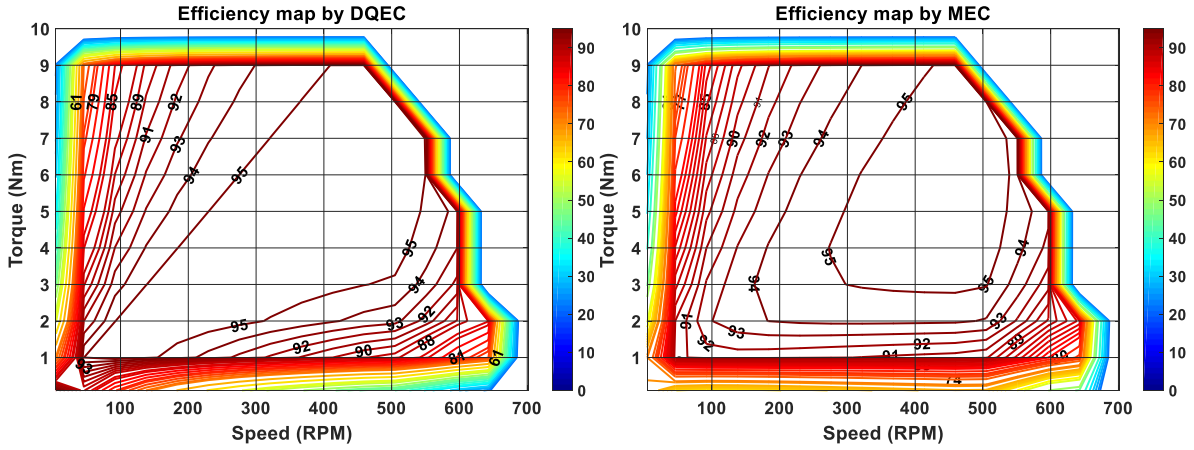

Figure A.II. 7 Efficiency map calculated by a) DQEC and b) MEC

$$\boldsymbol{Norm(E)\%} = \left\| \frac{|\boldsymbol{\eta_{MEC}} - \boldsymbol{\eta_{FEA}}|}{\boldsymbol{\eta_{FEA}}} \right\|_{\infty} \times \mathbf{100} \qquad \text{(AII-13)}$$

Regarding the efficiency definition in (AII-10), the error could be originated either from the calculation of copper loss, core loss, or output power. As the same speed is provided to all models, the output power error is actually representing the error of torque calculation. The whereabouts of these errors are explored in Figure A.II. 9. The narrow bars represent the error percentage from DQEC, and the wide bars represent the error from MEC. The values for the norm of error matrix are also reported in Table A.II. 5.

A summary of conclusions from comparing the results is as follows:

1) Errors are bigger in low-power regions (either in low-torque, or low-speed): The efficiency at low power is small, because the output power is not fully developed and the losses are from comparable sizes. This low efficiency will introduce big errors in the calculations, as in (AII-13), the denominator of formula is small at low-power. This can be seen all over the Figure A.II. 8 and Figure A.II. 9, including the error in core loss calculations.

2) Errors with MEC technique are generally smaller than those with DQEC technique.

3) The error of core loss calculation is big: As the absolute value of core losses is not comparable to the output power, the big error in core loss calculation will not be reflected in the efficiency map calculation (see Figure A.II. 8). Part of the core loss error is due to the fact that we could not know the core loss formula for non-sinusoidal excitation used by the FEA software, as it was a proprietary algorithm. Anyway, difficulties always exist in the nature of core loss modeling.

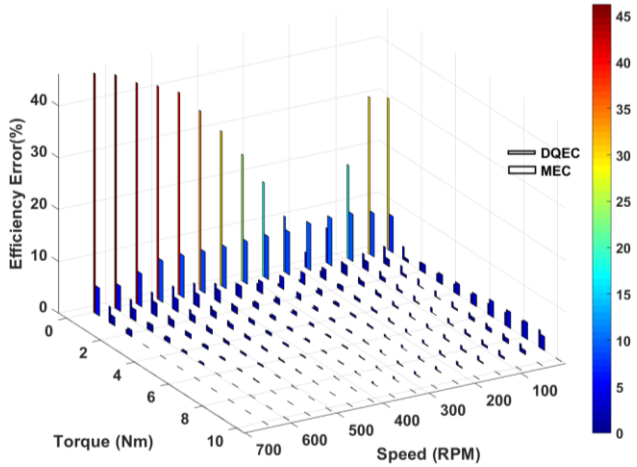

Figure A.II. 8 Efficiency map error for DQEC (narrow bars) and MEC (wide bars) compared to FEA

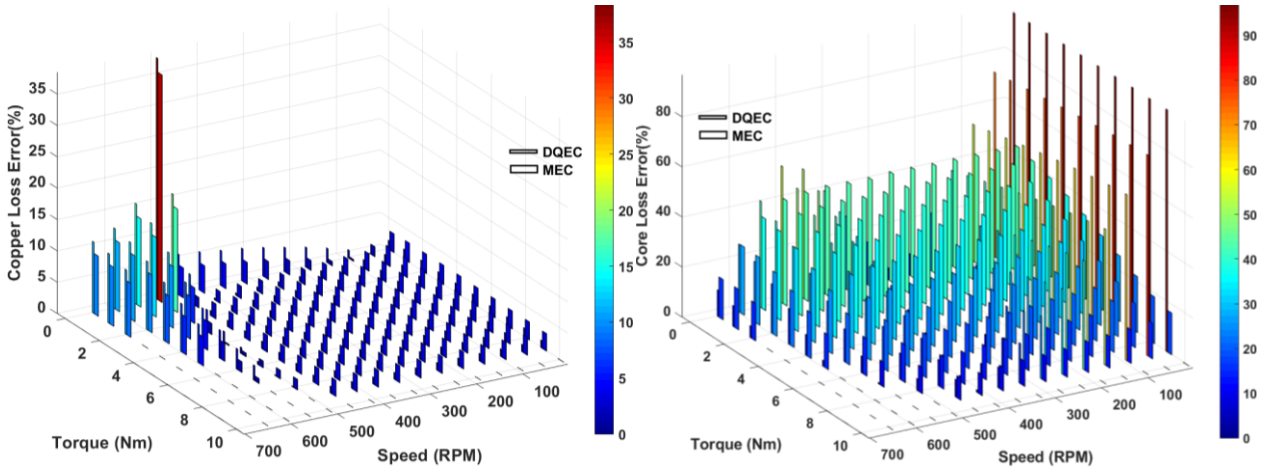

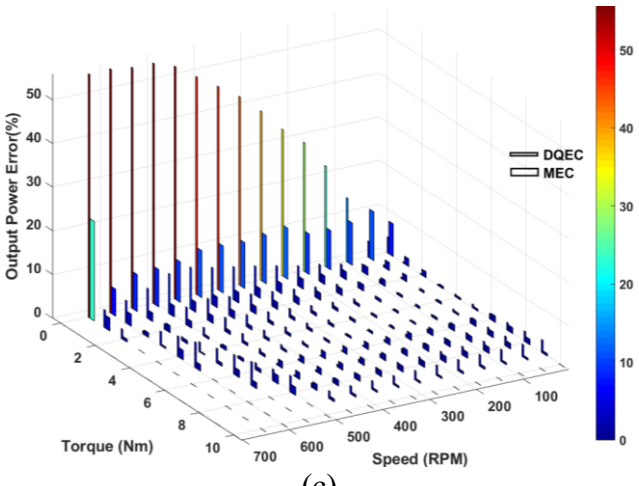

Figure A.II. 9 Error for a) copper loss, b) core loss, and c) output power with DQEC (narrow bars) and MEC approach (wide bars) compared to FEA (reference)

Regarding the above conclusions, one can select which modeling technique is suitable for the application under interest. E.g., if the most frequent operating points of the motor-drive (for a supposed driving cycle) are inside the low-error region, then the optimization is less akin to the selected method. In these cases, one may neglect these errors and select the fastest method. In addition, the accuracy of results are less sensitive to the errors in loss calculation, as long as the losses are small. However, the output power calculation has more impact and its errors cannot be tolerated. The similarity between the error of efficiency map (in Figure A.II. 8) and the error of output power (in Figure A.II. 9(c)), justifies this argument. Table A.II. 6 summarizes some characteristics of the three methods presented in this paper.

Table A.II. 5 Norm of the error matrix

Method	Efficiency	Copper Loss	Core Loss	Output Power
DQEC	1.21	0.58	5.03	1.63
MEC	0.32	0.52	3.48	0.45

Table A.II. 6 FEA, DQEC, and MEC comparison

Item	Unit	FEA	DQEC	MEC
Number of mesh elements	----	12078	----	704
Eff. Map Calc. time	s	94680	0.0186	29713
Norm of error matrix	----	ref.	1.21	0.32
Disk space needed	MB	11400	0.348	3.6

Conclusion

In EV drivetrain optimization, the accuracy and speed of models for motor-drive can be evaluated by efficiency map calculation and comparison for each model. Three methods were fully developed for efficiency map calculation, and were compared to each other over a full range of possible torque-speed combinations. This work underlines the suitability of MEC approach to model the electrical machine in the accurate EV optimization. It shows that the MEC method results more reliable values with the least errors, whereas, DQEC is still a viable solution with a very fast calculation time. Generally, both the DQEC and MEC have less accuracy over the lower-power operating regions. The future work, in this regard, is to develop a hybrid approach from MEC and DQEC, to increase the speed of calculations, while preserving the accuracy of predictions.

Appendix III. Small Scale Prototype Design

Abstract

In this appendix, the maximum absolute ratings for a HESM prototype are found to respond the requirements of an EV in e-TESC lab (Spyder). The full scale motor cannot be realized; instead, these limits are explored and taken into consideration to find the motor maximum absolute values. There are different aspects which limit the power, current, voltage, frequency, dimensions, and other characteristics of the HESM. Most of the limits are coming from the dynamometer and the inverter. At the end, the construction parts and their specifications, dimensions, and materials are reported for the rotor, stator, and outer stator.

Existing PMSM

The existing PMSM for Spyder has been chosen to be our bench mark. As we did not have access neither to the true PMSM data, nor to the target performance specifications of Spyder, a simulation has been performed to make a decision about the nominal values of the system. The input to the simulation is tabulated in Table A.III. 1.

Table A.III. 1 Spyder design specifications

Variable	Value	Units
Vehicle mass	500	kg
rolling resistance coefficient	0.02	--
aerodynamic drag coefficient	0.75	--
Vehicle front area	1.25	m2
Wheels effective radius	0.305	m
Gearbox transmission ratio	5.033	--

For this EV design and considering the existing motor data, the performance envelopes are calculated to match the existing PMSM. Once we launch the simulation, the characteristic and rated envelopes are disclosed. The characteristic envelope is the one related to the EV needs, and the rated envelope is the one that motor can give. From this definition, the rated envelope should be always below the rated envelope, meaning that the motor should be able to respond to EV needs. The nominal values for the existing PMSM are obtained as in Table A.III. 2.

Table A.III. 2 Rated values of the existing PMSM

Variable	Value	Units
Continuous Power ($\boldsymbol{P_{con}}$)	28,273	W
Peak Power ($\boldsymbol{P_{pk}}$)	50,109	W
Base Speed ($\boldsymbol{N_b}$)	4,065	RPM
Max Speed ($\boldsymbol{N_{max}}$)	6,566	RPM

With this motor, the EV possible target performance in permanent regime is calculated and reported in Table A.III. 3.

Table A.III. 3 Spyder expected performance

Variable	Value	Units
Maximum Speed	126.35	km/h
Acceleration Speed	100	km/h
Acceleration Time	7.8	s
Hill angle	5.93	degree
Hill Climbing Speed	98	km/h

As we can see in Figure A.III. 1, the characteristic envelope is very close to the rated envelope. Although the EV rated envelope should be always above its characteristic envelope, still at some speeds the operating points are beyond the rated envelope, and the PMSM operates in a slightly overload condition, e.g. around 85 km/h and 150 km/h. In addition, the simulation has supposed ideal components between the wheels and the motor shaft, such as the gearbox.

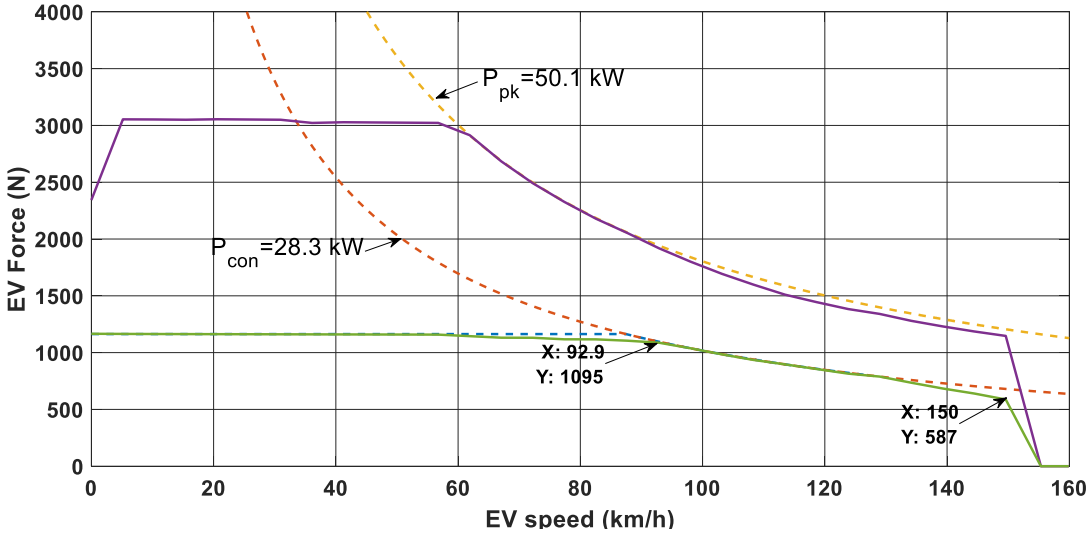

Figure A.III. 1 EV characteristic and rated (PMSM) envelopes for Spyder (dashed lines are the power levels)

Limiting Factors

The final test system is given in Figure A.III. 2. As we can see in this figure, the full-scaled HESM has limits to be realized and to be properly tested by the equipment in the test plan. The limiting factors are coming from the test facilities surrounding the HESM, as follows:

- **Dynamometer**
- **Inverter and Excitation Converter**

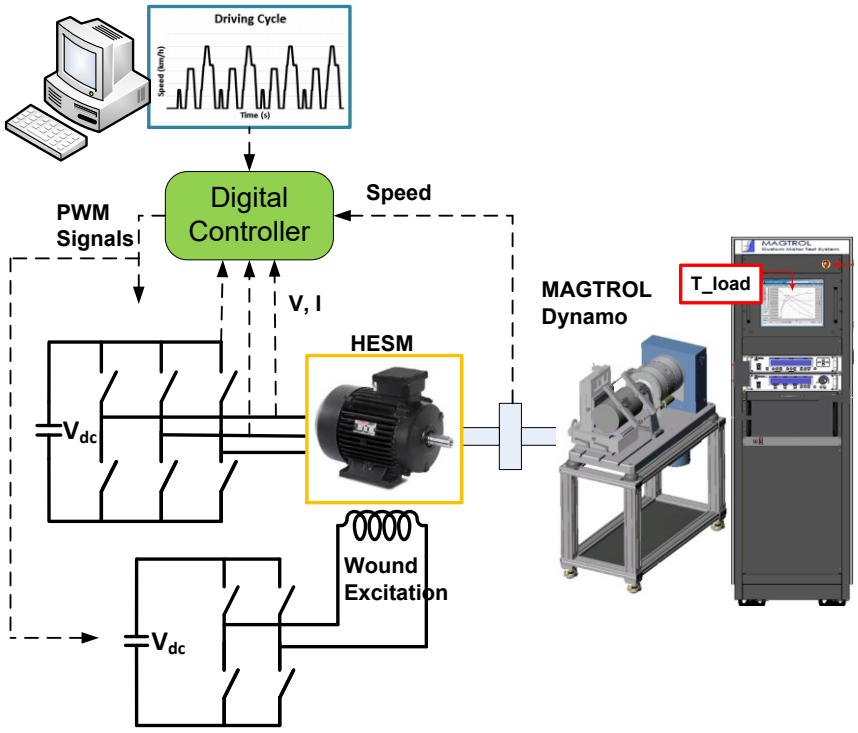

Figure A.III. 2 Test plan for the HESM prototype

In the next section, we will explore the test facility limiting effects, and then we will define down-scaling factors for prototyping the motor.

A. Dynamometer

The dynamometers model existing in e-TESC lab is a **HD-805** from **MAGTROL** Company [166], with a short specification in Table A.III. 4.

Table A.III. 4 MAGTROL dynamometer specifications

Model	Maximum Torque (Nm)	Drag Torque @ 1000 RPM	Nominal Input Inertia		Max. Power Ratings (W)		Max. Speed (RPM)	Brake Cooling Method
			lb·ft·s²	kg·m²	5 minute	4 hours		
HD-805	28	0.14	0.00881	0.0119	5300	3000	12000	Forced Air

The torque-speed envelope of the dynamometer is displayed in Figure A.III. 3. Depending on the selected base speed to test the HESM prototype, the dynamometer can provide certain torque and CPSRs. The continuous power at all conditions cannot be more than 3 kW. The relationships are as (6-1) and (6-2).

$$T_{con} = \frac{P_{con} \times 60}{N_b \times 2\pi} \tag{6-1}$$

$$CPSR = \frac{N_{max}}{N_b} \tag{6-2}$$

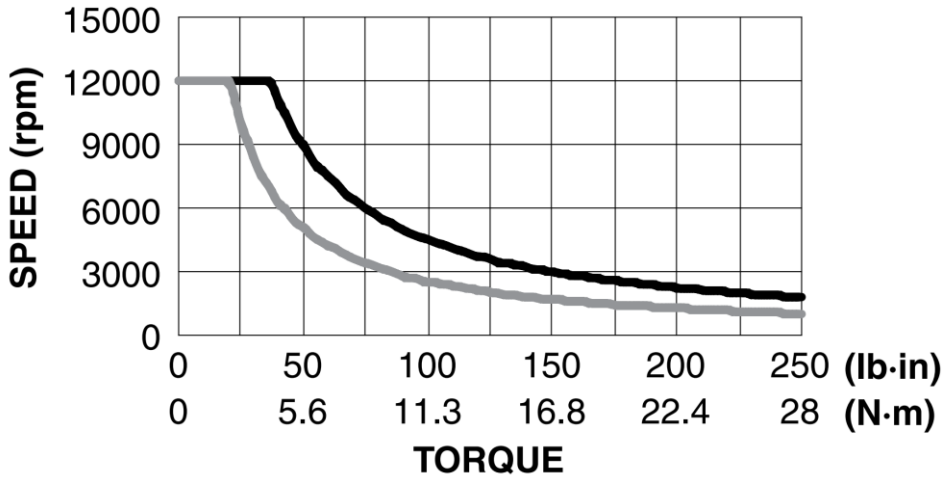

Figure A.III. 3 MAGTROL dynamometer torque-speed envelope (grey: continuous, black: peak)

As we apply the above formulas to the dynamometer envelope, we get the Table A.III. 5. For each row, the maximum continuous power is 3000 W and the maximum speed can reach to 12000 RPM.

Table A.III. 5 dynamometer limits for different base speeds

N_b (RPM)	T_{con} (Nm)	CPSR
1000	28.65	12.00
1500	19.10	8.00
2000	**14.32**	**6.00**
2500	11.46	4.80
3000	9.55	4.00
3500	8.19	3.43
4000	**7.16**	**3.00**
4500	6.37	2.67
5000	5.73	2.40
5500	5.21	2.18

If we select the HESM base speed equal to the base speed of current PMSM (N_b = 4065 RPM), we cannot test the flux weakening of the HESM to its full capacity. We expect a CPSR of 4 to 6 for our HESM. With N_b = 4065 RPM and CPSR=6, the maximum speed would be out of the dynamometer's range (N_{max} = 6×4065 = 24390 RPM). As a result, we select N_b = 2000 RPM, and N_{max} = 12000 to test the CPSR of 6. We can have up to 14.32 Nm of continuous torque at this condition, as is summed up in Table A.III. 6.

Table A.III. 6 dynamometer-limited motor absolute maximum ratings

P_{pk} (W)	P_{con} (W)	N_b (RPM)	N_{max} (RPM)	T_{con} (Nm)	CPSR
5300	3000	2000	12000	14.32	6

B. Inverter and excitation converter

For the inverter and excitation converter, we are going to use a SEMIKRON stack with the code Semikron08753450BB [167]. The specifications of this hardware are tabulated in Table A.III. 7.

Table A.III. 7 Inverter and excitation converter rated values

Circuit	Irms (A)	Ipk (A) @ 80 C	Vac / Vdc (max)	Types
B6CI	30	45	440 / 750	SEMITEACH - IGBT

On the other hand, the DC bus voltage is selected to be the same as the existing Spyder specifications. Table A.III. 8 tabulates the specification of the DC bus.

Table A.III. 8 DC bus specifications

Voltage Levels	DC bus voltage (V)
Nominal	96
Maximum	109
Minimum	83

For the peak and continuous power levels of the dynamometer (3000W and 5300 W, respectively) and supposing 90% of minimum efficiency, the nominal and peak current values that are expected from the inverter are as Table A.III. 9.

Table A.III. 9 Inverter's continuous and peak currents

Current Levels	Con. current (A)	Pk. current (A)
Nominal	34.72	61.34
Maximum	40.16	70.95
Minimum	30.58	54.03

Comparing Table A.III. 7 and Table A.III. 9, the inverter is not capable to benefit from the full capacity of the dynamometer. As a result, we have to limit the motor continuous and peak current to the inverter current levels, which is 30A and 45A, respectively. From the inverter current limit, the motor output specifications would be as Table A.III. 10 (with 90% total efficiency and minimum DC bus voltage).

Table A.III. 10 Inverter-limited motor absolute maximum ratings

$\boldsymbol{P_{pk}}$ (W)	$\boldsymbol{P_{con}}$ (W)	$\boldsymbol{N_b}$ (RPM)	$\boldsymbol{N_{max}}$ (RPM)	$\boldsymbol{T_{con}}$ (Nm)	$\boldsymbol{T_{pk}}$ (Nm)
3361	2241	2000	12000	11.55	17.33

In terms of switching frequency, we can use the equation (6-3).

$$f_{sw} \geq 10p(N_{max}/60) \tag{6-3}$$

Considering the selected topology of our HESM, the number of pair poles (p) is 4, which demands a switching frequency bigger than 8 kHz. Higher frequencies are preferable in terms of passive devices dimensions (inductors and capacitors of input and output filters) and dynamics of the controller, but limited to the switching losses. IGBT's maximum switching frequency is proportional with the on and off energies, the switching frequency, and the cooling system. With the current Semikron08753450BB, we expect the switching frequencies up to 20 kHz, something which is tested in the laboratory.

Scaled-Down HESM

Considering the above section about the reference PMSM and the limits of test facilities, the final absolute ratings of the HESM prototype are rounded down in Table A.III. 11 with enough safety factor.

Table A.III. 11 final HESM absolute maximum ratings

	P_{pk} (W)	P_{con} (W)	N_b (RPM)	N_{max} (RPM)	T_{con} (Nm)	T_{pk} (Nm)
Reference PMSM	50,109	28,273	4,000	6,566	71	185
Scaled-down HESM	3000	2000	2000	10000	9.5	16.7

Construction of the Prototype

A. General Specifications

The dimensions and specification of the optimal HESM prototype are reported in Table A.III. 12. The symbols' signification is represented in the general, as well as, the side views of the motor (see Figure A.III. 4 and Figure A.III. 5).

Table A.III. 12 Optimized HESM design

Variable	Unit	VALUE
HR_{opti}	---	0.8
Number of phases	---	3
Number of pole pairs	---	4
Number of slot/pole/phase	---	1
Nominal phase to neutral voltage (rms)	V	31.6
Nominal phase current (rms)	A	23
Excitation coil no. of turns (N_{exc})	---	138
Armature coil no. of turns (N_s)	---	2
Stator stack active length (l_s)	mm	115.6
Stator stack lamination length (l_{s-lam})	mm	122.1
Total motor length (l_{tot})	mm	192.2
Total motor length with lamination stacking effect	mm	198.7
Excitation coil slot width (W_{exc})	mm	23
Outer stator end cap length (l_{ssi})	mm	15.3
Radial airgap (g)	mm	0.5
Axial airgap (g_{exc})	mm	0.5
Rotor inside radius (R_{ri})	mm	20
PM width (W_{PM})	mm	93.5
PM height (h_{PM})	mm	12.4
Rotor outside radius (R_{ro})	mm	114.5
Stator tooth height (h_{st})	mm	6.4
Stator tooth height (W_t)	mm	21
Stator yoke (h_{sy})	mm	15
Outer stator solid iron height (h_{ssi})	mm	13.8
Total outside radius (R_{tot})	mm	150.2

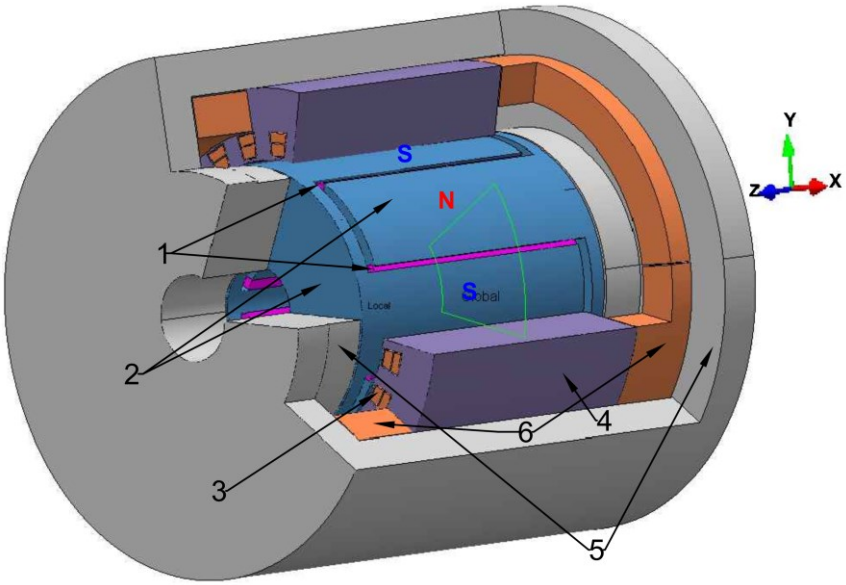

Figure A.III. 4 HESM global view: 1- PMs (ferrite), 2-rotor claws (iron–silicon alloy), 3- stator coils (copper magnetic wire), 4- stator (Fe-Si laminations), 5-outer stator (iron–silicon alloy), 6-WE coils (copper magnetic wire)

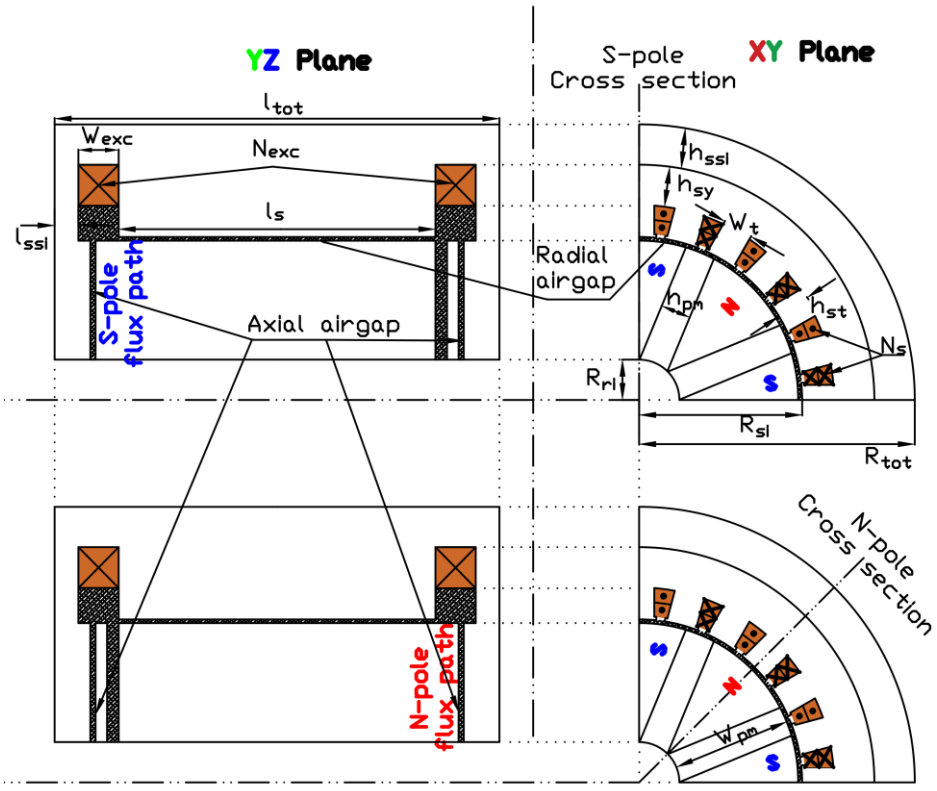

Figure A.III. 5 HESM cross sections of S-pole (top) and N-pole (bottom)

B. Rotor

Active materials:

The rotor consists of two similar claw poles, 8 ferrite PMs, a shaft, and two bearings. The two claw poles are displayed in Figure A.III. 6(a), and the assembly with 8 ferrite PMs is depicted in Figure A.III. 6(b). Detailed dimensional information is plotted in Figure A.III. 7 and Figure A.III. 8. The magnetic material of the rotor is selected from iron–silicon alloys. For instance, VALBRUNA Group produces the ferromagnetic materials for applications requiring higher electrical resistivity, higher permeability, lower coercive force and residual magnetism than provided by either carbon steels or soft magnetic stainless steels. The material selected from their catalogue for our application is called FeSi3P [168]. FeSi3P has an enhanced machining grade. Its Phosphorous and Sulphur contents allow it to overcome the typical machining difficulties of a soft ferritic structure. However, it should be protected after machining by anticorrosion coating or paint. Several properties of FeSi3P are displayed in Table A.III. 13.

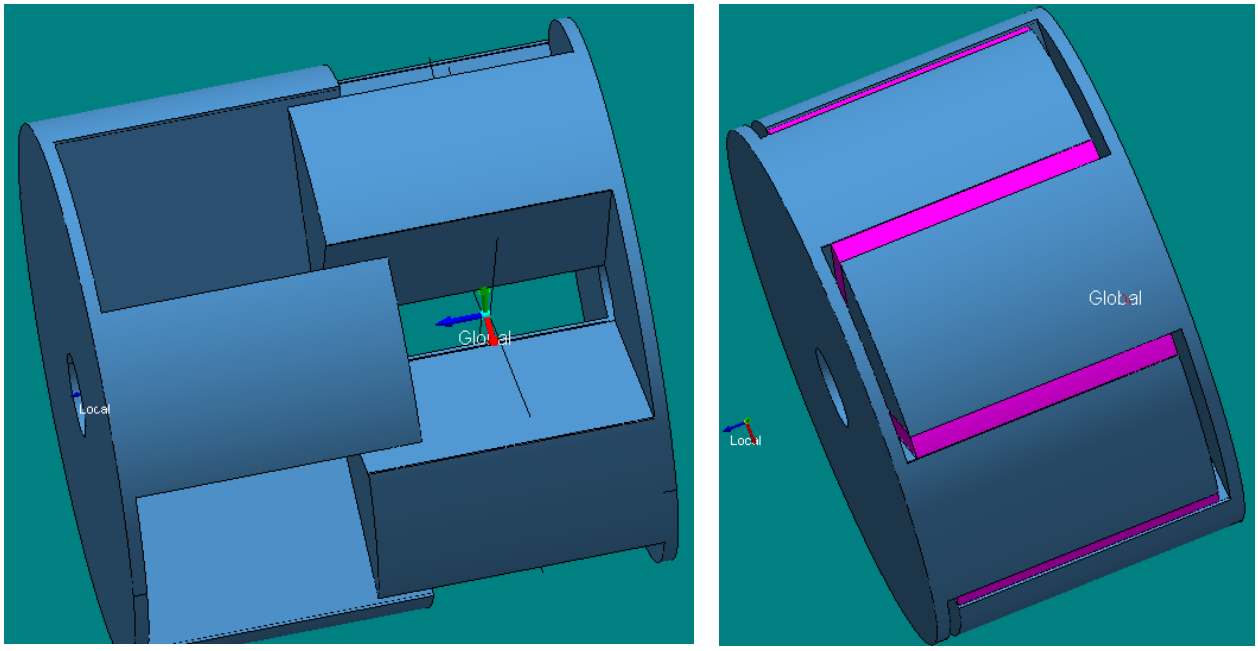

(a) (b)

Figure A.III. 6 HESM rotor (a) sections, (b) assembly with PMs

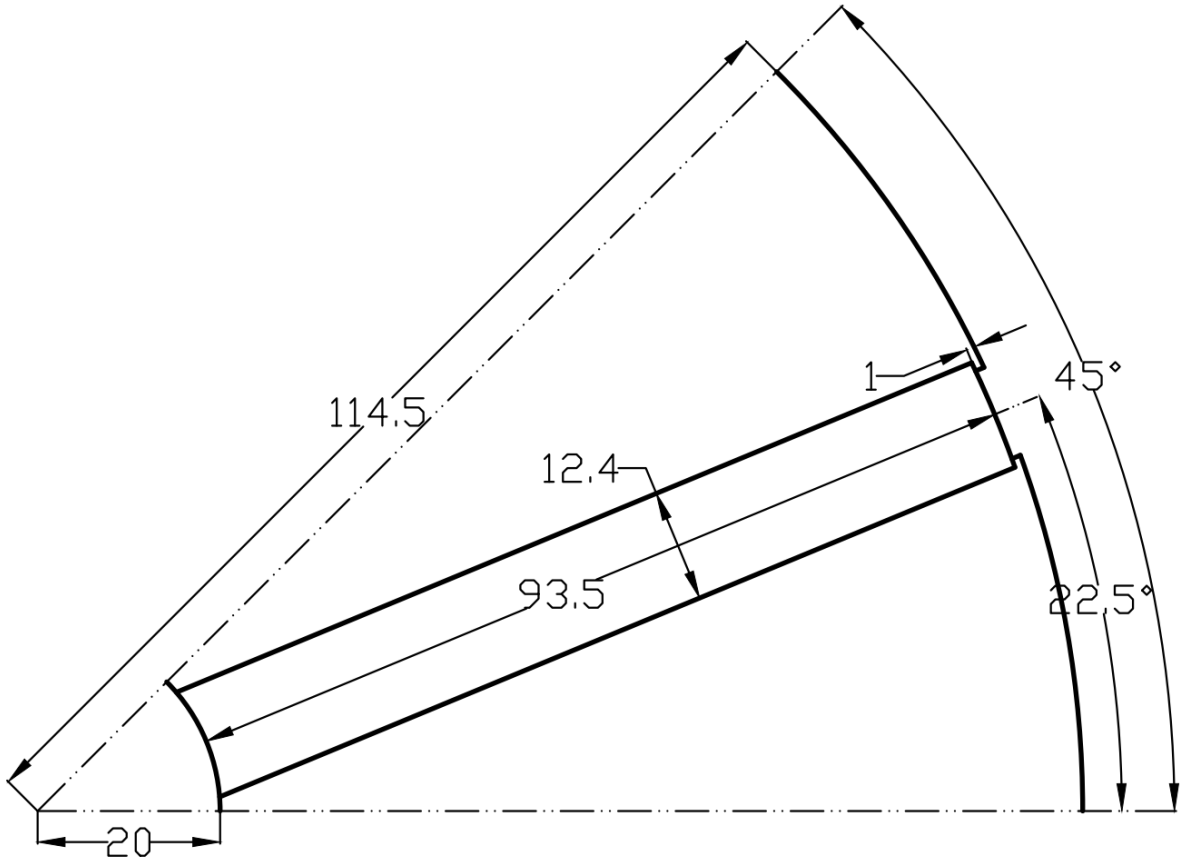

Figure A.III. 7 Rotor construction dimensions at XY plane

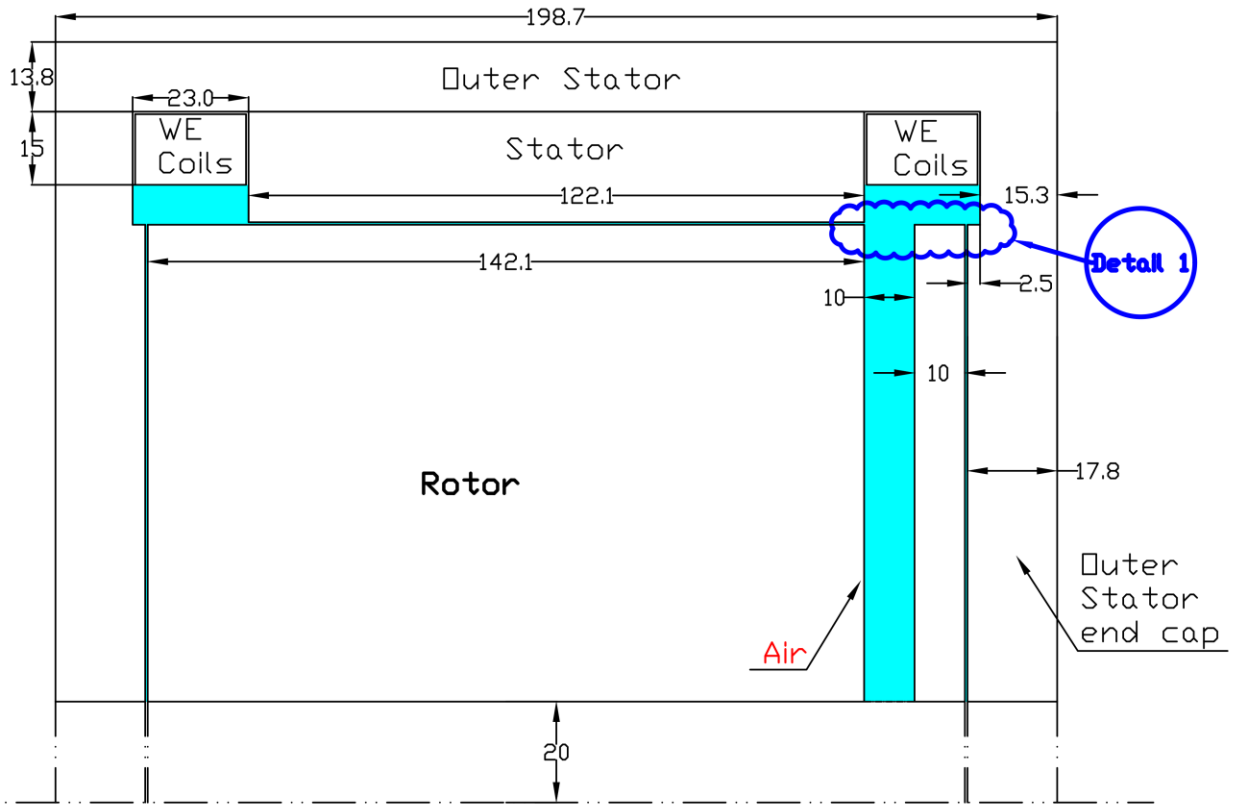

(a)

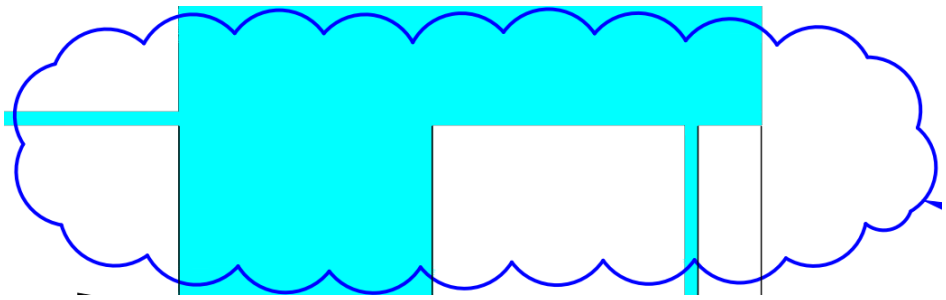

(b)

Figure A.III. 8 Rotor S-pole cross section at YZ plane (a) global view (b) Details 1

Table A.III. 13 Properties of rotor magnetic material: FeSi3P (from VALBRUNA Group)

Property	Value
Equivalent main steel type by silicon content	ASTM A 867 - Type 2F
Magnetic properties	
Saturation flux density, B_{sat} (T)	2.05
Relative magnetic permeability (μ_r)	5027
Coercive field srength, H_c (A/m)	56
Remanent flux density B_r (T)	0.73
Physical properties	
Mass density (kg/m^3)	7650
Resistivity (μΩ-mm)	400
Mean coefficient of thermal expansion for 20˚C-400˚C (10^{-6}/˚C)	13.2
Curie temperature (˚C)	750
Material percentage (C, Mn, Si, Cr, Ni, Mo, P, S)	(0.03, 0.5, 2.75, 0.3, 0.15, 0.05, 0.125, 0.03)%
Mechanical properties	
Ultimate tensile strength (N/mm^2)	719
$R_P0,2^*$	668
Maximum plastic strain, A4 (%)	26
RA** (%)	72
Hardness (Brinell Hardness)	216

* The amount of stress that will result in a plastic strain of 0.2%.
** The ability of the material to deform in a plastic manner without fracturing

Permanent Magnets (PMs):

Ceramic Ferrite PMs are one of the most widely used PM materials in the world. They are termed ceramic due to their excellent electrical insulation ability. At each pole, two Ceramic 10 rectangular block-shaped ferrite PMs are forming N- and S-poles. The closest standard shape is (5×4×0.5 inch), so the customized dimensions (122.1×93.5×12.4 mm or 4.8×3.7×0.5 inch) should be asked from the suppliers. Ferrite PMs are corrosion free and can be used at temperatures up to a maximum of +250˚C (in a few situations perhaps up to +300˚C). The minimum temperature could be as low as -60 ˚C.

Table A.III. 14 Properties of Ferrite PM: Ceramic 10

Property	Value
Naming convention	Magnetic Materials Producers Association (MMPA)
Equivalent type in Chinese standard	Y33H
Remanent flux density B_r at 20˚C (T)	0.4001
Normal coercivity, H_c (kA/m)	280
Intrinsic coercivity, H_c (kA/m)	284
Energy product at 20˚C(kJ/m^3)	30.04
Electrical Resistivity (μΩ-mm)	10^{11}
Thermal conductivity (W/(m.˚C))	2.9
Specific heat (J/(kg. ˚C))	775
Mass density (kg/m^3)	4900
Tensile Strength (N/mm^2)	34
Poisson's Ratio	0.28
Curie temperature (˚C)	450

Shaft:

Shaft material will be the non-magnetic 304 stainless steel (see Table A.III. 15), in order to prevent the short cutting of PM flux.

Table A.III. 15 Properties of shaft material: AISI Type 304 stainless steel

Property	Value
Relative magnetic permeability (μ_r)	1.008
Mass density (kg/m^3)	8030
Resistivity (μΩ-mm)	720
Mean coefficient of thermal expansion for 20˚C-500˚C (10^{-6}/˚C)	18
Material percentage (C, Mn, Si, Fe, Cr, Ni, P, S)	(0.08, 2, 1,70, 19, 9, 0.045, 0.03,)%
Ultimate tensile strength (N/mm^2)	505
Yield Tensile Strength (N/mm^2)	215
Modulus of elasticity (GPa)	197
Poisson's ratio	0.29

Bearings:

The most common bearing system for electric motors uses two deep groove ball bearings. In most cases, power output determines shaft size, and shaft size determines the bore (inside) diameter of the bearings. Although the non-drive end bearings are usually smaller than the drive end bearings, we have selected identical bearings for the prototype to keep it simple.

Motors using frequency converters using pulse width modulation (PWM) require special consideration for bearing selection. Although fast switching devices provide many advantages in motor control, their high $\frac{dv}{dt}$ spikes in inverter-fed machines causes a high frequency common

mode voltage. This voltage supplies the common mode circuit of an electrical machine in which the bearings are a part of. This will often run into problems with electrical erosion within short time of operation. Some solutions, like special shaft coatings or insulated end shields, can be more expensive than using **insulated bearings**. The important parameters to consider when selecting the appropriate bearings for an electric motor or generator are:

- Boundary dimensions
- Magnitude and direction of loads
- Speed: fixed, variable, or high
- Shaft and housing materials
- Coupling: belt or gear drive
- Horizontal or vertical mounting
- Environment
- Vibration level
- Noise level
- Temperature
- Required bearing life
- Lubrication: grease versus oil
- Maintenance
- Sealing: integral and/or external

Considering the parameters of our HESM and using the online selection tool from SKF hybrid (insulated) bearings [169], a SKF product with the code 6008-2RZTN9/HC5C3WT is selected, which has the dimensions and specifications according to Figure A.III. 9 and Table A.III. 16.

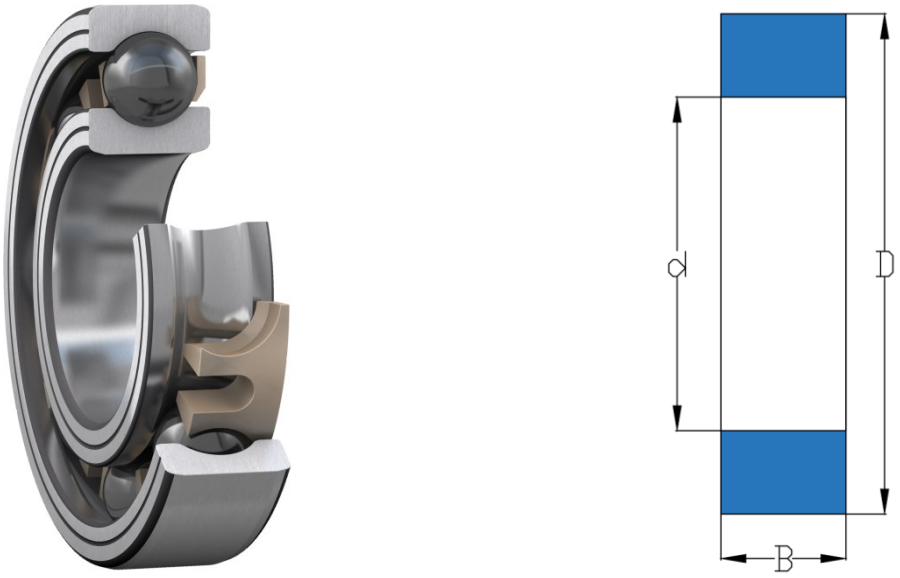

Figure A.III. 9 Hybrid deep groove ball bearing (a) global view (b) side view

Table A.III. 16 Bearing specifications for 6008-2RZTN9/HC5C3WT

Property	Value
Bore diameter, d (mm)	40
Outside diameter, D (mm)	68
Width B (mm)	15
Basic dynamic load rating (kN)	16.8
Basic static load rating (kN)	11
Fatigue load limit (kN)	0.355
Reference speed (RPM)	24000
Limiting speed (RPM)	12000
Mass (kg)	0.19

The position measurement will be accomplished by a resolver, which can deliver the rotor absolute angle position. The model and specifications will be according to the resolver selected for GAN-based inverter-controller board, which is under development in e-TESC lab. There are also 6 Hall-effect sensors plus three stator winding temperature sensors which are already selected at the design and development stages of aforementioned board, and will be placed in the stator slots.

C. Stator

Lamination:

The lamination sheet, selected for the construction of stator, is from M-19 (29 gauge) non-oriented fully processed Fe-Si according to American Iron and Steel Institute (AISI) standard. The approximate equivalents in other standards are M270-35A (EN 10106 (1995)), M270-35A5 (IEC 60404-8-4 (1998)), 36F155 (ASTM A677 (1999)), and so on. DI-MAX grades are selected as they have superior permeability at high inductions, low average core loss and good gauge uniformity. In addition, cold finishing plus strip annealing produce a smooth surface and reduce buckles and waves, resulting in excellent flatness and a high stacking factor. A detailed drawing for the laminations cutting is provided in Figure A.III. 10.

Table A.III. 17 Specifications of Stator Fe-Si sheets

Property	Value
Industrial code	M-19 29Ga
Thickness	29 gauge (0.356 mm)
Grade	DI-MAX
Specific loss density @ 1.5 T 50Hz	3.42 W/kg
Construction	cold-rolled
Magnetic direction	non-oriented
Density	7.65 g/cc
Insulation	C-4
Insulation thickness	0.02 mm
Stacking factor	0.947
Length of the packet	122.1 mm
Specific Heat	490 (J/kg.C)

Magnetic Wire:

The conductor used for the armature windings is a 10 AWG round magnetic wire with copper conductor. It is chosen from the insulation class H, and it should be inverter surge resistant enameled wire (e.g. aromatic polyamide paper-covered wire), such as KMKED-20E (class 0) from Hitachi Metals with 200˚C temperature index [170].

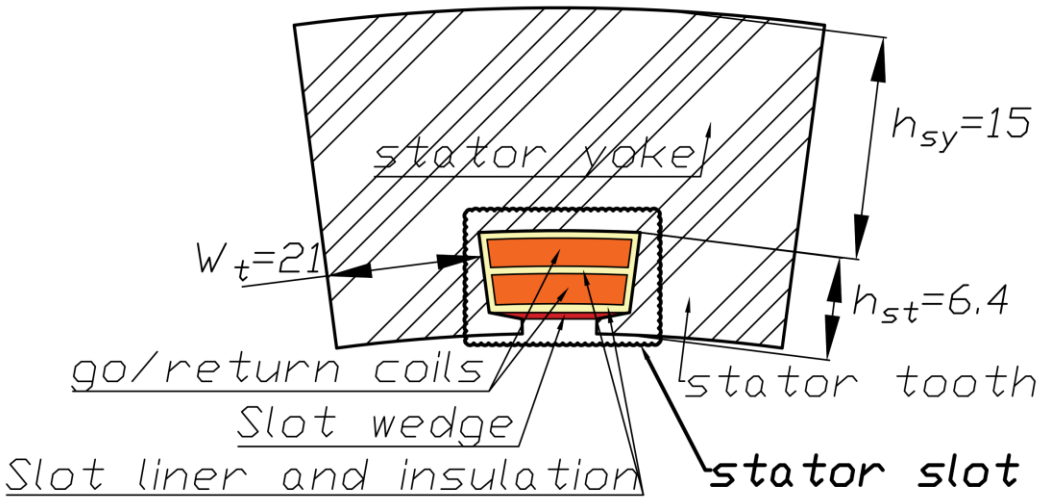

(a)

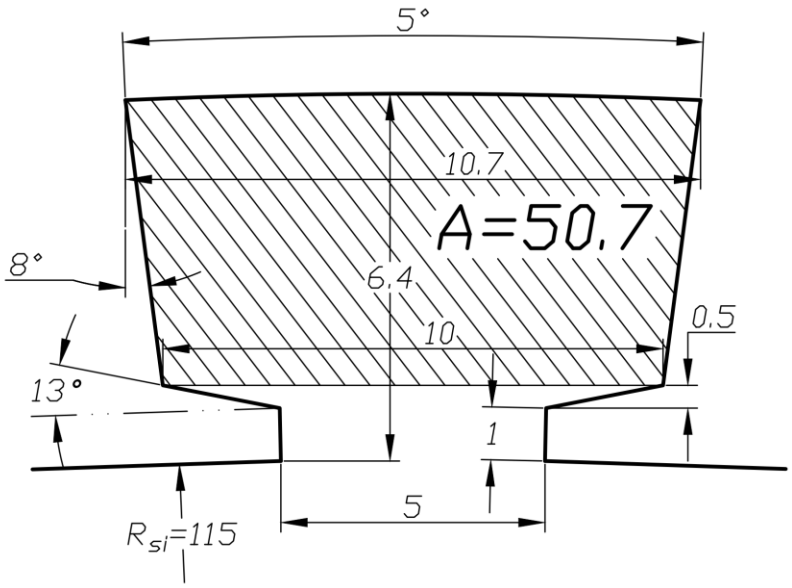

(b)

Figure A.III. 10 lamination drawing details for cutting (a) global view (b) stator slot

Table A.III. 18 Specifications of KMKED-20E magnetic wire

Diameter	Min. film thickness	Max. overall diameter	Estimated mass	Max. resistance 20˚C
2.6 mm	0.049 mm	2.778 mm	47.9 kg/km	3.324 Ω/km

The filling factor considered for the winding is maximum 50% of the slot area, and the maximum current density is meant to be less than 4 A/mm^2. For a nominal phase current of 23A, N_s=2, and two coils in each slot, we can calculate the total current of 92A in each slot. For this

current we need a copper area of $\frac{92}{4}$= 23mm^2 in each slot. Considering a filling factor of 0.5, we need a total slot area of 46 mm2, which is provided by the slot design in Figure A.III. 10. It should be noted that the current density at motor slot can go up to 5 A/mm^2 with natural convection cooling method.

For the WE coils, as we have maximum 3A and N_{exc}=138, for the same filling factor (50%), we need a free area of 207 mm^2 for this purpose. Looking at Figure A.III. 5, the area available in the drawing for the WE is $A_{exc} = W_{exc} \times h_{sy} = 23 \times 15$ =345mm^2, which is more than needed area that will be used for the armature end windings. Figure A.III. 10 displays the stator lamination with the WE coils assembly.

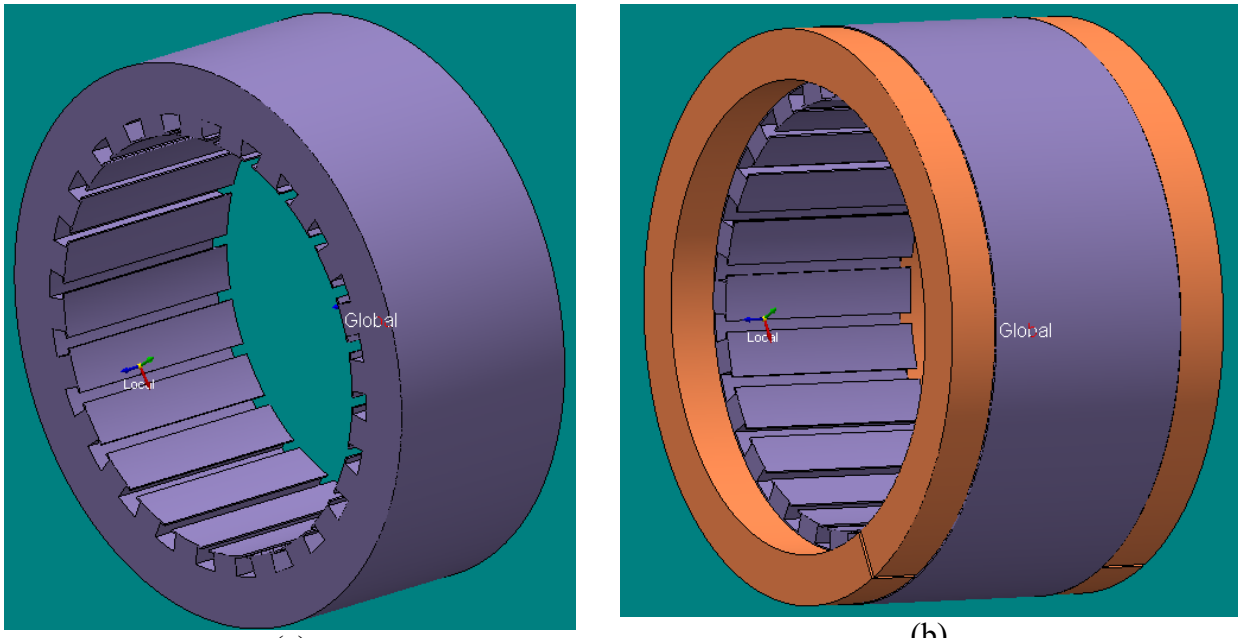

(a) (b)

Figure A.III. 11 HESM stator (a) laminations stack (b) WE coils assembled

Insulation:

For the slot insulation (slot liner, phase insulation, coil separator, and slot wedge), Nomex® papers and Nomex® based laminates are an ideal choice for almost any motor, helping to increase its reliability and service life in harsh operating conditions, such as traction applications. There are three reasons behind its selection, namely, excellent thermal, mechanical, and dielectric performance. Their outstanding dielectric endurance against high $\frac{dv}{dt}$ spikes in inverter-fed machines makes them the first candidate for today electric machine insulation. DuPont has developed specialized Nomex® papers to address this requirement. Other equivalent products to Nomex® 400 series can also be selected according to the availability. The short-term electrical stress withstand should be, at least, 18kV/mm, and it can go up to 34kV/mm. The safe,

permanent operating temperature must be higher than 220˚C, with little or no effect on the electrical and mechanical properties.

B. Outer stator

The material used for the outer stator is the same as the rotor claw pole pieces. The construction slice of the outer stator, plus its end caps is displayed in Figure A.III. 12.

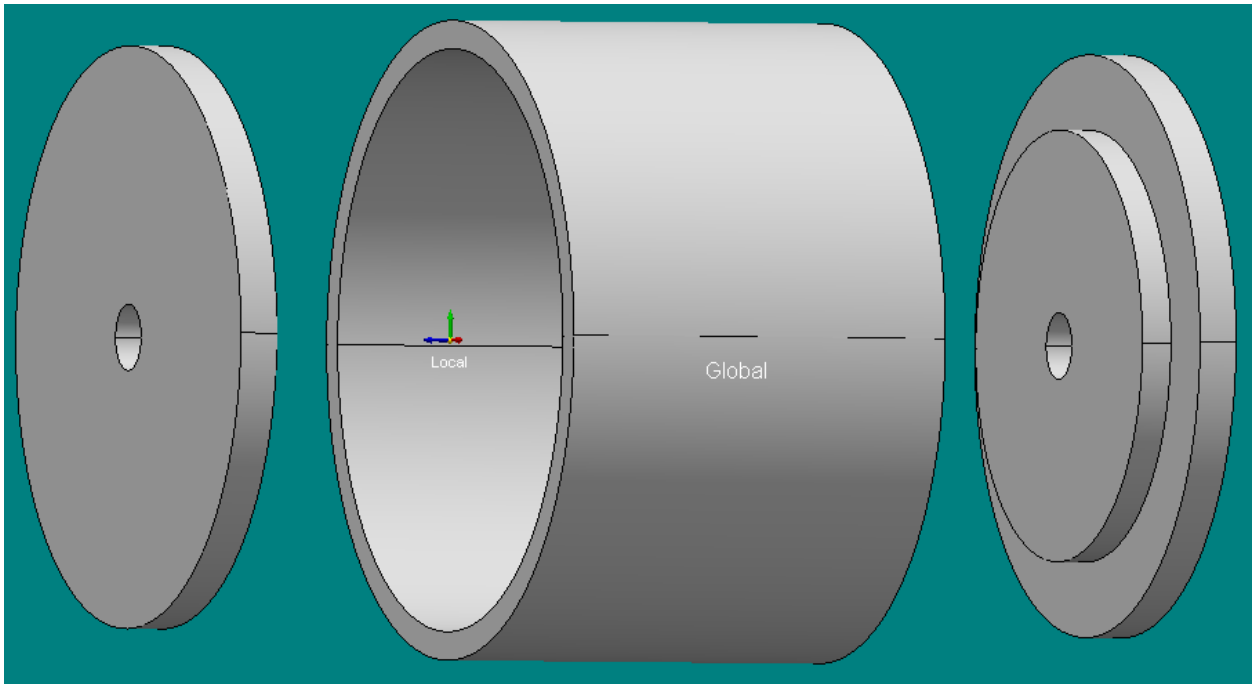

Figure A.III. 12 HESM outer stator

References

[1] C. Le Quéré *et al.*, "Global Carbon Budget 2018," *Earth Syst. Sci. Data*, vol. 10, no. April 2017, pp. 2141–2194, 2018.

[2] "CO_2 and Greenhouse Gas Emissions - Our World in Data." [Online]. Available: https://ourworldindata.org/co2-and-other-greenhouse-gas-emissions. [Accessed: 15-Nov-2019].

[3] National-level US Greenhouse Gas, "Fast Facts 1990–2014," no. April, pp. 2–4, 2016.

[4] M. Ehsani, Y. Gao, and A. Emadi, *Modern electric, hybrid electric, and fuel cell vehicles: fundamentals, theory, and design*. CRC press, 2015.

[5] F. Watson, "December global electric vehicle sales set new record: S&P Global Platts data," *S&P Glob. Platts*, Feb. 2019.

[6] D. W. Bernhart, D. T. Schlick, I. Olschewski, A. Busse, J. Garrelfs, and International Energy Agency, *E-mobility Index Q1 2017*, no. January. IEA Publications, 2017.

[7] "EV Sales: Global Top 20 - December 2018." [Online]. Available: http://ev-sales.blogspot.com/2019/01/global-top-20-december-2018.html. [Accessed: 15-Nov-2019].

[8] Staff, *Global Plug-in Sales for 2017-Q4 and the Full Year (prelim.)*. EVvolumes.com, 2018.

[9] Staff, "Global Plug-in Sales for 2016," *EV-Volumes.com*, 2017.

[10] C. C. Chan, "The state of the art of electric, hybrid, and fuel cell vehicles," *Proc. IEEE*, vol. 95, no. 4, pp. 704–718, 2007.

[11] J. P. F. Trovao and M. R. Dubois, "Energy- and Power-Split Management of Dual Energy Storage System for a Three-Wheel Electric Vehicle," *IEEE Trans. Veh. Technol.*, vol. 66, no. 7, pp. 5540–5550, 2017.

[12] NGUYỄN Bảo-Huy, "Energy management strategies of electric and hybrid vehicles supplied by hybrid energy storage subsystems," Université de Sherbrooke (Canada); Université de Lille (France), 2019.

[13] J. J. Eckert, L. C. A. Silva, E. S. Costa, F. M. Santiciolli, F. G. Dedini, and F. C. Corrêa, "Electric vehicle drivetrain optimisation," *IET Electr. Syst. Transp.*, 2016.

[14] A. S. Mohammadi and J. P. Trovao, "Electric Motors Evaluation Algorithm Based on Their Effect on Electric Vehicle Mass Reduction," in *Vehicle Power and Propulsion Conference (VPPC), 2016 IEEE*, 2016, pp. 1–6.

[15] M. Zeraoulia, M. E. H. Benbouzid, and D. Diallo, "Electric Motor Drive Selection Issues for HEV Propulsion Systems: A Comparative Study," *IEEE Trans,Vehicular Technol.*, vol. 55, no. 6, pp. 1756–1764, 2006.

[16] B. M. Nguyen and M. C. Ta, "Phase advance approach to expand the speed range of brushless DC motor," *Proc. Int. Conf. Power Electron. Drive Syst.*, pp. 1255–1262, 2007.

[17] C. Chakraborty, M. C. Ta, T. Uchida, and Y. Hori, "Fast search controllers for efficiency maximization of induction motor drives based on DC link power measurement," *Proc. Power Convers. Conf. 2002, PCC-Osaka 2002*, vol. 2, pp. 402–408, 2002.

[18] G. Pellegrino, A. Vagati, B. Boazzo, and P. Guglielmi, "Comparison of induction and PM synchronous motor drives for EV application including design examples," *IEEE Trans. Ind. Appl.*, vol. 48, no. 6, pp. 2322–2332, 2012.

[19] T. Rahman, R. C. P. Silva, K. Humphries, M. H. Mohammadi, and D. A. Lowther, "Design and optimization of fractional slot concentrated winding permanent magnet machines for class IV electric vehicles," *2016 IEEE Transp. Electrif. Conf. Expo, ITEC 2016*, 2016.

[20] A. Shah Mohammadi, J. P. Trovão, and M. R. Dubois, "Hybridisation ratio for hybrid excitation synchronous motors in electric vehicles with enhanced performance," *IET Electr. Syst. Transp.*, vol. 8, no. 1, pp. 12–19, 2018.

[21] A. S. Mohammadi and J. P. Trovao, "A Comparison of Different Models for Permanent Magnet Synchronous Machines: Finite Element Analysis, D-Q Lumped Parameter Modeling, and Magnetic Equivalent Circuit," *2019 IEEE 28th Int. Symp. Ind. Electron.*, pp. 197–202, 2019.

[22] J. L. K. Jr, "Traction Motor Design Considerations," *A concept Pap. response to FOA #DE-FOA-0000472 entitled 'Rare Earth Altern. Crit. Technol. Energy*, p. 11.

[23] N. Hashemnia and B. Asaei, "Comparative study of using different electric motors in the electric vehicles," *2008 18th Int. Conf. Electr. Mach.*, no. c, pp. 1–5, 2008.

[24] T. Finken, M. Felden, and K. Hameyer, "Comparison and design of different electrical machine types regarding their applicability in hybrid electrical vehicles," *Proc. 2008 Int. Conf. Electr. Mach. ICEM'08*, pp. 1–5, 2008.

[25] X. D. Xue, K. W. E. Cheng, and N. C. Cheung, "Selection of electric motor drives for electric vehicles," *Power Eng. Conf. AUPEC '08. Australas. Univ.*, pp. 1–6, 2008.

[26] K. Kiyota, H. Sugimoto, and A. Chiba, "Comparing electric motors: An analysis using four standard driving schedules," *IEEE Ind. Appl. Mag.*, vol. 20, no. 4, pp. 12–20, 2014.

[27] J. De Santiago *et al.*, "Electrical motor drivelines in commercial all-electric vehicles: A review," *IEEE Trans. Veh. Technol.*, vol. 61, no. 2, pp. 475–484, 2012.

[28] W. L. Soong and N. Ertugrul, "Field-Weakening Performance of Interior Permanent Magnet Motors," vol. 00, no. Im, pp. 1–8, 2002.

[29] K. J. Binns, W. R. Barnard, and M. a Jabbar, "Hybrid permanent-magnet synchronous motors," *Electr. Eng. Proc. Inst.*, vol. 125, no. 3, pp. 203–208, 1978.

[30] A. D. Aliabad and F. Ghoroghchian, "Design and analysis of a two-speed line start synchronous motor: Scheme one," *IEEE Trans. Energy Convers.*, vol. 31, no. 1, pp. 366–372, 2016.

[31] A. Castagnini, T. Kansakangas, J. Kolehmainen, and P. S. Termini, “Analysis of the starting transient of a synchronous reluctance motor for direct-on-line applications,” *Proc. - 2015 IEEE Int. Electr. Mach. Drives Conf. IEMDC 2015*, pp. 121–126, 2016.
[32] T. a. Lipo, “A doubly salient permanent magnet motor capable of field weakening,” *Proc. PESC ’95 - Power Electron. Spec. Conf.*, vol. 1, pp. 565–571, 1995.
[33] E. Sulaiman, T. Kosaka, and N. Matsui, “A novel hybrid excitation flux switching synchronous machine for a high-speed hybrid electric vehicle applications,” *2011 Int. Conf. Electr. Mach. Syst. ICEMS 2011*, pp. 6–11, 2011.
[34] Y. Gao, R. Qu, D. Li, J. Li, and L. Wu, “Design of Three-Phase Flux-Reversal Machines with Fractional-Slot Windings,” *IEEE Trans. Ind. Appl.*, vol. 52, no. 4, pp. 2856–2864, 2016.
[35] Y. Amara, L. Vido, M. Gabsi, E. Hoang, H. A. Ben Ahmed, and M. Lecrivain, “Hybrid excitation synchronous machines: Energy-efficient solution for vehicles propulsion,” *IEEE Trans. Veh. Technol.*, vol. 58, no. 5, pp. 2137–2149, 2009.
[36] W. Geng, Z. Zhang, K. Jiang, and Y. Yan, “A new parallel hybrid excitation machine: Permanent-magnet/variable-reluctance machine with bidirectional field-regulating capability,” *IEEE Trans. Ind. Electron.*, vol. 62, no. 3, pp. 1372–1381, 2015.
[37] V. Ostovic, “Memory motors,” *IEEE Ind. Appl. Mag.*, vol. 9, no. 1, pp. 52–61, 2003.
[38] H. L. and Z. Q. Z. Hui Yang, “Recent Advances in Variable Flux Memory Machines for Traction Applications: A Review,” *Ces Trans. Electr. Mach. Syst.*, vol. 2, no. 1, pp. 34–50, 2018.
[39] A. M. El-Refaie, “Motors/generators for traction/propulsion applications: A review,” *IEEE Veh. Technol. Mag.*, vol. 8, no. 1, pp. 90–99, 2013.
[40] K. T. Chau, C. C. Chan, and C. Liu, “Overview of permanent-magnet brushless drives for electric and hybrid electric vehicles,” *IEEE Trans. Ind. Electron.*, vol. 55, no. 6, pp. 2246–2257, 2008.
[41] Z. Yang, F. Shang, I. P. Brown, and M. Krishnamurthy, “Comparative Study of Interior Permanent Magnet, Induction, and Switched Reluctance Motor Drives for EV and HEV Applications,” *IEEE Trans. Transp. Electrif.*, vol. 1, no. 3, pp. 245–254, 2015.
[42] Y. Liu, Z. Zhang, C. Wang, W. Geng, and H. Wang, “Electromagnetic Performance Analysis of a New Hybrid Excitation Synchronous Machine for Electric Vehicle Applications,” *IEEE Trans. Magn.*, vol. PP, pp. 1–4, 2018.
[43] B. Kou, Y. Jin, H. Zhang, L. Zhang, and H. Zhang, “Analysis and design of hybrid excitation linear eddy current brake,” *IEEE Trans. Energy Convers.*, vol. 29, no. 2, pp. 496–506, 2014.
[44] W. Li, T. W. Ching, and K. T. Chau, “Design and analysis of a new parallel-hybrid-excited linear vernier machine for oceanic wave power generation,” *Appl. Energy*, vol. 208, no. March, pp. 878–888, 2017.
[45] Y. Amara, S. Hlioui, R. Belfkira, G. Barakat, and M. Gabsi, “Comparison of open circuit flux control capability of a series double excitation machine and a parallel double excitation machine,” *IEEE Trans. Veh. Technol.*, vol. 60, no. 9, pp. 4194–4207, 2011.
[46] G. Borocci, F. Giulii Capponi, G. De Donato, and F. Caricchi, “Closed-Loop, Flux-

Weakening Control of Hybrid-Excitation Synchronous Machine Drives," *IEEE Trans. Ind. Appl.*, vol. 53, no. 2, pp. 1116–1126, 2017.

[47] Y. Amara, S. Hlioui, H. Ben Ahmed, and M. Gabsi, "Power Capability of Hybrid Excited Synchronous Motors in Variable Speed Drives Applications," *IEEE Trans. Magn.*, vol. PP, pp. 1–12, 2019.

[48] G. Henneberger, J. R. Hadji-Minaglou, and R. C. Ciorba, "Design and test of permanent magnet synchronous motor with auxiliary excitation winding for electric vehicle application," in *Proc. Eur. Power Electron. Chapter Symp.*, pp. 645–649.

[49] X. Luo and T. A. Lipo, "A synchronous/permanent magnet hybrid AC machine," *IEEE Int. Electr. Mach. Drives Conf. IEMDC 1999 - Proc.*, vol. 15, no. 2, pp. 19–21, 1999.

[50] N. Naoe and T. Fukami, "Trial production of a hybrid excitation type synchronous machine," *IEMDC 2001 - IEEE Int. Electr. Mach. Drives Conf.*, pp. 545–547, 2001.

[51] F. Giulii Capponi, G. De Donato, G. Borocci, and F. Caricchi, "Axial-flux hybrid-excitation synchronous machine: Analysis, design, and experimental evaluation," *IEEE Trans. Ind. Appl.*, vol. 50, no. 5, pp. 3173–3184, 2014.

[52] J. S. Hsu, "Direct control of air-gap flux in permanent-magnet machines," *IEEE Trans. Energy Convers.*, vol. 15, no. 4, pp. 361–365, 2000.

[53] A. Dupas, S. Hlioui, E. Hoang, M. Gabsi, and M. Lecrivain, "Investigation of a New Topology of Hybrid-Excited Flux-Switching Machine with Static Global Winding: Experiments and Modeling," *IEEE Trans. Ind. Appl.*, vol. 52, no. 2, pp. 1413–1421, 2016.

[54] M. M. A. Mazlan, E. Sulaiman, A. Md Zarafi, and S. M. N. S. Othman, "Topologies of single-phase outer-rotor hybrid excitation flux switching motor for in wheel drive applications," *2014 IEEE Conf. Energy Conversion, CENCON 2014*, pp. 112–116, 2014.

[55] E. Hoang, H. Ben Ahmed, and J. Lucidarme, "Switching flux permanent magnet polyphased synchronous machines," *Eur. Conf. power Electron. Appl.*, 1997.

[56] Y. Liao, F. Liang, and T. A. Lipo, "A novel permanent magnet motor with doubly salient structure," *Conf. Rec. - IAS Annu. Meet. (IEEE Ind. Appl. Soc.*, vol. 1992-Janua, pp. 308–314, 1992.

[57] H. J. Kim, D. Y. Kim, J. S. Jeong, and J. P. Hong, "Proposition of structures for brushless hybrid-excitation synchronous motors with improved rotor," *IEEE Trans. Magn.*, vol. 52, no. 9, pp. 1–15, 2016.

[58] J. A. Tapia, F. Leonardi, and T. A. Lipo, "Consequent-pole permanent-magnet machine with extended field-weakening capability," *IEEE Trans. Ind. Appl.*, vol. 39, no. 6, pp. 1704–1709, 2003.

[59] D. Fodorean, A. Djerdir, I. A. Viorel, and A. Miraoui, "A double excited synchronous machine for direct drive application-design and prototype tests," *IEEE Trans. Energy Convers.*, vol. 22, no. 3, pp. 656–665, 2007.

[60] A. D. Akemakou and S. K. Phounsombat, "Electrical machine with double excitation, especially a motor vehicle alternator." Google Patents, 2000.

[61] P. Di Barba, M. Bonislawski, R. Palka, P. Paplicki, and M. Wardach, "Design of Hybrid Excited Synchronous Machine for Electrical Vehicles," *IEEE Trans. Magn.*, vol. 9464, no. c, pp. 1–1, 2015.

[62] F. Leonardi, T. Matsuo, Y. Li, T. A. Lipo, and P. McCleer, "Design considerations and test results for a doubly salient PM motor with flux control," *Ind. Appl. Conf. 1996. Thirty-First IAS Annu. Meet. IAS '96., Conf. Rec. 1996 IEEE*, vol. 1, pp. 458–463 vol.1, 1996.

[63] N. Pothi, Z. Q. Zhu, I. A. A. Afinowi, B. Lee, and Y. Ren, "Control strategy for hybrid-excited switched-flux permanent magnet machines," *IET Electr. Power Appl.*, vol. 9, no. 9, pp. 612–619, 2015.

[64] C. Pollock and M. Brackley, "Comparison of the acoustic noise of a flux-switching and a switched reluctance drive," *IEEE Trans. Ind. Appl.*, vol. 39, no. 3, pp. 826–834, 2003.

[65] W. Hua, P. Su, M. Tong, and J. Meng, "Investigation of a Five-Phase E-Core Hybrid-Excitation Flux-Switching Machine for EV and HEV Applications," *IEEE Trans. Ind. Appl.*, vol. 51, no. 5, pp. 1–1, 2016.

[66] Z. Xu, S. Xie, and P. Mao, "Analytical design of flux-switching hybrid excitation machine by a nonlinear magnetic circuit method," *IEEE Trans. Magn.*, vol. 49, no. 6, pp. 3002–3008, 2013.

[67] S. Hlioui, Y. Amara, E. Hoang, and M. Gabsi, "Overview of hybrid excitation synchronous machines technology," *2013 Int. Conf. Electr. Eng. Softw. Appl. ICEESA 2013*, no. 1, pp. 1–10, 2013.

[68] Y. Amara, S. Hlioui, R. Belfkira, G. Barakat, and M. Gabsi, "Comparison of open circuit flux control capability of a series double excitation machine and a parallel double excitation machine," *IEEE Trans. Veh. Technol.*, vol. 60, no. 9, pp. 4194–4207, 2011.

[69] S. Hlioui, L. Vido, Y. Amara, M. Gabsi, M. Lecrivain, and A. Miraoui, "PM and hybrid excitation synchronous machines: Performances Comparison," *Proc. 2008 Int. Conf. Electr. Mach. ICEM'08*, pp. 1–6, 2008.

[70] K. T. Chau and W. Li, "Overview of Electric and hybrid vehicles," *Int. J. Veh. Des.*, vol. 64, no. 1, pp. 46–71, 2014.

[71] M. Johnson, M. C. Gardner, and H. A. Toliyat, "A Parameterized Linear Magnetic Equivalent Circuit for Analysis and Design of Radial Flux Magnetic Gears - Part I: Implementation," *IEEE Trans. Energy Convers.*, vol. 33, no. 2, pp. 784–791, 2018.

[72] S. Mojlish, N. Erdogan, D. Levine, and A. Davoudi, "Review of Hardware Platforms for Real-Time Simulation of Electric Machines," *IEEE Trans. Transp. Electrif.*, vol. 3, no. 1, pp. 130–146, 2017.

[73] S. Asfirane, S. Hlioui, Y. Amara, and M. Gabsi, "Study of a Hybrid Excitation Synchronous Machine: Modeling and Experimental Validation," *Math. Comput. Appl.*, vol. 24, no. 2, p. 34, 2019.

[74] A. S. Al-Adsani and O. Beik, "Design of a Multiphase Hybrid Permanent Magnet Generator for Series Hybrid EV," *IEEE Trans. Energy Convers.*, vol. 33, no. 3, pp. 1499–1507, 2018.

[75] S. Asfirane, S. Hlioui, Y. Amara, O. La De Barriere, G. Barakat, and M. Gabsi,

"Global Quantities Computation Using Mesh-Based Generated Reluctance Networks," *IEEE Trans. Magn.*, vol. PP, no. 1, pp. 1–4, 2018.

[76] K. Tajima, K. Sato, T. Komukai, and O. Ichinokura, "Reluctance Network Analysis of an Orthogonal-Core Type Parametric Induction Motor," *IEEE Trans. Magn.*, vol. 35, no. 5 PART 2, pp. 3706–3708, 1999.

[77] K. T. Chau, M. Cheng, and C. C. Chan, "Nonlinear magnetic circuit analysis for a novel stator doubly fed doubly salient machine," *IEEE Trans. Magn.*, vol. 38, no. 5 I, pp. 2382–2384, 2002.

[78] H. Polinder, J. G. Slootweg, M. J. Hoeijmakers, and J. C. Compter, "Modelling of a linear PM machine including magnetic saturation and end effects: Maximum force to current ratio," *IEMDC 2003 - IEEE Int. Electr. Mach. Drives Conf.*, vol. 2, no. 6, pp. 805–811, 2003.

[79] B. Bekkouche, A. Chaouch, and Y. Mezari, "A Switched Reluctance Motors Analyse using Permeance Network Method," *Int. J. Appl. Eng. Res.*, vol. 1, no. 2, pp. 137–152, 2006.

[80] K. Nakamura and O. Ichinokura, "Dynamic simulation of PM motor drive system based on reluctance network analysis," *2008 13th Int. Power Electron. Motion Control Conf. EPE-PEMC 2008*, pp. 758–762, 2008.

[81] M. Johnson, M. C. Gardner, and H. A. Toliyat, "A Parameterized Linear Magnetic Equivalent Circuit for Analysis and Design of Radial Flux Magnetic Gears–Part II: Evaluation," *IEEE Trans. Energy Convers.*, vol. 33, no. 2, pp. 784–791, 2018.

[82] J. H. Sim, D. G. Ahn, D. Y. Kim, and J. P. Hong, "Three-Dimensional Equivalent Magnetic Circuit Network Method for Precise and Fast Analysis of PM-Assisted Claw-Pole Synchronous Motor," *IEEE Trans. Ind. Appl.*, vol. 54, no. 1, pp. 160–171, 2018.

[83] "MAGE : Models, Methods and Methodologies Applied to Electrical Engineering - G2ELAB." [Online]. Available: http://www.g2elab.grenoble-inp.fr/en/research/mage. [Accessed: 12-Dec-2019].

[84] H. W. Derbas, J. M. Williams, A. C. Koenig, and S. D. Pekarek, "A comparison of nodal- and mesh-based magnetic equivalent circuit models A Comparison of Nodal- and Mesh-Based Magnetic Equivalent Circuit Models," *IEEE Trans. Energy Convers.*, vol. 24, no. 2, pp. 388–396, 2009.

[85] M. Amrhein and P. T. Krein, "3-D Magnetic equivalent circuit framework for modeling electromechanical devices," *IEEE Trans. Energy Convers.*, vol. 24, no. 2, pp. 397–405, 2009.

[86] T. K. Hoang, L. Vido, F. Gillon, and M. Gabsi, "Structural optimization to maximize the flux control range of a double excitation synchronous machine," *Math. Comput. Simul.*, vol. 158, pp. 235–247, 2019.

[87] H. Trung Kien, "Design Optimization of a Double Excitation Synchronous Machine in Railway Traction," Université Paris-Saclay, et l''École Normale Supérieure de Cachan.

[88] A. Shah Mohammadi and J. P. F. Trovão, "System - level Optimization of Hybrid

Excitation Synchronous Machines for a Three - Wheel Electric Vehicle," *IEEE Trans. Transp. Electrif.*, no. under review, pp. 1–10, 2020.

[89] G. Lei, J. Zhu, Y. Guo, C. Liu, and B. Ma, "A review of design optimization methods for electrical machines," *Energies*, vol. 10, no. 12, 2017.

[90] M. E. Beniakar, P. E. Kakosimos, and A. G. Kladas, "Strength pareto evolutionary optimization of an in-wheel PM motor with unequal teeth for electric traction," *IEEE Trans. Magn.*, vol. 51, no. 3, pp. 1–4, 2015.

[91] A. M. Silva, F. J. T. E. Ferreira, M. V. Cistelecan, and C. H. Antunes, "Multiobjective Design Optimization of Generalized Multilayer Multiphase AC Winding," *IEEE Trans. Energy Convers.*, vol. 8969, no. c, pp. 1–10, 2019.

[92] X. Zhu, Z. Xiang, L. Quan, W. Wu, and Y. Du, "Multimode Optimization Design Methodology for a Flux-Controllable Stator Permanent Magnet Memory Motor Considering Driving Cycles," *IEEE Trans. Ind. Electron.*, vol. 65, no. 7, pp. 5353–5366, 2018.

[93] G. Bramerdorfer, J. A. Tapia, J. J. Pyrhonen, and A. Cavagnino, "Modern Electrical Machine Design Optimization: Techniques, Trends, and Best Practices," *IEEE Trans. Ind. Electron.*, vol. 65, no. 10, pp. 7672–7684, 2018.

[94] K. Deb, A. Member, A. Pratap, S. Agarwal, and T. Meyarivan, "A fast and elitist multi-objective genetic algorithm:NSGAII," *182 IEEE Trans. Evol. Comput.*, vol. 6, no. 2, pp. 182–197, 2002.

[95] J. Hui, M. Gao, and Y. Wang, "Design and optimisation of transverse flux machine with passive rotor and flux-concentrating structure," *IET Electr. Power Appl.*, vol. 13, no. 7, pp. 922–931, 2019.

[96] W. Zhao, A. Ma, J. Ji, X. Chen, and T. Yao, "Multi-Objective Optimization of a Double-Side Linear Vernier PM Motor Using Response Surface Method and Differential Evolution," *IEEE Trans. Ind. Electron.*, vol. PP, no. c, pp. 1–1, 2019.

[97] W. Yan *et al.*, "Design and multi-objective optimisation of switched reluctance machine with iron loss," *IET Electr. Power Appl.*, vol. 13, no. 4, pp. 435–444, 2019.

[98] A. Shah Mohammadi, J. P. F. Trovão, and C. H. Antunes, "Component-Level Optimization of Hybrid Excitation Synchronous Machines for a Specified Hybridization Ratio Using NSGA-II," *IEEE Trans. Energy Convers.*, no. under review, 2020.

[99] M. H. Mohammadi and D. A. Lowther, "A Computational Study of Efficiency Map Calculation for Synchronous AC Motor Drives including Cross-Coupling and Saturation Effects," *IEEE Trans. Magn.*, vol. 9464, no. c, pp. 1–1, 2017.

[100] C. Cavallaro, A. O. Di Tommaso, R. Miceli, A. Raciti, G. R. Galluzzo, and M. Trapanese, "Efficiency Enhancement of Permanent-Magnet Synchronous Motor Drives by Online Loss Minimization Approaches," *IEEE Trans. Ind. Electron.*, vol. 52, no. 4, pp. 1153–1160, 2005.

[101] Y. Kim, S. Member, and K. Nam, "Copper-Loss-Minimizing Field Current Control Scheme for Wound Synchronous Machines," vol. 32, no. 2, pp. 1335–1345, 2017.

[102] M. Bonislawski, M. Holub, and R. Palka, "Minimization of machine and inverter losses in hybrid excited machines for electric vehicles Key words," vol. 1, no. 3, pp. 171–175, 2016.

[103] Y. Amara *et al.*, "Flux weakening of hybrid synchronous machines," *IEMDC 2001 - IEEE Int. Electr. Mach. Drives Conf.*, pp. 367–373, 2001.
[104] N. Patin, L. Vido, E. Monmasson, J. P. Louis, M. Gabsi, and M. Lecrivain, "Control of a hybrid excitation synchronous generator for aircraft applications," *IEEE Trans. Ind. Electron.*, vol. 55, no. 10, pp. 3772–3783, 2008.
[105] L. Kefsi, Y. Touzani, and M. Gabsi, "Hybrid excitation synchronous motor control with a new flux weakening strategy," *2010 IEEE Veh. Power Propuls. Conf. VPPC 2010*, 2010.
[106] I. Boldea and V. Coroban-schramel, "BEGA Starter/Alternator—Vector Control Implementation and Performance for Wide Speed Range at Unity Power Factor Operation," *IEEE Trans. Ind. Appl.*, vol. 46, no. 1, pp. 150–158, 2010.
[107] Y. W. Z. Deng, "Parallel hybrid excitation machines and their control schemes for DC generation system," *IET Electr. Power Appl.*, vol. 6, no. 9, pp. 669–680, 2012.
[108] F. G. Capponi, G. Borocci, G. De Donato, and F. Caricchi, "Flux Regulation Strategies for Hybrid Excitation Synchronous Machines," *IEEE Trans. Ind. Appl.*, vol. 51, no. 5, pp. 3838–3847, 2015.
[109] J. J. Eckert, L. C. A. Silva, E. S. Costa, F. M. Santiciolli, F. G. Dedini, and F. C. Corrêa, "Electric vehicle drivetrain optimisation," *IET Electrical Systems in Transportation*, vol. 7, no. 1. pp. 32–40, 2017.
[110] P. D. Walker, S. A. Rahman, B. Zhu, and N. Zhang, "Modelling, Simulations, and Optimisation of Electric Vehicles for Analysis of Transmission Ratio Selection," *Adv. Mech. Eng.*, vol. 5, 2013.
[111] N. A. Patil, J. S. Lawler, and J. W. McKeever, "Determining constant power speed ratio of the induction motor from equivalent circuit parameters," *Conf. Proc. - IEEE SOUTHEASTCON*, pp. 460–467, 2008.
[112] P. B. Reddy, T. M. Jahns, and A. M. El-Refaie, "Impact of Winding Layer Number and Slot/Pole Combination on AC Armature Losses of Synchronous Surface PM Machines Designed for Wide Constant-Power Speed Range Operation," in *IEEE Industry Applications Society Annual Meeting*, 2008, pp. 1–8.
[113] M. Ehsani, Y. Gao, and S. Gay, "Characterization of Electric Motor Drives for Traction Applications," *IECON Proc. (Industrial Electron. Conf.*, vol. 1, pp. 891–896, 2003.
[114] P. Zhang, D. M. Ionel, and N. A. O. Demerdash, "Saliency Ratio and Power Factor of IPM Motors with Distributed Windings Optimally Designed for High Efficiency and Low-Cost Applications," *IEEE Trans. Ind. Appl.*, vol. 52, no. 6, pp. 4730–4739, 2016.
[115] A. S. Mohammadi and J. P. Trovao, "Electric Motors Evaluation Algorithm Based on Their Effect on Electric Vehicle Mass Reduction," in *IEEE Vehicle Power and Propulsion Conference (VPPC)*, 2016, pp. 1–6.
[116] Y. Amara, L. Vido, M. Gabsi, E. Hoang, M. Lecrivain, and F. Chabot, "Hybrid Excitation Synchronous Machines: Energy Efficient Solution for Vehicle Propulsion," *IEEE Veh. Power Propuls. Conf.*, vol. 58, no. 5, pp. 1–6, 2009.
[117] J. P. Trovao, M.-A. Roux, E. Menard, and M. Dubois, "Energy- and Power-Split

Management of Dual Energy Storage System for a Three-Wheel Electric Vehicle," *IEEE Trans. Veh. Technol.*, vol. 9545, no. c, pp. 1–1, 2016.
[118] J. Larminie and J. Lowry, *Electric Vehicle Technology Explained*. 2012.
[119] T.A. Lipo and M. Aydin, "Field Weakening of Permanent Magnet Machines – Design Approaches," *Univ. Wisconsin - Madison*, 2004.
[120] R. Mbayed, G. Salloum, E. Monmasson, and M. Gabsi, "Hybrid excitation synchronous machine finite simulation model based on experimental measurements," *IET Electr. Power Appl.*, vol. 10, no. 4, pp. 304–310, 2016.
[121] Y. Gao, R. Qu, D. Li, and J. Li, "A Novel Hybrid Excitation Flux Reversal Machine for Electric Vehicle Propulsion," in *IEEE Vehicle Power and Propulsion Conference (VPPC)*, 2016, pp. 1–6.
[122] R. Mbayed, G. Salloum, L. Vido, E. Monmasson, and M. Gabsi, "Control of a hybrid excitation synchronous generator connected to a diode rectifier supplying a DC bus," *IET Electr. Power Appl.*, vol. 7, no. 1, pp. 68–76, 2013.
[123] R. Mbayed, G. Salloum, L. Vido, E. Monmasson, and M. Gabsi, "Hybrid excitation synchronous motor control in electric vehicle with copper and iron losses minimization," *IECON Proc. (Industrial Electron. Conf.*, pp. 4886–4891, 2012.
[124] T. M. Jahns, "Component rating requirements for wide constant power operation of interior PM synchronous machine drives," *Conf. Rec. 2000 IEEE Ind. Appl. Conf. Thirty-Fifth IAS Annu. Meet. World Conf. Ind. Appl. Electr. Energy (Cat. No.00CH37129)*, vol. 3, no. 1, pp. 1697–1704, 2000.
[125] E. Ben Sedrine, J. Ojeda, M. Gabsi, and I. Slama-Belkhodja, "Fault-tolerant control using the GA optimization considering the reluctance torque of a five-phase flux switching machine," *IEEE Trans. Energy Convers.*, vol. 30, no. 3, pp. 927–938, 2015.
[126] F. Van der Sluis, L. Romers, G.-J. Van Spijk, and I. Hupkes, "CVT, Promising Solutions for Electrification," in *SAE Technical Paper*, 2019.
[127] Y. Liu, Z. Zhang, and X. Zhang, "Design and Optimization of Hybrid Excitation Synchronous Machines with Magnetic Shunting Rotor for Electric Vehicle Traction Applications," *IEEE Trans. Ind. Appl.*, vol. 53, no. 6, pp. 5252–5261, 2017.
[128] B. G. You, J. S. Kim, B. K. Lee, G. B. Choi, and D. W. Yoo, "Optimization of powder core inductors of buck-boost converters for hybrid electric vehicles," *J. Electr. Eng. Technol.*, vol. 6, no. 4, pp. 527–534, 2011.
[129] J. Perho, "Reluctance Network for Analysing Induction Machines," Helsinki University of Technology, Finland, 2002.
[130] Ranjit K. Roy, *A primer on the Taguchi Method*, Second edi. Society of Manufacturing Engineers, 1990.
[131] D. Kalyanmoy and B. A. Ram, "Simulated Binary Crossover for Continuous Search Space," *Complex Syst.*, vol. 9, no. 2, pp. 115–148, 1995.
[132] M. M. Raghuwanshi and O. G. Kakde, "Survey on multiobjective evolutionary and real coded genetic algorithms," in *Proceedings of the 8th Asia Paciflc Symposium on Intelligent and Evolutionasy Systems*, 2004, pp. 150–161.
[133] A. Seshadri, "NSGA-II: A multi-objective optimization algorithm," *MAT-Lab Cent. Implementierung*, 2009.
[134] D. A. Staton, R. P. Deodhar, S. Member, W. L. Soong, T. J. E. Miller, and S. Member,

"Torque Prediction Using the Flux-MMF in AC , DC , and Reluctance Motors," *IEEE Trans. Ind. Appl.*, vol. 32, no. 1, pp. 180–188, 1996.

[135] K. Hoang, L. Vido, M. Gabsi, and F. Gillon, "Flux control range broadening and torque ripple minimization of a double excitation synchronous motor," *IEEE Trans. Magn.*, vol. 53, no. 1, pp. 1–10, 2017.

[136] L. Vido, Y. Amara, M. Gabsi, M. Lécrivain, and F. Chabot, "Compared performances of homopolar and bipolar hybrid excitation synchronous machines," *Conf. Rec. - IAS Annu. Meet. IEEE Ind. Appl. Soc.*, vol. 3, pp. 1555–1560, 2005.

[137] M. Le Guyadec, L. Gerbaud, E. Vinot, V. Reinbold, and C. Dumont, "Use of reluctance network modelling and software component to study the influence of electrical machine pole number on hybrid electric vehicle global optimization," *Math. Comput. Simul.*, vol. 158, pp. 79–90, 2019.

[138] F. C. Trutt, E. A. Erdfilyi, and R. E. Hopkins, "Representation of the Magnetization Characteristic of DC Machines for Computer Use," *IEEE Trans. Power Appar. Syst.*, vol. PAS-87, no. 3, pp. 665–669, 1968.

[139] J. Rivas, C. Pereira, and E. Martín, "Simple Approximation for Magnetization Curves and Hysteresis Loops," *IEEE Trans. Magn.*, vol. 17, no. 4, pp. 1498–1502, 1981.

[140] J. Cale, S. D. Sudhoff, and J. Turner, "An Improved Magnetic Characterization Method for Highly Permeable Materials," *IEEE Trans. Magn.*, vol. 42, no. 8, pp. 1974–1981, 2006.

[141] G. Liu, S. Jiang, W. Zhao, and Q. Chen, "A new modeling approach for permanent magnet Vernier machine with modulation effect consideration," *IEEE Trans. Magn.*, vol. 53, no. 1, pp. 1–12, 2017.

[142] G. Liu, L. Ding, W. Zhao, Q. Chen, and S. Jiang, "Nonlinear equivalent magnetic network of a linear permanent magnet vernier machine with end effect consideration," *IEEE Trans. Magn.*, vol. 54, no. 1, 2018.

[143] D. Lin, P. Zhou, W. N. Fu, Z. Badics, and Z. J. Cendes, "A dynamic core loss model for soft ferromagnetic and power ferrite materials in transient finite element analysis," *IEEE Trans. Magn.*, vol. 40, no. 2 II, pp. 1318–1321, 2004.

[144] C. C. Chan, "The state of the art of electric and hybrid vehicles," *Proc. IEEE*, vol. 90, no. 2, pp. 247–275, 2002.

[145] Z. Rahman, K. Butler, and M. Ehsani, "Effect of extended-speed, constant-power operation of electric drives on the design and performance of EV-HEV propulsion system," *Sae Tech. Pap. Ser.*, no. 2000-01–1557, 2000.

[146] E. Power, O. A. Mahgoub, and S. A. Zaid, "Development of a New Approach for Wide Speed Range of PMSM Mohamed Taha Keywords Mathematical model of a PMSM for vector control," *Power Electron. Appl. (EPE'15 ECCE-Europe)*, pp. 1–10, 2015.

[147] B. S. Umesh and K. Sivakumar, "Multiphase induction motor drive with 1:3:9:15 speed ratios for gear free electric vehicle application," *7th International Conference on Information and Automation for Sustainability*. pp. 1–6, 2014.

[148] L. Masisi and P. Pillay, "Control Strategy for a Variable Winding Synchronous

Reluctance Machine for Traction Applications," *Vehicle Power and Propulsion Conference (VPPC), 2015 IEEE*. pp. 1–4, 2015.
[149] M. Taha, O. A. Mahgoub, and S. A. Zaid, "Development of a new approach for wide speed range of PMSM," *Power Electronics and Applications (EPE'15 ECCE-Europe), 2015 17th European Conference on*. pp. 1–10, 2015.
[150] J. P. Trovão and M. R. Dubois, "Battery and SuperCapacitor Hybridization for a Pure Electric Three-Wheel Roadster," 2015.
[151] G. Y. Lu and D. W. Wong, "An adaptive inverse-distance weighting spatial interpolation technique," *Comput. Geosci.*, vol. 34, no. 9, pp. 1044–1055, 2008.
[152] Z. Xu, J. Guan, and J. Zhou, "A distributed inverse distance weighted interpolation algorithm based on the cloud computing platform of Hadoop and its implementation," *Fuzzy Systems and Knowledge Discovery (FSKD), 2015 12th International Conference on*. pp. 2412–2416, 2015.
[153] A. C. Ortiz F., Buisset R., "VEDELIC: New Technologies for Electric Vehicles, Results of Tests and Demonstration," in *Proceedings 15th Electric Vehicle Symposium, Brussels*, 1998.
[154] F. Machado and C. H. Antunes, "Semi-Active Hybrid Topology with Three-level DC-DC Converter for Electric Vehicle Application," 2015.
[155] X. Wu, B. Cao, X. Li, J. Xu, and X. Ren, "Component sizing optimization of plug-in hybrid electric vehicles," *Appl. Energy*, vol. 88, no. 3, pp. 799–804, 2011.
[156] K. Ahn, A. E. Bayrak, and P. Y. Papalambros, "Electric Vehicle Design Optimization: Integration of a High-Fidelity Interior-Permanent-Magnet Motor Model," *IEEE Trans. Veh. Technol.*, vol. 64, no. 9, pp. 3870–3877, 2015.
[157] E. Carraro, M. Morandin, and N. Bianchi, "Traction PMASR Motor Optimization According to a Given Driving Cycle," *IEEE Trans. Ind. Appl.*, vol. 52, no. 1, pp. 209–216, 2016.
[158] S. M. Lukic and A. Emado, "Modeling of electric machines for automotive applications using efficiency maps," in *Proceedings: Electrical Insulation Conference and Electrical Manufacturing and Coil Winding Technology Conference (Cat. No.03CH37480)*, 2003.
[159] T. Letrouvé, A. Bouscayrol, W. Lhomme, N. Dollinger, and F. Mercier Calvairac, "Different models of a traction drive for an electric vehicle simulation," *2010 IEEE Veh. Power Propuls. Conf. VPPC 2010*, 2010.
[160] S. Tahi and R. Ibtiouen, "Finite Element Calculation of the dq -Axes Inductances and Torque of Synchronous Reluctance Motor," *Electr. Sci. Technol. Maghreb (CISTEM), 2014 Int. Conf.*, pp. 1–5, 2014.
[161] Z. Hanic, M. Vrazic, and Z. Maljkovic, "Steady-state synchronous machine model which incorporates saturation and cross-magnetization effects," *Int. Conf. Power Eng. Energy Electr. Drives*, vol. 5, no. 1, pp. 1553–1557, 2013.
[162] M. H. Mohammadi and D. A. Lowther, "A Computational Study of Efficiency Map Calculation for Synchronous AC Motor Drives Including Cross-Coupling and Saturation Effects," *IEEE Trans. Magn.*, vol. 53, no. 6, pp. 1–4, 2017.
[163] S. Stipetic, J. Goss, D. Zarko, and M. Popescu, "Calculation of Efficiency Maps Using a Scalable Saturated Model of Synchronous Permanent Magnet Machines," *IEEE*

Trans. Ind. Appl., vol. 54, no. 5, pp. 4257–4267, 2018.

[164] J. Goss, P. H. Mellor, R. Wrobel, D. A. Staton, and M. Popescu, "The design of AC permanent magnet motors for electric vehicles: a computationally efficient model of the operational envelope," *6th IET Int. Conf. Power Electron. Mach. Drives (PEMD 2012)*, pp. B21–B21, 2012.

[165] P. Liang, F. Chai, L. Chen, and Y. Wang, "Analytical prediction of no-load stator iron losses in spoke-Type permanent-magnet synchronous machines," *IEEE Trans. Energy Convers.*, vol. 33, no. 1, pp. 252–259, 2018.

[166] "Hysteresis Dynamometers - HD Series Dynamometer Specifications." [Online]. Available: http://www.magtrol.com/motortest/hd_specifications.html. [Accessed: 13-Dec-2017].

[167] "SEMIKRON 08753450BB." [Online]. Available: http://shop.semikron.com/en/Products-and-Shop/Product-Groups/STACKs/SEMITEACH/SEMITEACH-B6U-E1CIF-B6CI.html. [Accessed: 13-Dec-2017].

[168] "Valbruna Catalogue: Soft Magnetic Steels, stainless steel and iron–silicon alloys." .

[169] "Hybrid deep groove ball bearings, single row." [Online]. Available: https://www.skf.com/group/products/bearings-units-housings/engineered-products/hybrid-bearings/deep-groove-ball-bearings-single-row-hybrid-bearings/index.html. [Accessed: 08-Jan-2020].

[170] HitachiMetals, "Magnet wire: Selection and use directions for magnet wire," *White Pap.*, 2015.